Flexible Organic Crystalline Materials for Photonic Integrated Circuits

A Thesis Submitted in Partial Fulfilment for the DOCTOR OF PHILOSOPHY



BY

JADA RAVI

Reg. No: 16CHPH11

School of Chemistry
University of Hyderabad
(An Institution of Eminence)
Hyderabad-500046
INDIA
June-2022

Dedicated to my Beloved Parents and Brothers

CONTENTS

Declaration			
Certificate			II
Acknowledge	nents		III-IV
List of Acrony	ns		V-IX
Chapter-1	Introduction		1-44
1.1.	Photonic Integrated Ci	rcuits (PICs)	1
1.2.	Silicon-based PICs		3
1.3.	Types of Inorganic Mat	erials for PICs Fabrication	3
1.4.	Optical Properties of Materials	Inorganic and Organic	5
1.5.	Principles of Optical Co	nfinement in Waveguides	8
	1.5.1. Optical Losses i	n Waveguides	9
1.6.	Fabry–Pérot (F-P) and (WGM) Resonators	Whispering Gallery Mode	13
	1.6.1. Parameters of Resonators	Interest in WGM and F-P	14
	1.6.1.1. Free Spe	ctral Range (FSR)	14
	1.6.1.2. Quality I	-actor (Q)	15
	1.6.1.3. Photon L	ifetime (τ _P)	16
	1.6.1.4. Finesse ((F)	16
	1.6.1.5. Spatial S	tructure of Optical WGMs	16
	1.6.1.6. Mode Vo	olume (V _{eff})	17
1.7.	Silicon-based Compone	ents for PICs Fabrication	17

	1.7.1.	Silicon Waveguides	17
	1.7.2.	Directional Couplers (DCs)	19
	1.7.3.	Silicon Microring Resonators	19
	1.7.4.	Add-Drop Filters	20
1.8.	Drawba	acks of Si-based PICs	21
1.9.	All-orga	anic Material Platforms	22
1.10.	Active a	and Passive Organic Optical Waveguides	23
1.11.	Mechai Crystall	nical Characteristics of Organic ine Materials	24
	1.11.1.	Characteristics of Mechanically Flexible Organic Crystals	25
	1.11.2.	Brittle Crystals	26
	1.11.3.	Mechanically Bendable Elastic Crystals	27
	1.11.4.	Mechanically Bendable Plastic Crystals	30
1.12.		nophotonics (Mechanical Processing of Crystals)	33
	1.12.1.	Pathways to Applying Crystal Manipulation Techniques (Mechanophotonics) Toward OPICs	35
1.13.		e Organic Crystal Photonic Components Cs Fabrication	36
	1.13.1.	2×2 Directional Couplers	36
	1.13.2.	Organic Mach-Zehnder Interferometers	37
	1.13.3.	Organic Add-Drop Filters	38

	1.13.4. Organic Microlasers	40
1.14.	Overview of thesis	41
Chapter-2	Mechanically Reconfigurable Organic Photonic Integrated Circuits Made from Two Electronically Different Flexible Microcrystals	45-63
2.1.	Abstract	46
2.2.	Introduction	46
2.3.	Results and Discussion	47
	2.3.1. Synthesis of DPIN and BPIN	47
	2.3.2. Preparation of Microcrystals	50
	2.3.3. Single Crystal X-ray Diffraction (SCXRD) and Molecular Packing Analysis of BPEA	50
	2.3.4. UV-Visible Spectroscopy Studies	52
	2.3.5. Mechanical and Photonic Aspects of Microcrystals	53
	2.3.6. Fabrication of μ-OPICs from Microcrystals	57
2.4.	Conclusion	62
Chapter-3	Micromechanical Fabrication of Resonator Waveguides Integrated Four-Port Photonic Circuit from Flexible Organic Single Crystals	
3.1.	Abstract	65
3.2.	Introduction 6	
3.3.	Results and discussion	

	3.3.1.	Mechanical Flexibility and Optical Properties of DPIN	66
	3.3.2.	Optical Waveguiding Studies of DPIN Microcrystal	67
	3.3.3.	Mechanical Bending of DPIN Crystal into a Ring-Resonator	68
	3.3.4.	Fabrication of DPIN Crystal Circuit	70
3.4.	Conclus	sion	74
Chapter-4	Organi from	etrically Reconfigurable, 2D, All- c Photonic Integrated Circuits Made Two Mechanically and Optically ilar Crystals	75-92
4.1.	Abstrac	t	76
4.2.	Introdu	Introduction	
4.3.	Results and Discussion		77
	4.3.1.	Synthesis of NDIPH	77
	4.3.2.	Preparation of BPEA and NDIPH Microcrystals	77
	4.3.3.	Single Crystal X-ray Structure Analysis of BPEA and NDIPH	78
	4.3.4.	UV-Visible Spectroscopy Studies	80
	4.3.5.	Micromechanical Manipulation of NDIPH and BPEA Crystals	81
	4.3.6.	Mechano-photonic Studies of OPICs	86
4.4.	Conclus	ion	91

Chapter-5	Maneu Hybrid	ıverable	c Chip fo	Ports in a second secon	echanically n Organic Steering of	93-112
5.1.	Abstrac	t				94
5.2.	Introdu	ction				94
5.3.	Results	and Discu	ssion			95
	5.3.1.	Synthesis	of CPIN			95
	5.3.2.	Preparation Microcrys	on of DPIN tals	and CPIN		97
	5.3.3.	Structural DPIN Crys		lexibility (of CPIN and	97
	5.3.4.	Optical Pr	operties o	f CPIN and	I DPIN	99
	5.3.5.		ion of Ring Properties		(RR) and its	100
	5.3.6.	Fabrication of CPIN	n of FOPIC	-A from R	R and OW2	102
	5.3.7.	Optical W	aveguiding	g Studies o	of FOPIC-A	104
	5.3.8.	Construct	ion of FOP	IC-B from	FOPIC-A	105
	5.3.9.	Fabricatio	n of FOPIC	s I–IV fror	n FOPIC-B	105
	5.3.10.	Optical W	aveguiding	g Studies o	of FOPIC-I-IV	106
5.4.	Conclus	sion				111
Chapter-6	Summ	ary				113-115
	References			116-123		

Appendix A (Materials)	124
Appendix B (Instrumentation)	125
Appendix C (Crystal data)	129
Research Publications	131
Presentations in Conferences and Symposiums	133
Curriculum Vitae	134

DECLARATION

I hereby declare that the matter embodied in this thesis entitled "Flexible Organic Crystalline Materials for Photonic Integrated Circuits" is the result of investigations carried out by me at the School of Chemistry, in the University of Hyderabad, Hyderabad, India under the supervision of Prof. Rajadurai Chandrasekar.

In keeping with the general practice in reporting scientific observations, due acknowledgements have been made wherever the work described is based on the finding of other investigators. Any omission that might have occurred due to oversight or error in judgement is regretted.

Jada Ravi

Reg. No: 16CHPH11



CERTIFICATE

This is to certify that the thesis entitled "Flexible Organic Crystalline Materials for Photonic Integrated Circuits" submitted by Jada Ravi bearing registration number 16CHPH11 in partial fulfillment of the requirements for the award of Doctor of Philosophy in the School of Chemistry is bonafide work carried out by him under my supervision and guidance. This thesis is free from plagiarism and has not been submitted previously in part or in full to this or any other University or institution to award any degree or diploma. Further, the student has 15 publications before submitting the thesis for adjudication and has produced evidence for the same in the form of reprints.

Parts of this thesis have been published in the following four publications:

- 1. J. Ravi et. al. Adv. Funct. Mater. 2021, 31, 2100642 (Chapter-2)
- 2. J. Ravi et. al. Adv. Opt. Mater. 2021, 9, 2100550 (Chapter-3)
- 3. J. Ravi et. al. Adv. Funct. Mater. 2021, 31, 2105415 (Chapter-4)
- 4. J. Ravi et. al. Adv. Opt. Mater. 2022, 10, 2102545 (Chapter-5)

He has also presented oral/poster presentations in the following conferences:

- 1. Oral presentation, CHEMFEST-2021, SoC, UoH, Hyderabad, India.
- 2. Poster presentation in CHEMFEST-2021, SoC, UoH, Hyderabad, India.
- Poster presentation in DCBCS-2021, GITAM University, Visakhapatnam, and Hyderabad, India.

Further, the student has passed the following courses towards the fulfillment of the coursework requirement for Ph. D.:

	Course	Title	Credits	Pass/Fail
1.	CY-801	Research Proposal	3	Pass
2.	CY-805	Instrumental Methods A	3	Pass
3.	CY-806	Instrumental Methods B	3	Pass
4.	CY-454	Statistical Thermodynamics	3	Pass

Prof. Rajadurai Chandrasekar

(Ph.D. Supervisor)

Dr. R. CHANDRASEKAR
Professor
School of Chemistry
University of Hyderabad
Hyderabad-500046, India

Arlini Mangre Dean

School of Chemistry

Dean
School of Chemistry
University of Hyderabad
P.O. Central University
Gachibowli, Hyderabad-500 046.

ACKNOWLEDGEMENT

On the occasion of the completion of my thesis, it is my pleasure to express my sincere gratitude for all those support and encouragement made my Ph. D. research journey much easier.

First of all, I would like to express my sincere thanks to my supervisor, Prof. Rajadurai Chandrasekar; without his innovative ideas and thoughts, it would not have been possible to accomplish my dissertation. I am grateful to him for allowing me to work on the topic of Flexible Organic Crystals for Photonic Circuit Applications. I take this opportunity to express my gratitude to my mentor for the beneficial discussions during group meetings. Instead of being in the limelight, my supervisor guided, encouraged, and provided support from the back of the stage. His approach to a scientific problem, interpreting the data, developing concepts, and reaching a conclusion instigated me to improve substantially in scientific research. It has been a wonderful experience working with him. I hope to keep this scientific experience as a source of inspiration and creativity for my future endeavors.

Also, I would like to acknowledge my doctoral committee members, Prof. Samar Kumar Das and Prof. K. Muralidharan for their valuable suggestions. I thank the present and former Deans for the excellent facilities in the department.

My special gratitude to Prof. Panče Naumov, and Dr. Durga Prasad Karothu, New York University, Abu Dhabi, for crystal data, mechanical studies, and fruitful collaboration.

The five years in the RC lab were intellectually stimulating. I am grateful for the numerous discussions with past and present students and postdocs: Dr. M. Annadhasan, Dr. G. Mallesham, Dr. D. Venkatakrishnarao, Dr. U. Venkataramudu, Dr. V. Radhika, V. Vinay Pradeep. A. Vinod Kumar, Rohullah, M. Jyothi, J. Melchi, A. Khapre, G. Sinduja, and A. Anand Kumar.

I extend my gratitude to the financial sponsor, UGC, New Delhi for providing a research fellowship and the Centre for Nanotechnology (CFN) for various instrument facilities. I am thankful to University of Hyderabad for the excellent atmosphere and world-class research facilities. It's my pleasure to acknowledge all the faculty and

nonteaching staff, Mr. Sunil for FESEM analysis, Mr. Durgesh for NMR measurements, and Parveige for ESI-Mass studies, and Mr. Bhaskar for LCM analysis.

I am incomplete without my family members Tejaswi, Odevva, Rekha, Ravinder, Laxmi, Saiteja, Ramya, Vignesh, Vishnu Vardhan, Ashmitha, and Srihith.

Lastly, but not least my beloved parents and brothers J. Lachaiah, J. Ellavva, J. Narsaiah, J. Shanker, struggled and suffered for me and managed to bring me up to what am today.

Jada Ravi

LIST OF ACRONYMS

BCIP	(E)-2,4-dibromo-6-(((2,5-dichlorophenyl)imino) methyl) phenol
CPIN	(E)-1-(4-(chloro)phenyl)
DPIN	Iminomethyl-2-hydroxyl-naphthalene (E)-1-(4-(dimethylamino)- phenyl)iminomethyl-2-hydroxyl-naphthalene
BPIN	(E)-1-(4-bromo)iminomethyl-2- hydroxyl-naphthalene
TPI	2,4,5-triphenylimidazole
DCM	4-(Dicyanomethylene)-2-methyl-6-(4-dimethylaminostyryl)-4H-pyran
CNB	4-chloro-3-nitrobenzoic
HAM	4-hydroxybenzoic acid-monohydrate
BPEA	9,10-bis(phenylethynyl)anthracene
DCA	9,10-dicyanoanthracene
α	Absorption coefficient
Å	Angstrom
p	Angular mode
ASPICs	Application-specific photonic integrated circuits
AMZI	Asymmetric Mach-Zehnder interferometer
AFM	Atomic force microscope
φ	Azimuthal angle
т	Azimuthal mode number
β	Beta
ав	Bohr radius
а в	Bohr radius
k	Boltzmann constant
CdS	Cadmium sulfide
CAF	Caffeine
¹³ C-NMR	Carbon nuclear magnetic resonance
cm	Centimeter
СТ	Charge-transfer
δ	Chemical shift
CW	Clockwise
CMOS	Complementary metal-oxide-semiconductor
СВ	Conduction band

H _c	Contact hardness
CCW	Counter-clockwise
θ_{c}	Critical angle
λ_c	Cut-off wavelength
dB	Decibel
Det.	Detection
CDCl ₃	Deuterated chloroform
D	Diameter
DMF	Dimethylformamide
DC	Directional coupler
m*	Effective mass
$m_{ m e}^*$	Effective mass of electron
m_{h}^*	Effective mass of hole
$m_{ m eff}$	Effective reduced mass
n _{eff}	Effective refractive index
ε	Electric permittivity
χ	Electric susceptibility
EBL	Electron beam lithography
е	Electron charge
eV	Electron volt
ET	Energy transfer
eq	Equivalent
Exc.	Excitation
Ев	Exciton binding energy
a _{ex}	Exciton Bohr radius
EP	Exciton-polariton
Q_{E}	External coupling
F-P	Fabry–Pérot
FESEM	Field emission scanning electron microscopy
F	Finesse
FDTD	Finite difference time domain
FOPIC	Flexible organic photonic integrated circuit
FL	Fluorescence
ε_0	Free space permittivity
FSR	Free spectral range
FWHM	Full width at half maximum

CaN	
GaN	Gallium nitride
GPa	Gigapascal
h	Height
НСВ	Hexachlorobenzene
НОМО	Highest occupied molecular orbital
InP	Indium phosphide
l _{in}	Inner crystal length
P _{in}	Input laser power
1/0	Input/Output
ltip	Intensity at collection point
lbody	Intensity at excitation point
Q_{L}	Intrinsic cavity loss
INAH	Isonicotinic acid hydrazide
K	Kelvin
PbS	Lead sulphide
L	Length
LiDAR	Light detection and ranging
Δω	Line-width of the resonant mode
LUMO	Lowest unoccupied molecular orbital
LPCVD	Low-pressure chemical vapor deposition
MZI	Mach-Zehnder interferometer
m	Mass of electron
MHz	Megahertz
m.p.	Melting point
MOSFET	Metal oxide semiconductor field-effect transistor
μ	Micro
μL	Microliter
μт	Micrometer
MIR	Mid-infrared
meV	Millielectron volt
mL	Milliliter
mm	Millimeter
mmol	Millimoles
m	Mode number
V _{eff}	Mode volume

NDIPH	N,N'-bis(p-tolyl)-1,4,5,8-naphthalenediimide
ns	Nano second
nm	Nanometer
NIR	Near-infrared
NLO	Non-linear optics
NMR	Nuclear magnetic resonance
1D	One-dimensional
α΄	Optical loss
OW	Optical waveguide
OPIC	Organic photonic integrated circuit
I ₀	Original crystal length
lout	Outer crystal length
Pout	Output laser power
II	Parallel
ppm	Parts per million
%	Percentage
Т	Perpendicular
PL	Photoluminescence
Tρ	Photon lifetime
PIC	Photonic integrated circuit
pm	Picometer
π-π	Pi-Pi interaction
PECVD	Plasma-enhanced chemical vapor deposition
θ	Polar angle
1	Polar mode number
Р	Power
Т	Power transmission ratio
¹ H-NMR	Proton nuclear magnetic resonance
Q	Quality factor
q	Radial mode number
R	Radius
Rc	Radius of curvature
μ	Reduced mass
ħ	Reduced Planck's constant
θ ₁	Reflected beam angle
θ_2	Refracted beam angle

μr Relative permittivity ω Relative permittivity ω Resonance frequency RR Ring-resonator RT Room temperature SEM Scanning electron microscope χ(2) Second order electric susceptibility Si Silicon SiO2 Silicon dioxide Silicon Silicon order electric susceptibility Si Silicon SiO2 Silicon dioxide Silicon Silicon order electric susceptibility SiO Silicon dioxide Silicon Silicon order electric susceptibility Silicon Silicon order electric Strain Silicon order electrics Strain Silicon order electric T Temperature TO Theresonal order electric TC Thiacyanie 3D Three dimensional 3PL Three photon luminescence Ø Total internal reflection TE Transverse electric TM Transverse magnetic<	n	Refractive index
ω Resonance frequency RR Ring-resonator RT Room temperature SEM Scanning electron microscope X ⁽²⁾ Second order electric susceptibility Si Silicon SiO2 Silicon dioxide SiO2 Silicon nitride SOI Silicon-on-insulator SC-XRD Single crystal X-ray diffraction ε Strain σ Stress T Temperature TO Thermo-optic TC Thiacyanine 3D Three dimensional 3PL Three photon luminescence O Torsional angle TIR Total internal reflection TE Transverse electric TM Transverse magnetic 2D Two-dimensional 2PL Two-photon luminescence UV Ultraviolet VIS Visible D Wavelength Visible Wavelength D Wavelength maximum WGM Whispering gallery mode	μr	Relative permeability
RR RT Room temperature SEM Scanning electron microscope χ ⁽²⁾ Second order electric susceptibility Si Silicon SiO ₂ Silicon dioxide Silicon nitride SOI Silicon-on-insulator SC-XRD Single crystal X-ray diffraction ε Strain σ Stress T Temperature TO Thermo-optic TC Thiacyanine 3D Three dimensional 3PL Three photon luminescence σ Tosional angle TIR Total internal reflection TE Transverse electric TM Transverse magnetic D Two-dimensional 2PL Two-photon luminescence UV Ultra violet UV-Vis Ultra violet UV-Vis Ultraviolet-visible VB Valence band VIS Visible D Waveguiding distance λ λ Manex Wavelength maximum WGM Whispering gallery mode E Young's modulus/Elastic modulus	E _r	Relative permittivity
RT SEM Scanning electron microscope χ ⁽²⁾ Second order electric susceptibility Si Silicon SiO ₂ Silicon dioxide Silicon nitride SOI Silicon-on-insulator SC-XRD Single crystal X-ray diffraction ε Strain σ Stress T Temperature TO Thermo-optic TC Thiacyanine 3D Three dimensional 3PL Three photon luminescence Θ Torsional angle TIR Total internal reflection TE Transverse electric TM Transverse magnetic 2D Two-dimensional 2PL Two-photon luminescence UV Ultra violet UV-Vis Ultra violet UV-Vis Ultra violet Visible D Waveguiding distance λ Manax Wavelength λ Manax Wavelength Wavelength maximum WGM Whispering gallery mode ε Young's modulus/Elastic modulus	ω	Resonance frequency
SEM Scanning electron microscope χ ⁽²⁾ Second order electric susceptibility Si Silicon SiO ₂ Silicon dioxide Silicon intride SOI Silicon-on-insulator SC-XRD Single crystal X-ray diffraction ε Strain σ Stress T Temperature TO Thermo-optic TC Thiacyanine 3D Three dimensional 3PL Three photon luminescence Θ Torsional angle TIR Total internal reflection TE Transverse electric TM Transverse magnetic 2D Two-dimensional 2PL Two-photon luminescence UV Ultra violet UV-Vis Ultraviolet VB Valence band VIS Visible Φ Wavelength λ _{max} Wavelength maximum WGM Whispering gallery mode E Young's modulus/Elastic modulus	RR	Ring-resonator
Second order electric susceptibility Si Silicon SiO ₂ Silicon dioxide Silicon nitride SOI Silicon-on-insulator SC-XRD Single crystal X-ray diffraction ε Strain σ Stress T Temperature TO Thermo-optic TC Thiacyanine 3D Three dimensional 3PL Three photon luminescence Θ Torsional angle TIR Total internal reflection TE Transverse electric TM Transverse magnetic 2D Two-dimensional 2PL Two-photon luminescence UV Ultra violet UV-Vis Ultraviolet UV-Vis Ultraviolet-visible VB Valence band VIS Visible D Wavelength Namax Wavelength maximum WGM Whispering gallery mode E Young's modulus/Elastic modulus	RT	Room temperature
Silicon SiO2 Silicon dioxide Silicon nitride SOI Silicon-on-insulator SC-XRD Single crystal X-ray diffraction ε Strain σ Stress T Temperature TO Thermo-optic TC Thiacyanine 3D Three dimensional 3PL Three photon luminescence Θ Torsional angle TIR Total internal reflection TE Transverse electric TM Transverse magnetic 2D Two-dimensional 2PL Two-photon luminescence UV Ultra violet UV-Vis Ultraviolet—visible VB Valence band VIS Visible D Wavelength Namax Wavelength maximum WGM Whispering gallery mode E Voung's modulus/Elastic modulus	SEM	Scanning electron microscope
SiO2 Silicon dioxide SiaN3 Silicon nitride SOI Silicon-on-insulator SC-XRD Single crystal X-ray diffraction ε Strain σ Stress T Temperature TO Thermo-optic TC Thiacyanine 3D Three dimensional 3PL Three photon luminescence Θ Torsional angle TIR Total internal reflection TE Transverse electric TM Transverse magnetic 2D Two-dimensional 2PL Two-photon luminescence UV Ultra violet UV-Vis Ultraviolet-visible VB Valence band VIS Visible D Waveguiding distance λ Wavelength λmax Wavelength maximum WGM Whispering gallery mode E Young's modulus/Elastic modulus	$\chi^{(2)}$	Second order electric susceptibility
Sol Silicon nitride Sol Silicon-on-insulator Sc-XRD Single crystal X-ray diffraction ε Strain σ Stress T Temperature TO Thermo-optic TC Thiacyanine 3D Three dimensional 3PL Three photon luminescence Θ Torsional angle TIR Total internal reflection TE Transverse electric TM Transverse magnetic 2D Two-dimensional 2PL Two-photon luminescence UV Ultra violet UV-Vis Ultra violet UV-Vis Ultraviolet—visible VB Valence band VIS Visible D Waveguiding distance λ Wavelength λ _{max} Wavelength WGM Whispering gallery mode E Young's modulus/Elastic modulus	Si	Silicon
SOI Silicon-on-insulator SC-XRD Single crystal X-ray diffraction ε Strain σ Stress T Temperature TO Thermo-optic TC Thiacyanine 3D Three dimensional 3PL Three photon luminescence Θ Torsional angle TIR Total internal reflection TE Transverse electric TM Transverse magnetic 2D Two-dimensional 2PL Two-photon luminescence UV Ultra violet UV-Vis Ultra violet UV-Vis Ultraviolet-visible VB Valence band VIS Visible D Waveguiding distance λ Wavelength λ _{max} Wavelength maximum WGM Whispering gallery mode Ε Young's modulus/Elastic modulus	SiO ₂	Silicon dioxide
SC-XRD Single crystal X-ray diffraction Strain Stress T Temperature TO Thermo-optic TC Thiacyanine 3D Three dimensional 3PL Three photon luminescence Θ Torsional angle TIR Total internal reflection TE Transverse electric TM Transverse magnetic 2D Two-dimensional 2PL Two-photon luminescence UV Ultra violet UV-Vis Ultraviolet—visible VB Valence band VIS Visible D Waveguiding distance λ Wavelength λ Wavelength Wamax Wavelength maximum WGM Whispering gallery mode E Young's modulus/Elastic modulus	Si ₄ N ₃	Silicon nitride
Strain σ Stress T Temperature TO Thermo-optic TC Thiacyanine 3D Three dimensional 3PL Three photon luminescence Θ Torsional angle TIR Total internal reflection TE Transverse electric TM Transverse magnetic 2D Two-dimensional 2PL Two-photon luminescence UV Ultra violet UV-Vis Ultraviolet—visible VB Valence band VIS Visible D Waveguiding distance λ Wavelength λ _{max} Wavelength WGM Whispering gallery mode E Young's modulus/Elastic modulus	SOI	Silicon-on-insulator
T Temperature TO Thermo-optic TC Thiacyanine 3D Three dimensional 3PL Three photon luminescence Θ Torsional angle TIR Total internal reflection TE Transverse electric TM Transverse magnetic 2D Two-dimensional 2PL Two-photon luminescence UV Ultra violet UV-Vis Ultraviolet VB Valence band VIS Visible D Waveguiding distance λ Wavelength λ _{max} Wavelength maximum WGM Whispering gallery mode E Young's modulus/Elastic modulus	SC-XRD	Single crystal X-ray diffraction
T Temperature TO Thermo-optic TC Thiacyanine 3D Three dimensional 3PL Three photon luminescence Θ Torsional angle TIR Total internal reflection TE Transverse electric TM Transverse magnetic 2D Two-dimensional 2PL Two-photon luminescence UV Ultra violet UV-Vis Ultraviolet—visible VB Valence band VIS Visible D Waveguiding distance λ Wavelength λ _{max} Wavelength maximum WGM Whispering gallery mode E Young's modulus/Elastic modulus	ε	Strain
TO Thermo-optic TC Thiacyanine 3D Three dimensional 3PL Three photon luminescence Θ Torsional angle TIR Total internal reflection TE Transverse electric TM Transverse magnetic 2D Two-dimensional 2PL Two-photon luminescence UV Ultra violet UV-Vis Ultraviolet—visible VB Valence band VIS Visible D Waveguiding distance λ Wavelength λ _{max} Wavelength maximum WGM Whispering gallery mode E Young's modulus/Elastic modulus	σ	Stress
TC Thiacyanine 3D Three dimensional 3PL Three photon luminescence Θ Torsional angle TIR Total internal reflection TE Transverse electric TM Transverse magnetic 2D Two-dimensional 2PL Two-photon luminescence UV Ultra violet UV-Vis Ultraviolet VB Valence band VIS Visible D Waveguiding distance λ Wavelength λ _{max} Wavelength maximum WGM Whispering gallery mode E Young's modulus/Elastic modulus	Т	Temperature
3D Three dimensional 3PL Three photon luminescence Θ Torsional angle TIR Total internal reflection TE Transverse electric TM Transverse magnetic 2D Two-dimensional 2PL Two-photon luminescence UV Ultra violet UV-Vis Ultraviolet—visible VB Valence band VIS Visible D Waveguiding distance λ Wavelength λ _{max} Wavelength maximum WGM Whispering gallery mode E Young's modulus/Elastic modulus	ТО	Thermo-optic
Three photon luminescence O Torsional angle TIR Total internal reflection TE Transverse electric TM Transverse magnetic 2D Two-dimensional 2PL Two-photon luminescence UV Ultra violet UV-Vis Ultraviolet—visible VB Valence band VIS Visible D Waveguiding distance λ Wavelength λ _{max} Wavelength maximum WGM Whispering gallery mode E Young's modulus/Elastic modulus	TC	Thiacyanine
Θ Torsional angle TIR Total internal reflection TE Transverse electric TM Transverse magnetic 2D Two-dimensional 2PL Two-photon luminescence UV Ultra violet UV-Vis Ultraviolet-visible VB Valence band VIS Visible D Waveguiding distance λ Wavelength λ Wavelength maximum WGM Whispering gallery mode E Young's modulus/Elastic modulus	3D	Three dimensional
$ \begin{array}{cccccccccccccccccccccccccccccccccccc$	3PL	Three photon luminescence
TETransverse electricTMTransverse magnetic2DTwo-dimensional2PLTwo-photon luminescenceUVUltra violetUV-VisUltraviolet—visibleVBValence bandVISVisible D Waveguiding distance λ Wavelength λ_{max} Wavelength maximumWGMWhispering gallery mode E Young's modulus/Elastic modulus	Θ	Torsional angle
TM Transverse magnetic 2D Two-dimensional 2PL Two-photon luminescence UV Ultra violet UV-Vis Ultraviolet—visible VB Valence band VIS Visible D Waveguiding distance λ Wavelength λ _{max} Wavelength maximum WGM Whispering gallery mode E Young's modulus/Elastic modulus	TIR	Total internal reflection
2D Two-dimensional 2PL Two-photon luminescence UV Ultra violet UV-Vis Ultraviolet—visible VB Valence band VIS Visible D Waveguiding distance λ Wavelength λ _{max} Wavelength maximum WGM Whispering gallery mode E Young's modulus/Elastic modulus	TE	Transverse electric
$ \begin{array}{cccccccccccccccccccccccccccccccccccc$	TM	Transverse magnetic
$\begin{array}{c cccc} & & & & & & & \\ & & & & & & & \\ & & & & & & \\ & & & & & & \\ & & & & & & \\ & & & & & & \\ & & & & & & \\ & & & & & & \\ & & & & & & \\ & & & & & & \\ & & & & & & \\ & & & & & & \\ & & & & & & \\ & & & & & & \\ & & & & & \\ & & & & & \\ & & & & & \\ & & & & & \\ & & & & & \\ & & & & & \\ & & & & & \\ & & & & & \\ & & & & \\ & & & & & \\ & & & \\ & & & & \\ & & & & \\ & & & & \\ & & & \\ & & & & \\ & & & \\ & & & & \\ & & & \\ & & & & \\ & & & \\ & & & & \\ & & & & \\ & & & \\ & & & \\ & & & & \\ & & & \\ & & & \\ & & & \\ & & & \\ & & & \\ & & & & \\ & & & $	2D	Two-dimensional
$\begin{array}{cccccccccccccccccccccccccccccccccccc$	2PL	Two-photon luminescence
VB Valence band VIS Visible D Waveguiding distance λ Wavelength λ_{max} Wavelength maximum WGM Whispering gallery mode E Young's modulus/Elastic modulus	UV	Ultra violet
$\begin{array}{cccc} VIS & Visible \\ \hline \textbf{\textit{D}} & Waveguiding distance \\ \hline \lambda & Wavelength \\ \hline \lambda_{max} & Wavelength maximum \\ \hline WGM & Whispering gallery mode \\ \hline \textbf{\textit{E}} & Young's modulus/Elastic modulus \\ \hline \end{array}$	UV-Vis	Ultraviolet-visible
$\begin{array}{cccc} \textbf{\textit{D}} & & & & & & & \\ \lambda & & & & & & & \\ \lambda_{\text{max}} & & & & & & \\ \text{Wavelength} & & & & & \\ \text{Wavelength maximum} & & & & \\ \text{WGM} & & & & & & \\ \textbf{\textit{E}} & & & & & & \\ \textbf{\textit{Young's modulus/Elastic modulus}} \end{array}$	VB	Valence band
$\begin{array}{ccc} \lambda & & & & & \\ \lambda_{\text{max}} & & & & & \\ \text{WGM} & & & & & \\ \text{E} & & & & & \\ \end{array}$	VIS	Visible
λ _{max} Wavelength maximum WGM Whispering gallery mode E Young's modulus/Elastic modulus	D	Waveguiding distance
WGM Whispering gallery mode E Young's modulus/Elastic modulus	λ	Wavelength
E Young's modulus/Elastic modulus	λ_{max}	Wavelength maximum
	WGM	Whispering gallery mode
ZnO Zinc oxide	Е	Young's modulus/Elastic modulus
	ZnO	Zinc oxide

Introduction

1.1. Photonic Integrated Circuits (PICs)

The electric signal moves through electronic components in traditional electronic circuits, [1] like transistors, microcontrollers, resistors, transformers, capacitors, circuit breakers, etc. (Fig. 1.1a). In the case of photonic integrated circuits (PICs), [2] photons travel across optical components, such as optical waveguides (similar to electrical wire), cavities, electro-optic modulators, filters, and lasers (identical to transistors), polarizers, beam splitters, waveplates and so on (Fig. 1.1b). PICs are embedded on the surface of a chip, like in electronic circuits. However, PICs manipulate the light rather than the electrical signals. A PIC is operated by introducing the laser light source to the optical components, similar to how the electricity passes in the electronic components when turning on the switch of an electronic circuit. [3] PIC technology solves the electronic device's limitations by using a light source instead of electricity.

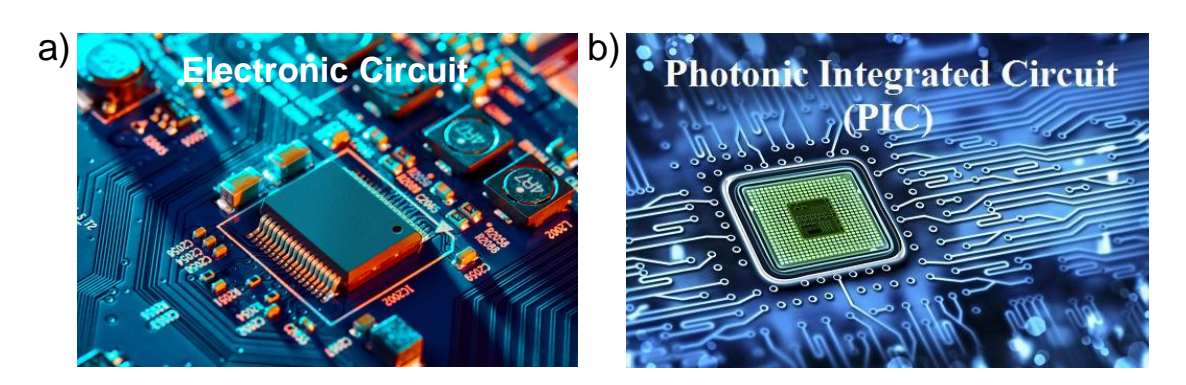


Fig. 1.1. a,b) Images of electronic and photonic integrated circuits, respectively. Figures adopted from ref. 1,2.

The PICs are good at data transfer and processing analog data, and the electronic circuits are good at digital computation. PICs are extensively used in optical communications; apart from this, they have numerous applications where light has a significant role, like biology, sensors in spectroscopy, metrology, and classical and quantum information data handling process. [4-6] Most PICs are made for one specific application, called application-specific PICs (ASPICs). Here, the optical path direction is fixed, so these PICs can be high power-efficient and compact.

The electronic circuit limitations include low efficiency, low integration ability, low thermal tolerance, and low speedy data transfer. The current electronic devices use charging and discharging to transfer information. As a result, maximum energy is expended on charge and discharge cycles instead of carrying out a logical function. Due to energy efficiency and speed, PICs are unquestionably an alternative to conventional electronic data systems.^[7] Further, the photon's coherence, ability to travel in different refractive media without being disturbed by the surroundings, and quantum-information-transmission efficiency, are crucial for the PICs.

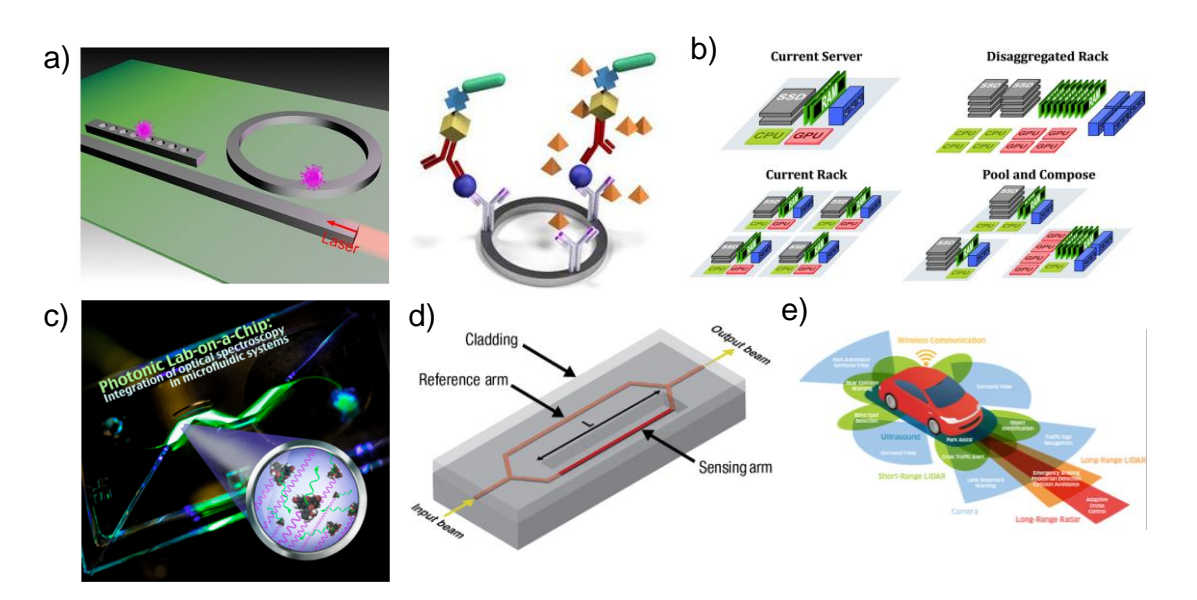


Fig. 1.2. Applications of PICs in various fields. a) On-chip optical detection of viruses, b) data center transfer communication, c) photonic lab-on-a-chip for optical spectroscopy, d) interferometric PICs in biochemical sensors, and e) Light Detection and Ranging (LiDAR) applications. Figures adopted from ref. 8-12.

PICs also have advantages like high-speed data transmission, high integration ability, miniaturization, less thermal effect, and compatibility with existing complementary-metal-oxide-semiconductor (CMOS)[†] processes.^[7,13-16] The latter advantage permits bulk production, high yield, and cost-effectiveness. Along with these, PICs have potential applications in sensors,^[12] aeronautics, the agriculture industry, biomedical lab-on-a-chip systems^[8,17] intra- and inter-data center transfer communication,^[9] aerospace, LiDAR^[11] defense industry, and astronomy (**Fig. 1.2a-e**).

[†]CMOS is a metal oxide semiconductor field-effect transistor (MOSFET) manufacturing process, which utilizes symmetrical, and complementary pairs of p-type, and n-type MOSFETs for logical operations.

1.2. Silicon-based PICs

Silicon (Si) PICs are alternatives to conventional electronic-based devices due to the latter being less energy-efficient and slower than the former. Silicon is an indirect bandgap material with the optical spectrum band covering $\lambda = 1300 - 1620$ nm. These Sibased components are optically transparent and are used widely in telecommunication systems. Si and Si-based PICs have many advantages over other materials, like high refractive index (n), fow optical bending loss, high-efficiency fiber-chip coupling, wide spectral bandwidth, amenability for fabrication with sub-submicron-sized optical waveguides, photodetectors, high-speed modulators, dense packing on the device and suitability of CMOS compatible fabrication technologies. The high n of silicon compared to silicon dioxide (SiO₂) permits dense waveguide geometry on the chip (silicon on insulator; SOI), with bending radii as small as 1 μ m. The fabrication techniques like electron-beam lithography used for electronic-based circuits are also applied for photonics-based PICs fabrication.

1.3. Types of Inorganic Materials for PICs Fabrication

Various materials like silicon, silica, and silicon nitride (Si₃N₄) are used in silicon photonics as a materials platform to produce passive optical waveguiding devices with low optical loss (**Fig. 1.3a**). The optical absorbance range of these materials is shown in **Fig. 1.3b**. [23,24] The n and thermo-optic (TO)[†] coefficients range of silica, silicon, silicon nitride (in the near-infrared range; NIR), and organic materials are listed in **Table 1.1**. The n of silicon, silicon nitride, and silica are 3.467, \approx 2, and 1.44, respectively. Silicon has the highest n among the three, allowing dense packing of optical waveguide devices.

[£]Refractive index (n): $n = \sqrt{\varepsilon_r} \mu_r$, where μ_r = relative permeability. $\mu_r \approx 1$, for nonmagnetic materials, Hence, $n = \sqrt{\varepsilon_r}$. Since ε_r is a complex function with both imaginary and real parts, $\varepsilon_r = \varepsilon'_r + \mathrm{i}\varepsilon''_r$ and so the value of n is also a complex function, $\varepsilon_r = n^2 = (n' + \mathrm{i}n'')^2$.

^{*}SOI: The fabrication of silicon semiconductor devices using SOI technology involves layering silicon-insulator-silicon substrates to reduce dependent capacitance within a device and enhance its performance.

[†]Thermo-optical (TO) coefficient: TO of a material is the variation in n with the response to temperature, n(T).



The contact hardness (H_c) and Young's modulus (*E*) of the silicon nitride are higher than silicon, silica, and organic materials (**Table 1.1**).^[25-27]

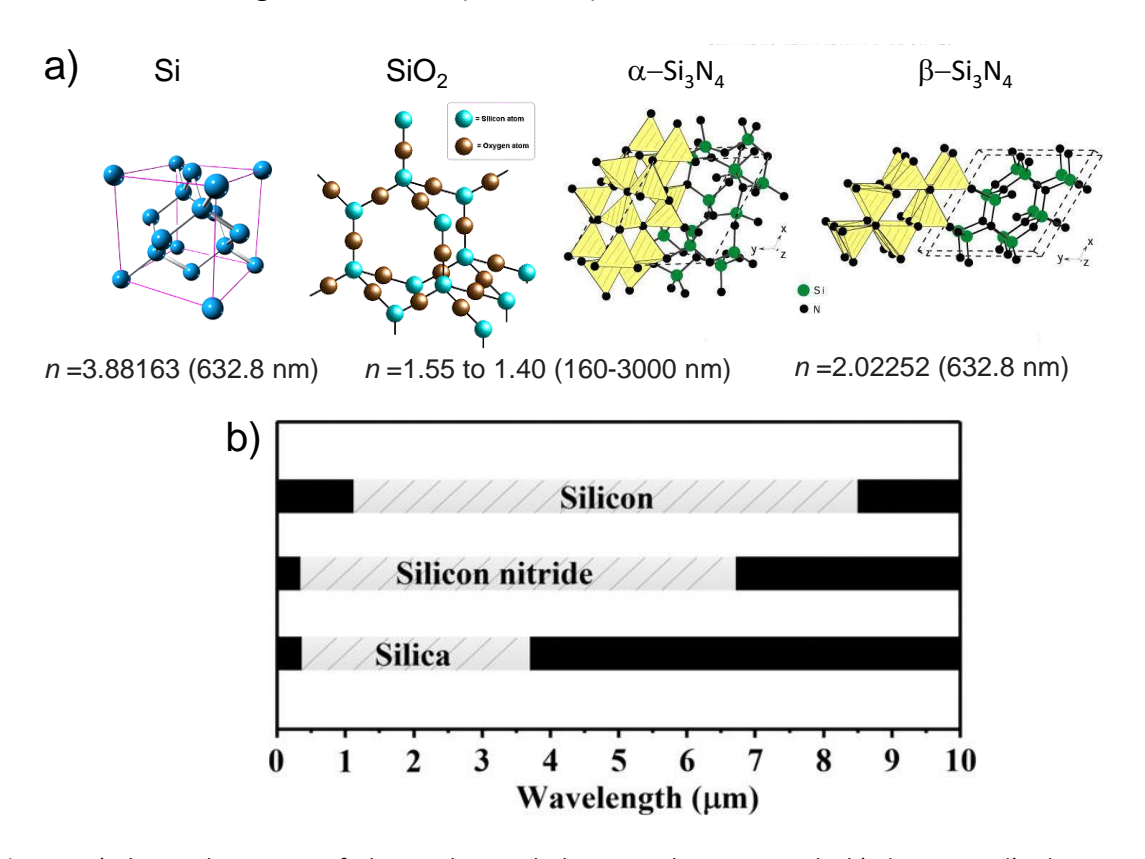


Fig. 1.3. a) Chemical structure of silicon, silica, and silicon nitride, respectively. b) The material's absorption properties of silicon, silica, and silicon nitride. The grey bands indicate the optical transparency, whereas the black bands display the absorption loss. Figure adopted from ref. 19-22.

Table 1.1. Characteristics of silicon, silica, silicon nitride, and organic crystals.

Material	Refractive index (n)	TO coefficient (K ⁻¹)	Contact hardness (H _c) GPa	Youngs modulus (E) GPa
Silicon (Si)	3.46	1.86 × 10 ⁻⁴	12.5	185
Silica (SiO ₂)	1.44	$0.95 imes 10^{-5}$	9.5	72.8
Silicon nitride (Si ₃ N ₄)	≈2	2.45 × 10 ⁻⁵	50.3	≈400
Organic materials	≈1.7	1.0 × 10 ⁻⁴	<0.15-0.72	<4—16

Silica material has low absorption in the visible to NIR region. Silica is a good material for passive PICs because it has low optical waveguide propagation loss and compatibility with

silica optical fibers.^[27] These silica-based PICs are used in the integrated passive devices for mid-infrared (MIR) telecommunication. Silicon nitride has a broad bandgap ranging from 2.7 - 5 eV upon varying the Si and N ratio. Therefore, the silicon nitride transparent window starts from the visible to MIR region.^[28] Si₃N₄ is implemented in Si devices, where the wavelength is less than 1100 nm. Silicon materials cover the NIR and MIR regions, with the absorption band ranging from 1100 to 8500 nm. These materials are not a choice for shorter wavelength range applications, for example, data communication at 850 nm.

The low-pressure chemical vapor deposition (LPCVD) and plasma-enhanced CVD (PECVD) are used to produce Si_3N_4 . In these deposition processes, LPCVD provides stoichiometry near the Si_3N_4 , and it has an n of about 2 in the telecommunication region. The photonic characteristics of the PECVD Si_3N_4 rely on the deposition process. By varying the silicon and nitrogen ratio, nitrogen-rich (lower n) or silicon-rich (higher n) optical waveguides can be achieved. Because of the large silicon's TO coefficient, a switch with ultra-low energy consumption and wavelength filters with high TO alteration coherence were realized. Per TO coefficient values of silica and silicon nitride are lower than the silicon. Silicon nitride has an insignificant two-photon absorbance in the NIR region than the silicon. The silicon nitride optical waveguides are employed in frequency comb generation and supercontinuum. [31,32]

1.4. Optical Properties of Inorganic and Organic Materials

A fascinating type of light-matter interaction in semiconductors materials is photons absorption through an inter-band optical transition. This electronic transition produces a hole in a valence band (VB), and an electron in the conduction band (CB). The electron-hole pair is bound together because of the electrostatic Coulomb forces, denoted as "exciton". In a hydrogen atom, the distance separation between the proton and its electron is 0.053 nm, called the Bohr radius (a_B). Like hydrogen atom, the exciton produced in semiconductive materials is termed as "exciton Bohr radius (a_{ex})"

$$a_{\rm ex} = \frac{4\pi \, \hbar^2 \varepsilon \, \varepsilon_0}{e^2 \mu} \qquad \qquad \cdots \rightarrow (1.1)$$



Here, a_B is Bohr radius, \hbar is reduced Planck constant, μ is the reduced electron mass, ε_0 and ε are free space permittivity and materials electric permittivity.

The exciton mass's ratio to the free electron's mass is known as the effective mass $(m^*)^{\ddagger}$ of the excitons.

$$a_{\text{ex}} = a_B \frac{(\varepsilon/\varepsilon_0)}{m^*} = a_B \frac{\varepsilon_r}{m^*} \qquad \cdots \rightarrow (1.2)$$

Here, ε_r is relative permittivity or dielectric constant, it is a function of frequency, ε_r (ω).

Different materials have different $a_{\rm ex}$ values; for instance, the $a_{\rm B}$, $m_{\rm eff}$, and $\varepsilon_{\rm r}$ values for CdS are 3, 0.16, and 8.9 nm, respectively, and 18, 0.05, and 17.3 nm for PbS, respectively. When a photon combines with exciton, it produces a quasi-particle termed exciton-polariton (EP).^[35-37] The electron-hole pair interactions stabilization energy subsequently decreases the pair energy associated with unbound hole and electron. This exciton can either thermally dissipate (non-radiative decay) or recombine into a photon (radiative recombination). The excitons generated in organic and inorganic semiconductor materials vary in their exciton-binding energies ($E_{\rm B}$), and $E_{\rm B}$ associated with the $a_{\rm B}$ can be given as:

$$E_B = \frac{e^2}{2\varepsilon_r a_B} \qquad \cdots \rightarrow (1.3)$$

where e is the charge of the electron, ε_r is connected to electric susceptibility ($\chi^{(1)}$) and n of the material as given in below equation.

[†]Bohr radius: It is defined as a radius from which there is a high probability of finding a ground-state electron in a hydrogen atom; $a_B = \frac{4\pi\epsilon_0\hbar^2}{me^2} = 53$ pm or 0.053 nm or 0.529 Å.

Here, e is the charge of an electron, and m is the mass of the electron.

The orbit motion of an electron in an atom can generate centrifugal force, allowing it to fly away from its nucleus. However, to have a stable atom, the assumption that this generated centrifugal force was balanced by an opposing centripetal force pulling the electron inward via Coulombic attraction between nucleus and electron.

Effective mass: By fitting parabolic functions around the CB or VB using the following equations, one can determine the effective mass of the electron (m_e^) and hole (m_h^*) along with selected directions. $m^* = \pm \hbar^2 [d^2 E_k/dk^2]^{-1}$, Where \hbar is reduced Planck constant, E is the energy of an electron.

$$n = \sqrt{\varepsilon_r} = 1 + \chi^{(1)}$$
 (1.4)

The ε_r values are from 6-12 and 3 for organic and inorganic semiconductors, respectively. In organic semiconductors, the band structure is encompassed by energy difference [Lowest Unoccupied Molecular Orbital (LUMO), and Highest Occupied Molecular Orbital (HOMO)] and orbitals. In the case of inorganic materials, band structure contains distinct bands with empty CB and filled VB.^[38-40] For both HOMO/LUMO, dispersions are comparatively even.

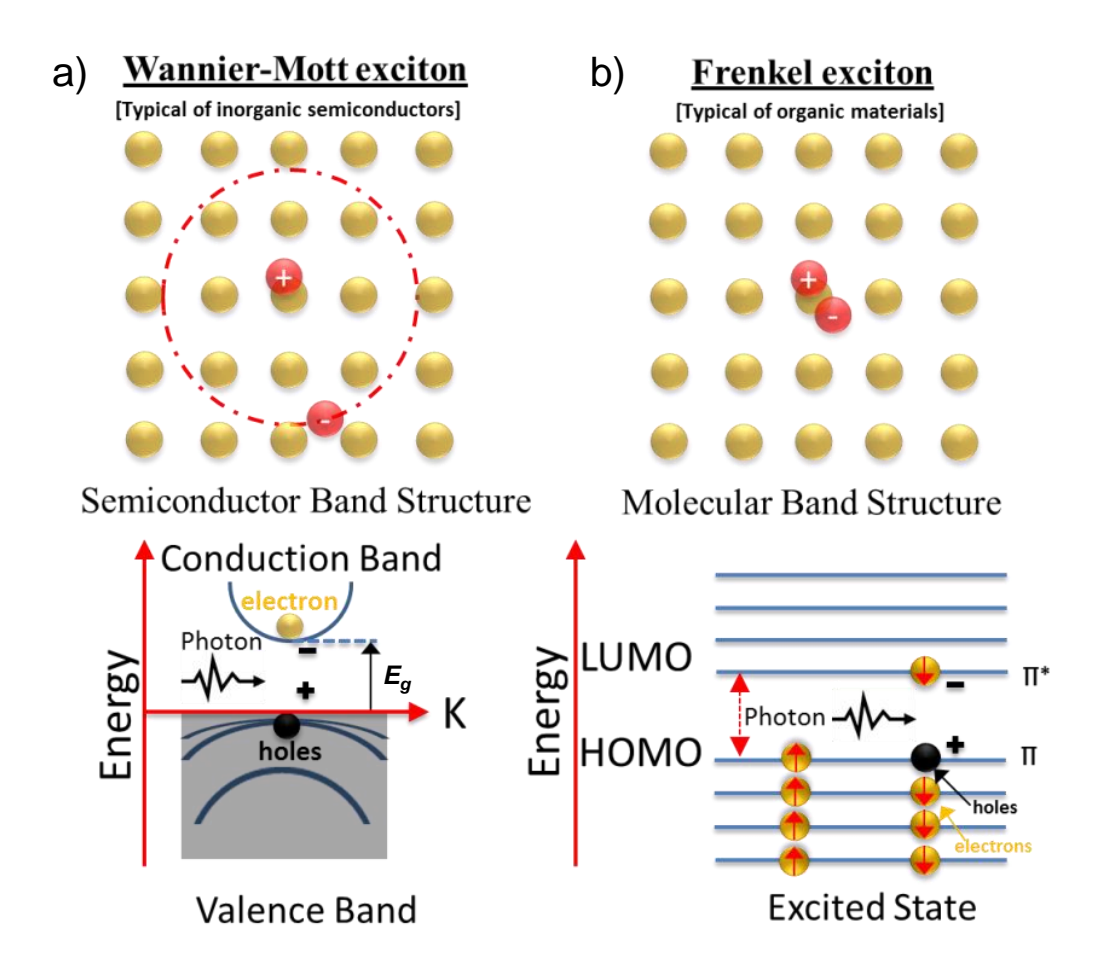


Fig. 1.4. Qualitative diagram of the band structure in a) inorganic and b) organic semiconductor crystalline materials. Figure adopted from ref. 42.

In GaAs semiconducting material, [41] the lower binding energy of the excitons prevents the strong coupling between the light and matter at room temperature (RT). Moreover, high exciton binding energies in semiconducting materials like ZnO and GaN were reported. [43-45] Wannier-Mott excitons are the lowest-lying electronic excitations in inorganic semiconductors (**Fig. 1.4a**). In an inorganic semiconductor, the higher value of ε_r , rises the

dielectric screening in the lattice and leads to the reduction of E_B due to the decrease of Coulomb interaction among holes and electrons. Therefore, the Wannier-Mott type excitons possess a larger radius (\approx 10 nm), which is higher than the lattice spacing. Most of these excitons^[46] have a low reduced effective mass. Therefore, their E_B 's are lesser in the order of \sim 10–20 meV, this value is smaller than the RT energy [kT = 25.6 meV; here, T is the temperature in Kelvin and k is the Boltzmann constant (8.6173303 \times 10⁻⁵ eV K⁻¹)]; consequently they dissociate at RT.

Frenkel-type excitons are typically found in organic semiconductor materials (with charge-transfer properties) (**Fig. 1.4b**). The E_B range of Frenkel excitons^[47] is 0.1-1 eV, much higher than the inorganic semiconductors due to the hole and electron being situated in the same molecule (small a_B). This indicates the organic Frenkel excitons are stable at RT. In charge-transfer excitons, the charge carriers are often found on the near or next-nearest neighbor molecules. In organic semiconductor devices, particularly for lasing applications, excitons play a significant role. ^[48]

Although, compared to the inorganic counterparts, the organic nano/micro-structures materials possess low n (low ε_r), they have advantages such as easy vapor or solution phase processing and tunability of optical performance. The organic micro/nano-structures are produced via non-covalent interactions like π - π stacking, [49] charge-transfer interactions, [50] van der Waals forces, [51] and hydrogen bonding. [52] Organic solids display attractive physical properties like mechanical-/photo-flexibility, [53] optoelectronic properties, and polarizability [54] depending on the molecular structure and packing. The mechanical flexibility of organic crystals is quite attractive for fabricating photonic circuits.

1.5. Principles of Optical Confinement in Waveguides

According to Snell's law, when a light beam propagates from a rarer (for air; n = 1) medium to the denser medium (for organic material; $n \approx 1.6$), at the boundary, a fraction of the beam reflected by the medium towards low refractive index and some portion of light is refracted into the medium having a high refractive index (**Fig. 1.5a,b**). The reflected beam angle (θ_1) is equal to the angle of the incident beam. The incident light beam angle

is higher than the refracted beam angle (θ_2). If the incident light angle is more than the critical angle, then the light propagates within the high refractive medium (n = 1.6) via total internal reflection (TIR). During TIR, the entire light beam is not reflected into the waveguide because a small portion of the light is leaked to the n = 1 medium (**Fig. 1.5c,d**). This seeped light decays exponentially as a function of distance from high n medium

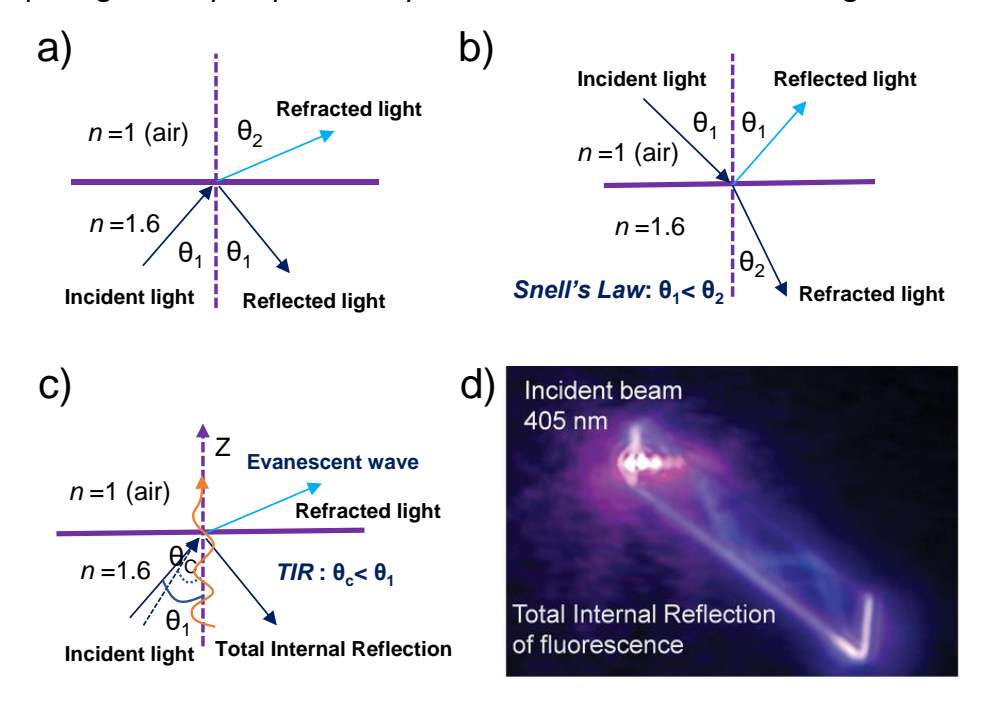


Fig. 1.5. a,b) Refraction condition according to Snell's law. The refractive index values for random substrate and air are 1.6 and 1, respectively. c) The total internal reflection (TIR) condition and formation of exponentially decaying evanescent field/wave in the z-direction. d) TIR of the FL wave in an organic microcrystal. Figure adopted from ref. 56.

surface to low (n = 1) refractive medium termed an evanescent field or wave. The evanescent field is very useful in optical coupling between two waveguides, fiber tapping, exciting optical cavities, optical splitters production, and wireless photonic devices.

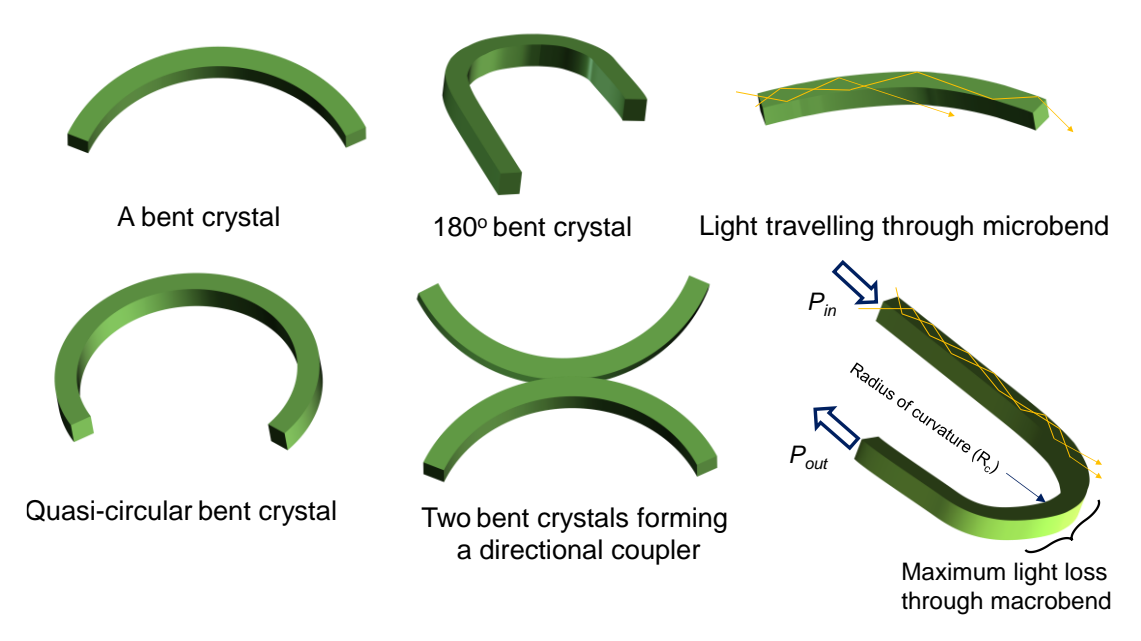
1.5.1. Optical Losses in Waveguides

When the light propagates through the waveguide, it usually undergo optical losses primarily because of the scattering; this occurs due to the defects in a waveguide or microscopic difference in the structural or material inhomogeneity. [58-60] For organic waveguides, optical loss is less because of the single crystalline nature with smooth surfaces. Generally, material composition is predominantly associated with absorption



loss. This specific optical loss is because of the dispersion of some light into other forms, such as acoustic, electrical, and electromagnetic energy. Semiconductors are vulnerable to electromagnetic loss due to different band gaps.

On the other hand, the absorption loss is minimum when a passive optical waveguide works away from its absorption area. When effective n of the particular mode lies within the waveguides clad n, radiation losses occur. This type of loss mainly arises



Scheme 1.1. Graphical representation of various bent-shaped geometries of one-dimensional waveguides and optical light transduction via macro-and micro-bend.

when the light propagates along a sharp curve waveguide, termed bending-induced loss. (**Scheme 1.1**). Most of the optical/photonic devices require sharp curves in the waveguide. The bending loss of a waveguide is high on the macro-scale and low on the micron-scale bend. The macro-bending waveguide creates a curvature radius (R_c) greater than the optical waveguide's cross-section diameter/dimension. A 180° bent waveguide possesses very high optical loss at the bent region compared to a linear or acutely bent waveguide.

The organic crystals with different geometries, linear, L- and U- shapes optical losses were calculated theoretically using finite-difference time-domain (FDTD) calculations (Fig. 1.6).

Chapter-1 Introduction

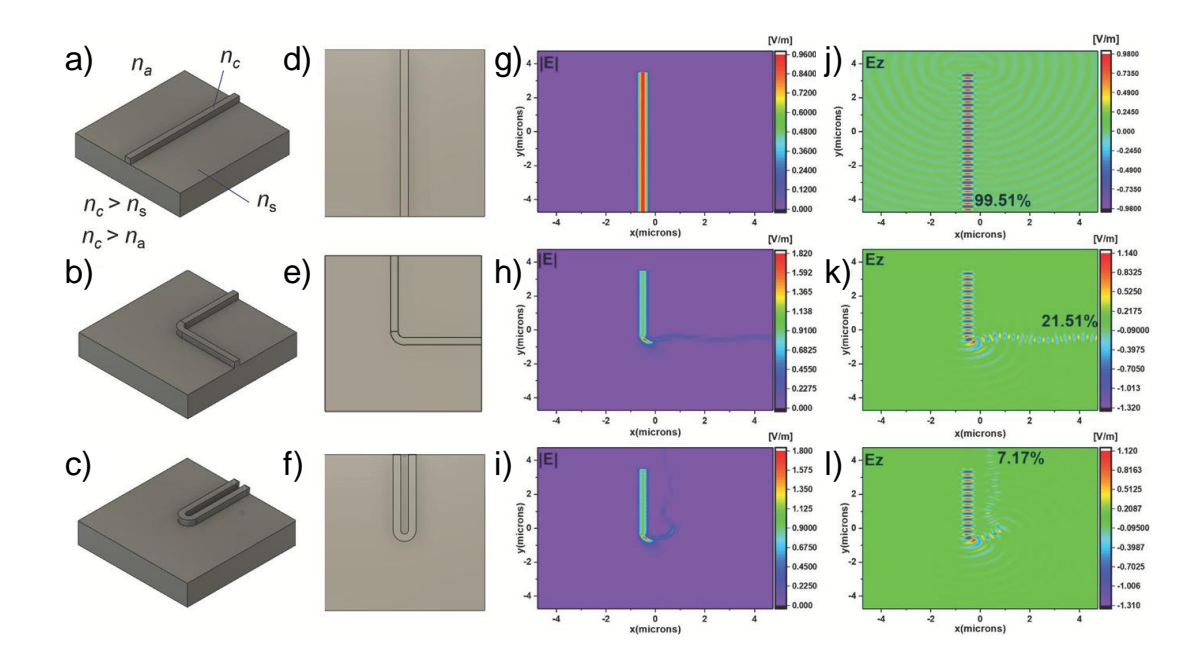


Fig. 1.6. a-c) 3-Dimensional view and d-f) top view of linear, L-shaped, and U-shaped geometries, respectively. g-i) The electric-field distribution and j-l) transverse electric-field distribution observed along the longitudinal cross-section. The substrate and organic crystal's refractive indices are denoted as n_s and n_c . Figure adopted from ref. 57.

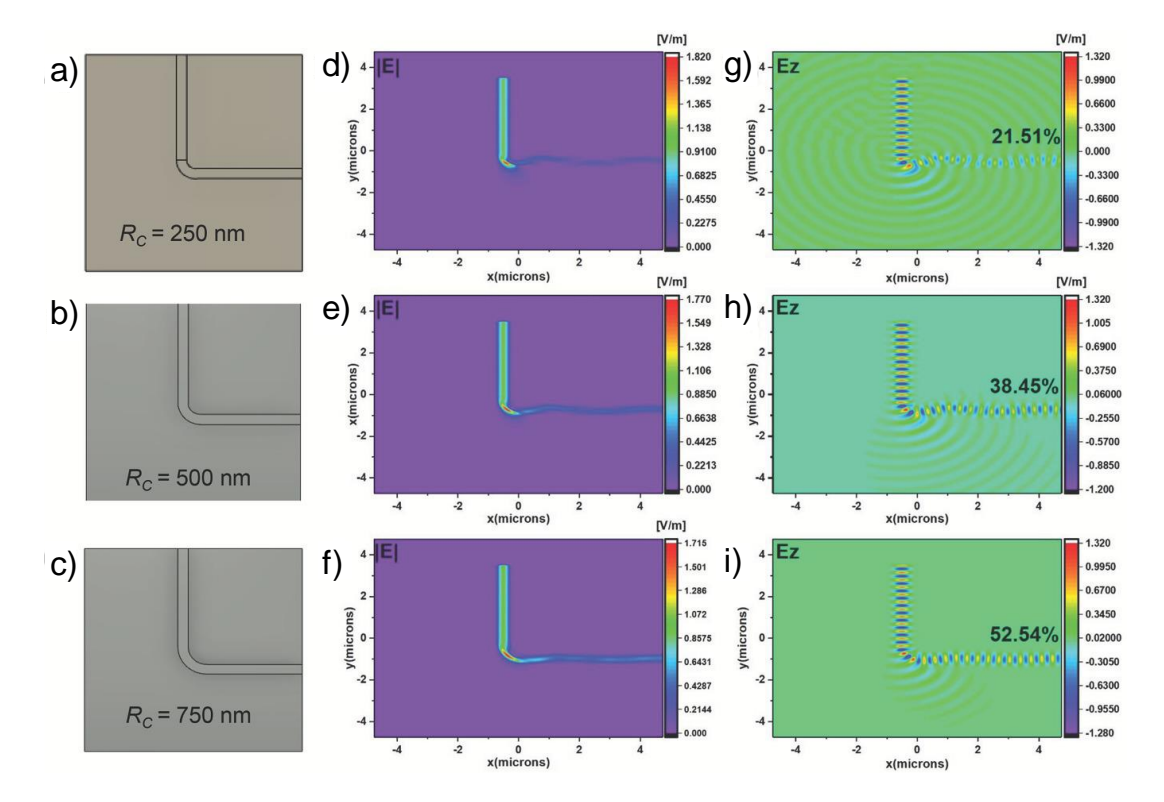


Fig. 1.7. a-c) L-shaped optical waveguides top view, d-f) distribution of overall electric-field and g-i) TE field along longitudinal cross-section of waveguides with different radius of curvature. Figure adopted from ref. 57.

Chapter-1

Here, glass is used as a substrate, and air (n = 1) acts as a cladding layer (**Fig. 1.6a-c**). For both U- and L-shaped waveguides, inner bent geometry R_c is 250 nm (**Fig. 1.6e,f**). The calculated optical transmission efficiencies for the straight, L-and U- shaped passive waveguides are 99.51%, 21.51%, and 7.17%, respectively. (**Fig. 1.6j-l**). These losses are mainly due to the bending-induced loss. The seepage of the light from the bent portion of L- and U-shaped waveguides is presented in **Fig. 1.6k,l**. Upon reducing the R_c , bent loss rises. The simulation results of three waveguides possessing width, height, R_c [1:1:2, 1:1:1, and 1:1:3, respectively], are displayed in **Fig. 1.7d-f**. As the R_c decreases (**Fig. 1.7a-c**), the light seepage through the waveguide increases but reduces the transmission efficiency (**Fig. 1.7g-i**).

Generally, the overall transmission effectiveness can differ based on *n*, excitation mode and beam polarization, and cladding material when the waveguide materials, substrate, and bent angles are the same. The attenuation in passive waveguides restricts the light from transducing to the output. Due to the bending loss, light absorption and light scattering attenuation are produced.^[58-60]

The quantity of light power lost during the transmission from the input to the output terminal of a waveguide with length L, can be calculated via attenuation coefficient or absorption coefficient (α), given in reciprocal length

$$T = \frac{P_{\text{out}}}{P_{\text{in}}} = e^{-\alpha L} \qquad \dots \longrightarrow (1.5)$$

where, $P_{\rm in}$ and $P_{\rm out}$ are the input and output laser power, respectively. The value of $\frac{P_{\rm out}}{P_{\rm in}}$ is the optical power transmission ratio (T). The radiation energy decays exponentially with L, as stated in Beer's Law.

On the other hand, the subsequent equation allows calculating α in decibel (dB) loss.

$$\alpha\left(\frac{\mathrm{dB}}{\mathrm{mm}}\right) = \frac{10}{L} \log_{10} \frac{P_{\mathrm{in}}}{P_{\mathrm{out}}} \qquad \cdots \rightarrow (1.6)$$

The dB term compares the two power values rather than explicitly expressing the power.



Lesser the dB value, the greater the output transmission. $P_{\rm out} \approx P_{\rm in}$, for a perfect optical waveguide.

Generally, the majority of organic crystals act as active optical waveguides. These waveguides absorb UV or Visible light, generating photoluminescence (PL) (FL/phosphorescence). The generated PL is transduced to the output terminal via 2D confinement. The power (*P*) component in equation 1.5 is substituted by FL or phosphorescence intensity, assuming that the waveguide absorbs input optical energy and there is no PL reabsorption.

The lower the optical loss, the greater the crystal's waveguiding quality. The below equation calculates optical loss.

$$\frac{I_{tip}}{I_{body}} = e^{-\alpha \mathbf{D}} \qquad \qquad \dots \longrightarrow (1.7)$$

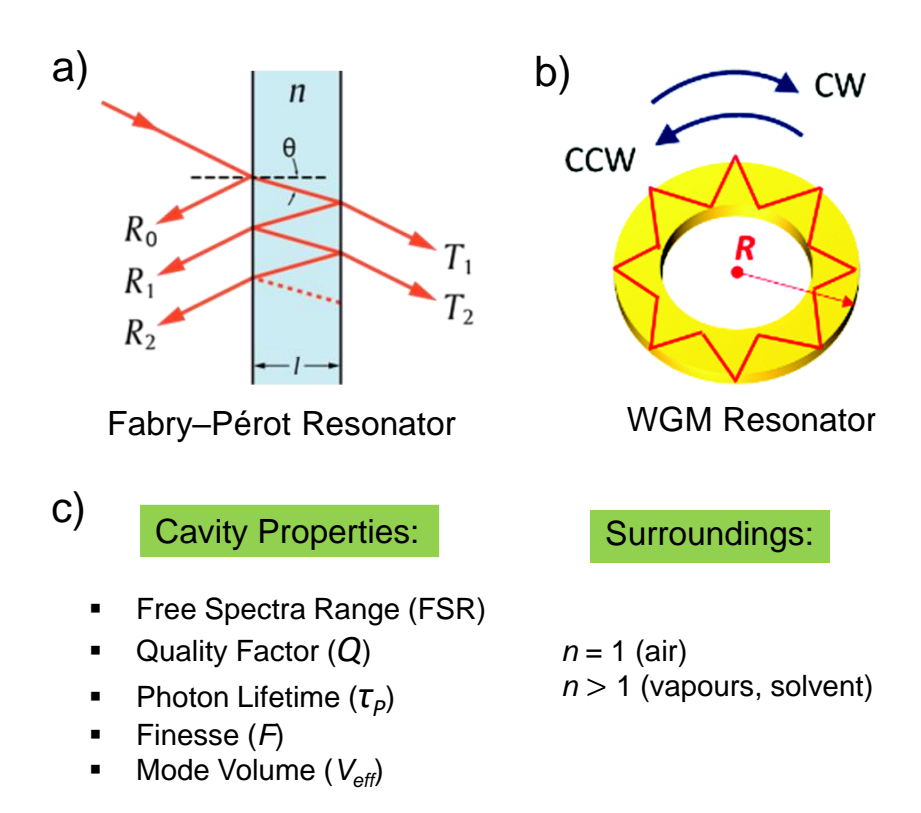
Here, I_{tip} and I_{body} are FL intensities at collection and excitation positions, respectively. D is the waveguiding distance between the excitation and collection position.

Nonetheless, the roughness of the crystal output and input terminals differs in most organic crystal waveguiding studies, leading to differential light scattering. For an assessment of transmitted FL light, the precise estimation of L is important and the real detection/excitation direction (parallel or orthogonal) with respect to the waveguide must be parallel. Primarily, the dimension, geometry, and several defects differ from crystal to crystal for the same compound. Therefore, the α is unique to a particular crystal and can't be applied to all crystals of the same compound. The molecular electronic transition is not allowed in passive optical waveguides; therefore, no optical emission. Optical loss in the passive type is mainly because of Raman scattering, which arises from transferring input light power to the molecular vibrations.

1.6. Fabry–Pérot (F-P) and Whispering Gallery Mode (WGM) Resonators

Based on the crystal geometry, light can be trapped inside the crystal's repeated circulation (whispering gallery mode, WGM) (**Scheme 1.2b**) or through back-and-forth reflection (Fabry–Pérot; FP) because of the smooth light-reflecting crystal's facets

(Scheme 1.2a). Consequently, destructive and constructive optical interferences lead to the WGM or FP resonances. Therefore, a multi-wavelength spectrum (optical modes) can be created by confining the wideband FL light. In the WGM resonator, light that satisfies the resonance requirement, $q\lambda = 2\pi Rn_{eff}$, will be amplified through constructive interference, whereas others will be eliminated via destructive interference. In the equation, R is the optical resonator radius, λ is the wavelength of light, n_{eff} is an effective refractive index of the resonating mode, and q is an integer number associated with a circulating light's angular momentum.



Scheme 1.2. a, b) Schematic representation of Fabry–Pérot micro-resonator and whispering gallery mode micro-ring resonator, respectively. c) Representation of various properties associated with FP and WGM resonators. CW and CCW stand for clockwise and counter-clockwise, respectively. Figure adopted from ref. 61,62.

1.6.1. Parameters of Interest in WGM and F-P Resonators

1.6.1.1. Free Spectral Range (FSR)

Free spectral range (FSR) is described as the separation between two adjacent optical modes (m, m+1), represented as $\Delta\lambda = \lambda_m - \lambda_{m+1}$. FSR is inversely proportional to the size[length (*L*) or width (*D*)] of the resonator

FSR or
$$\Delta \lambda = \lambda^2_{\text{m}}/2Ln_{\text{eff}}$$
 (1.8)

where λ is the maximum wavelength of the mode, and L is the length of the resonator.

The total number of modes increases with the size; therefore, the required number of modes can be obtained by regulating the size. Based on the input light path, the ring, square, circle, and spherical-shaped optical cavity that facilitate WGM resonance property can be incorporated during organic PICs (OPICs) production to direct the input light anti-clockwise or clockwise. Numerous silicon-based PICs involve ring-shaped geometries to control the direction of the input light.

1.6.1.2. Quality Factor (Q)

The quality factor describes the light-trapping capability of a resonator. Q is the ratio of optical energy stored in a resonator to the amount of light energy lost during each roundtrip rotation. Equation 1.9 is used to estimate Q.

Where, $\Delta\omega$ is full width at half maximum (FWHM)/line-width of the resonant mode, and ω is the resonance frequency

Q value increases with the increase of the mode's FWHM. The various optical loss terms are used to estimate the true Q-factor. Which can be expressed as [63,64]

$$\frac{1}{Q} = \frac{1}{Q_{\text{sur}}} + \frac{1}{Q_{\text{mat}}} + \frac{1}{Q_{\text{hend}}} + \frac{1}{Q_{\text{scat}}} \qquad \cdots \rightarrow (1.10)$$

Here, the surface absorption of the material contributes to the loss in terms of $Q_{\rm sur}$, $Q_{\rm mat}$ is related to material's (intrinsic) cavity absorption, $Q_{\rm bend}$ is an optical loss because of bending, which depends on λ and radius of the resonator, and $Q_{\rm scat}$ arises because of light scattered by the resonator due to surface roughness and inhomogeneity. The high Q resonators play a significant role in micro-laser production. Moreover, increasing the resonator's size increases the Q-factor to a specific threshold. In WGMRs, the Q-factor from 10^3 to 10^6 is considered high, and more than 10^7 is ultrahigh. The resonators find their applications in micro-lasing, which mandate Q-factors as high as 10^6 . However, a



resonator with Q-factor value of few hundred possesses a WGM spectrum along with the background FL spectrum. [65-72]

1.6.1.3. Photon Lifetime (τ_P)

The time required for a photon to reduce to 1/e inside a resonator can be determined using the equation shown below $(1.11)^{[63,64]}$

$$\tau_{P} = \frac{Q}{\omega} \qquad \cdots \rightarrow (1.11)$$

The τ_P increases with the increase of the Q-factor. For high Q-factor cavities, light storing time inside the resonator is proportionally longer, called cavity ring-down lifetime or photon lifetime. The light-matter interaction predominantly increases due to the photon trapping effect, a significant application of larger photon lifetime (cavities with high-Q). Usually, Q values of resonators increase at low temperatures.

1.6.1.4. Finesse

It's an additional significant parameter of FP and WGMRs. F is determined from the ratio between FSR and FWHM of a specific resonance line. High F values are usually needed.

$$F = \frac{\text{FSR}}{\text{FWHM}} = Q(\frac{\lambda}{n\pi D}) \qquad \qquad \dots \longrightarrow (1.12)$$

1.6.1.5. Spatial Structure of Optical WGMs

WGMs are described using a spherical coordinate system using spherical Bessel, Hankel functions, and adjoint Legendre polynomials. ^[73,74] These are indicated by integer three-mode numbers, namely, polar (I), radial (q), and azimuthal (m) mode numbers $I \gg 1$, $q \ge 1$, and $m \gg 1$, respectively (**Fig. 1.8**). The numbers q and I, are associated with the electromagnetic waves in the radial and azimuthal paths. The number of electric field oscillations in the polar θ -direction is represented by the angular mode number (p), p = I - m = 0, 1, 2, 3,... The optical emission spectra can be used to determine the presence of WGMs and the number of modes. The long-lasting WGMs are confined near the sphere's equator called Transverse Electric (TE, where the propagation plane's perpendicular to



the E vector), and Transverse Magnetic (TM, with the H vector of that plane perpendicular to it) fields.

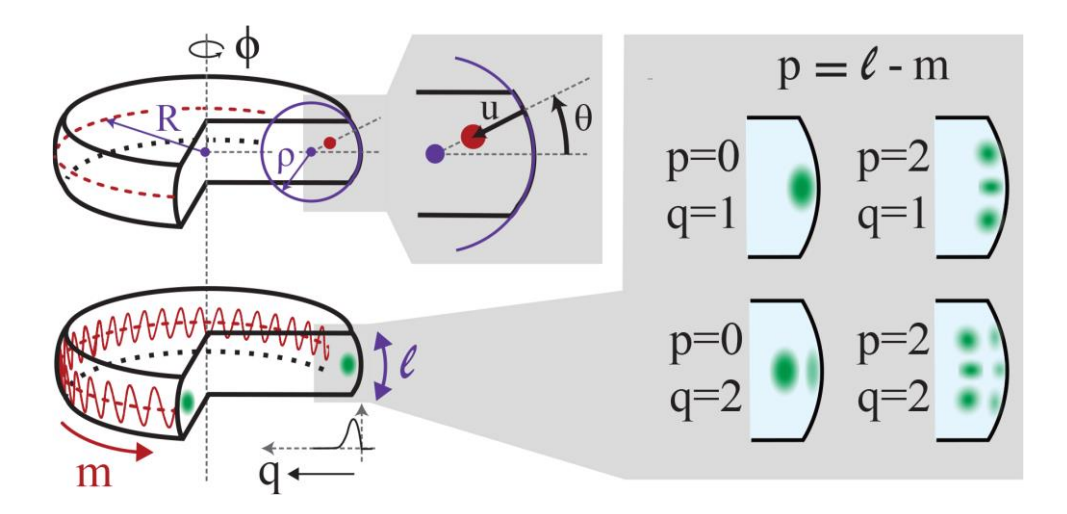


Fig. 1.8. WGMs spatial structure. The electric field distributions of azimuthal angle (φ) , radial distance (u), and the polar angle (θ) . Angular mode numbers (p=l-m) and radial mode numbers q, intensity distributions are shown on the right side. Figure adopted from ref. 73.

1.6.1.6. Mode Volume (Veff)

The mode volume (V_{eff}) describes the ratio of the total amount of light energy confined in a particular cavity mode to its highest energy density.

 V_{eff} = stored energy/maximum energy density

The lower value of V_{eff} gives a larger FSR value. The stimulated and spontaneous emission rates are inversely related to V_{eff} . Additionally, the lasing threshold is also directly related to V_{eff} . [63,64]

1.7. Silicon-based Components for PICs Fabrication

1.7.1. Silicon Waveguides

Silicon PICs are composed of various optical elements, such as optical waveguides, ring resonators, add/drop filters, etc. Waveguides are essential elements for PIC fabrication. Most silicon waveguides are fabricated on SOI wafers (**Fig. 1.9a**). Si has an indirect bandgap of 1.12 eV at ≈1100 nm wavelength, and intrinsically, silicon shows negligible absorption in these telecom bands.^[76] All the waveguide architectures obey the



same basic principles of light transduction. In SOI waveguides, the input light is confined and guided in the silicon core as Si has a higher n than SiO₂.

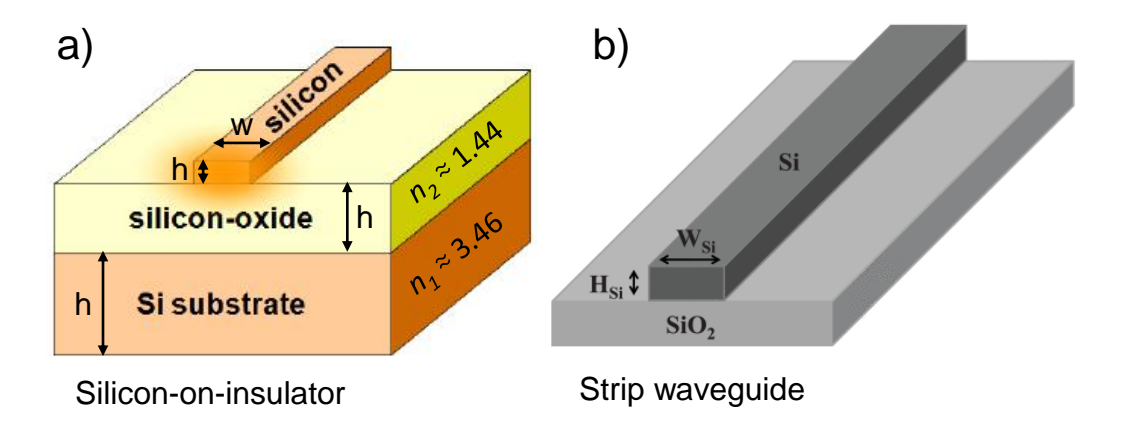


Fig. 1.9. a,b) Schematic diagram of SOI and strip waveguides, respectively. Figure adopted from ref. 75.

In most PIC systems, the waveguides are anticipated to confine and guide the input light inside the PIC at a very low optical loss. The key to attain effecient light propagation and minimal material losses is to find the materials with a smaller free carrier absorption coefficient and high n.^[77] Silicon is a very efficient optical waveguide material with low absorption loss and high n ($n \approx 3.5$ at 1550 nm).^[77] In the CMOS platform, the primary material of choice is silicon. Si-based SOI waveguides are an exceptional selection in the NIR and MIR regions (2-20 μ m) as it is transparent to 8 μ m wavelength.^[78]

A strip waveguide is the simplest kind of waveguide; it's a nanowire with a rectangular cross-section of a high index material like silicon (**Fig. 1.9b**). The strip optical waveguides were epitaxially grown on the highly doped silicon substrate single crystals; therefore, these waveguides are termed single-crystalline silicon layer waveguides. Mostly, these waveguides are cladded with a low-index material like SiO_2 . The cladding shields the waveguide and decreases propagation loss from the waveguide sidewalls and line edge roughness. The n difference among the silicon guiding and substrate layers is about 0.01 in Si-on-Si waveguides, which is relatively low. The waveguide light propagation loss is around 15 dB cm⁻¹ for 1.3 μ m; [79,80] it is because of the low optical confinement of the core waveguide and huge light leakages into the substrate. In strip waveguides, reducing the n contrast decreases the effect of roughness at the material interface, mainly due to the linear loss at modest intensities. [81] However, lower index



contrast decreases the scattering from roughness, reducing the mode volume and light confinement. The bottom and top surfaces of the etched SOI waveguide have the smoothest surfaces and are even smoothened to sub-nanometer roughness in wafer fabrication by chemical mechanical polishing.^[82]

1.7.2. Directional Couplers (DCs)

The directional couplers (DCs) are important to split, combine and redirect optical signals. The two bent optical waveguides are coupled in their concave and convex bends of top and bottom waveguides, respectively, to fabricate 2 × 2-directional coupler with ports 1-4 (**Fig. 1.10a**). In a directional coupler, the input light signal splits at the junction of two bent waveguides through an evanescent wave. **Fig. 1.10b** shows, the FDTD simulation of light energy distribution for TE mode (at 1520 nm) propagating in ports 3 and 4 for the input light given at port 1.^[83]

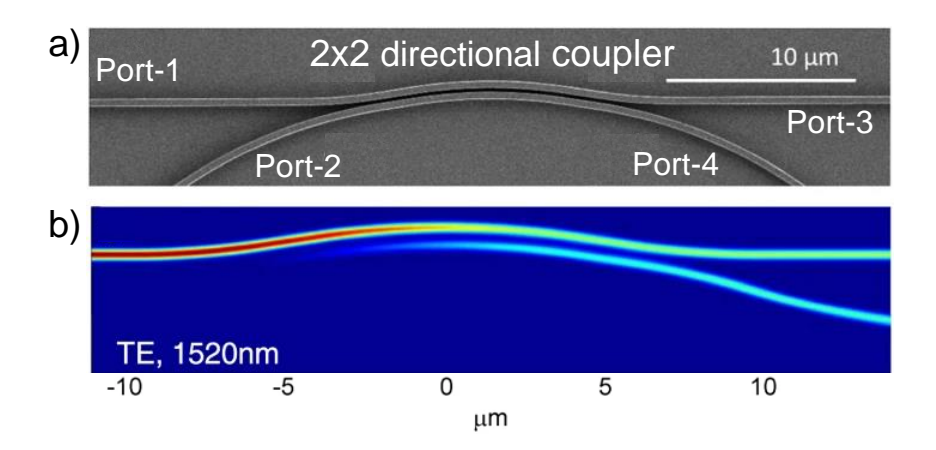


Fig. 1.10. a) SEM image of the constructed DC. b) Fabricated bent coupler optical energy distribution modeled using FDTD numerical calculations. Figure adopted from ref. 83.

1.7.3. Silicon Microring Resonators

The microring waveguide is usually fabricated using electron-beam lithography (EBL). Recently, a silicon microring resonator was constructed on a single crystalline silicon-on-insulator (SOI) wafer with a Si slab (thickness \approx 250 nm) on top of Si buffer film (thickness \approx 3 μ m to ensure no optical modes seepage into bottom wafer. The micro-ring comprised a 450 \times 250 nm cross-section with a 20 μ m radius. The SEM image of a linear



waveguide coupled to one side of the microring with an air gap of 120 nm is shown in **Fig. 1.11a**.

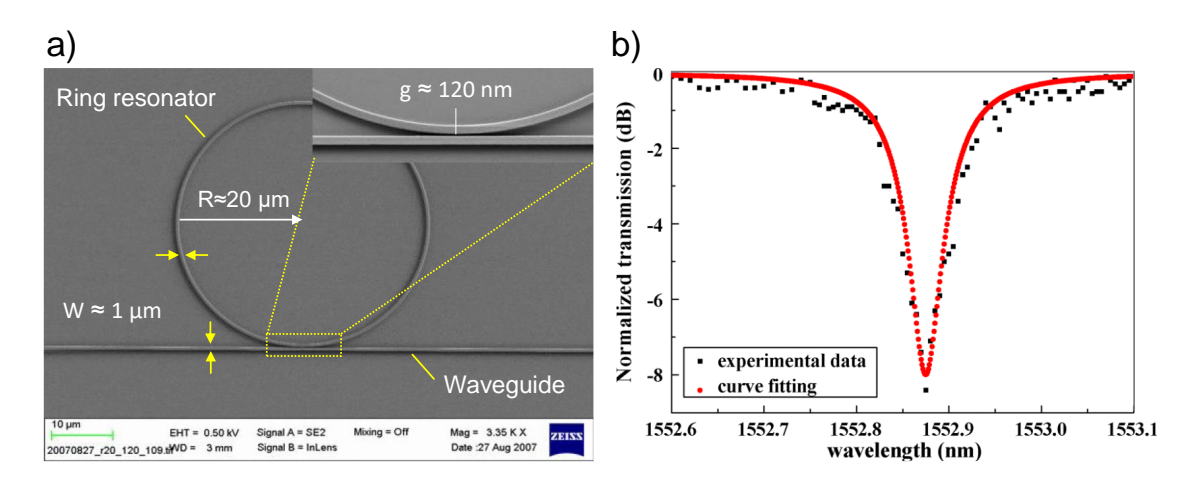


Fig. 1.11. a) An SEM image of a Si micro-ring resonator. The inset shows a close view of the waveguide junction and ring. b) Spectral response of the ring resonator. Figure adopted from ref. 84.

The microring resonator spectral response shows resonance at 1548 nm with a bandwidth of ≈ 0.1 nm (**Fig. 1.11b**). The obtained cavity Q factors associated with the intrinsic cavity loss (Q_L) and external coupling (Q_E) were 3×10^4 and 0.7×10^4 , respectively. An optical loss of 10 dB cm⁻¹ and a coupling coefficient of 0.270 was estimated for the resonator.

1.7.4. Add-Drop Filters

The EBL fabricated micro-ring add/drop filter with a radius of 1.5 μ m on an SOI wafer comprising a 1 μ m buried oxide layer (n = 1.45), and a 0.34 μ m Si layer (n = 3.5) is shown in **Fig. 1.12a**. The waveguide width and coupling space among the linear waveguide and the micro-ring are 310 \pm 5 and 180 \pm 5 nm, respectively.

The spectral results of the device's through and drop ports are displayed in **Fig. 1.12b.** The FSR value of the resonance mode numbers at m = 13 and 14 of the transmission spectra was 52 nm. The dashed lines shown in **Fig. 1.12c** are calculated responses of the device for 1568 nm resonance, almost matching the obtained results. The micro-ring's intrinsic Q-factor is 3100. This value is lower than the theoretical Q-factor 9300 obtained from bending loss alone. These outcomes reveal the waveguide sidewall roughness and scattering from coupling junctions are responsible for the loss. However, the surface



roughness was minimized by refining the etching process, whereas the crystal geometry was improved to reduce the coupling loss at the junction.^[85]

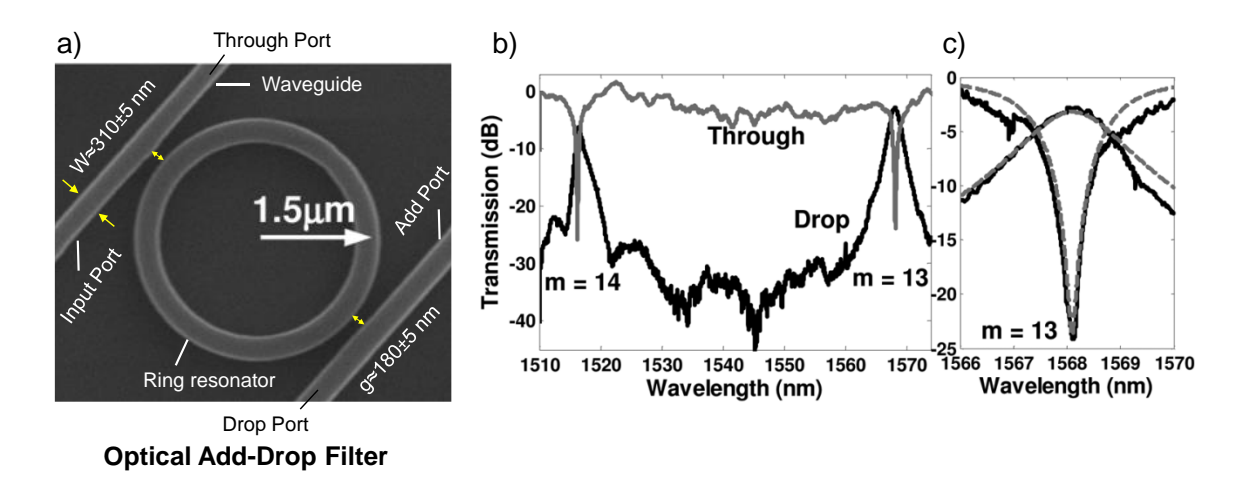


Fig. 1.12. a) The SEM image of silicon-on-insulator micro-ring add/drop filter. b,c) The spectral response of the device at through- and drop-ports. Figure adopted from ref. 85.

1.8. Drawbacks of Si-based PICs

Though the high n of Si and Si-derivative is an asset, it becomes a problem providing lower device permanence when there is nanoscale size variation in the device dimension. It has low thermal stability i.e., n(T), which leads to undesirable bandwidth changes. PICs are made using the conventional EBL technique and are rigid and non-reconfigurable. As a result, the circuit lacks geometrical flexibility and subsequently fixed optical path direction. The Si-based optical circuits need optical modulators to produce different output wavelength signals for different logical functions. [55]

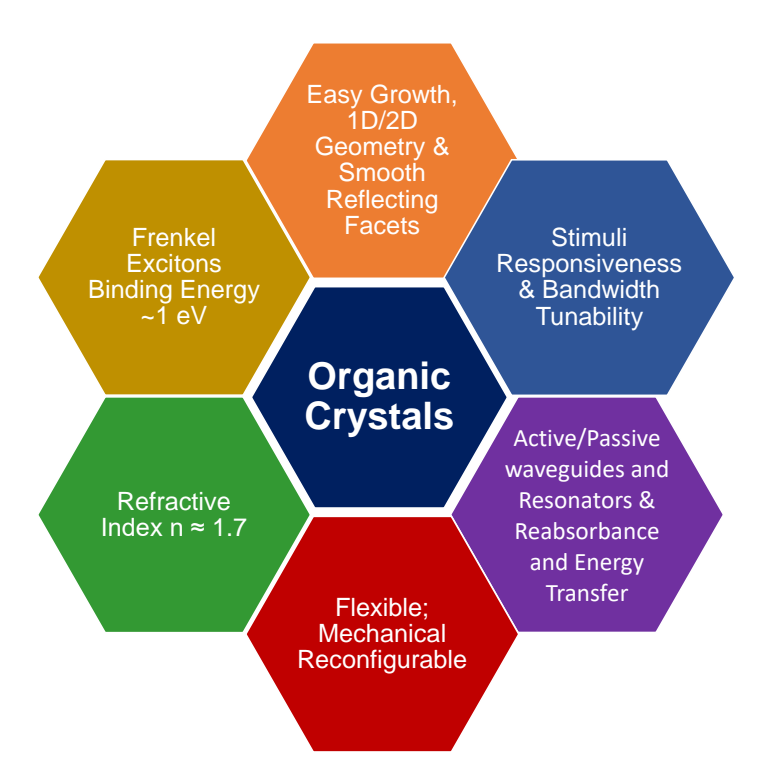
Silicon is centrosymmetric; as a result, it is not suitable for producing second harmonic generation (frequency doubling) - an important nonlinear optical (NLO) conversion process. Therefore, strained Si is used to achieve this NLO property. Materials like InP (n = 3.53), silicon nitride (n = 2.02), and silicon PICs have high refractive indices. Similar to the electronic circuits manufacturing process, PICs depend on wafer-scale processing. The optical waveguide losses vary between 0.1 to 1 dB cm⁻¹ depending on the quality of material and processing grade. Most of the photonic circuit's technology compatibility with a single layer of photonic waveguides leads to the circuit connection



being limited to one plane. The construction of multidimensional optical waveguides, like two-dimensional (2D) and three-dimensional (3D), facilitates the circuit performance and flexibility and lowers the impression. Multilayer silicon PICs are fabricated in amorphous Si layers and Si₃N₄. In this multilayer silicon photonics platform, the optical waveguides transduce the light vertically by reducing the optical loss. The multilayers facilitate the optical waveguides crossing between the layers of the different planes with cross-talk and ultra-low optical loss.

1.9. All-organic Material Platforms

An alternative non-silicon-based material with some characteristics described in Scheme 1.3 is essential for realizing all-OPICs. [55] The important conditions are high n, thermal stability, high quantum yield, active and passive waveguiding propensities, wavelength tunability, and mechanical flexibility. [57,61] Organic single-crystals generate



Scheme 1.3. General characteristics of organic crystals.

Frenkel excitons which are stable at RT upon exposure to light due to their high binding energy (up to 1 eV). These excitons are combined with confined light, producing exciton-polaritons (EPs). Exciton binding energies of organic crystals are much higher than those

of the inorganic materials (Wannier excitons). However, the sizeable exciton-binding energy reduces the effective n of organic crystals to ≈ 1.7 . The definite geometries (1D/2D) of organic microcrystals with smooth surfaces are essential for OPIC construction because of their mirror-like light-reflecting facets.

NLO crystalline organic materials can produce and self-guide second ($\chi^{(2)} \neq 0$)/ third harmonic signals, 2PL (two photon luminescence), and 3PL (three photon luminescence) based on their charge-transfer characteristics of molecular building blocks and packing symmetry. Chiral molecular crystalline materials with charge-transfer features can generate and propagate the NLO signals showing circular dichroism and optical rotation (chiro-optical effects). [87,88]

1.10. Active and Passive Organic Optical Waveguides

For the fabrication of OPICs, optical waveguides are essential components. Due to high n, organic crystals act as a waveguide on a silica surface (**Fig. 1.13a**). Organic optical waveguides are classified into active^[57, 89-101] and passive types.^[102-105] These two kinds of waveguides are fundamental for OPIC operations. The active type waveguides guide the generated fluorescence (FL) or phosphorescence to the output (**Fig. 1.13b**), while the passive type waveguides transmit the same input signal/light directly to the output (**Fig. 1.13c**). Micro-PL imaging tools are employed for the characterization of active-type waveguides. The light propagation path of passive waveguides can be detected using

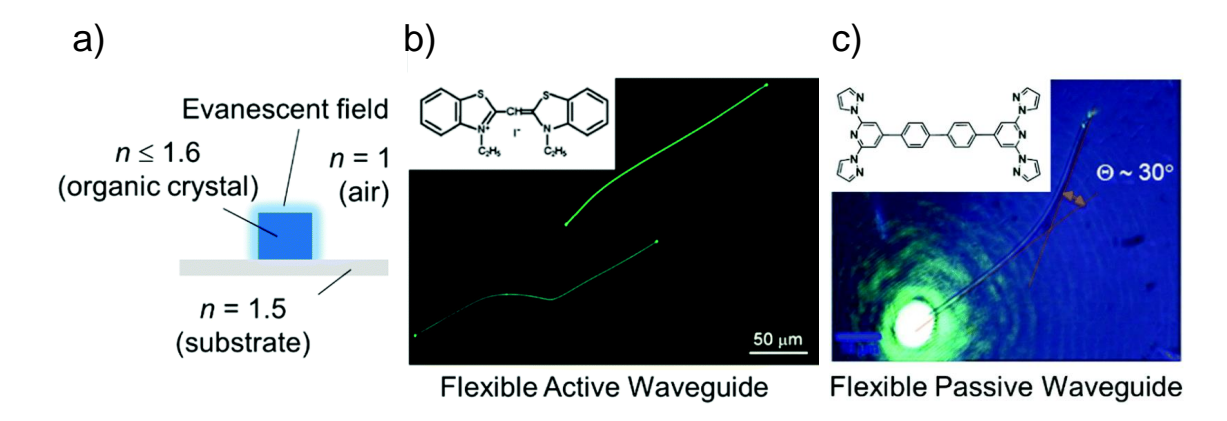


Fig.1.13. a) Graphical illustration of organic crystal-based optical waveguide on a Si layer. b,c) Organic-based flexible active-type and passive-type waveguides, respectively. Figure adopted from ref. 61, 106, 104.

micro-Raman imaging techniques. The direction of light propagation depends on the geometry of the waveguides.

The light beam propagates in optical waveguides due to TIR. A beam's roundtrip phase should be an integer multiple of 2π for waves to survive inside the waveguide. Therefore, the permitted light beams propagating in the waveguide must possess definite angles, leading to the waveguide modes. We can estimate the no. of allowable optical modes for a waveguide, the cut-off wavelength (λ_c), effective n (n_{eff}), and polarization using the analytical or numerical simulation method. The light travels inside the waveguides as TM modes have been demonstrated, [107] and the following equation limits the no. of possible optical modes (m). [106,108-114]

$$m < \frac{2w}{\lambda} \cdot \frac{n_{\perp}}{n_{||}} \sqrt{n_{||}^2 - n_s^2} \qquad \qquad \cdots \longrightarrow (1.13)$$

Here, λ denotes the propagated light wavelength, n_s represents the substrate n, $n_{||}$, and n_{\perp} denotes the n parallel and perpendicular to the waveguide, respectively, and w represents the waveguide width.

Equation 1.13 states that the w is essential for the transduction of a 380 nm light is \approx 300 nm when n and n_{\perp} are nearly 1.65 and m = 1.^[110]

For an optical mode, the cut-off wavelength (λ_c) that is guided through the waveguide is

$$\lambda_{\rm c} = \frac{2n_{\perp}w}{m} \qquad \qquad \cdots \rightarrow (1.14)$$

Optical devices like ring resonators, polarization converters, and multimode interference couplers use the fundamental structure of an optical waveguide.

1.11. Mechanical Characteristics of Organic Crystalline Materials

The mechanical properties of crystals can be analyzed using the stress (σ) versus strain (ϵ) plot (**Fig. 1.14**). According to Hook's law, many organic crystals normally show a straight σ – ϵ relation up to a specific σ value named proportional limit (A). The stiffness of a crystal measured from $\Delta\sigma/\Delta\epsilon$ slop is the E. The removal of stress at point B might cause



the crystal to regain its initial geometry called yield point or elastic limit (*B*), and among points, *B* and *A*, Hooks's law is not obeyed by the crystal.

The crystal can be classified as brittle and hard if it fractures within the elastic region. Typically, these crystals show brittleness if the intermolecular contacts are the same in all directions. [115] At point C, by removing stress, the crystal may not return to its initial state

and permanently deform, called plastic deformation. The crystal may exhibit a permanent distortion at points C to D even for modest applied stress (breaking stress). From point D to point E (breaking point), even when the external stress is decreased, the crystal displays high distortion until E and ultimately breaks the crystal. Generally, nanoindentation experiments are implemented to measure molecular crystalline materials' mechanical

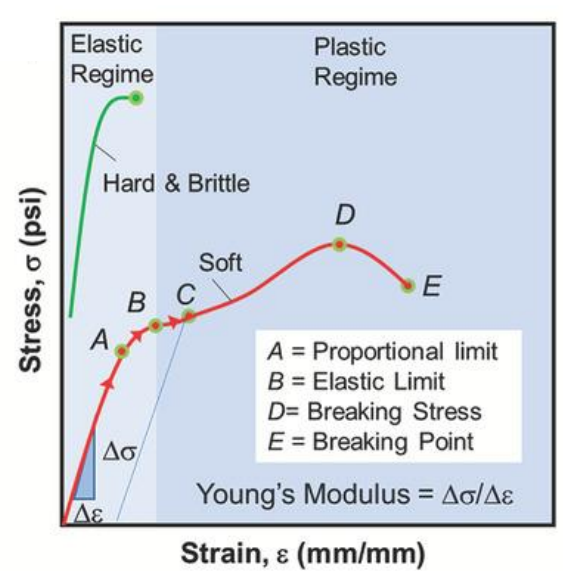


Fig. 1.14. A plot depicting the relationship between stress-strain of solid materials. Figure adopted from ref. 57.

attributes like H_c and E. Usually, the E of crystals is <4, 4-6, and 6-16 GPa, and they are named super-complaint, compliant, and intermediate stiff, respectively.

For super-soft, soft, and medium-hard crystals, the H_c values are <0.15 GPa, 0.15–0.26, and 0.26–0.72, respectively. [116] For 90% of brittle crystals, the E/H_c value is below 35, though the crystals with larger E/H_c value displayed plasticity. [116] The degree of E relies on several factors like the alignment of intermolecular hydrogen bonds, strength, and cavities in the crystal and molecular packing efficacy. H_c is determined by the ease of the crystal's irreversible slip of molecular layers. [116,117]

1.11.1. Characteristics of Mechanically Flexible Organic Crystals

Flexible crystals are divided into two classes based on the mechanical response, namely elastic and plastic crystals. Plastically bendable crystals show permanent

deformation even after removing external stress, while elastic crystals regain their initial state after removing external stress. In comparison to metallic crystals, plastic bending in organic crystals does not display a significant variation in the lengths of the outer and inner bends, volume, and thickness. The general characteristics of brittle, elastic, and plastic molecular crystals are shown in **Fig. 1.15b**. Plastic bending requires i) the presence of slip planes and ii) angles among the bending faces and crystal top change noticeably to conserve the original crystal length (I_0) in the outer (I_{out}) ($I_{out} = I_0 = I_{in}$) (**Fig. 1.15a**). In elastic crystals bending needs, i) the absence of slip planes, ii) the length of the I_{out} is greater than the I_0 and I_{in} ($I_{out} > I_0 > I_{in}$), and interfacial angles are preserved ($\theta_0 = \theta$) (**Fig. 1.15a**).

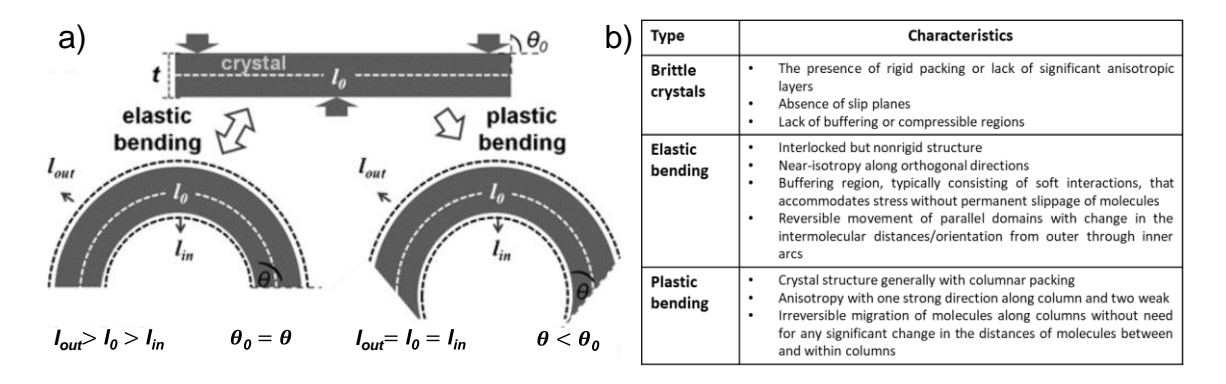


Fig. 1.15. a) Graphical depiction of a crystal before bending (top), plastic (right), and elastic (left) bending, respectively. b) Structure to property correlation for different mechanical responses of organic molecular crystals. Figure adopted from ref. 118,119.

1.11.2. Brittle Crystals

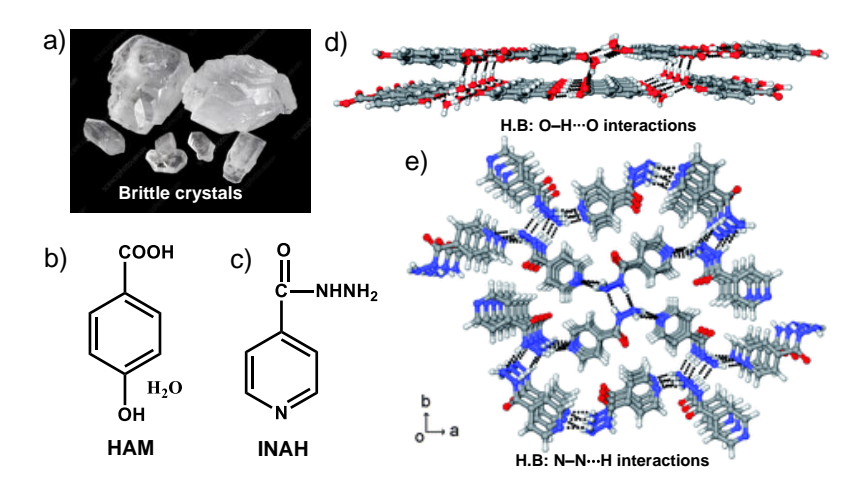


Fig. 1.16. a) Brittle crystals image. b,c) Molecular structures of HAM and INAH, respectively. d) HAM packing exhibits 2D-interlayer H-O hydrogen interactions. e) INAH molecular packing view along the crystallographic c-axis displaying the H···N intermolecular packing interactions. Figures adopted from ref. 120,121.

Brittle crystals are very common. Crystals that break or separate into pieces by applying external mechanical stress in any direction are referred to as "brittle crystals" (Fig. 1.16a). The molecules are interlocked with isotropic interactions in all three dimensions (3D) of the structure in brittle types of molecular crystals. For example, in an isonicotinic acid hydrazide (INAH) crystal (Fig. 1.16c), N···H contacts link the molecules in all directions, producing a 3D interlocked packing (Fig. 1.16e). [120] Another example of brittle crystals is the 4-hydroxybenzoic acid-monohydrate (HAM) (Fig. 1.16b). In the crystal structure, the molecules connected with O–H···O interactions and form 2D planar sheets; these sheets are further linked in the third dimension (3D) via one more set of O–H···O interactions (Fig. 1.16d). [121]

1.11.3. Mechanically Bendable Elastic Crystals

Organic elastic crystals are studied by nanoindentation (stress-strain profile), X-ray diffraction methods, microscopy, and various spectroscopic techniques. [99,122-131] For elasticity, molecular crystals require i) evenly dispersed weak and dispersive bonds or interactions in three dimensions. These weak bonds could rupture to disperse the elastic energy during mechanical bending and restructure once the external force is removed. ii) Energetically almost isotropic packing in the crystals. iii) Absence of molecular slip planes in the crystal structure, and iv) π - π -stacking contacts lead to the corrugated molecular packing across the crystallographic plane. It also must be interlocked to prevent longrange movements inside the molecular crystal.

In the year 2005, Takazawa et al. demonstrated the first organic flexible self-assembled TC-dye-based nanofiber (**Fig. 1.17a**).^[106] Later, in 2013 Chandrasekar et al. reported the first naturally bent flexible organic optical passive waveguides.^[104] The rectangular-shaped H-aggregated nanofibers displayed active optical waveguiding behavior. (**Fig. 1.17b**). Though, these nanofibers display different FL emissions based on the concentrations and solvents employed for the fiber preparation. These nanofibers' crystallinity and type of intermolecular interactions involved in the aggregation process are not demonstrated. The three-point bending involving forceps and needles with oil as



a lubricant is one of the common techniques for millimeter to centimeter dimensions crystals. [118,134]

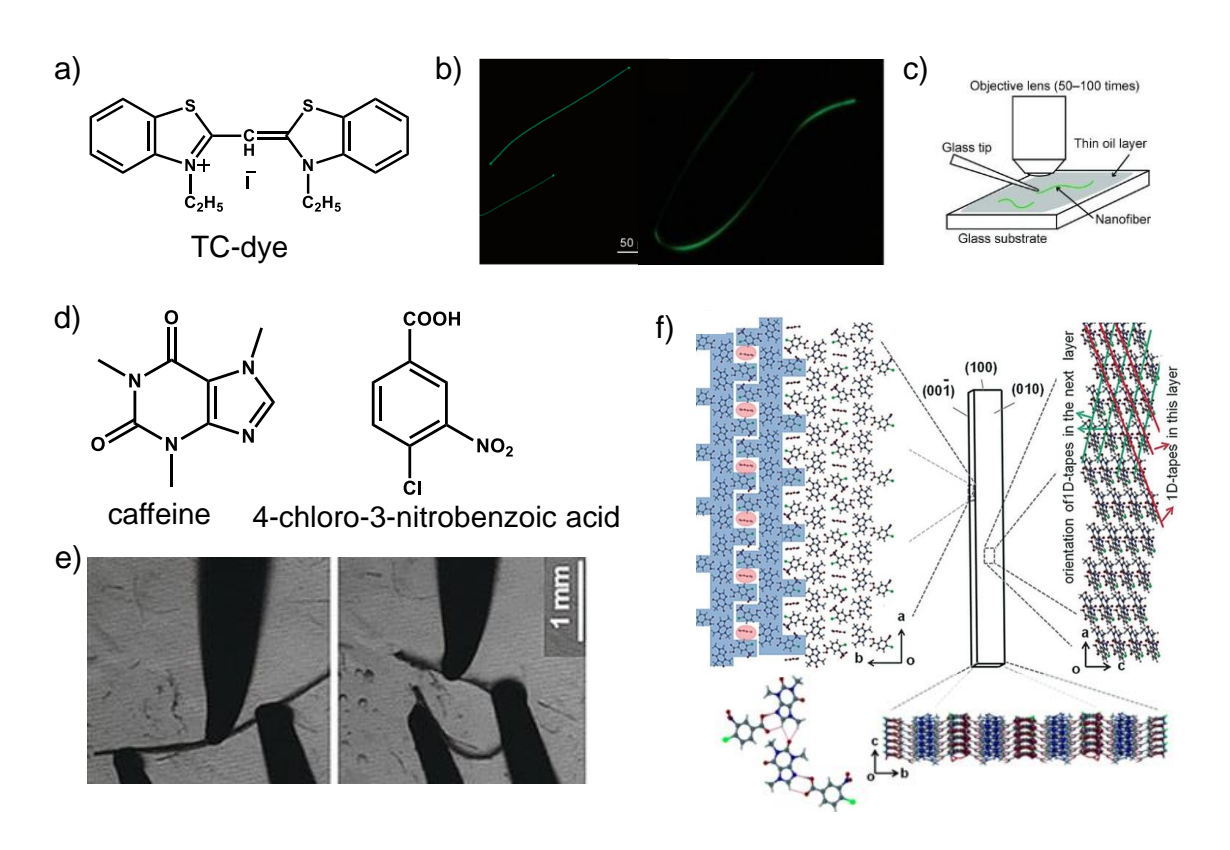


Fig. 1.17. a) Molecular structure of TC-dye. b) PL images of a straight and bent TC fiber. c) Graphical depiction of micromanipulation of nanofibers. d) Molecular structures of 4-chloro-3-nitrobenzoic acid and caffeine. e) Elastic bending of a needle-like CAF-CNB (caffeine-4-chloro-3-nitrobenzoic acid) cocrystal. f) Molecular packing view in different planes showing 1D tapes in (010) face and comb-like 2D layers (marked with blue). Figure adopted from ref. 131-133.

However, this technique lacks accuracy, which frequently leads to damage to the crystals. Hence, this technique is not suitable for microcircuit fabrication using microcrystals. During manipulation, a high refractive index oil layer all over the crystal^[83,118, 134-135] is undesirable (however suitable), and the effect of the cladding layer (lubricant) on optical loss was not established (**Fig. 1.17c**). Also, most mechanically bendable elastic microcrystals regain their original shape after removing external force.

Later, C. M. Reddy et al. investigated the structural basis for the elasticity of methanol solvated cocrystal of 4-chloro-3-nitrobenzoic acid (CNB) and caffeine (CAF) (**Fig. 1.17d**).^[131,136] These elastic single crystals could be folded into a circle mechanically; upon

removing external stress, the crystals retain their original geometry (**Fig. 1.17e**). The extreme elasticity of these crystals is due to the absenteeism of slip planes and 3D weak and diffusive C-H··· π contacts (**Fig. 1.17f**). The presence of solvent molecules inside the crystals helps bend the crystals (**Fig. 1.17f**). The standard packing structure does not break down upon desolvation; however, crystals lose their elasticity. *E* of elastic cocrystal is around 10 GPa.

Chandrasekar and Naumov et al. structurally examined elastically bendable single crystals of (E)-2,4-dibromo-6-(((2,5-dichlorophenyl)imino) methyl) phenol (BCIP) (Fig. 1.18a). When the stress is applied perpendicular to the crystal's long axis, they bend easily without damage (Fig. 1.18b). The distortion reverses, and the crystals regain their initial geometry after removing external stress. The single-crystals can be constantly bent multiple times without any harm using external stress.

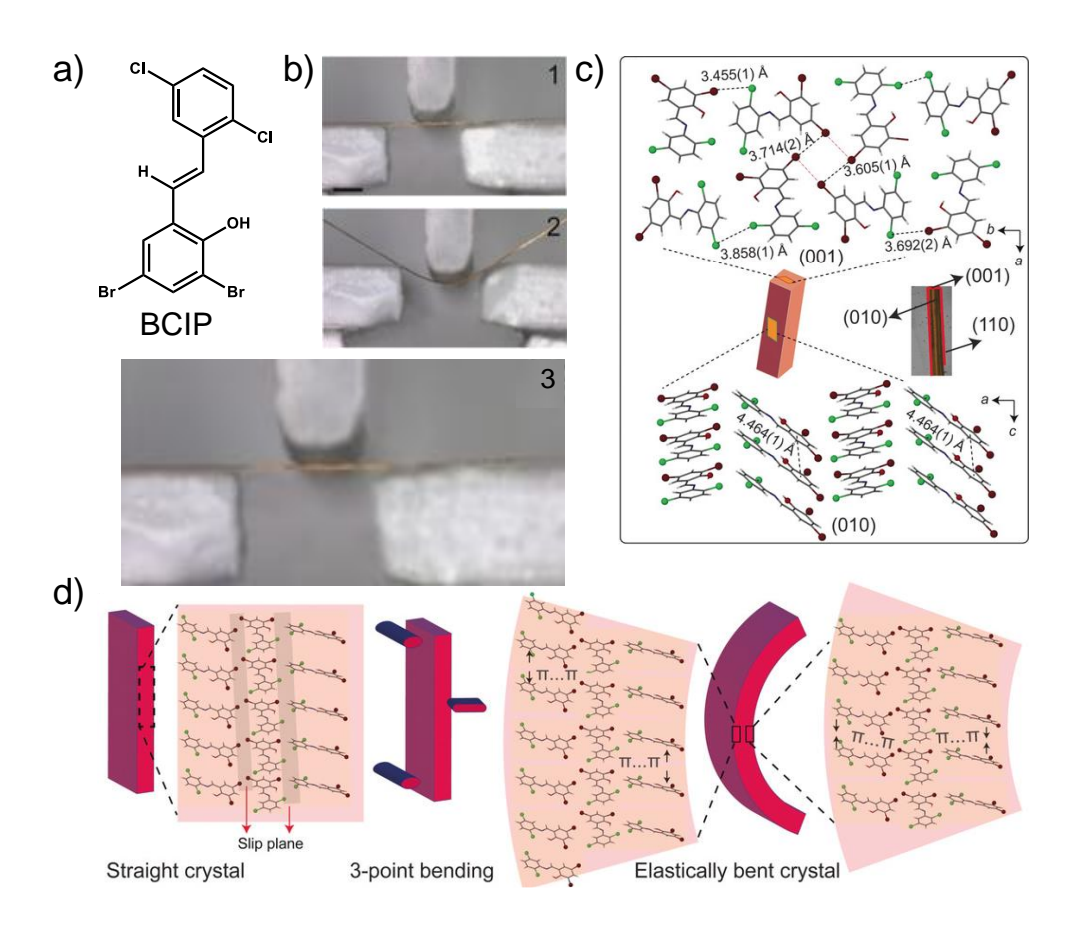


Fig. 1.18. a) Molecular structure of BCIP. b) Elastic behavior of BCIP microcrystal bent using the three-point bending technique. c) BCIP's crystal molecular arrangement is viewed perpendicular to the (001), and (010) faces. d) Mechanism of elastic bending of the BCIP microcrystals. Figure adopted from ref. 96.

As shown in the (**Fig. 1.18c**), the crystal (BCIP) is bending in two pairs of bendable planes, that is, on $(\bar{1}\bar{1}0)/(110)$ and $(0\bar{1}0)/(010)$ by applying force on these faces. The crystal structure analysis of BCIP shows the four molecules connected through type-II Br···Br interactions[†] (3.605(1) Å, 170.53(2)°, 91.24(3)°; 3.714(2) Å, 164.87(1)°, 84.37(2)°), producing a tetrameric unit (**Fig. 1.18c**). These tetrameric units are further connected via two type-II Br···Cl interactions (3.692(2) Å, 122.77(1)°, 105.91(1)°; 3.455(1) Å, 86.38(2)°, 166.75(1)°), and one type-II Cl···Cl interaction (3.858(1) Å, 157.82(2)°, 74.60(1)°) in corrugated molecular layers along the crystallographic *b*-axis. Along the *c*-axis, these molecules are connected through π ··· π -stacking (d ≈ 4.464(1) Å) interactions (**Fig. 1.18c**).

The elastic bending in a single crystal of BCIP is mainly due to the slight sliding of the adjacent molecules and molecular tilting within the π - stacks. These are the reasons for expansion and compression on the concave and convex sides of the mechanically bent region, respectively (**Fig. 1.18d**).^[130] The BCIP single crystals *E*, measured on the (010) plane to be 0.53–0.61 GPa. Mostly, molecular crystals exhibit a strain of 4.4%^{[130],} and metals (elastic materials) display a moderate strain of up to 1%.^[137,138]

1.11.4. Mechanically Bendable Plastic Crystals

In 2005, Desiraju and co-workers first observed mechanical bending in single-crystals of hexachlorobenzene (HCB) with P2₁/n space group (**Fig. 1.19a**). [139,120] In molecular crystals, bending arises due to the presence of anisotropic crystal packing in such a way that weak (Cl···Cl) and relatively strong (π ··· π) interactions patterns form in nearly perpendicular directions. [140,141] Interestingly, these crystals can be compressed and bent into different shapes by changing the direction and point of force applied to

[†]Halogen bonding: When there is an attractive interaction between an electrophilic environment of a halogen atom with the nucleophilic region of another halogen atom in a molecular unit within the same or different molecules, the interaction may be termed a halogen bond or X···X bond. Geometrically and chemically, two types of X···X bonds are possible, namely, type I and II.

Type-I halogen bonding is not following the IUPAC definition as it is based only on a geometric contact between halogen entities in a close-packing environment. In contrast, type-II interactions comprise the pairing between the electrophilic area on one halogen atom and the nucleophilic area on the other.

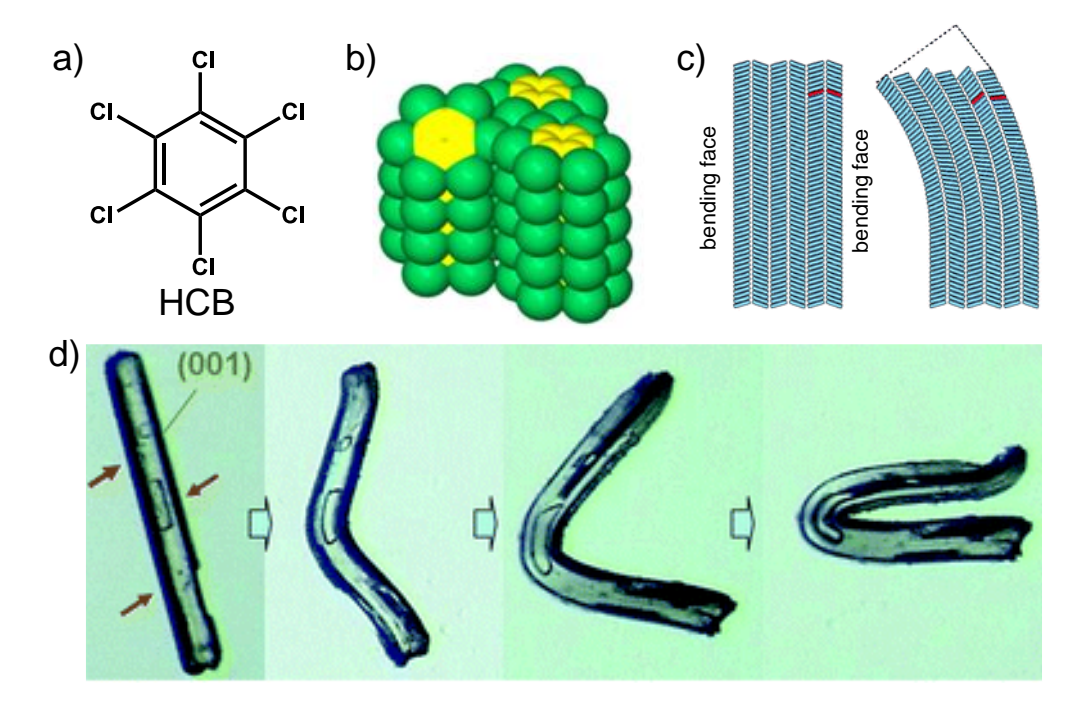


Fig. 1.19. a) Chemical structure of HCB. b) Molecular packing in HCB crystal structure along the crystal long axis. c) Schematic representation of the molecular orientation in the crystal before and after mechanically bent. d) HCB crystal before bending, after bending different snapshots in the bending process. Figure adopted from ref. 139,120.

the crystals (**Fig. 1.19d**).^[140] The three-point force applied on the bendable (001) plane leads to the formation of corrugated layers (**Fig. 1.19b**),^[139] which slide on top of one another, where molecular layers are elongated on the convex side and a little flattened on the concave side (**Fig. 1.19c**). Among these layers, Cl···Cl contacts are weakened and possibly fragmented and reformed after the sliding due to smooth boundary, conserving the total integrity of the crystal. The plasticity of the crystals is mainly due to the presence of soft Cl···Cl interactions and a lack of stronger interactions. The sliding of layers occurs by slight compression on the concave side, weakening and breaking of π ··· π interactions on the convex side, ultimately leading to the breakage of the crystal. Hence, the π ··· π and Cl···Cl interactions dominate molecular packing in different directions as a function of the way of applied external mechanical stress.

Naumov et al. reported the plastically bendable single crystals of 9,10-dicyanoanthracene (DCA) that show passive and active waveguiding properties (**Fig. 1.20a**). [90,100]



These DCA yellow needle-shaped single crystals are obtained via slow evaporation from various organic solvents. The crystal structure analysis shows that the DCA crystal is a

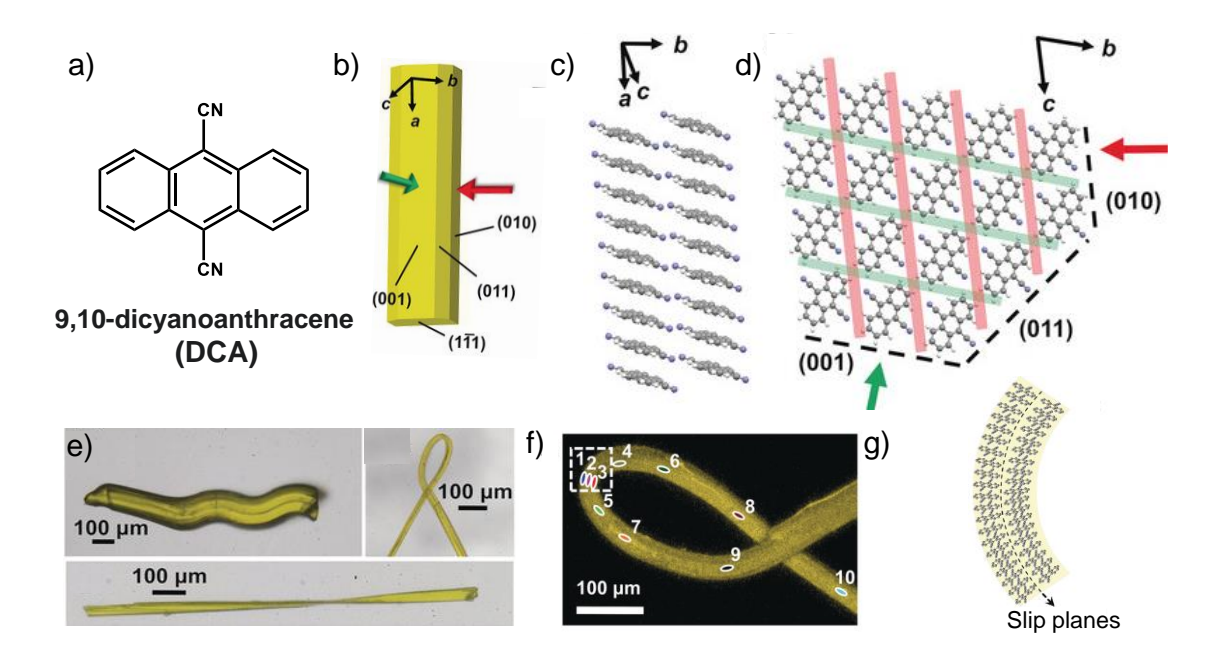


Fig. 1.20. a) Molecular structure of 9,10-dicyanoanthracene (DCA). b) Schematic picture of a DCA single-crystal with face indices. The red (010) and green (001) arrow represents the plastically bendable faces. c) Molecular packing view along the a-axis. d) DCA's crystal structure viewed in the [100] direction. e) Plastic bending of DCA single-crystals into various geometries. f) Optical microscopy image of extremely bent DCA crystal. g) Graphical picture of the molecular packing in the extremely bent crystal (dotted arrow). Figure adopted from ref. 142.

triclinic system with $P\overline{1}$ space group. When the stress is applied perpendicular to either (010) (red arrow) or (001) (green arrow) faces, the crystals exhibit plastic bending behavior (**Fig. 1.20b**). The crystal face indexing showed that the crystals bend plastically when the force is applied perpendicular to either (001) or (010) faces. Analogous to the π -conjugated structures, [124,125] the plastic behavior of these crystals is mainly due to weak dispersive interactions among (energy \approx 32 kcal mol⁻¹) π - π stacked columnar packing of molecules. [143] The feeble van der Waals contacts include slip planes (**Fig 1.20g**) in (010), and (001) planes, which allow slippage of the adjacent DCA columns, eventually leading to enhanced plasticity in two dimensions (2D). Weak (van der Waals) interactions among the π - π stacked columnar packing (in the [100]) of molecules lead to the slippage of molecules, which enables the plastic nature in DCA crystals (**Fig. 1.20c,d**). The *E*, calculated using the three-point bending technique on the (001) bendable face (widest face), is 0.6



± 0.2 GPa.^[144] These crystals can be bent to an angle of 235°, above which the crystal break. (**Fig. 1.20e,f**).

1.12. Mechanophotonics (Mechanical Processing of Organic Crystals)

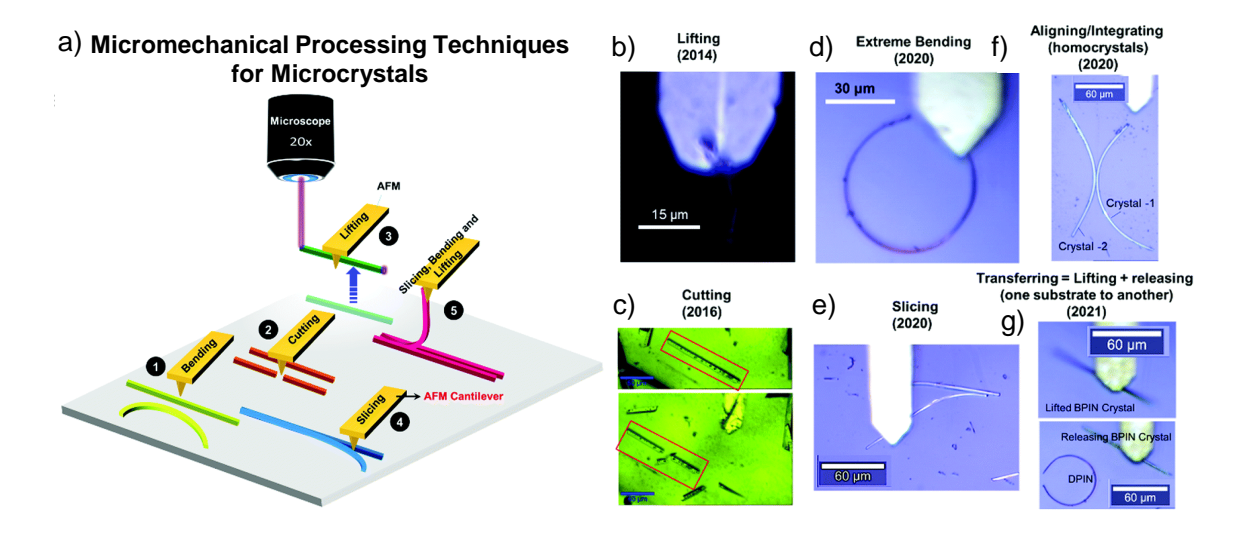


Fig. 1.21. a) Mechanical processing of single-crystals towards OPICs through various mechanical micromanipulation operations using an atomic force microscopy cantilever tip. b-g) Experimentally demonstrated micromanipulation operations for fabrication of hybrid and monolithic organic crystal-based circuits. Figure adopted from ref. 96, 145-148.

Many reported literature has investigated the photonic attributes of millimeter-long mechanically flexible molecular crystals utilizing the three-point bending approach with oil as a lubricant. [118,130,149,150] This macroscale approach's implementation involves needles and forceps, which frequently leads to a lack of accuracy in attaining required geometry and damage because of unequal applied stress. Further, this technique cannot be extended to micro-sized crystals. The fabrication of OPICs requires a lubricant-free micromanipulation technique, micro-sized crystals, and crystal shape irreversibility upon removal of external mechanical force. Fabrication of OPICs involves assembling various organic optical micro components such as optical waveguides (OWs), [87,92-95,102-104,151] cavities, [66,67,70,86,91,152-154] lasers, [65,155-157] modulators, [105] on a chip. The specific organization of multiple optical components in an orderly fashion necessitates an adaptable manufacturing technique. Mechanical manipulation of organic-based microcrystals is one of the important techniques for the fabrication of OPICs. [55,57,96,148,158] The mechanical micromanipulation toward circuit construction has not been attempted

Chapter-1

earlier because of the unavailability of suitable tools for circuit fabrication. At the University of Hyderabad, Chandrasekar and his group developed a novel micromanipulation technique called *Mechanophotonics*. [57,69,96,145] It is a new discipline in nanophotonics that deals with precise mechanical manipulation of flexible organic optical microcrystals using atomic force microscopy (AFM) cantilever tip. [57,69,145,146] This discipline involved controlled mechanical manipulation of microcrystal processing methods like crystal *bending*, *aligning*, *integrating*, *cutting*, *transferring* (*lifting* + *dropping*), and *slicing* essential for the OPICs fabrication (**Fig. 1.21a**).

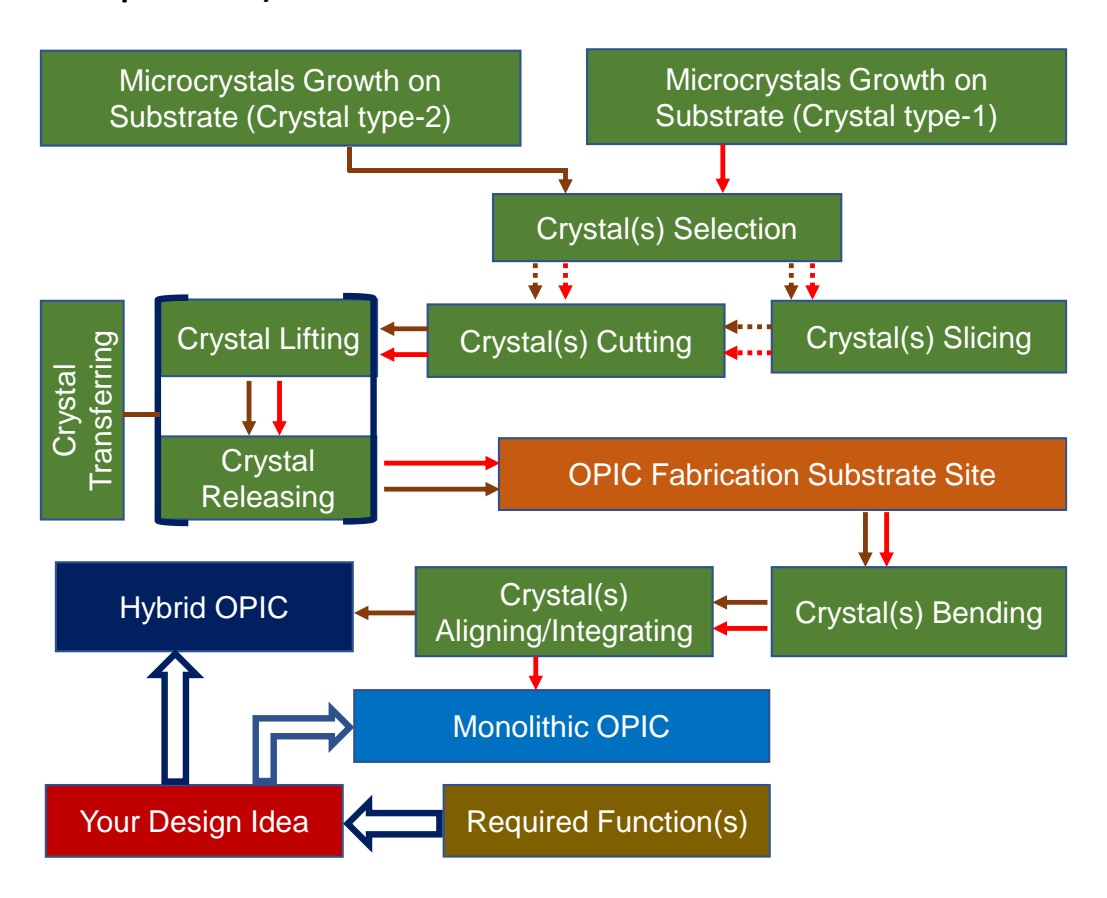
To rule out substrate influence on a microcrystal waveguide's light propagation capability, Chandrasekar et al. lifted a crystal waveguide via the AFM tip in 2014 (Fig. **1.21b**). [145] For OPICs construction, this lifting technique is applied to select a perfect crystal from the substrate. [69] Regulating the crystal dimensions is crucial for the fabrication of geometrically precise OPICs. For this, accurate cutting of a DCM dye microcrystal (FP resonator) orthogonal to crystal long axis was elegantly established in 2016 (Fig. 1.21c).^[70] Later, in 2020, an abnormal pseudo-plastic character of an elastic microcrystal (absence of oil) on a silica substrate was observed during mechanical manipulation with AFM. [96] These crystals were erstwhile classified as elastic crystals when their dimensions were in millimeters. [118,119,134,159,160] The unusual microcrystal pseudoplasticity is due to the larger adhesion between the crystal and its substrate than the crystal shape regaining force. [96] This fundamental discovery created a path for constructing various extremely bent optical components and geometrically stable ringresonators needed for OPICs fabrication (Fig. 1.21d). A slicing method was introduced to separate the combined single microcrystals (Fig. 1.21e). [96] The exact integration of crystals is essential for transferring light energy in a circuit from one crystal to another. The critical integration step needs a suitable arrangement of chosen microcrystals (Fig. 1.21f).[148] Recently, a monolithic circuit was fabricated by aligning two bent crystals at the proper orientation via the AFM technique. [148] The crystal's transfer technique involves lifting (substrate-1) and dropping it close to the OPIC fabrication site (substrate-2).[147] This



technique is helpful for the construction of hybrid OPICs from two chemically different microcrystals (Fig. 1.21g).

The microcrystals by pseudo-plastic character enabled the production of various geometrically stable circuits. The development of organic flexible micro-crystals as photonic elements such as resonators, optical waveguides (OWs), modulators, tuneable ring resonators, splitters, delay lines, lasers, and add/drop filters was set to profoundly improved the construction of modern OPIC technologies.^[55,57]

1.12.1. Pathways to Applying Crystal Manipulation Techniques (Mechanophotonics) Toward OPICs



Scheme 1.4. Graphical illustration of various paths involved in the mechanical manipulation of microcrystals (mechanophotonic) technique towards the fabrication of hybrid and monolithic organic-based circuits.

For an organic microcrystal circuit fabrication, essential photonic functions must be understood before an appropriate OPIC plan (**Scheme 1.4**). Next, grow the required crystals on the substrate based on our electronic emission and absorption choice. The



critical stage is to choose a suitable microcrystal of a desired length/width. Crystals can be separated using the crystal slicing approach when they aggregate. The crystal cutting technique has been employed to control the crystal length. Lifting of chosen crystal and releasing it onto the OPIC fabrication place (same substrate or different) are used where two or more identical or different crystals can be transferred onto the OPIC fabrication site. Next, using an AFM cantilever, the crystals can be bent mechanically into ring-shaped and bent-shaped geometry. Lastly, these ring- and bent-shaped crystals could be perfectly oriented and combined to create a monolithic OPIC. The transferring technique offers a chance to select and integrate mechanically and electronically dissimilar crystals to construct hybrid OPICs, which is not possible in Si-based circuits. The monolithic and hybrid circuits can be fabricated with active and passive optical waveguiding functions.

1.13. Flexible Organic Crystal Photonic Components for OPICs Fabrication

1.13.1. 2×2 Directional Couplers

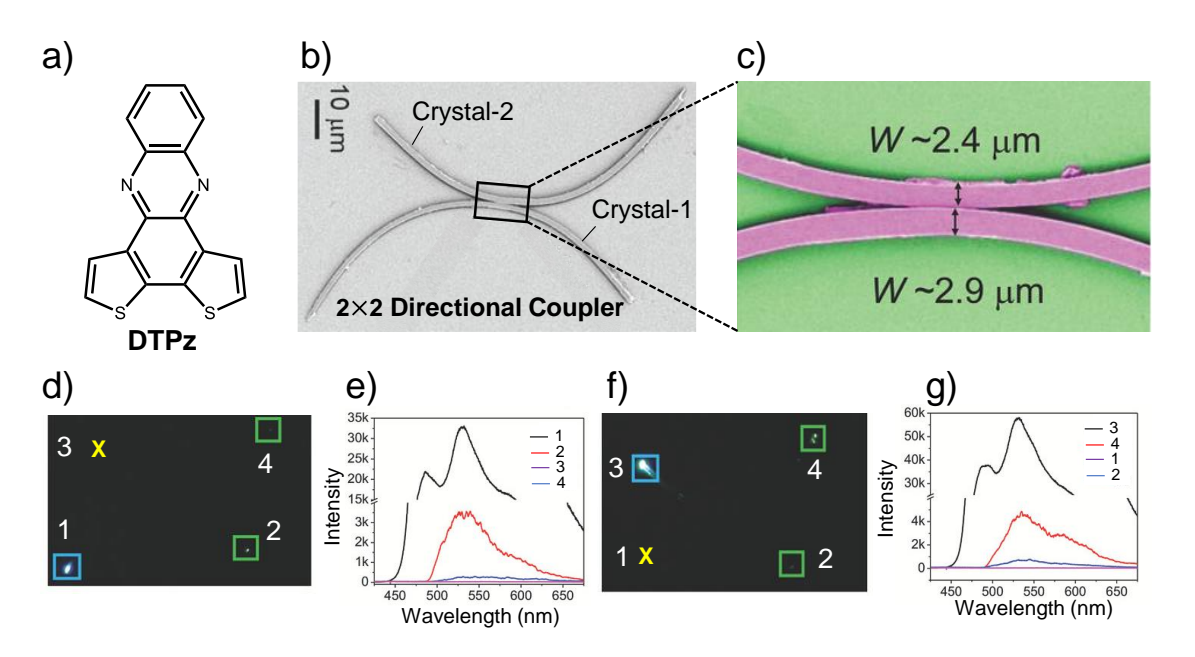


Fig. 1.22. a) Molecular structure of DTPz. b) FESEM image of a 2×2-DC. c) The corresponding false color-coded close view image reveals the widths of the crystals at the coupling area. d,f) FL images of coupled 2×2-DC with two light inputs at terminals 1, and 3, respectively. e,g) The corresponding FL spectra. The yellow crosses represent that there is no output signal. Figure adopted from ref. 148.

In OPICs DC is a fundamental component to split, divert and combine light signals. A monolithic 2×2 DC with four ports was fabricated using two flexible microcrystals of

dithieno-[3,2-a:2',3'-c]phenazine (DTPz) via a mechanophotonic approach (**Fig. 1.22a**). The FESEM picture of the DC showed the widths of the bow-shaped crystals were between $2.4-2.9~\mu m$, with no visible gap at the coupling zone (**Fig. 1.22 b,c**). Excitation at tip-1 of the crystal generated blue FL, which transduced to the coupling junction. At the junction, the light (after reabsorbance) split into two beams propagating towards outputs 2 and 4 (**Fig. 1.22d**). Interestingly, no FL emission was detected at terminal 3. The FL collected at 1, 2, and 4 showed differences in their FL intensities and weak FP-type optical modes. In a crystal-1, the FL efficiency from input 1 to output 2 was \approx 11%, and the FL splitting ratio between output 2 and 4 was \approx 90:10 (**Fig. 1.22e**). Similarly, by exciting the terminal-3 of crystal-2 (**Fig. 1.22f**), the corresponding output FL signal was recorded at 4 and 2. As expected, no signal was detected at terminal 1. The FL emission splitting ratio among termini 4 and 2 was \approx 85:15 (**Fig. 1.22g**). [148]

1.13.2. Organic Mach-Zehnder Interferometers

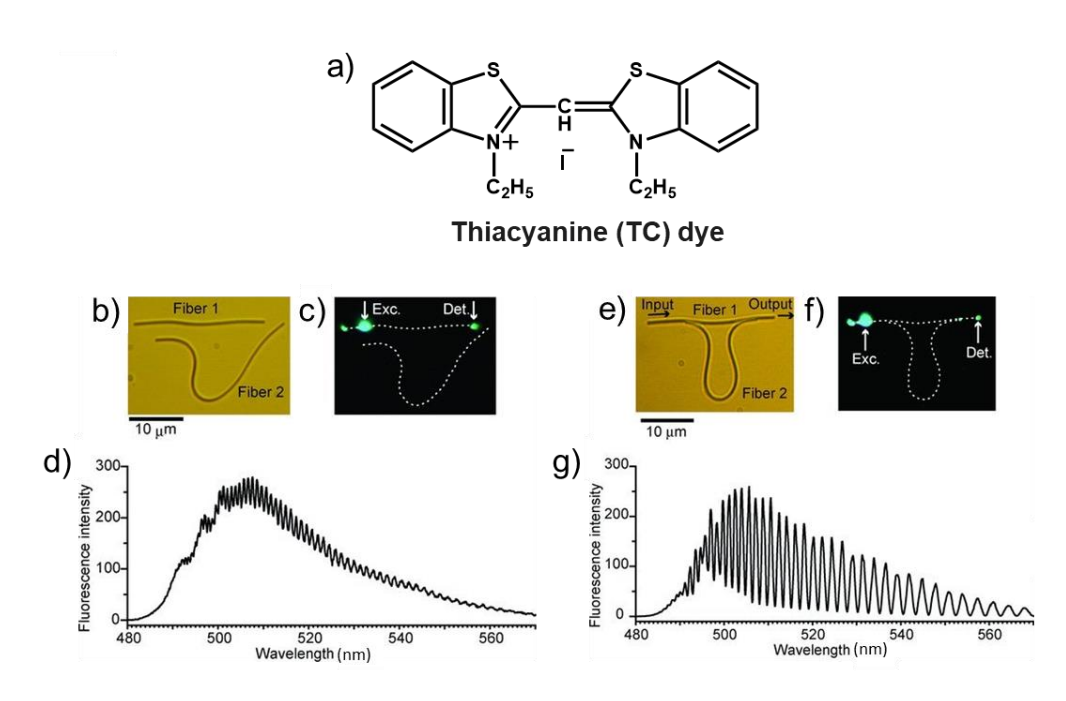


Fig. 1.23. a) Chemical structure of TC dye. b,e) Optical micrographs of TC-fibers employed for the construction of AMZI. c,f) Corresponding FL microscopy images of fiber 1 input at "Exc." position with a laser. d,g) Corresponding spatially resolved FL spectra collected at the "Det." point. Figure adopted from ref. 133.

In most photonic circuits, the Mach-Zehnder interferometer (MZIs) is widely used as modulators, switches, and channel-drop filters. An asymmetric Mach-Zehnder

interferometer (AMZI) was recently demonstrated using TC dye organic-based fibers by Takazwa et al. [133] A small quantity of oil was placed onto a glass surface (substrate: microscope coverslip; 22 mm \times 22 mm). The mechanical operation was enhanced by using a thin oil coat (n =1.48) to avoid the TC-fibers from adhering to the glass substrate surface. The substrate surface was cleaned constantly using a lens cleaning paper to make a thin oil layer. The nanofibers solution was drop-casted onto a substrate, and the solvent was slowly evaporated. For the nanofiber's micromanipulation, a glass terminal was connected to a micro-manipulator under optical microscopic observations. [135]

The optical micrographs of nanofiber 1 ($L \approx 24.1 \,\mu\text{m}$) and 2 ($L \approx 39.3 \,\mu\text{m}$) with equal widths ($w \approx 210$ nm) are presented in **Fig. 1.23b**. Before AMZI fabrication, the waveguiding property of nanofiber 1 was studied. The left tip of fiber 1 was excited with a 405 nm laser, and FL (bandwidth ≈480 to 570 nm) was recorded at its right tip (Fig. 1.23c). [135,161-163] This experiment confirmed the transduction of EPs to the fiber tip from the excitation point. Further, the multiple reflections of the EPs at both nanofiber tip facets led to the rapid fluctuation in the FL intensity with a period of 1-2 nm ascribed to the FP-type optical modes (Fig. 1.23d).[162,164] For the fabrication of an AMZI, fiber 2 was bent, and both tips were coupled to fiber 1 (Fig. 1.23e). The generated EPs from fiber 1 parted into two at the first junction via evanescent coupling. They recombined at the second junction after traveling via two optical paths with dissimilar lengths of 26.4 µm (Fig. 1.23f). This optical interference produced fringes in the output FL spectrum at fiber 1 (right tip) (Fig. 1.23g). The splitting ratio can be tuned at the coupling area by altering the coupling length among the two fibers. The coupling junction length was adjusted to ≈1 µm, and the fiber 1 left tip was excited and collected FL spectra at the right tip (Fig. 1.23f). The recorded spectra reveal the sharp interference fringes demonstrating that this device worked as an AMZI (Fig. 1.23g).

1.13.3. Organic Add-Drop Filters

Takazawa et al. fabricated a miniature ring-resonator, which can circulate optical resonance modes in clockwise and counter-clockwise paths. They fabricated an add-drop filter from an active type waveguide and ring resonator (RR) with a length of 19.3 μ m and

13.8 μ m, respectively. A ring resonator is necessary for wavelength mode filtering in an optical waveguide circuit ^[163] and sensing device applications. ^[165,166] This device operates as an input/output (I/O) bus channel (**Fig. 1.24a**). The generated exciton-polaritons (EPs)

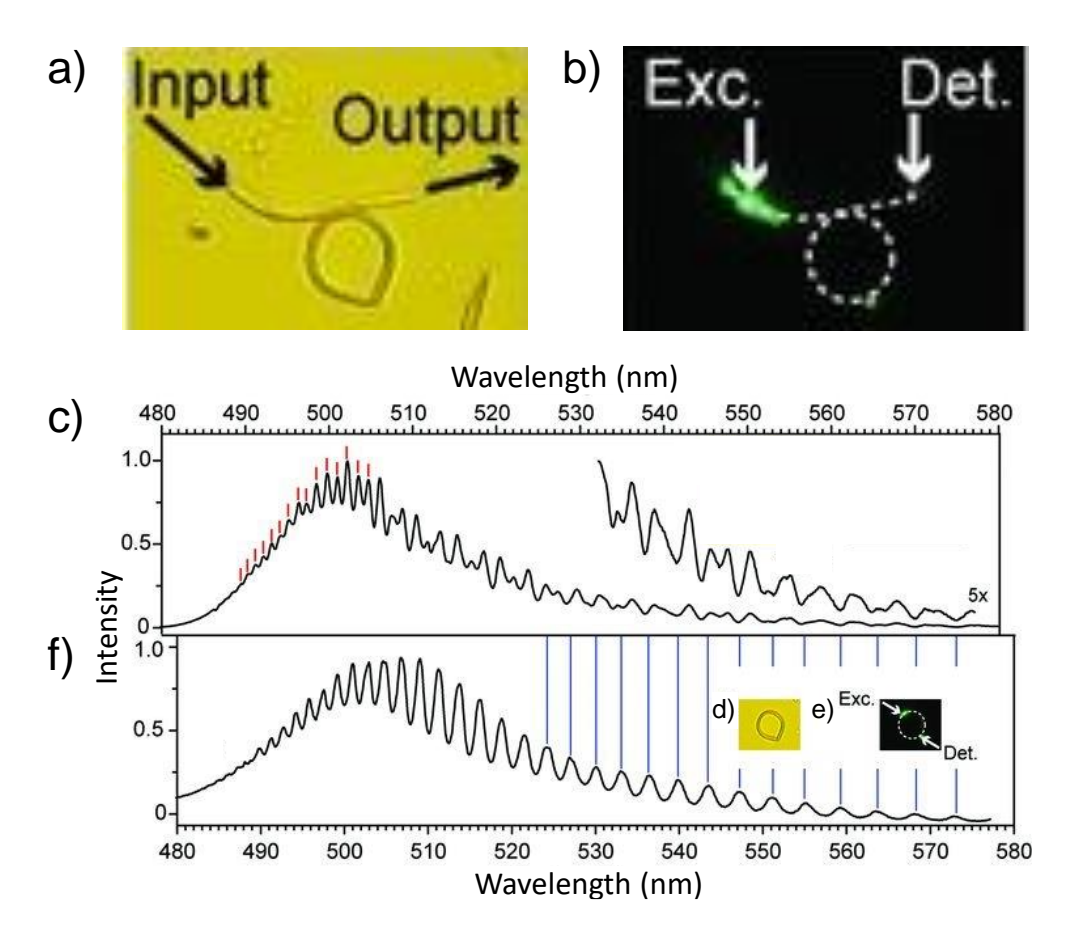


Fig. 1.24. a) Optical image of TC-dye-based ring resonator coupled bus fiber. b) FL image attained from excited at the left tip of the bus fiber (Exc.). c) Corresponding spatially resolved FL spectrum collected at the right tip (Det.). The modes denoted by red lines are the FP-type optical modes of the bus waveguide. d) Optical image of the same ring without the bus waveguide. e) FL microscopy picture of ring excited at "Exc." point. f) Corresponding spatially resolved FL spectrum recorded at the point at "Det". The positions of the ring modes are represented with blue lines. Figure adopted from ref. 135.

transduced through the straight bus fiber coupled to the RR and the EPs of the ring destructively interfered with straight bus fiber EPs at the coupling zone. The left tip of the fiber was excited and collected the spectra at the right terminal, reducing the distance between the bus fiber and the ring (**Fig. 1.24b**). When the fiber waveguide was coupled to the ring, a sequence of dips emerged at $\lambda > \approx 530$ nm when the bus fiber was coupled to the ring (**Fig. 1.24c**). The locations of the dips coincide with the ring optical modes with a small constant shift (**Fig. 1.24d-f**). The $\lambda < \approx 505$ nm, spectrum reveals F-P modes of the

bus waveguide, suggesting that there is no coupling between fiber and ring (red lines; Figure 1.24c).

1.13.4. Organic Microlasers

Lasers are very high intense monochromatic, directional and coherent light energy sources. For advanced OPIC technology, electrically-pumped microlasers are very important, and their construction is highly challenging. Organic-based resonator crystals prepared via solution processing methods offer a chance to produce microlasers with high

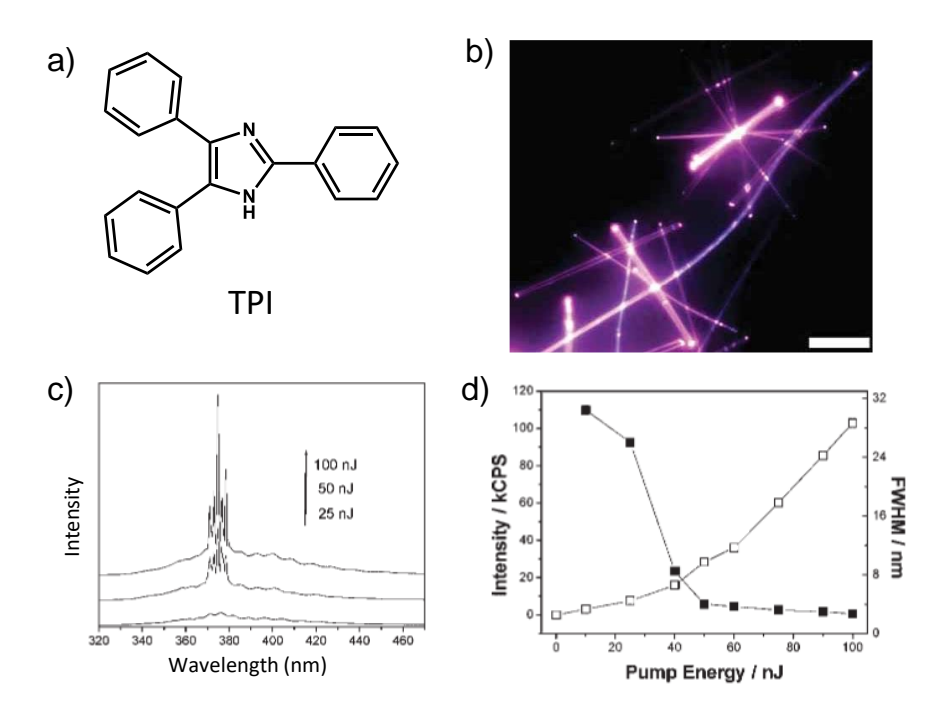


Fig. 1.25. a) Chemical structure of TPI molecule. b) FL photograph of TPI microcrystals. c) TPI nanowires power-dependent FL spectra. d) Line width (filled square box) and power-dependent FL intensity spectrum (open square box). Figure adopted from ref. 110.

optical gain, spectral tunability, lasing mode-control, and low threshold. Yao and Zhao et al. demonstrated an optical-pumped 2,4,5-triphenylimidazole (TPI) based single-crystal nanowires laser made using the physical vapor deposition (**Fig. 1.25a**). ^[110] Using equation (1.13), they measured 300 nm minimal width, which is essential for the transduction of 380 nm light when m = 1. TPI microcrystals showed an active optical waveguiding behavior producing FL at 325 nm upon optical irradiation (**Fig. 1.25b**). Excitation of TPI crystal (W = 400 nm and $L = 15 \text{ }\mu\text{m}$) using a femtosecond laser ($\lambda = 325 \text{ nm}$) generated UV FL ($\lambda_{\text{max}} = 375 \text{ nm}$). The produced FL was transduced to the opposite termini showing the pump

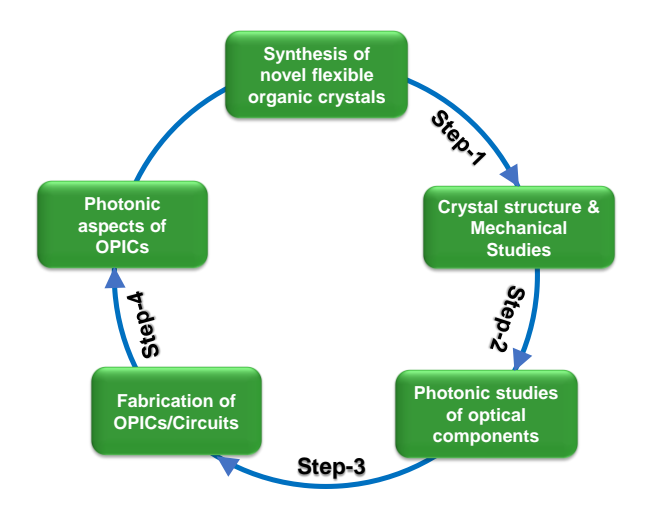


energy-dependent FL spectra with FP-type optical modes (**Fig. 1.25c**). Further, fullwidth-at-half-maximum (FWHM) and power-dependent FL intensity of the emission peak exhibited a threshold and nonlinear gain demonstrating lasing from the microcrystal (**Fig. 1.25d**).

1.14. Overview of Thesis

This interdisciplinary thesis outlines the usage of organic, flexible crystalline materials to address the limitations of conventional Si and Si-based photonic circuit technologies. The current photonic technologies rely heavily on silicon as a light manipulation medium. Si photonics witnessed tremendous growth due to its

manufacturing compatibility with the CMOS. The high n (n = 3.5), low loss bending radius, and high thermal expansion coefficient of Si make it an ideal material for constructing waveguides (linear and bent) and ring resonators. Si-based PICs fabrication involved the use of an electron beam lithography process. However, Si's large H_c (\approx 150 GPa) makes these PICs rigid and non-reconfigurable, confining their



Scheme 1.5. A Multi-disciplinary approach of the thesis.

utility to single-task specific applications. Notably, fabricating hybrid PICs using two different optical materials is tedious and costly. The next-generation photonic technologies mandate reconfigurable and multi-tasking capable PICs. The emergence of organic materials as an alternative to Si photonics is only possible when FOCs demonstrate the functions incapable of Si-based materials. Si-photonics lack functions such as active/passive light transport, ease of hybrid PIC fabrication, reabsorbance, energy transfer mechanisms for circuit operations, and post-fabrication circuit reconfigurability. Addressing this problem requires an innovative, flexible materials platform.

Chapter-1

The main objective of the thesis is to fabricate reconfigurable PICs from microscale flexible organic crystals (FOCs) with fluorescent attributes. The accomplishment of this goal requires a deeper understanding of the fundamentals governing photonics and the mechanical flexibility of organic crystals. Organic FOCs are rapidly evolving superior materials for OPICs owing to their potential use as optical elements like waveguides, RRs, and interferometers. The fabrication of OPICs with FOCs requires the development of a suitable microcrystal processing technique. For this mechanophotonics, an approach employing an atomic force microscope (AFM) cantilever tip for micromanipulation is an ideal choice. One important aspect of microcrystals that distinguishes them from the bulk crystals is the weak adherence of microcrystals to the substrate's surface, the so-called pseudo-plasticity. This special property enables mechanical manipulation to craft a variety of crystal geometries (bent waveguides, loops, and rings) and monolithic OPICs. For the micromanipulation operations like bending, slicing, cutting, moving, transferring, lifting, aligning, and integrating. Notably, the lifting, transferring and integrating operations enable the integration of two different optically emissive flexible crystals required to achieve reconfigurable hybrid OPICs. FOC materials can be used as active and passive photonic components, reabsorbance and energy transfer mechanisms for circuit operations, and post-fabrication circuit reconfigurability.

The general approach followed in this thesis is presented in **Scheme 1.5.** As most of the crystals are brittle and FOCs are quite rare. The mechanical flexibility of FOCs is accredited to their unique molecular packing stabilized by weak and dispersive intermolecular forces. Therefore, preparation of custom-made molecules namely, (*E*)-1-(4-bromo)iminomethyl-2-hydroxyl-naphthalene, (BPIN) and (*E*)-1-(4-(dimethylamino)-phenyl)iminomethyl-2-hydroxyl-naphthalene (DPIN), 9,10-bis(phenylethynyl)anthracene (BPEA), and N,N'-bis(p-tolyl)-1,4,5,8-naphthalenediimide (NDIPH) was planned. These molecules have the potential to provide conducive π --- π stacking, H-bonding, and C-H--- π interactions necessary for crystals flexibility. Crystallization of the synthesized molecules yielded FOCs with various optical (absorbance and fluorescence) and mechanical (elastic and plastic) properties.

Chapter-1

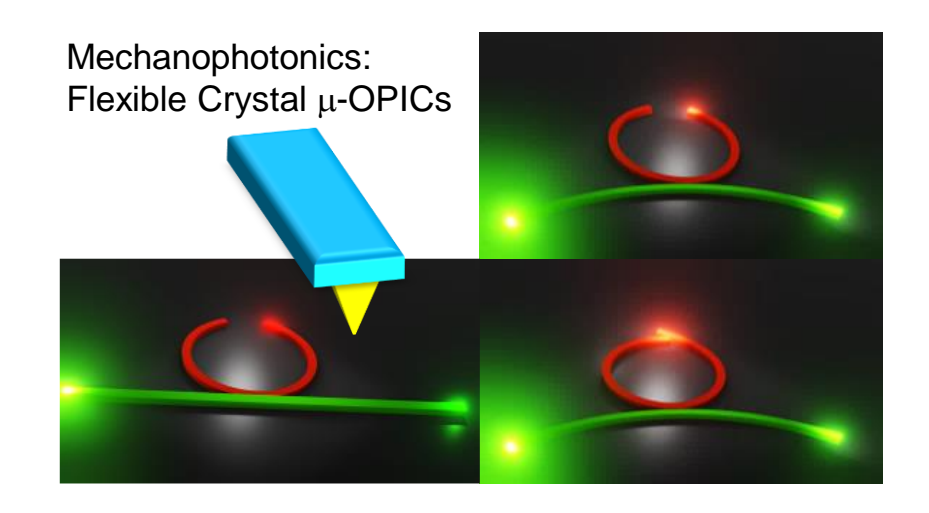
The Schiff-base FOCs, namely DPIN and BPIN can be used to fabricate reconfigurable hybrid OPICs via the mechanophotonics approach. The construction of a DPIN single-crystal ring resonator (RR) is a crucial optical element to route the light in clockwise or anti-clockwise paths. Micromechanical transferring of RR to another substrate facilitates its integration with BPIN crystal waveguide and fabrication of OPIC-I. Later, the crystal's pseudo-plasticity can be exploited to produce three geometrically dissimilar OPICs II and III. The bright-green emission of the BPIN microcrystal can optically stimulate DPIN single-crystal through an ET mechanism, whereas in DPIN the signal transduces to the BPIN passively. The OPICs can also demonstrate input positiondependent optical output signals via passive, active, and ET mechanisms. Another strategy is the use of DPIN elastic crystals for the construction of a monolithic four-port OPIC by integrating two optical waveguides and RR. When RR is integrated with waveguides, it can regulate the light transduction path in the waveguides because of its either clockwise or counter-clockwise light directing function. The complex operations such as mechanismselective (active and passive) light routing, excitation-position-dependent, and mode filtering ability of the resulting four-ports circuit can be established in detail.

Construction of OPIC using mechanically and optically different crystals, for example, plastic NDIPH and elastic BPEA crystals, is a novel strategy. The advantage of plastic NDIPH crystals makes the optical elements capable of mechanical reconfiguration. The electronic energy variance among these organic materials would enable light energy transfer from NDIPH to BPEA crystal through evanescent coupling. The plan is to fabricate an OPIC-I from plastic NDIPH RR with a waveguide tail made from a linear NDIPH waveguide and integrate it with a straight BPEA waveguide resulting in a three-port circuit. Later, the functional complexity can be augmented by combining with one more plastic NDIPH RR with a tail to OPIC-I. Here, the number of signals may be increased to four. OPIC-II can also be mechanically reconfigured to OPIC-III by bending the NDIPH waveguide's direction by 90°. Furthermore, it may be possible to operate the circuit using passive, active, and energy-transfer mechanisms.

One more challenging issue in Si-based PICs is to steer optical signals over 360° on a 2D plane for need-based varying of the optical signals with various optical bandwidths. This goal can be achieved using CPIN and DPIN flexible organic microcrystals, emitting green and orange FL, respectively. The fabrication of OPICs with DPIN RR coupled to DPIN or CPIN waveguides offers the first port-angle reconfigurable FOPICs. Production of different bandwidth optical output signals and 2D signal re-routability over different angles (0 to 360°) on a chip can illustrate the circuit's flexibility for programmable nanophotonic applications.



Mechanically Reconfigurable Organic
Photonic Integrated Circuits Made from
Two Electronically Different Flexible
Microcrystals



This chapter is adapted from:

J. Ravi, M. Annadhasan, A. V. Kumar, and R. Chandrasekar.* Adv. Funct. Mater. 2021, 31, 2100642.



2.1. Abstract

This chapter demonstrates microscale organic PICs (μ -OPIC) fabrication from two chemically and electronically different flexible crystals via a mechanophotonics approach. The experiments focus on the mechanical micromanipulation of orange-emitting (E)-1-(4-(dimethylamino)-phenyl)iminomethyl-2-hydroxyl-naphthalene (DPIN) and green-emitting (E)-1-(4-bromo)iminomethyl-2-hydroxyl-naphthalene (BPIN) crystals with an atomic force cantilever tip. The flexibility of these crystals originate from molecular H-bonding, C-H··· π , and π ··· π stacking interactions. These mechanically compliant crystals form exceedingly bent and photonically relevant reconfigurable geometries during micromanipulation, including three μ -OPICs. Remarkably, these μ -OPICs operate through passive-, active-waveguiding, and energy transfer mechanisms. Depending on the crystal's electronic nature (BPIN or DPIN) receiving the optical signal input, the circuit executes mechanism-selective and direction-specific optical outputs. The presented proof-of-principle concepts can be used to fabricate complex photonic circuits with diverse, flexible crystals performing multiple optical functions.

2.2. Introduction

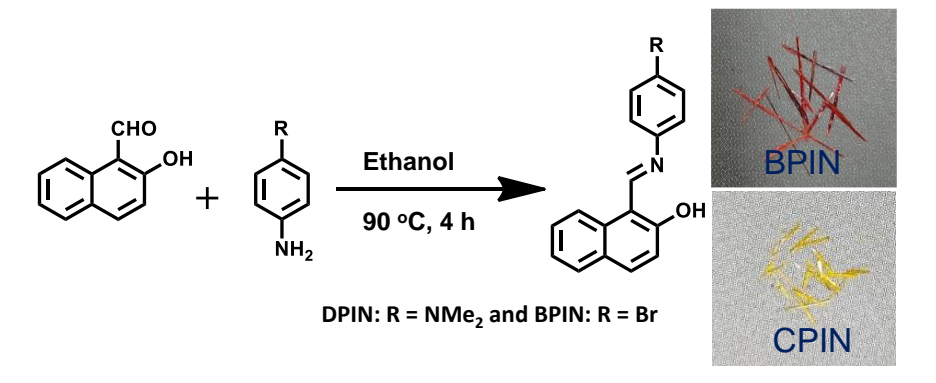
A hybrid PIC is a device that integrates at least two different components with optical functions such as active $[^{165,87,95,103,92-94,155-157]}$ or passive $[^{90,104,102,151]}$ optical waveguides (OWs) or cavities useful for micro-communication, biomedical, and quantum computation applications. $[^{167]}$ However, the idea of fabricating hybrid μ -OPIC with two different organic single crystals has not been realized yet, $[^{97]}$ until this study. The utilization of flexible crystals with energy-transfer (ET), passive, and active optical waveguiding traits are imperative for accomplishing complex optical functions in a μ -OPIC. For the construction of single-crystal organic μ -OPICs, the use of two structurally close but electronically different, Schiff-base flexible crystals, namely, (E)-1-(4-(dimethylamino)-phenyl)iminomethyl-2-hydroxyl-naphthalene (DPIN) and (E)-1-(4-bromo)iminomethyl-2-hydroxyl-naphthalene, (BPIN) was envisioned (**Scheme 2.1**). Zhang et al. demonstrated the optical waveguiding propensity of highly flexible DPIN crystals of millimeter size. $[^{97}]$ BPIN is also expected to form a relatively planar π -conjugated structure akin to DPIN due

to the intramolecular hydrogen bonding interaction between the OH and HC = N groups.^[168] DPIN and BPIN molecules differ only at the terminal position with different dimethylamino and bromine group substitutions. However, this functional group variation alters the electronic state energies and their optical absorbance and emission properties, allowing energy transfer (ET) from BPIN to DPIN.

This chapter discusses the μ -OPICs fabricated with DPIN and BPIN flexible crystals employing the AFM-based micromanipulation technique. These organic crystals are flexible due to specific packing provided by H-bonding, C-H··· π , and π ··· π stacking interactions. The green FL of BPIN crystal optically excites DPIN crystal via ET. After a series of mechanical manipulation operations, these microcrystals provide three geometrically different μ -OPICs. All μ -OPICs show remarkable input signal position-dependent optical outputs through active-, passive-OW, and ET mechanisms.

2.3. Results and Discussion

2.3.1. Synthesis of DPIN and BPIN



Scheme 2.1. Synthesis of DPIN and BPIN; its single-crystal photographs at ambient conditions.

DPIN and BPIN compounds were synthesized according to reported literature. [169] N', N'-dimethylbenzene-1,4-diamine (10 mmol, 1eq), and 2-Hydroxy-1-naphthaldehyde (10 mmol, 1eq) were taken in a 100 mL two-necked round bottom flask and dissolved in ethanol (30 mL). The reaction mixture was heated at 90 °C for 4 h. After completion of the reaction, the mixture was cooled to room temperature, and the precipitate was filtered off and recrystallized in chloroform to obtain DPIN crystals. A similar procedure was adopted for the preparation of BPIN by using 4-bromoaniline instead of dimethylbenzene-1,4-diamine. Yields: 90% (DPIN) and 85% (BPIN).

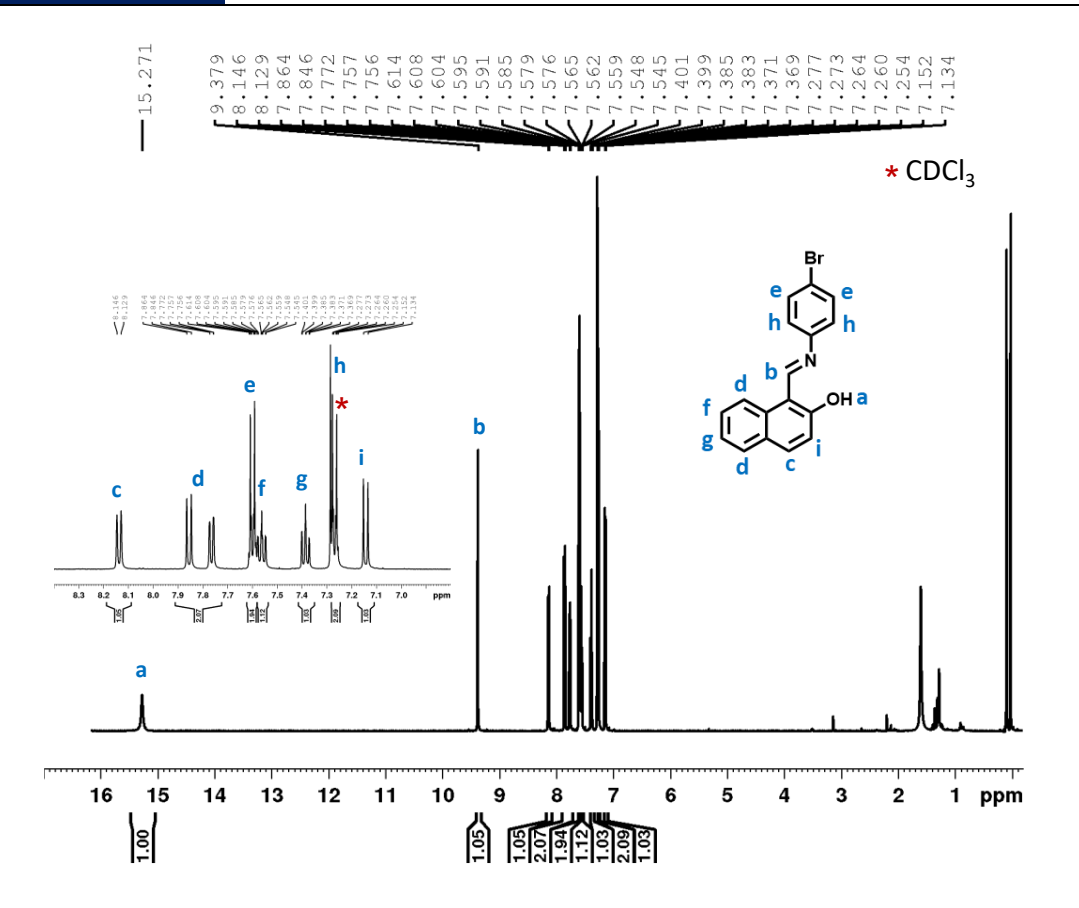


Fig. 2.1. ¹H-NMR spectrum of BPIN in CDCl₃ solvent.

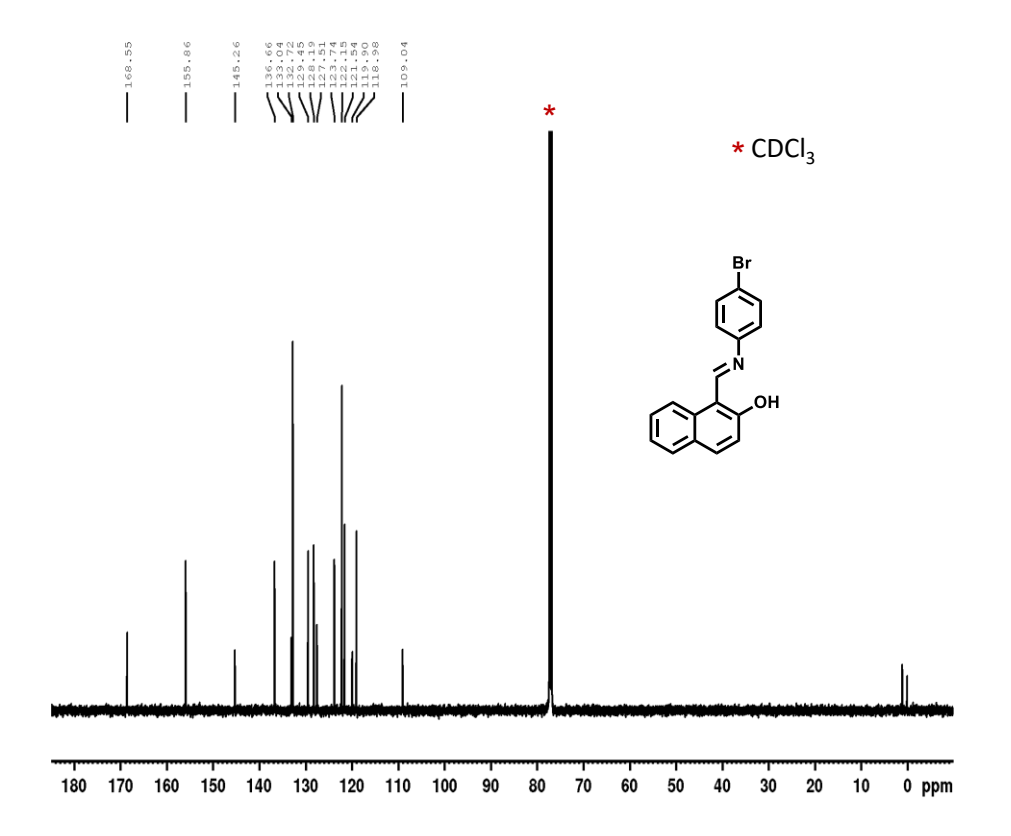


Fig. 2.2. ¹³C-NMR spectrum of BPIN in CDCl₃ solvent.

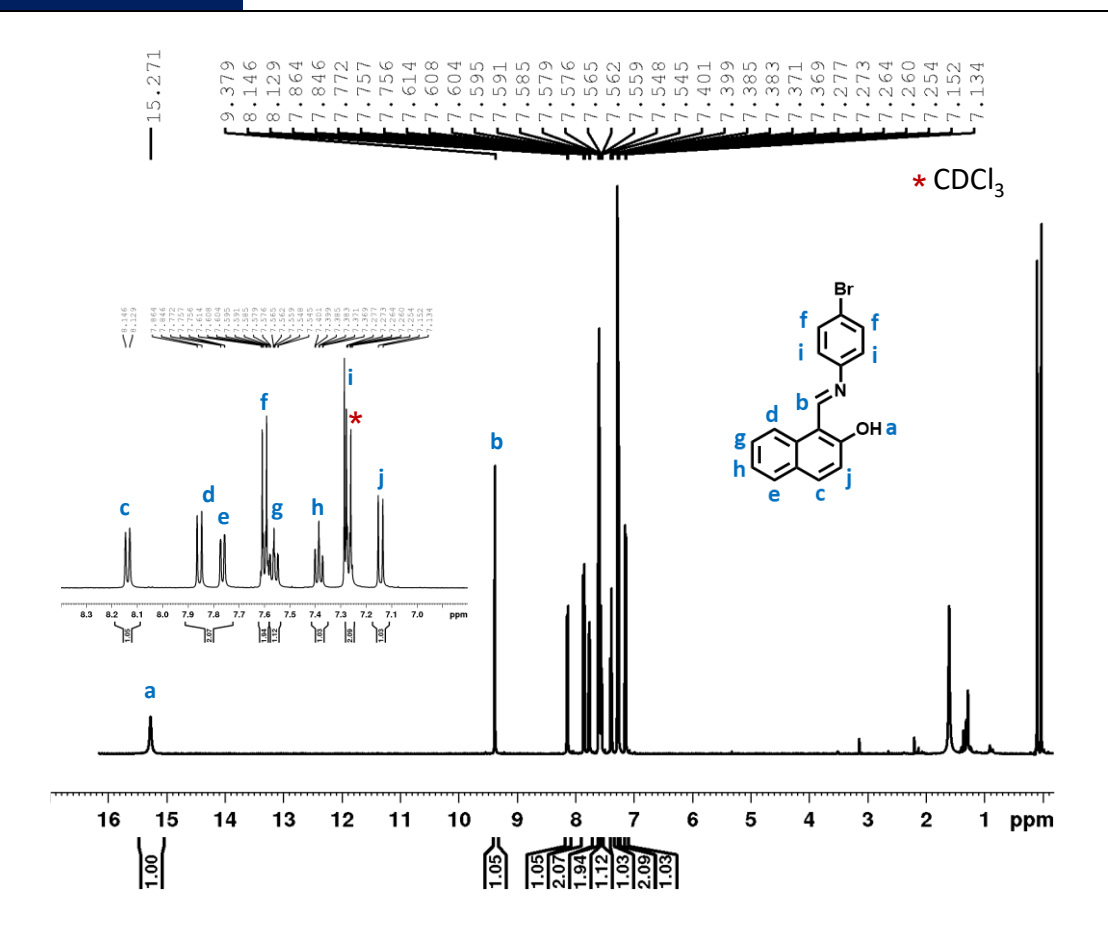


Fig. 2.3. ¹H-NMR spectrum of DPIN in CDCl₃ solvent.

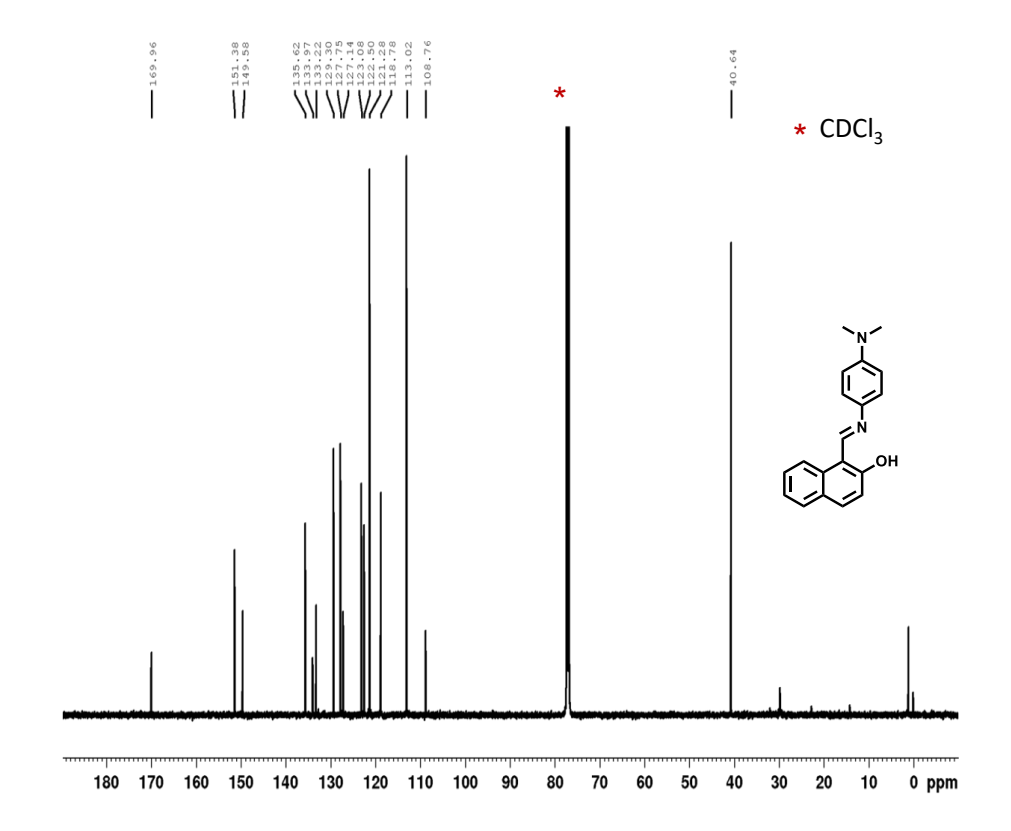


Fig. 2.4. ¹³C-NMR spectrum of DPIN in CDCl₃ solvent.

DPIN: ¹**H NMR** (400 MHz, CDCl₃): δ (ppm) 15.99 (s, 1H), 9.31 (s, 1H), 8.11 (d, 1H), 7.78–7.71 (m, 2H), 7.52 (m, 1H), 7.36–7.31 (m, 3H), 7.10 (d, 1H), 6.80 (d, 2H), 3.03 (s, 6H); ¹³**C NMR** (100 MHz, CDCl₃): δ (ppm) 169.36, 151.38, 149.58, 135.62, 133.97, 133.22, 129.30, 127.75, 127.14, 123.08, 122.50, 121.28, 118.78, 113.02, 108.76, 40.64; UV-Vis (Solidstate): λ_{abs} band width \approx 300-630 nm and $\lambda_{FL-max.}$ = 597 nm (orange emission); m.p. \approx 202-206 °C.

BPIN: ¹**H NMR** (400 MHz, CDCl₃): δ (ppm) 15.27 (s, 1H), 9.37 (s, 1H), 8.13 (d, 1H), 7.80 (dd, 2H), 7.61-7.57 (m, 2H), 7.55 (m, 1H), 7.4-7.36 (m, 1H), 7.26 (m, 2H), 7.14 (d, 1H); ¹³**C NMR** (100 MHz, CDCl₃): δ (ppm) 168.55, 155.86, 145.26, 136.66, 133.04, 132.72, 129.45, 128.19, 127.51, 123.74, 122.15, 121.54, 119.90, 118.98, 109.04; UV-Vis (Solid-state): λ_{abs} band width 300 - 560 nm and $\lambda_{FL-max.}$ = 540 nm (bright green emission); m.p. ≈ 197-201 °C.

2.3.2. Preparation of Microcrystals

Preparation of DPIN Microcrystals: In a clean vial, DPIN (2 mg) was dissolved in chloroform (2 mL) and added methanol (2 mL) on top of the solution. The solution was left undisturbed for 12 h; the resulting solution (20 μ L) was drop-casted onto a clean glass coverslip, and after solvent evaporation, micro-rods were observed under the confocal microscope.

Preparation of BPIN Microcrystals: Similarly, BPIN (2 mg) was dissolved in chloroform (2 mL) and left undisturbed at rt for 6 h under slow evaporation conditions rod-like crystals were formed. For microscopic studies, the obtained BPIN micro-crystals were dispersed in hexane and drop-casted (20 μ L) onto a clean glass coverslip.

2.3.3. Single Crystal X-ray Diffraction (SCXRD) and Molecular Packing Analysis of BPEA

Single-crystal X-ray structures revealed that the crystal packing of BPIN is quite similar to DPIN; both are monoclinic with $P2_1/n$ and $P2_1/c$ space groups, respectively. The crystal structure of BPIN showed an intramolecular hydrogen bonding (O-H···N: 1.79 Å) interaction between HC=N and OH units, akin to DPIN providing molecular rigidity (**Fig. 2.5a**). This interaction also provided near coplanarity of the phenyl and naphthalene units stacking (distance ≈ 3.5 Å), intermolecular phenyl, and OH (C-H···O: 2.57 Å) hydrogen with

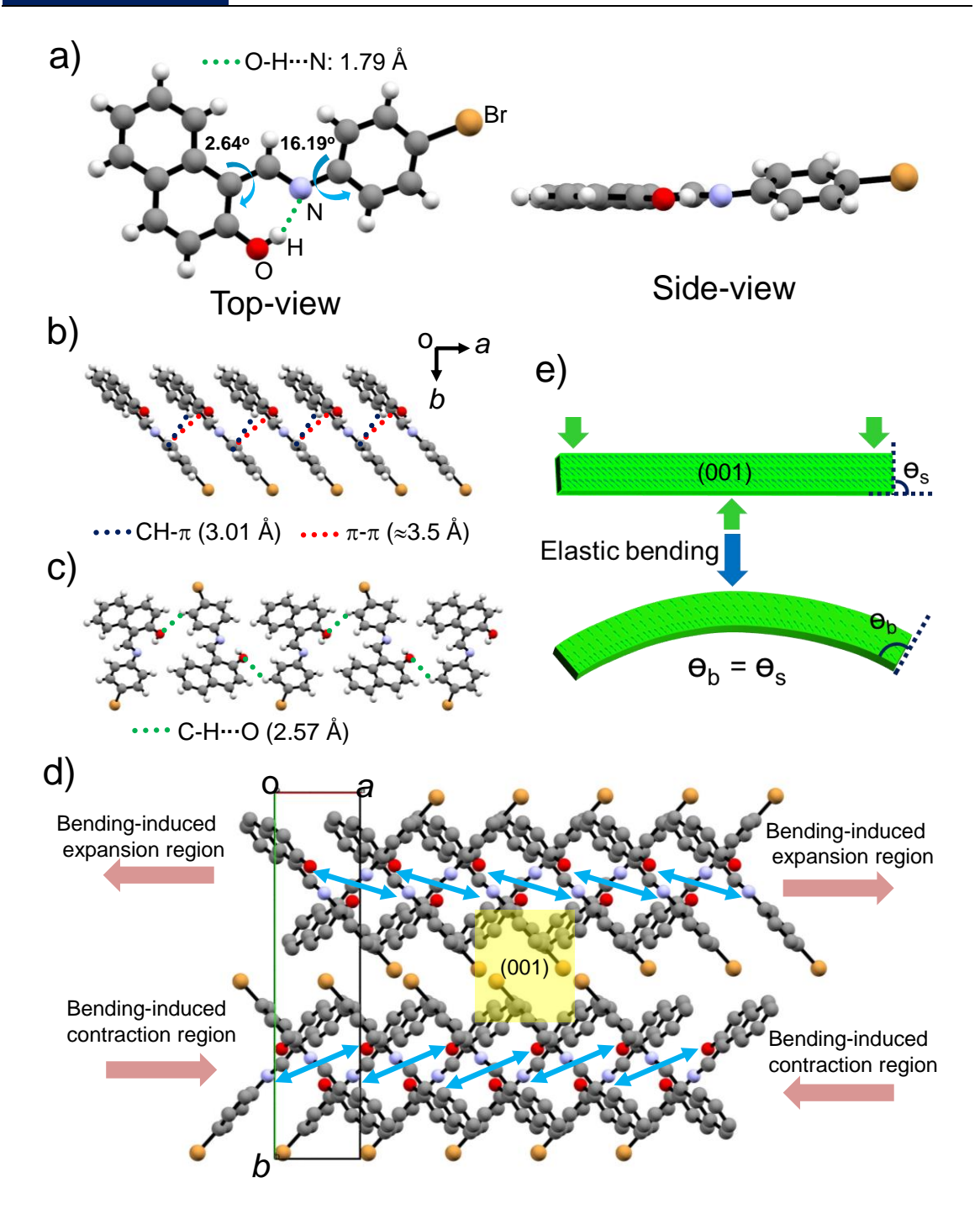


Fig. 2.5. a) Single-crystal XRD structure of BPIN. b) Formation of BPIN chains facilitated by C-H··· π and π ··· π interactions. c) C-H···O hydrogen bonding interactions between BPIN along the chain. d) Molecular packing viewed along crystallographic c-axis displaying the criss-cross pattern of molecular chains. e) Cartoon representation of compression and expansion of molecular chains in a mechanically bent BPIN crystal.

a torsional angle of 16.19°. Weak interactions such as the intermolecular $\pi\cdots\pi$ interactions and C-H··· π interaction (3.01 Å) facilitated the formation of a molecular chain along the crystallographic *c*-axis (**Fig. 2.5b,c**). These interactions lead to a crisscross packing of the molecular chains along the (001) plane (**Fig. 2.5d**). Further, the C-H···Br (3.32 Å)

intermolecular interactions connected each crisscross molecular chain propagating along the crystallographic a-axis. [170] As a result of near similar solid-state packing in BPIN and DPIN, the former molecular crystal also exhibited mechanical flexibility analogous to the latter one. In the crystal lattice, the flexibility arises due to contraction and expansion of the crisscross molecular chains along the inner and outer bends, respectively. The schematic depiction of BPIN straight and mechanically bent crystal geometry displays the expansion and compression of molecular chains (**Fig. 2.5e**).

2.3.4. UV-Visible Spectroscopy Studies

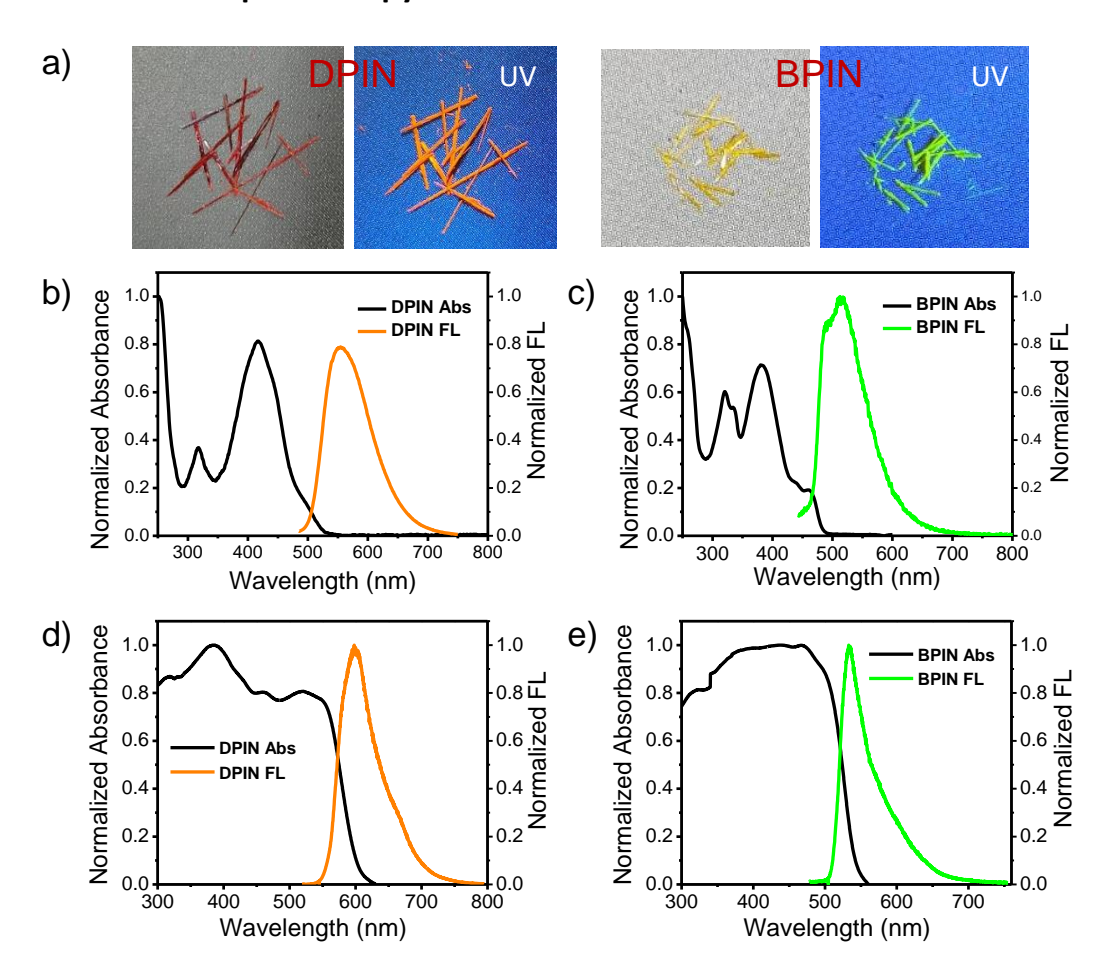


Fig. 2.6. a) Single crystals of DPIN and BPIN under ambient and UV light, respectively. b,c) Solution-state (CHCl₃ solvent) absorption and FL spectra of DPIN and BPIN, respectively. d,e) Solid-state UV-vis absorbance and emission spectra of DPIN and BPIN, respectively.

The optical images of microcrystals of DPIN and BPIN under ambient and UV light, respectively presented in **Fig. 2.6a**. The UV-Vis absorption and emission spectra of DPIN and BPIN are presented in **Fig. 2.6b-e**. The solution state (CHCl₃ solvent) absorption of



DPIN showed two maxima at 318 and 417 nm and emission at $\lambda_{max} \approx 554$ nm (**Fig. 2.6b**). Similarly, the absorption spectrum of BPIN has two maxima centered at 320 and 390 nm with shoulders at 330 and 460 nm. It displayed an emission band in the green region ($\lambda_{max} \approx 512$ nm) (**Fig. 2.6c**).

The solid-state absorption of DPIN appeared in the 300-630 nm range, while its emission bandwidth covered the 545 to 750 nm region (**Fig. 2.6d**). Similarly, the absorption of BPIN appeared from 300-560 nm; with an emission bandwidth of 500-700 nm and λ_{max} at 540 nm (**Fig. 2.6e**). The steady-state optical studies reveal the possibility of energy transfer from BPIN to DPIN as FL emission of BPIN falls within the absorption region of DPIN.

2.3.5. Mechanical and Photonic Aspects of Microcrystals

To test the suitability of DPIN crystal for microcircuits, initially, the intention was to craft a nearly circular-shaped crystal. For that, a DPIN microcrystal of $L \approx 164 \, \mu \text{m}$ was identified. By positioning the AFM cantilever tip towards the middle of the crystal, a gentle force was applied in the forward direction (-y) to bend the crystal with the tip-to-tip distance of $L \approx 156 \,\mu\text{m}$ (Fig. 2.7ai-ii). Later, the left side of the crystal was pulled backward by applying a reverse cantilever force (+y) to reduce further the tip-to-tip distance $L \approx 129$ μm (**Fig. 2.7aiii**). By applying force in the (-x) direction of the right tip, the crystal was bent to create a nearly half-circular shape (with a tail) with a tip-to-tip distance $L \approx 75 \, \mu \text{m}$ (Fig. 2.7aiv-v). Unceasingly, the resultant bent crystal was subjected to intricate cantilever maneuvers in two different directions. Initially, the force was applied on the left tail part of the crystal in the (+x) direction, followed by (+y) direction. These two operations reduced the distance between; (i) the right and left tips to ≈ 33 μm, and (ii) the right tip to the left body to ≈15 μm (Fig. 2.7bvii). The extremely curved crystal diameter of 45 μm shown in Fig. 2.7bi was subjected to optical waveguiding (OW) experiments. The crystal was excited at different points (ii-viii) along its long axis with a 355 nm laser, and the corresponding FL spectra were recorded at the left output terminal (see the white circle) (Fig. 2.7b). Remarkably, the orange FL at different excitation positions of the crystal efficiently transduced to both termini. The FL spectra showed excitation positiondependent Fabry–Pérot (FP) type optical modes^[70] (due to the interference of FL waves), inferring the light trapping potential of the crystal (**Fig. 2.7c**).

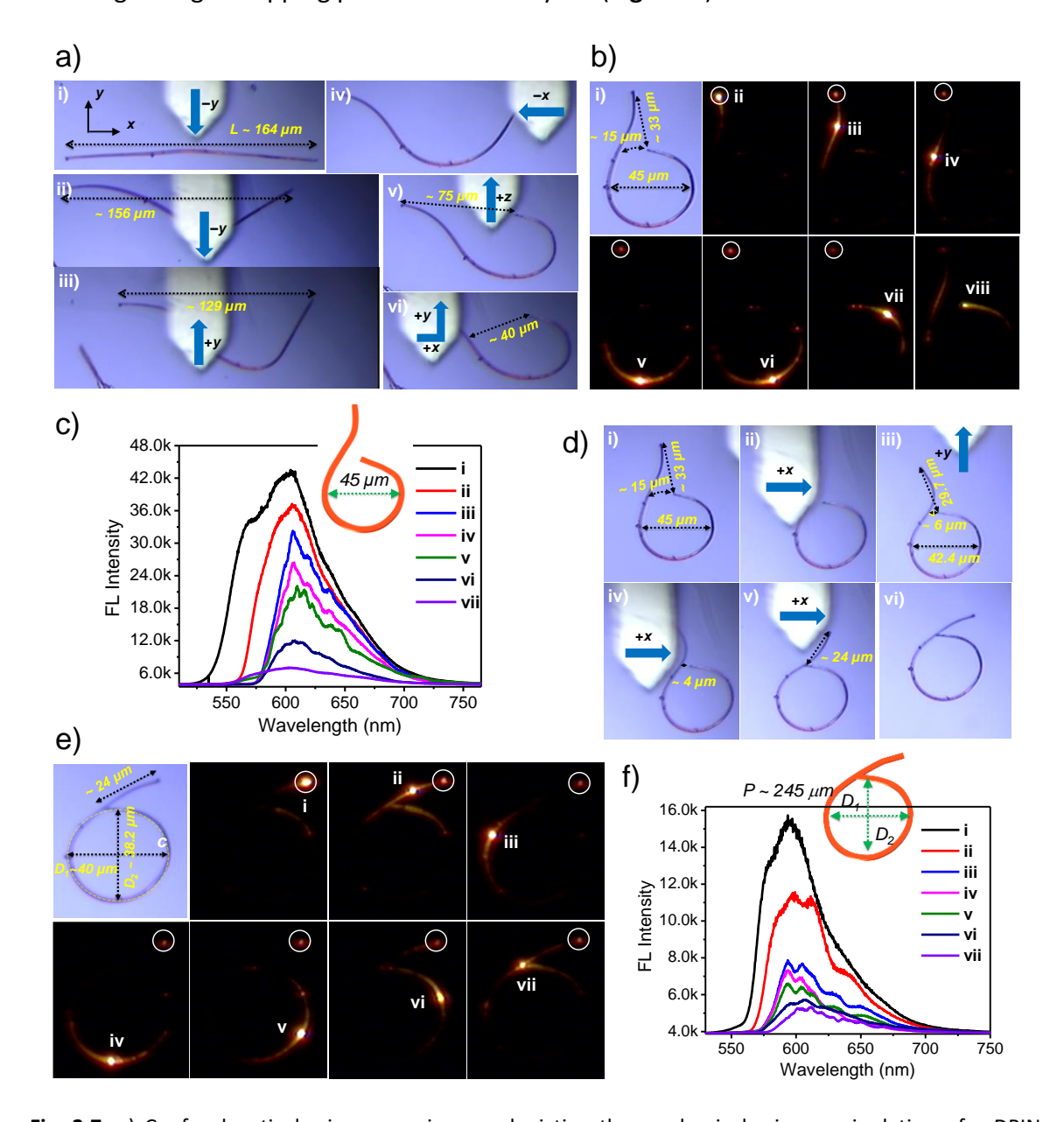


Fig. 2.7. a) Confocal optical microscope images depicting the mechanical micromanipulation of a DPIN microcrystal with AFM tip from straight to near-circular geometry with a tail (i-vi). b) FL images of an overly bent crystal excited at different positions (i-viii) and c) it's corresponding FL spectra. d) Confocal optical microscope images illustrating the micromanipulation of a near-circular DPIN crystal with a tail into an elliptical loop with a tail (i-vi). e) Confocal/FL images of an overly bent crystal excited at different positions (i-vii) and f) it's corresponding FL spectra. The white circles show the FL spectra recorded sites. c,f) The cartoon representation (inset) of extremely bent crystal's geometries.

To produce an elliptical crystal path for the continuous flow of light (**Fig. 2.7d**, **viii**), the tail part (\approx 33 μ m) of the crystal was pushed to the right side (+x) of the crystal to

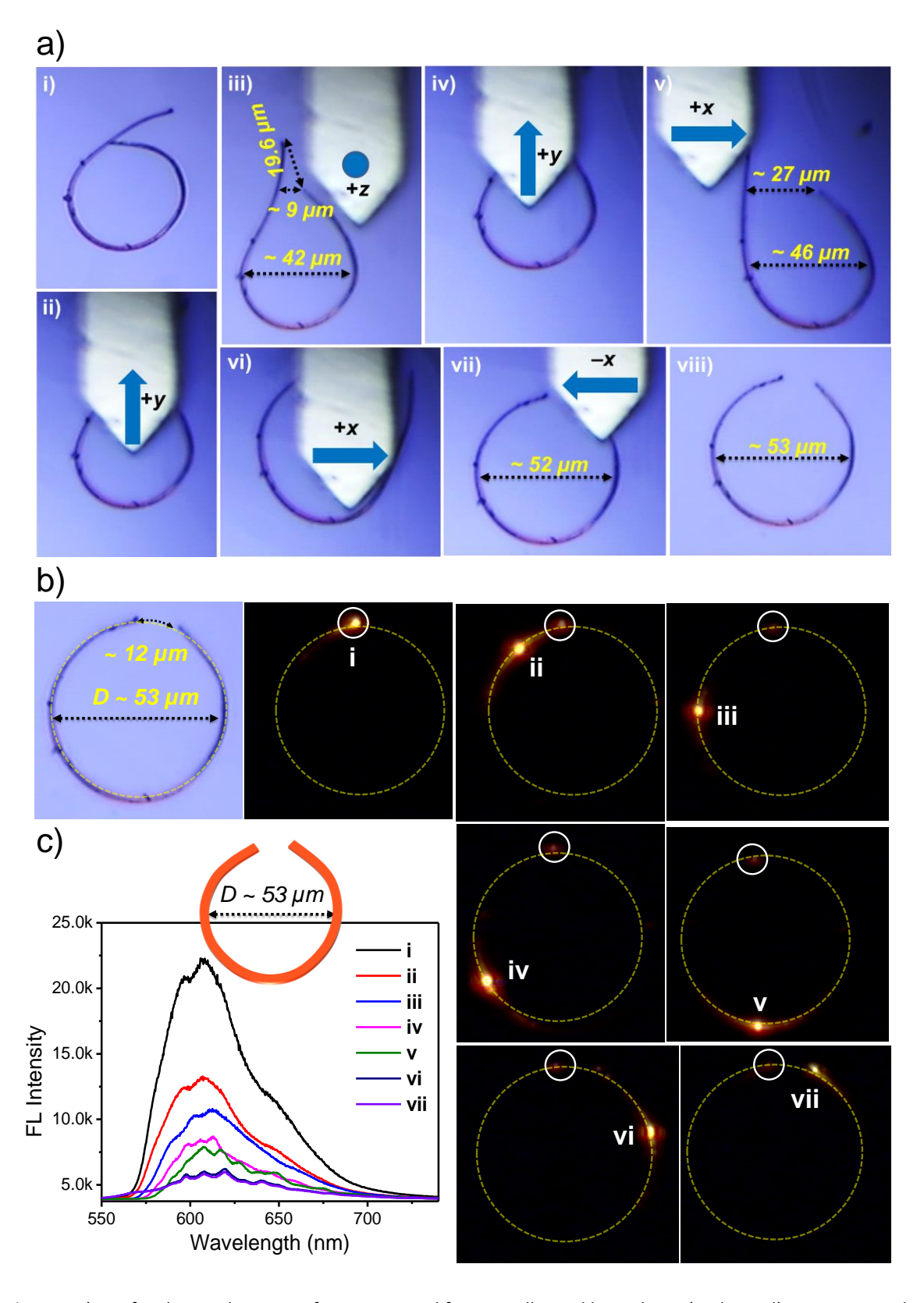


Fig. 2.8. a) Confocal optical images of a DPIN crystal from an elliptical loop shape (with a tail) to a truncated circular shape using micromanipulation. b) FL images of a truncated circular shape crystal excited at different positions (i-vii). c) The corresponding excitation position-dependent FL spectra. The white circles show the FL spectra recorded site. The cartoon representation (inset) of the truncated circular-shaped crystal geometry.

minimize the gap from \approx 15 to \approx 6 μ m (Fig. 2.7d, ix-x). An additional applied force towards the +x direction connected the right terminal with the crystal's left-side body, creating an elliptical loop along with \approx 24 μ m long tail (Fig. 2.7d, xiii). The diameter of the long (D_1) and short (D_2) axes of the ellipse were 40 and 38.2 μ m, respectively, with a perimeter value of \approx 245 μ m (Fig. 2.7e). Optical excitation of the elliptical loop at different positions produced an outcoupled light at the tail end (Fig. 2.7e, i-vii). The corresponding excitation position-dependent FL spectra recorded at the tail end of the crystal (see white circle) showed optical modes (Fig. 2.7f) different from the spectra shown in Fig. 2.7c due to a change in the geometry of the microcrystal.

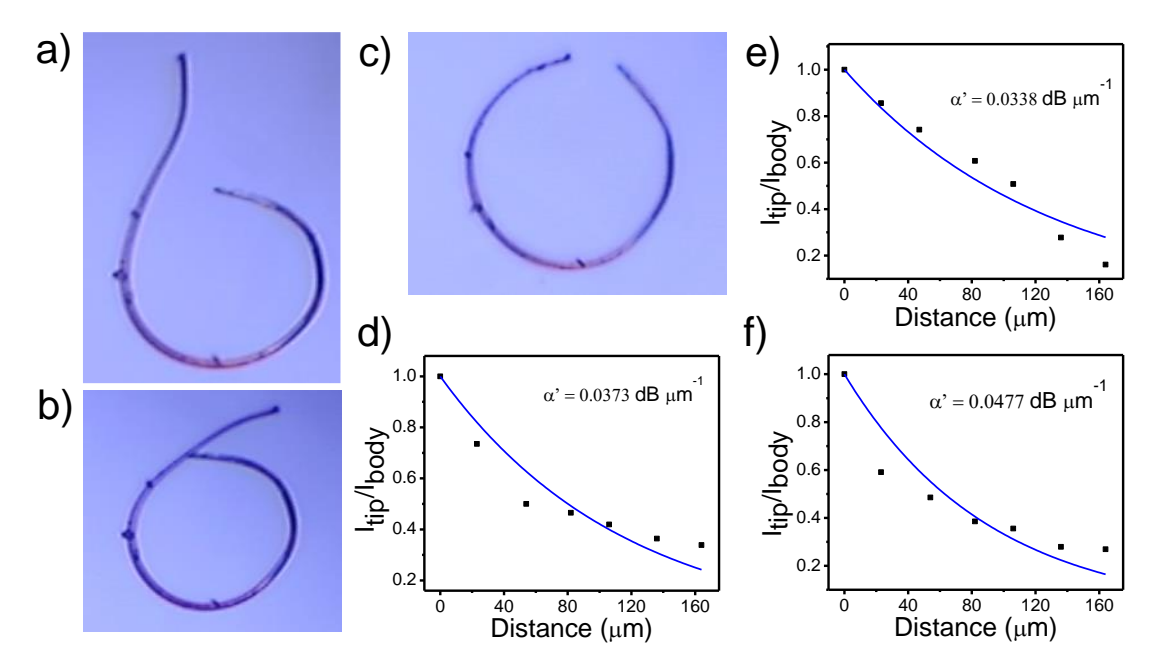


Fig. 2.9. a-c) Confocal images of near-circular geometry with a tail, elliptical loop, and truncated circular shape crystal of DPIN, respectively. d-f) The corresponding optical loss coefficient plots.

Later, a truncated circle from the DPIN-OW crystal was created, as shown in the fabrication steps given in **Fig. 2.8a**. Firstly, the cantilever was lifted from the surface in the +z direction and positioned inside the elliptical loop. Secondly, to open up the loop of the crystal tail was pulled outside in the +y direction (**Fig. 2.8a, ii**), initially to a gap of 9 μ m and later increasing it to \approx 27 μ m (**Fig. 2.8a, iii-v**). Then the right (+x) and left (-x) sides of the crystal were positioned in such a way to make a truncated circular loop with a tip-to-tip distance of 12 μ m and D of 53 μ m (**Fig. 2.8a, vi-viii**). path toward its termini depending upon the excitation positions, **I-VII** (**Fig. 2.8b**). The corresponding excitation-position



dependant spectra collected at the left terminal also revealed FP modes in the FL signal (Fig. 2.8c).

The optical loss coefficient (α) plot of near-circular geometry with a tail, elliptical loop, and truncated circular shape (**Fig.2.9**, **a-c**) crystals of DPIN is shown in **Fig. 2.9**, **d-f**. The optical loss coefficient estimated using equation 1.7 is high for a truncated circular shape, followed by an elliptical loop and near-circular geometry with a tail. The truncated circular loop possesses the highest optical loss coefficient for various structures made from the same crystal. This observation can be understood by invoking the fact that more light leakage takes place at curved surfaces. Surprisingly, a less strained structure like near-circular geometry with a tail has more light leakage compared to an elliptical loop with a tail. This is because there is a major loss at the acute bent angle at the tip crystal in the near-circular geometry. Hence, a larger optical loss is observed than in an elliptical loop crystal.

2.3.6. Fabrication of μ -OPICs from Microcrystals

To create μ -OPICs using DPIN and BPIN crystals, the optical waveguiding propensity of the BPIN was initially tested using a crystal length of $L \approx 114 \,\mu\text{m}$ (Fig. 2.10a). Excitation of the crystal at one of the termini with 355 nm light generated green FL at the excitation position (Fig. 2.10b) and confined the FL during the transduction till it was emitted as an output at the opposite terminal. The laser excitation position-dependent experiments along the crystal body revealed output signals at both crystal termini confirming the OW propensity of BPIN. The output FL signal intensity correspondingly decreased with the increase of the optical path (Fig. 2.10c). The optical loss coefficient of BPIN-OW was measured to be 0.03875 dB μm^{-1} (Fig. 2.10d).

The integration of linear BPIN-OW with truncated circular-shaped DPIN crystal via micromanipulation is a challenging task. For that, the BPIN crystal was *lifted* (-z) from substrate-1 using an AFM cantilever tip, *transferred* towards substrate-2, and carefully *deposited* near the truncated-circular shaped DPIN crystal (**Fig. 2.11a**). These two mechanical operations were impeccably executed, as shown in **Fig. 2.11a**, **i-ii**. The deposited BPIN-OW was pushed towards the DPIN crystal in two sequential directions (-y and -x) to produce an integrated hybrid, namely, μ -OPIC I (**Fig. 2.11a, iv**).

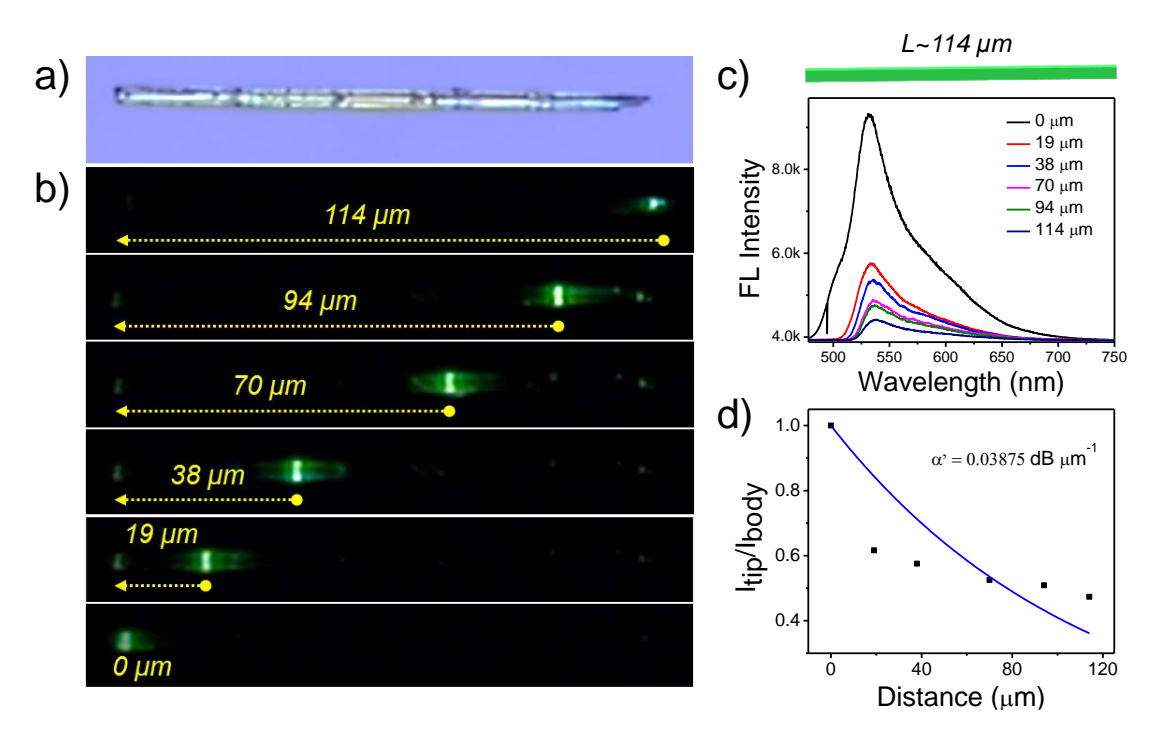


Fig. 2.10. a) Confocal optical image of a BPIN microcrystal ($L \approx 114$ um). b) The corresponding FL images of a BPIN crystal are selectively excited with a 355 nm laser at different positions. c) The excitation-position dependent FL spectra. The top inset shows the cartoon representation of the straight BPIN crystal. d) Calculated optical loss plot of BPIN straight crystal.

Later, the straight BPIN-OW was bent to a bow-shaped geometry by moving both sides of the tips in the *y*-direction (**Fig. 2.11b, v-vi**), and finally pulling it towards a truncated circular loop. The hybrid circuit geometry of μ -OPIC II was further altered by connecting two truncated circular-shaped DPIN-OW crystal terminals. This micromanipulation provided a μ -OPIC III, wherein the DPIN-OW formed a closed-circular loop of D of \approx 50 μ m with an exposed crystal terminal (**Fig. 2.11b, ix**). The field emission scanning electron microscope (FESEM) images of the hybrid crystal μ -OPIC III are shown in **Fig. 2.11c**. From the FESEM images, the estimated width of the DPIN and BPIN crystals around the junction were \approx 1 μ m and \approx 2.2 μ m, respectively. A closer look at the junction confirmed that the crystals are in contact with each other at the junction. The extraordinary flexibility shown by the BPIN and DPIN crystals is due to their elasticity. However, these crystals exhibited very high flexibility so that even a circular geometry (**Fig. 2.11b, ix**) could be made.

The extreme geometrical stability of the crystal demonstrates that crystal-coverslip surface adhesion energy is higher than the shape-regaining energy of the crystals. [96,148] When the nearly circular-shaped crystal was deliberately lifted from the

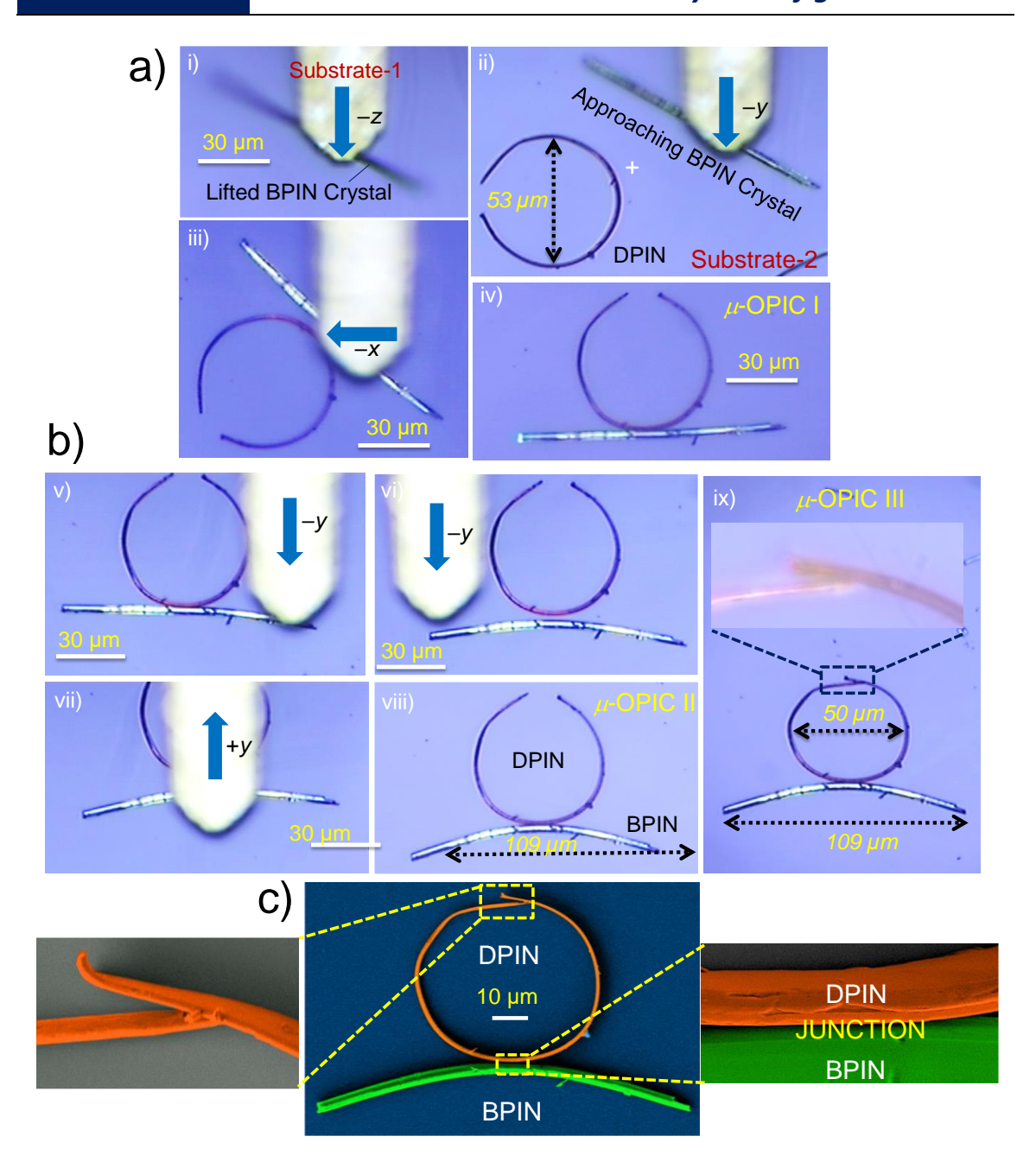


Fig. 2.11. Confocal optical images depicting a) the mechanical manipulation steps involved in integrating straight BPIN crystal with truncated circular DPIN crystal to create a μ -OPIC I (i-iv). b) Mechanical bending of BPIN crystal to bow-shape to produce μ -OPIC II (v-viii) and construction of a ring from truncated circular-shaped DPIN-OW crystal creating μ -OPIC III (ix). c) FESEM images of μ -OPIC III.

surface, it immediately regained its original straight shape, confirming the role of surface adhesion energy in stabilizing various geometrical shapes of the bent crystal.

To test the function of μ -OPICs, the left terminal of the BPIN-OW of μ -OPIC I (**Fig. 2.12b**) was optically excited with a 355 nm laser. For the input-1, the generated green FL at the excitation terminal propagated till junction α (**Fig. 2.12b, i**), and split into two. The

unsplit *active* green optical signal traveled straight to the BPIN crystal output terminal b. As expected, the intensity of FL spectra recorded at junction (a) was lower than the signal collected at terminal b, due to the tight confinement of propagating light (**Fig. 2.12b, c**; μ -OPIC I). The FL spectrum of DPIN at terminal c revealed a highly intense $\lambda_{\text{max}} \approx 600$ nm *active* signal along with a very low intensity *passive* $\lambda_{\text{max}} \approx 540$ nm signal. This spectral feature indicated that the green signal from BPIN-OW (≈ 540 nm) split at the junction and evanescently coupled to the DPIN crystal. A major part of the coupled green light excited the DPIN crystal through ET and produced an orange signal (≈ 600 nm) transducing only to output c, and no spectra were observed at output d (**Fig. 2.12c**; μ -OPIC I). The remaining part of the coupled green light *passively* propagated to the output terminal c.

The excitation (input-2) at terminal c of the DPIN crystal (Fig. 2.12b, ii) split part of the orange FL at the junction. The unsplit part of the ≈600 nm signal traveled in a circular path and out coupled at terminal g, revealing a highly intense FL spectrum with FP-type optical modes (Fig. 2.12c, μ -OPIC I). These optical modes arise from the constructive and destructive interference of the propagating orange signal within the waveguiding cavity. The split signal (≈600 nm) was passively coupled to BPIN-OW and propagated to output terminal h, without any output at terminal f (Fig. 2.12b, c μ -OPIC I). Interestingly, the passive light outcoupled at terminal h also exhibited optical modes (Fig. 2.12c). These experiments demonstrated the function of μ -OPIC I to carry out complex operations via optically passive-, active- and ET mechanisms. The μ -OPIC II is slightly different from μ -OPIC I due to the bent geometry of BPIN-OW (Fig. 2.12a μ -OPIC I, II). However, the optical experiments exhibited results similar to μ -OPIC I, except for the position of the optical modes observed at terminal h (Fig. 2.12c, μ -OPIC II). The μ -OPIC III is quite distinctive as the DPIN crystal has an optical path for light circulation (Fig. 2.12a μ -OPIC III). Optical excitation of the left terminal of the bent BPIN-OW exhibited an active output signal at terminal b of BPIN, and a mixed active orange (via ET), passive green signals at terminal c of DPIN (Fig. 2.12b,v and 2.12c; μ -OPIC III). The collected FL spectrum at the junction α showed no special features. However, when the point close to c of DPIN was excited, the detected active FL terminal g disclosed optical modes (**Fig. 2.12b**, **vi** and **2.12c**; μ -OPIC III). The generated active FL is passively coupled to BPIN via junction and out-coupled at terminal h with optical modes (Fig. 2.12b, vi, and Fig. 12c μ -OPIC III). The table given in



Fig. 2.12d summarizes the mechanism-selective (passive, active, or both and ET-active) and directional-specific optical outputs from μ -OPIC I-III depending upon the electronic nature of the crystal receiving the optical input.

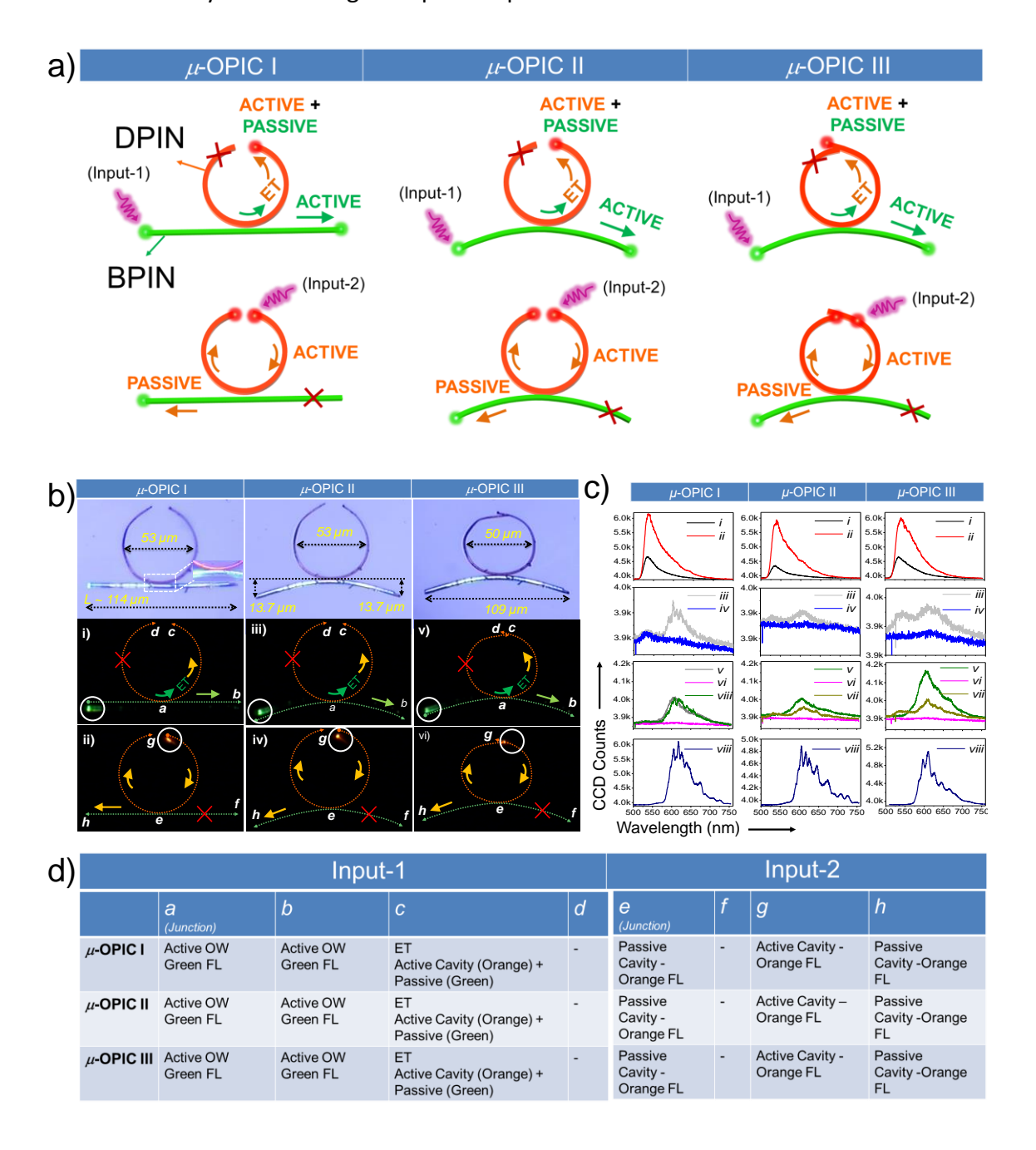


Fig. 2.12. a) Schematic representation of μ -OPIC I, II, and III. b) Confocal microscope (top) and FL images (i-vi) of μ -OPICs. Active, ET-active, and passive types are shown in i), iii), and v). passive type is presented in ii), iv) and vi). c) FL spectra of μ -OPIC I, II, and III. d) Input-dependent mechanism-selective and directional-specific optical outputs from μ -OPICs.

A comparative analysis of the FL spectra recorded at terminal g of μ -OPIC I-III with truncated circular shape DPIN crystal (**Fig. 2.13a, b**) disclosed apparent alterations in the

position of optical modes. The observed variation in the wavelength of the optical modes confirms the alterations of the light field distribution due to the difference in the geometries of μ -OPICs.

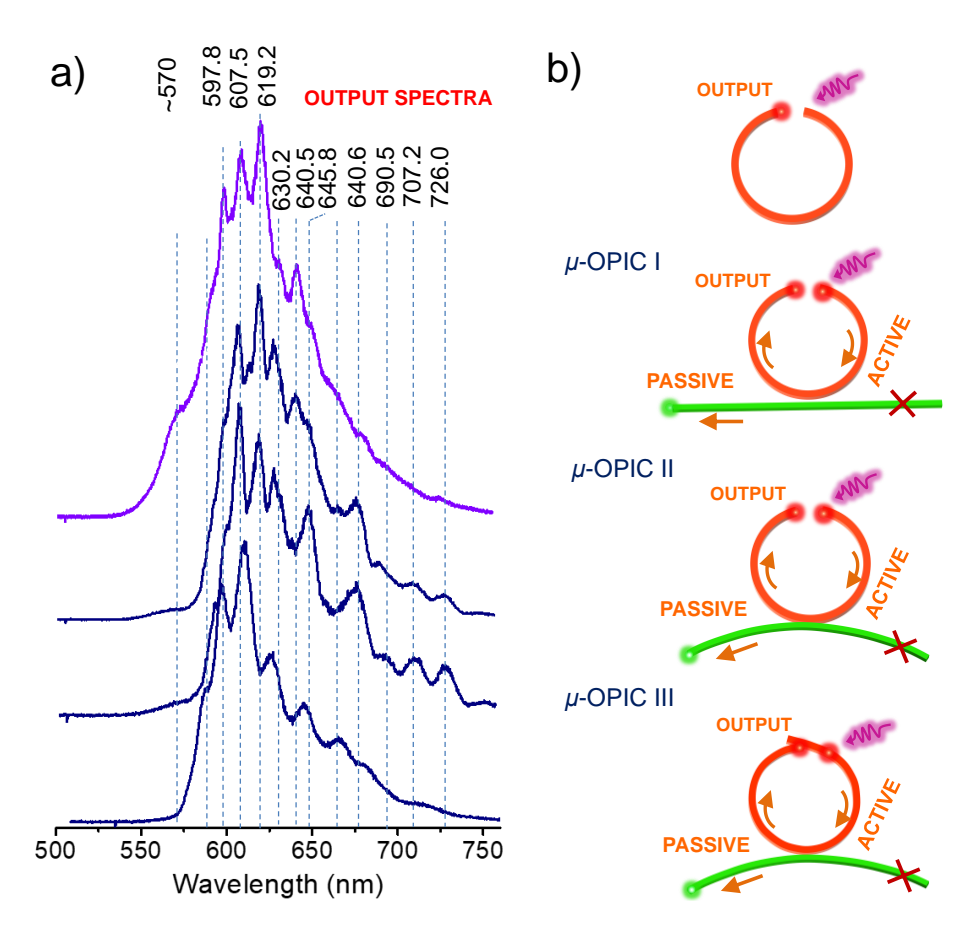


Fig. 2.13. a) FL spectra and b) schematic representation of the mechanism of light propagation in a truncated circular shape crystal of DPIN, μ -OPIC I, II, and III of DPIN.

2.4. Conclusion

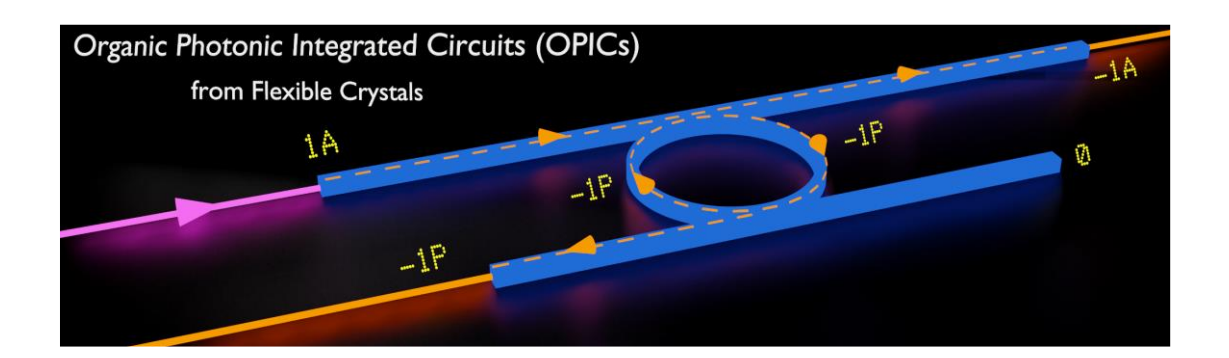
In this chapter, for the first time, μ -OPICs were fabricated using two different flexible organic crystals, namely, DPIN and BPIN. The molecules are structurally very close except in the dimethylamino and bromo functional groups. The extraordinary flexibility of these two crystals arises as a result of H-bonding, C-H··· π , and π ··· π stacking interactions. DPIN and BPIN emitted orange and green FL, respectively. Using the mechanophotonics approach, these two electronically different crystals were bent into different shapes stepwise to construct three geometrically different organic μ -OPICs. The formed μ -OPICs function through active, passive, and ET mechanisms, confirming the characteristics of a μ -OPIC. The observation of FP modes from these OWs established their light-trapping



potential. It is expected that the mechanophotonics approach presented here can be extended to construct diverse geometries of μ -OPICs using both elastic and plastic crystals to route diverse optical signals effectively.



Micromechanical Fabrication of Resonator Waveguides Integrated Four-Port Photonic Circuit from Flexible Organic Single Crystals



This chapter is adapted from:

J. Ravi, and R. Chandrasekar.* Adv. Opt. Mater. 2021, 9, 2100550.



3.1. Abstract

Micromanipulation of flexible organic microcrystals of (E)-1-(4-(dimethylamino)-phenyl)iminomethyl-2-hydroxyl-naphthalene (DPIN) using a mechanophotonics approach provides dual-waveguides coupled ring-resonator. The flexibility of the DPIN crystal arises due to its spring-like expansion and contraction of $\pi \cdots \pi$ stacked molecular chains along the (002) plane. The crystals also act as optical waveguides in straight and bent geometries with low optical loss coefficients. The FL spectra of the guided light display Fabry-Pérot modes. Precise mechanical manipulation of microcrystals with atomic force microscopy cantilever tip bent a straight crystal waveguide to 360 ° angle forming a ring-shaped crystal resonator. The positioning and integration of two straight parallelly oriented waveguiding crystals (bus and drop) along the convex edge of the ring resonator forms the first of its kind organic crystal-based dual-waveguides coupled ring-resonator. The fabricated circuit with four ports selectively guides the produced input FL to through and drop ports via active and passive waveguiding mechanisms.

3.2. Introduction

For OPICs fabrication, [55,147] resonators (ring resonators or cavities) and optical waveguides are essential components. When physically integrated with waveguides, a resonator could be used to control light propagation direction in the waveguides due to its clockwise or anti-clockwise light routing operation. The resultant OPIC also could act as filters, sensors, routers, and delay lines. However, the fabrication of a single crystal ring resonator (RR) is a challenging task. It requires bending a flexible microcrystal to 360° angle without causing damage to attain a ring-shaped crystal. The single-crystal RR can be integrated with two (bus and drop) straight organic crystal waveguides, creating an OPIC with four ports. Among these four ports, at any time, only two ports can function as through and drop points for a single optical input, and the fourth port remains inactive. Further, the molecular crystal's active and passive light propagation mechanisms can be utilized to alter the bandwidth and direction of the propagating light in the circuit. However, the above idea of fabricating and testing single-crystal OPICs had not been realized before this work.



This chapter demonstrates the fabrication of a monolithic OPIC via mechanical micromanipulation using (E)-1-(4-(dimethylamino)-phenyl)iminomethyl-2-hydroxyl-naphthalene $(DPIN)^{[97]}$ flexible crystals (**Fig. 3.1a**). The *mechanophotonics* approach converts a DPIN straight crystal into a RR and integrates it precisely with two straight (bus and drop) optical waveguides to produce a four-port monolithic OPIC. This chapter also illustrates the excitation-position-dependent and mechanism-selective (passive and active) light routing and mode filtering capability of the four-ports OPIC.

3.3. Results and Discussion

Preparation of DPIN microcrystals: DPIN microcrystal was prepared as per the procedure given in Chapter-2.

3.3.1. Mechanical Flexibility and Optical Properties of DPIN

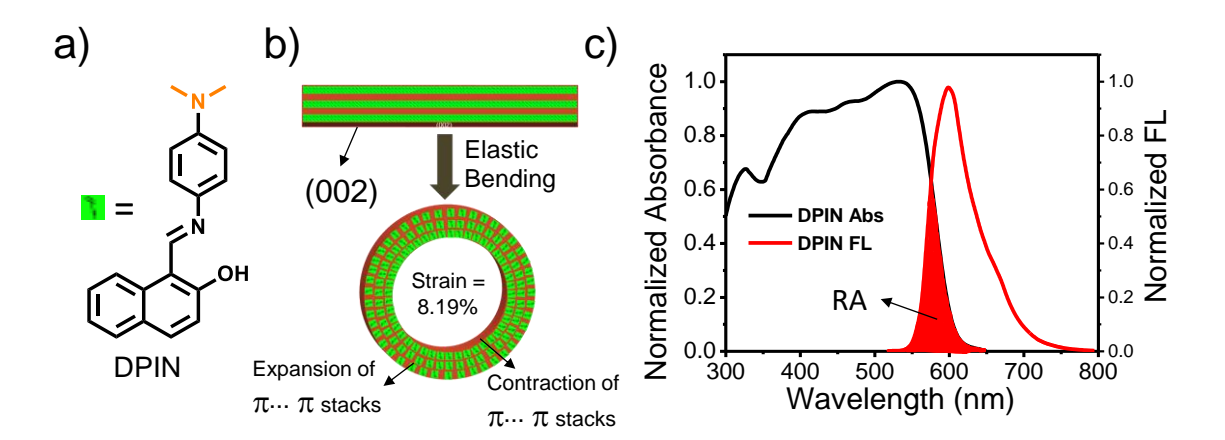


Fig. 3.1. a) Molecular structure of DPIN along with its symbolic square representation. b) Schematic representation of molecular movements from the equilibrium position during the bending of DPIN straight crystal along the (002) plane into a ring shape. c) Solid-state absorbance and FL spectra. RA stands for reabsorbance.

The DPIN molecule in crystal state possesses an intramolecular hydrogen bond between the OH and HC=N groups giving planarity to the molecule. It forms infinite $\pi\cdots\pi$ stacked (3.4 Å) molecular chains along the crystallographic a-axis. [97] The exceptional mechanical flexibility of crystal along the (002) plane arises due to the spring-like expansion and contraction of $\pi\cdots\pi$ stacking distances during molecular movements from their equilibrium positions in the respective outer and inner parts of the ring-shaped



crystal (**Fig. 3.1b**). The solid-state absorption and fluorescence (FL) spectra of the DPIN molecule (**Fig. 3.1c**) revealed a substantial reabsorbance of FL in the range of ≈550-650 nm.

3.3.2. Optical Waveguiding Studies of DPIN Microcrystal

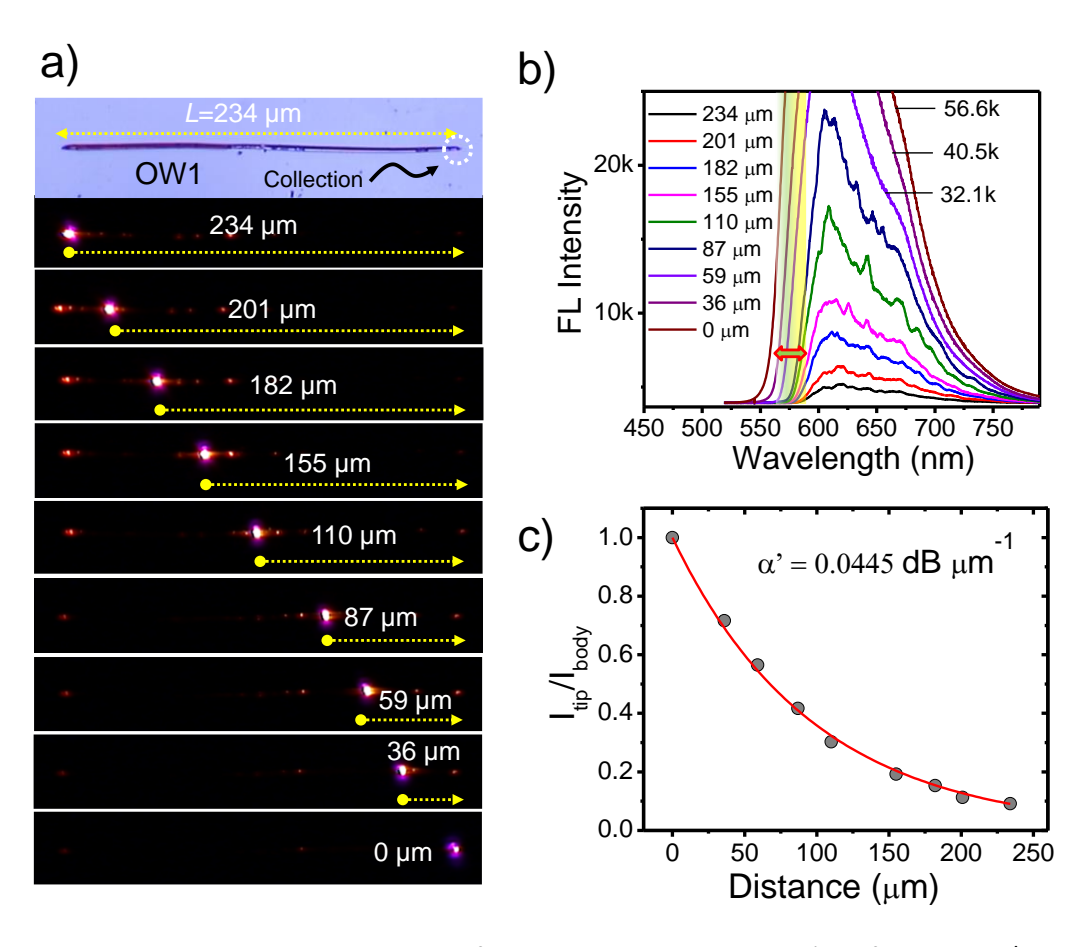


Fig. 3.2. Excitation-position-dependent output from DPIN crystal waveguide. a) Confocal optical /FL images and b) FL spectra. c) Estimation of optical loss coefficient (α ') from the plot of I_{tip}/I_{body} versus light propagation distance.

Optical excitation (continuous wave laser; λ_{ex} = 405 nm) of a terminal of a 234 μ m long crystal (OW1) transduced the red FL to its opposite terminal, confirming its optical waveguiding tendency. The FL images recorded during excitation-position-dependent optical waveguiding studies are presented in **Fig. 3.2a**. By varying the excitation positions along the waveguide's long axis, the output signals were recorded at the right-side terminal of OW1 (**Fig. 3.2a**; white dotted circle). The output FL spectra exhibited light propagation distance (optical path length)-dependent progressive reabsorption effect

from 0 to 87 µm (**Fig. 3.2b**). An optical path length of \approx 87 µm facilitated complete reabsorbance of the lower wavelength (\approx 550-575 nm) region of FL. The FL spectra also revealed optical modes (**Fig. 3.2b**). Due to the nearly rectangular cross-section of the OW1, it is expected that the modes arise due to Fabry-Pérot (FP) resonances. [146,171,172] The OW1 supports these modes due to the mirror-like light-reflecting facets of the crystals. The cross-sectional dimension also varied along the long axis of the crystal. As a result, the mode's intensities and positions also varied. The waveguide's optical loss coefficient (α) of 0.0445 dB µm⁻¹ was calculated by fitting the plot of intensity ratio (I_{tip}/I_{body}) versus propagation distance (D) (**Fig. 3.2c**) using equation 1.7, [60] It can be seen that the reabsorption of light also caused an optical loss on the shorter wavelength side.

As per equation 1.13, in a rectangular waveguide with uniaxial dielectric components ε_{\perp} and ε_{\parallel} the transverse magnetic (TM) modes of the light (lie in the xy-plane) can propagate with m number of possible modes as per the following relation. [86,104]

Where w is the width of the waveguide, λ is the wavelength, and $\varepsilon_{\rm S}$ is the dielectric constant of the substrate (borosilicate coverslip). With an assumption that the waveguide is optically isotropic ($\varepsilon_{\rm iso} = \varepsilon_{\perp} = \varepsilon_{\parallel}$), the cutoff wavelength ($\lambda_{\rm cutoff}$) of a propagation mode (when m < 1) is given by

$$\lambda_{\text{cutoff}} = 2w\sqrt{\varepsilon_{\text{iso}} - \varepsilon_{\text{S}}}$$
 (3.2)

By using the n values [$\varepsilon_{\rm iso}=n_{\rm iso}^2=2.62$ and $\varepsilon_{\rm S}=n_{\rm S}^2=2.34$] and average width OW1 ($w=4.8~\mu{\rm m}$), the $\lambda_{\rm cutoff}$ is calculated to be 499 nm. The implication of the result is also evident from the low α' value shown by the waveguide. In addition to that naturally, the red FL of the waveguide is also falling out of the $\lambda_{\rm cutoff}$ region.

3.3.3. Mechanical Bending of DPIN Crystal into a Ring-Resonator

Creating a ring-resonator from OW1 requires the bending of a single crystal mechanically to 360° angle using an AFM cantilever tip. The optical images of the micromanipulation operations performed on the crystal are presented in **Fig. 3.3**. The



crystal was bent in a step-wise manner by applying force on the crystal's right terminal with the cantilever along the -y, -x, and +y directions (**Fig. 3.3, i-iii**).

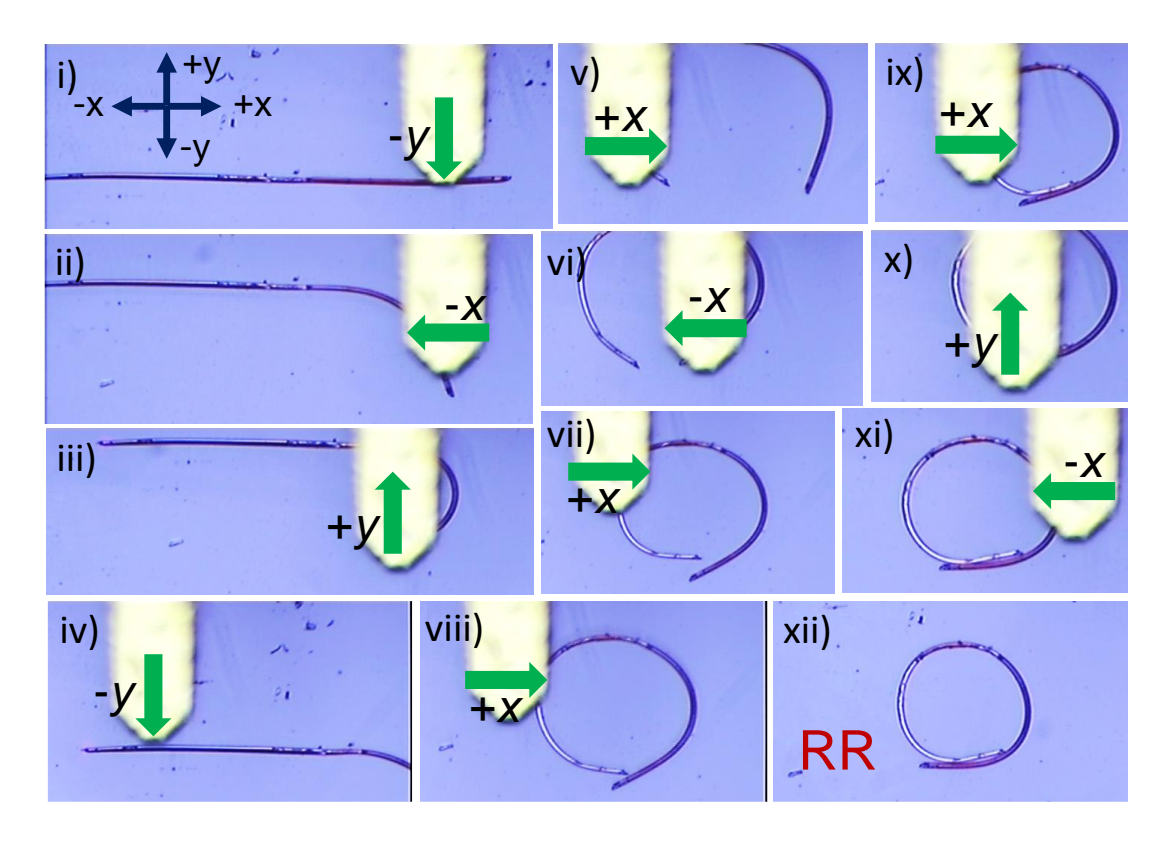


Fig. 3.3. Confocal microscopy images depicting various steps involved in the mechanical micromanipulation of DPIN (OW1) into a ring-resonator (RR) using an AFM cantilever tip.

Similarly, the application of force on the the left terminal of the crystal in the -y and +x directions (Fig. 3.3, iv-v) formed an inverted U-shaped crystal geometry with both termini lying nearly parallel to each other (Fig. 3.3,vi). Subsequent alternative combination movements of the crystal in the +x,-y, and +y directions closed the crystal termini forming a ring-resonator (RR) geometry (Fig. 3.3, vii-xii). The diameter of the RR was measured to be \approx 58.6 μ m and the inset shows the close-up view of the spectral collection point (Fig. 3.4a). The excitation-position-dependent optical waveguiding studies (Fig. 3.4b) revealed optical modes in the FL spectra (Fig. 3.4c). The RR exhibited a slightly higher α ' value of 0.0488 dB μ m⁻¹ due to bending-induced optical loss (Fig. 3.4d). The RR strain was measured to be approximately 8.19% ($T\approx$ 2.4 μ m).

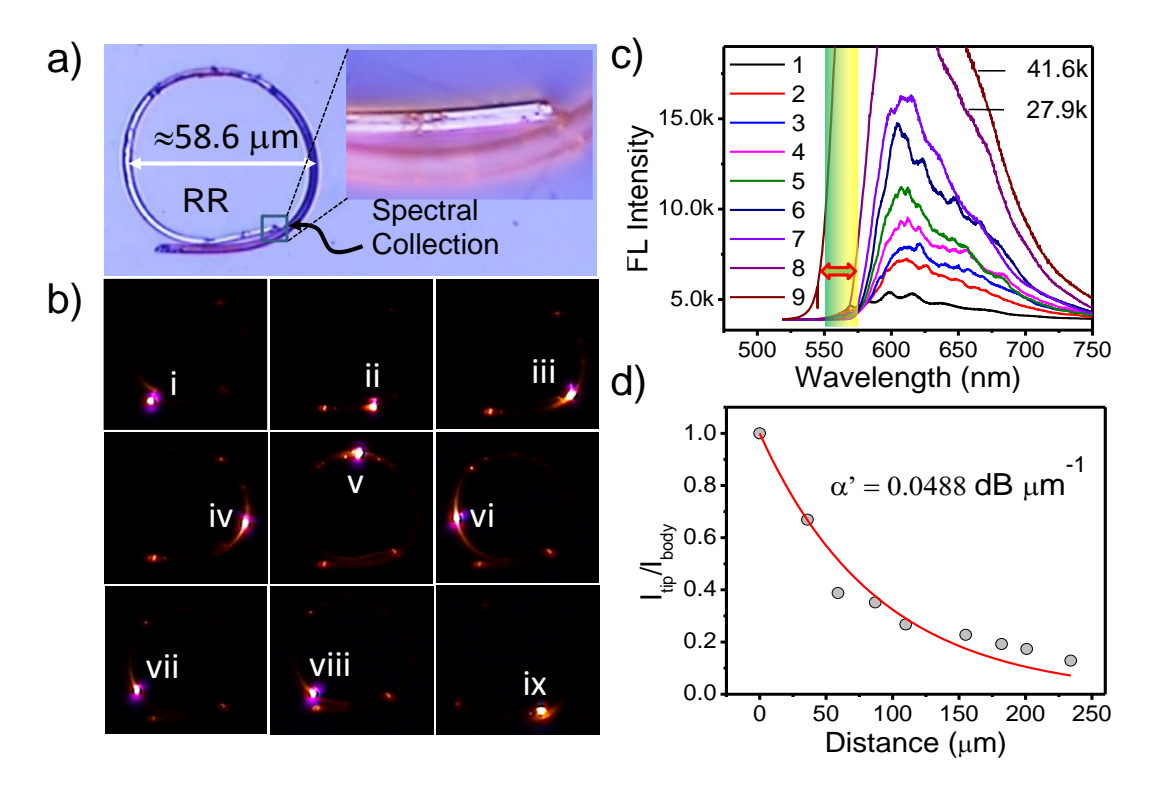


Fig. 3.4. a) Confocal optical image of RR of diameter \approx 58.6 μ m. b) FL images and c) FL spectra depicting excitation-position-dependent output from RR. d) Estimation of α' from the plot of I_{tip}/I_{body} versus light propagation distance.

3.3.4. Fabrication of DPIN Crystal Circuit

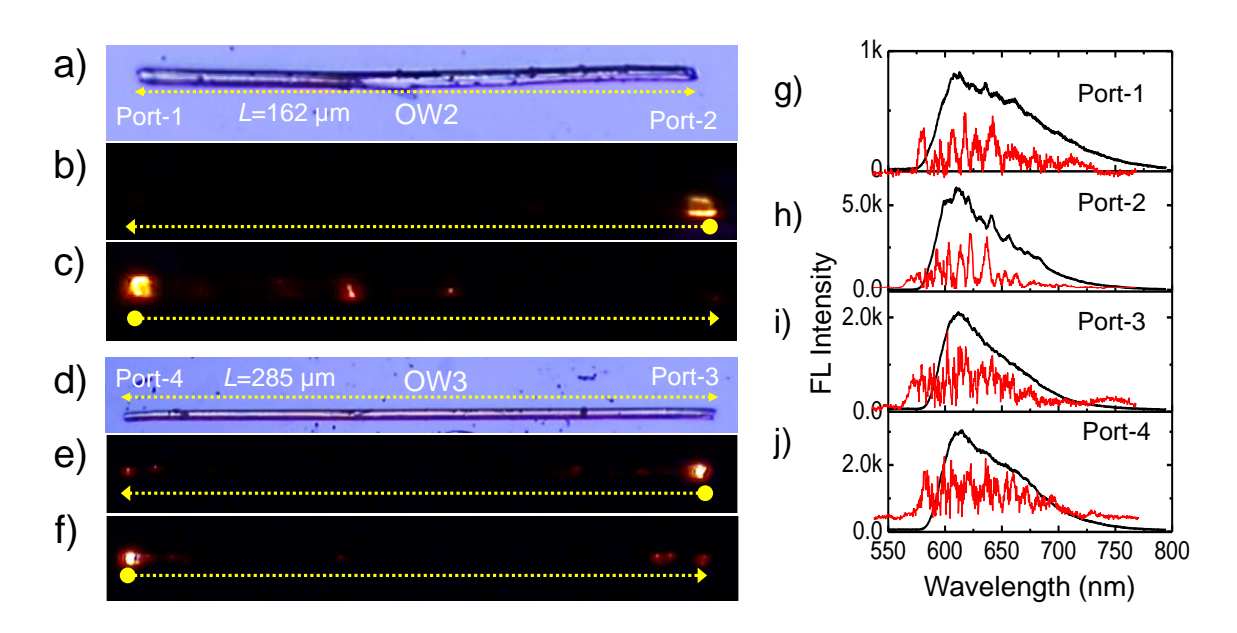


Fig. 3.5. Confocal optical images of a) OW2 and d) OW3 crystal waveguides of DPIN. b,c) FL images of OW2 and e,f) OW3 excited at right and left termini, respectively. g-j) FL spectra recorded at port-1, port-2, port-3, and port-4. The extracted optical modes from the spectra are shown in red lines.

For the creation of a ring-resonator coupled optical waveguide circuit, two more DPIN crystal waveguides having the length of $L \approx 162$ (OW2) and $\approx 285 \, \mu m$ (OW3) were used (Fig. 3.5a, d). The optical waveguiding experiments confirmed the light transducing ability of both crystals. Interestingly, excitation at any of the two termini of the crystals revealed optical modes in the FL band (Fig. 3.5b-f). The modes' positions and their intensity recorded at each terminal were significantly different for the same waveguide. This variation could result from a slight variation in the cross-sectional geometry of the crystal at the terminal. The quality factor (Q) of the modes was estimated from the extracted spectra (red color) shown in Fig. 3.5g-j is in the range of ≈ 100 . After confirming the waveguiding character of OW2 and OW3, we envisioned integrating the waveguides with RR in a step-wise manner. For that, we lifted OW2 from the substrate using the AFM cantilever tip and dropped it close to RR. To integrate OW2 with RR, the tip force was applied in the +y direction, initially at the right and left side and later to the center of OW2 (Fig. 3.6a-c). These mechanical micromanipulation operations facilitated RR coupled waveguide (RR-OW2) formation, as shown in Fig. 3.6d.

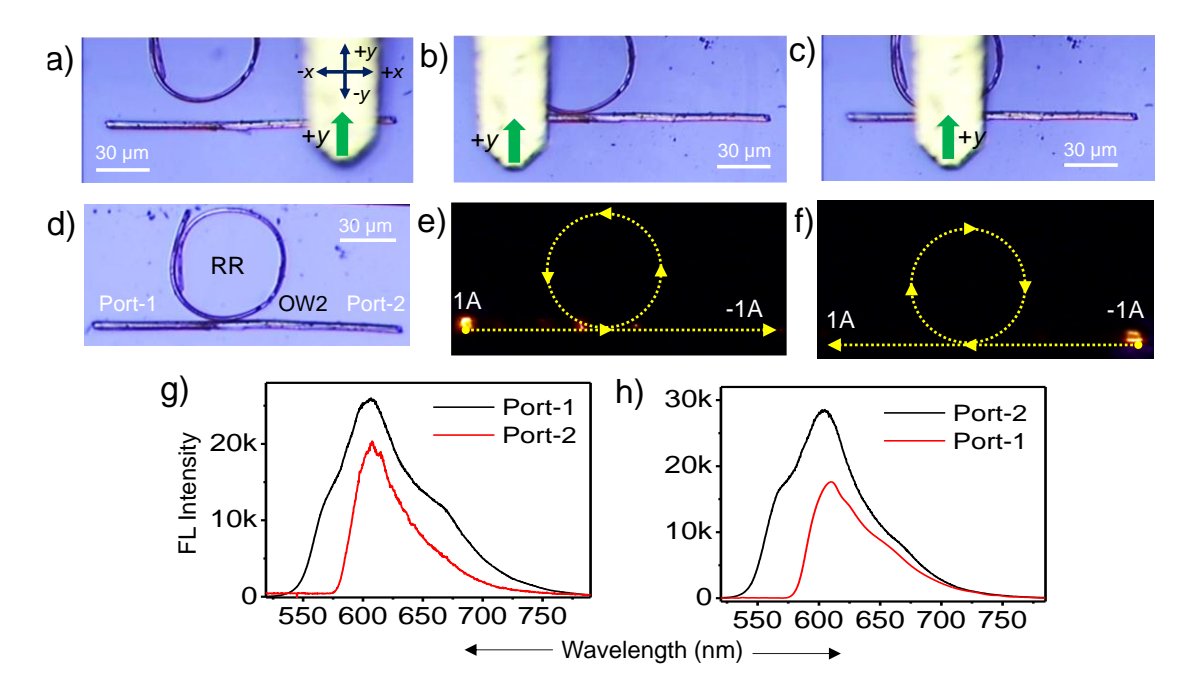


Fig. 3.6. Steps involved in the mechanical micromanipulation of OW2 using an AFM cantilever tip. a-c) Confocal microscopy images depicting application of mechanical force to the right-left, and center of OW2 in the +y direction, respectively. d) The geometry of RR integrated OW2 with two ports. e,f) FL images of OW2-RR excited at port-1 and port-2, respectively. g, h) its corresponding FL spectra, respectively.

To test the optical function of OW2-RR, the port-1 was excited with a 405 nm laser. The generated red FL from the excitation point travelled to port-2 actively (Fig. 3.6e) and corresponding spectra recorded at port-1 and 2 are given in Fig. 3.6f. At the junction, the FL coupled evanescently to RR passively in an anticlockwise direction. Similarly, port-2 was excited and collected the spectra at port-1 and 2. At the junction between the RR and waveguide the light transduced to the RR in the clockwise direction (Fig. 3.6g,h).

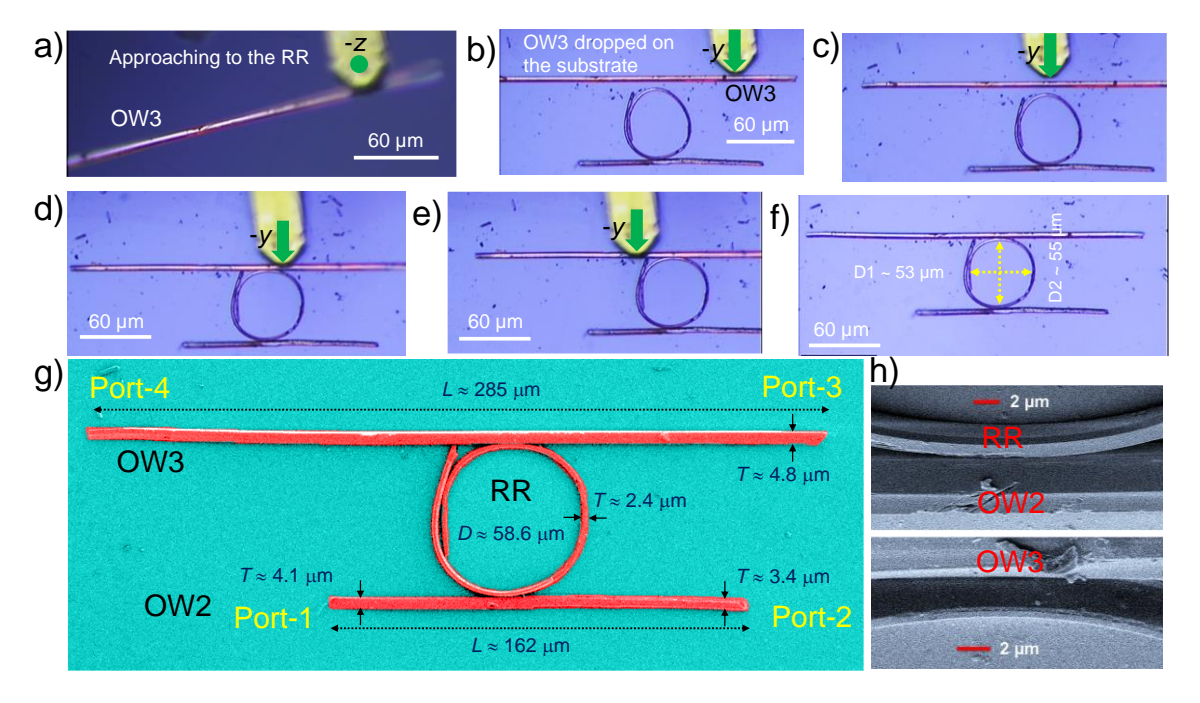


Fig. 3.7. Confocal microscopy images depicting steps involved in the fabrication of OW2-RR-OW3 (OPIC) using an AFM cantilever. a) Lifting of OW3 in the –z direction using cantilever tip. b-e) Dropping of OW3 adjacent to RR-OW2 and applying force in the –y direction. f) The geometry of OPIC, where RR bridges OW2 and OW3. g) False-colour FESEM image of a 4-port OPIC, and h) close view of the junction, where RR was coupled to both the waveguides.

Later, OW3 was lifted from the substrate with the AFM cantilever, transferred, and dropped close to the location of RR-OW2 (**Fig. 3.7a**). By applying force in the –*y* direction (**Fig. 3.7b-e**), the OW3 crystal was integrated so that the long axis of both OW2 and OW3 are parallel to each other. This finally completed the circuit fabrication via manipulation process is shown in **Fig. 3.7f**. The circuit's FESEM image is presented in **Fig. 3.7g**. The image revealed that the thickness (*T*) of the RR, OW2, and OW3 are about 2.4, 3.4–4.1, and 4.8 μm, respectively. Further, FESEM revealed that OWs are in physical contact with RR at the junctions (**Fig. 3.7h**). The cross-section geometry of crystal waveguides and RR confirms that these crystal's optical modes arise due to FP resonance. The fabricated organic

microcircuit consisting of configuration OW2-RR-OW3 has four ports (**Fig. 3.8a**). Here, the geometry of the RR coupled to two straight waveguides is such that under resonance conditions, photons traveling in any one of the waveguides will be diverted to RR to circulate. Further, the light will also be transmitted from RR to the second waveguide and outcouple at the port, which is not diagonally opposite to the input port.

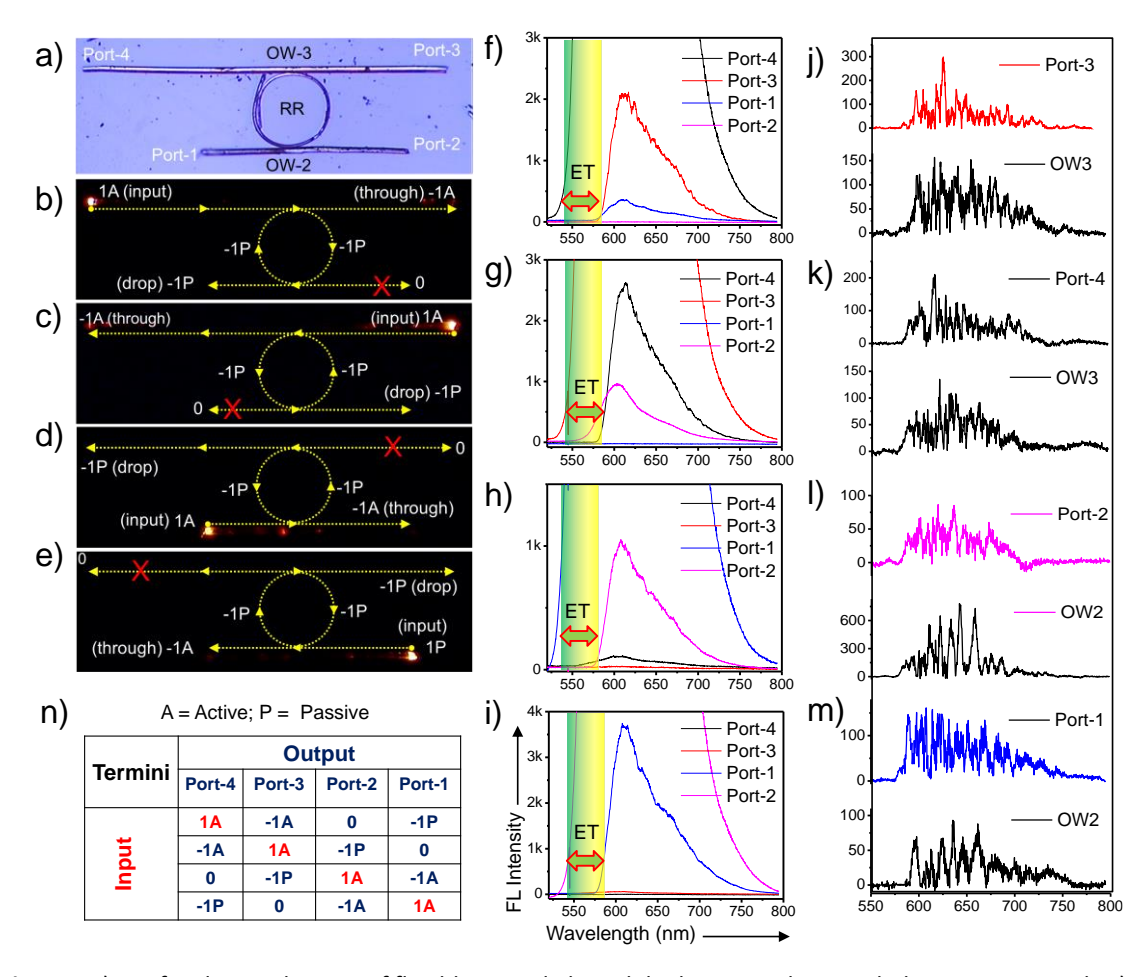


Fig. 3.8. a) Confocal optical image of flexible crystals-based dual waveguides coupled ring-resonator. b-e) FL images, f-m) the corresponding spectra of dual waveguides coupled ring-resonator excited at different ports displaying mechanism-selective and directional-specific optical outputs. n) Table summarizing the different optical outputs from three ports for the input signals via a passive (P) and active (A) mechanism.

In the experiment, for a given optical input at port-4, the produced FL at the excitation point is transmitted (signal: 1A, where A stands for active) via an active mechanism along the waveguide. Due to the self-absorbance of part of FL (≈525-580 nm region), only the bandwidth-altered light (coded as a signal: -1A) with optical modes outcoupled at (through) port-3 (**Fig. 3.8b,f**). The optical modes recorded at port-3 differ from those recorded at the same terminal before integrating with the circuit (**Fig. 3.8j**).



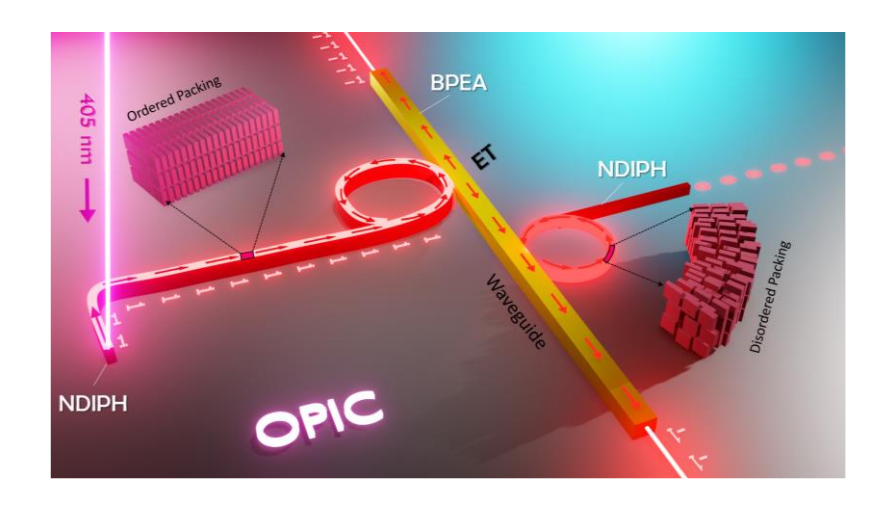
During guided transmission of FL, part of the -1A signal evanescently transferred at the RR-OW3 junction from OW3 to RR and passively (signal: 1P, where P stands for passive) circulated along the ring in a clockwise direction. Successively, the FL from RR transferred to OW2 via evanescent coupling, and the passively guided FL outcoupled at (drop) port-1 (signal: -1P). No light (signal: 0) was recorded at port-2 (Fig. 3.8f), which confirms the directional specific light-guiding tendency of the circuit. When the light input was given at port-3 (Fig. 3.8c), the generated FL (signal: 1A), after the reabsorbance of part it, actively transduced and outcoupled at port-4 as a signal -1A. The optical modes observed in signal -1A significantly differ from port-4 of OW2 before integration with the circuit (Fig. 3.8k). Further, the bandwidth-altered light (signal: -1P) entered RR, passively circulated in an anti-clockwise direction, and thereby selectively outcoupled at port-2 as a -1P signal (Fig. 3.8g). No light (signal: 0) was detected at port-1 (Fig. 3.8k). The excitation of port-1 also produced signals -1A, -1P, and 0 at port-2, port-4, and port-3, respectively. Likewise, for the light input at port-2, signals -1A, -1P, and 0 were recorded at ports-1, 3, and 4, respectively (Fig. 3.8d,h,i). The optical modes shown by the signals at port-2 and -1 of the circuit were significantly altered compared to the isolated waveguide (OW2). The alteration of the optical modes recorded at ports 1-4 of the circuit compared to individual waveguides confirmed the optical interferences within the circuit.

3.4. Conclusion

In this chapter, the fabrication of OPIC using a flexible organic crystal waveguide (DPIN) using the AFM-micromanipulation technique was demonstrated. The proof-of-principle top-down experiments showed that flexible optical waveguiding crystal can be bent precisely into a circular shape (360°) to enable it to act as a ring-resonator. Two straight optical waveguide crystals (bus and drop) can also be mechanically integrated with a ring-resonator to create a four-port photonic circuit geometry. The fabricated circuit demonstrates directional-specific and mechanism-selective optical outputs at three different ports via the active and passive mechanism, for an input signal. A similar microfabrication strategy can be applied to fabricate flexible crystal-based intricate circuits useful for OPICs.



Geometrically Reconfigurable, 2D, All-Organic Photonic Integrated Circuits Made from Two Mechanically and Optically Dissimilar Crystals



This chapter is adapted from:

J. Ravi, A. V. Kumar, D. P. Karothu, M. Annadhasan, P. Naumov, and R. Chandrasekar.* *Adv. Funct. Mater.* **2021**, *31*, 2105415.



4.1. Abstract

With the rising concerns about global cybersecurity, safe data transduction that would be impervious to cyber-attacks necessitates an immediate shift from electron-based to light-based devices. Here, the construction of silicon-free, all-organic PICs by micromanipulation of organic crystals of two mechanically different materials with complementary optical properties, one of which is plastically bendable, is described. The resulting optical circuits are endowed with mechanical reconfiguration at two levels: first, the individual components can be processed into arbitrary shapes before integration into the circuit, and second, the circuit itself is reconfigurable even after it is fabricated. The results do not only demonstrate the infinite structural variations in optical microstructures one can build by using organic crystals, but they also show that deformable light transducive organic crystals carry an untapped potential for lightweight all-organic optical minicircuitry.

4.2. Introduction

Unlike high-index and non-absorbing photonic circuits, a combination of such active-type plastic crystal ring resonators and optical waveguides could enable control over the photoluminescent light propagation direction due to clockwise and anticlockwise light-routing operation by the resonators. However, fabrication and integration of organic crystal-based optical waveguides and ring resonators toward flexible OPICs is challenging and has not been accomplished yet. This requires the transfer of microcrystals from one substrate to another and releasing the crystals at a specific location where they can be integrated with other optical elements of the circuit. The actual protocol for building an OPIC configuration includes a set of basic manipulation procedures such as cutting, moving, bending, lifting, and slicing^[55,57,69,96,145,147,148,173,174] of very small, soft, flexible crystals while ensuring full retention of their integrity.

This chapter demonstrates procedures for transferring crystals from one substrate to another and integrating two chemically different crystals to fabricate OPICs that consist of optically and mechanically different optical elements. One of the advantages of using plastic crystals as optical components is their ability for mechanical reconfiguration. Specifically, a plastically bendable single crystals of N,N'-bis(p-tolyl)-1,4,5,8-

naphthalenediimide (NDIPH) (**Fig. 4.1**) and 9,10-bis(phenylethynyl)anthracene (BPEA) are utilized as optical elements for OPICs. It is envisaged that the electronic energy difference between the two materials would facilitate optical energy transfer (from NDIPH to BPEA) via an evanescent field coupling. This would allow the change in the optical output direction of the waveguides in 2D at will, without physically restructuring the entire circuit. Additionally, this chapter demonstrates that the OPICs constructed from two different optical crystals can deliver input-position-selective and direction-specific optical signals by manipulating the light via active, passive, and energy-transfer mechanisms.

4.3. Results and Discussion

4.3.1. Synthesis of NDIPH

NDIPH was synthesized by condensation of the 1,4,5,8-naphthalenetetracarboxylic dianhydride with two equivalents of *p*-toluidine in DMF above 393 K for 12 hours.¹⁷⁵ After the completion of the reaction, water was added to the mixture and the compound was extracted by ethyl acetate. The compound was purified by recrystallization from ethanol. Yield: 80%.

Scheme 4.1. Synthesis of NDIPH molecule.

4.3.2. Preparation of BPEA and NDIPH Microcrystals

Preparation of BPEA micro-crystals: Elongated orange (form A) single crystals of BPEA were grown from toluene at ambient conditions. Yellow needle crystals of NDIPH were grown from dichloromethane at ambient conditions.



Preparation of NDIPH micro-crystals: Fiber-like crystals of NDIPH were prepared from dichloromethane solution at ambient conditions and were transferred onto a glass substrate and used for micromanipulation.

4.3.3. Single Crystal X-ray Structure Analysis of BPEA and NDIPH

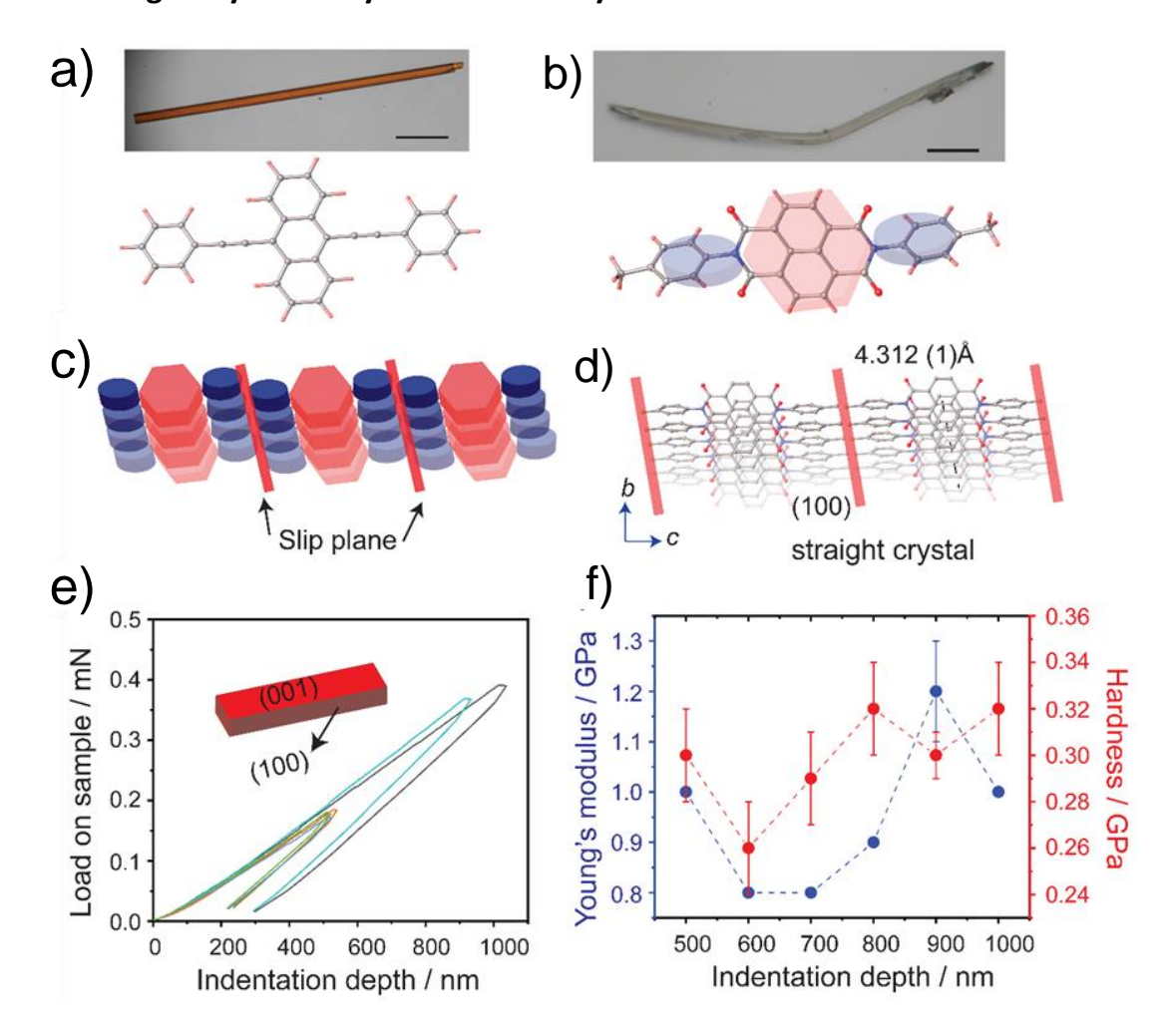


Fig. 4.1. Mechanistic insights into the plastic bending of NDIPH. a,b) Optical microscopic images of crystals of BPEA form-A (a) and NDIPH (b) and their corresponding ball-and-stick models of the single-crystal structures of BPEA and NDIPH at 290 K. c) Schematic representation of the molecular packing found in the crystal of NDIPH showing hydrogen-bonded molecular sheets that are separated by slip planes. d) Molecular packing in the crystal of NDIPH, showing the π - π stacking and slip planes that are thought to be responsible for the plastic bending of NDIPH crystals. e,f) Mechanical properties of a crystal of NDIPH, showing *E* and H_c determined by nanoindentation on the crystal's (001) face. Scale bars: (a) 500 and (b) 300 μm.

The crystallization of NDIPH and BPEA forms yellow and orange needle-shaped crystals, respectively (**Fig. 4.1a,b**). X-ray diffraction analysis confirmed that the crystals of BPEA were of polymorph A, which crystallizes in the monoclinic space group C2/c with one molecule in the asymmetric unit, ^[176] where the molecules are nearly planar (**Fig. 4.1a**).

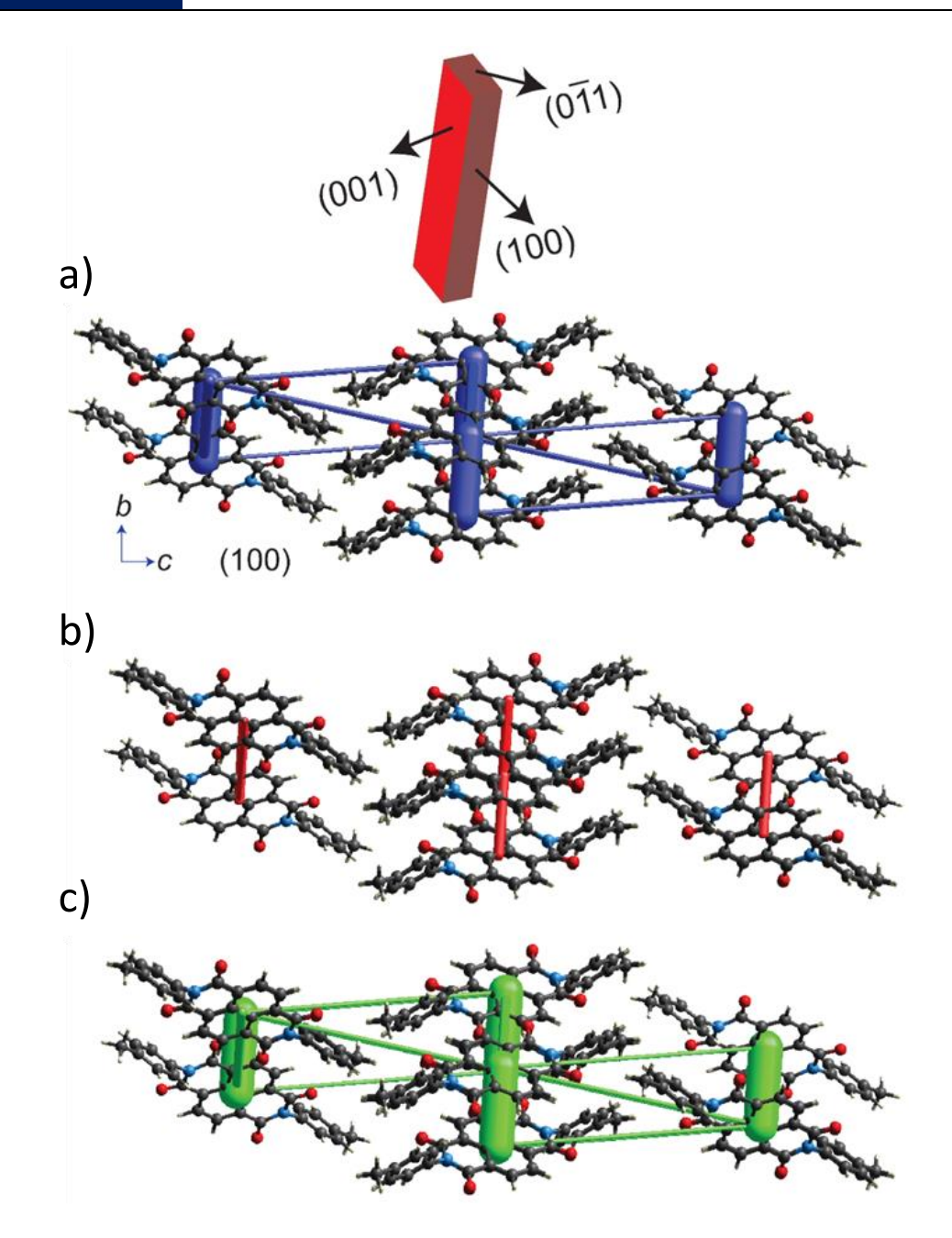


Fig. 4.2. a-c) Energy frameworks of total energy (blue) along with decomposed electrostatic (red) and dispersive (green) components for NDIPH crystal viewed along [100] crystallographic direction. The thickness of each tube is proportional to the strength of the respective interaction.

Analysis of the crystal structure of NDIPH showed that the compound crystallizes in the monoclinic space group P21/c with one molecule in the asymmetric unit (**Fig. 4.1b**). In the latter structure, the molecules are arranged to form smooth slip planes perpendicular to the [001] direction (**Fig. 4.1c**). The aromatic groups (naphthalene diimide) form columns along the [010] direction by using weak π – π interactions at 4.312(1) Å. [128] The mechanical behavior of the NDIPH crystals was initially analyzed by a three-point bending on the (001)

face (**Fig. 4.1b**). It was found that the crystals are plastically bendable while they break when pressed on the other faces. No macroscopically observable deterioration was observed during mechanical bending. Reference to the crystal structure reveals that the bending on the (001) face occurs parallel to the slip planes (**Fig. 4.1d**).

The load-displacement curves were obtained by nanoindentation at varying penetration depths (500–1000 nm) on the (001)/ (001) face (**Fig. 4.1e**). The crystal faces of NDIPH that were accessible for nanoindentation were matched with the Bravis–Friedel–Donnay–Harker morphology of the crystal. The curves are smooth and do not indicate slippage of molecular layers or a phase transition. The E of an NDIPH crystal on its (001) face was found to be $E = 0.95 \pm 0.02$ GPa, and its H_c was = 0.30 \pm 0.02 GPa (**Fig. 4.1f**). A comparison of E with relevant literature data^[177-179] indicates that the NDIPH crystals are pronouncedly soft. The relation of the mechanical properties with the crystal structure was further assessed by analyzing the energy frameworks (**Fig. 4.2a-c**).^[180] The pairwise interaction energies of the structure of the NDIPH crystal are represented as cylinders that correspond to the electrostatic ($E_{\rm elec}$), polarization ($E_{\rm pol}$), dispersion ($E_{\rm disp}$), and repulsion ($E_{\rm rep}$) energies. The radii of each cylinder are directly proportional to the relative strength of the intermolecular interactions.

4.3.4. UV-Visible Spectroscopy Studies

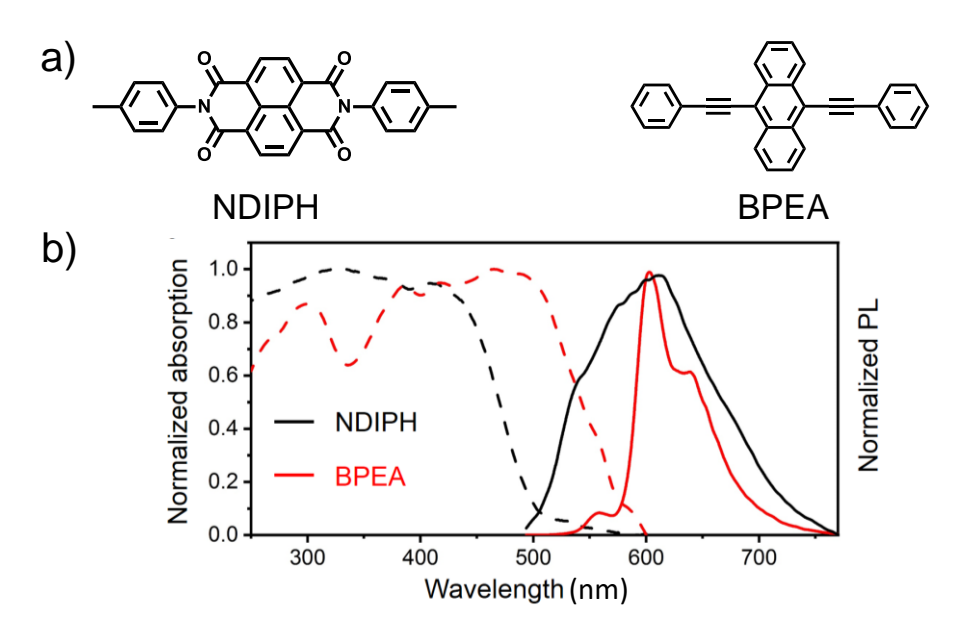


Fig. 4.3. a) Molecular structures of the NDIPH and BPEA molecules. b) Solid-state absorption (dotted line) and emission spectra (thick line) of NDIPH and BPEA.



The molecular structures of the NDIPH and BPEA molecules are presented in **Fig 4.3a**. The electronic absorption spectra (**Fig. 4.3b**) showed that NDIPH absorbs below ≈575 nm, whereas BPEA absorbs below 600 nm. As shown in **Fig. 4.3b**, part of the fluorescence spectrum of NDIPH overlaps with the absorption of BPEA, and it is expected that this overlap will facilitate the energy-transfer of the emission from NDIPH to BPEA.

4.3.5. Micromechanical Manipulation of NDIPH and BPEA Crystals

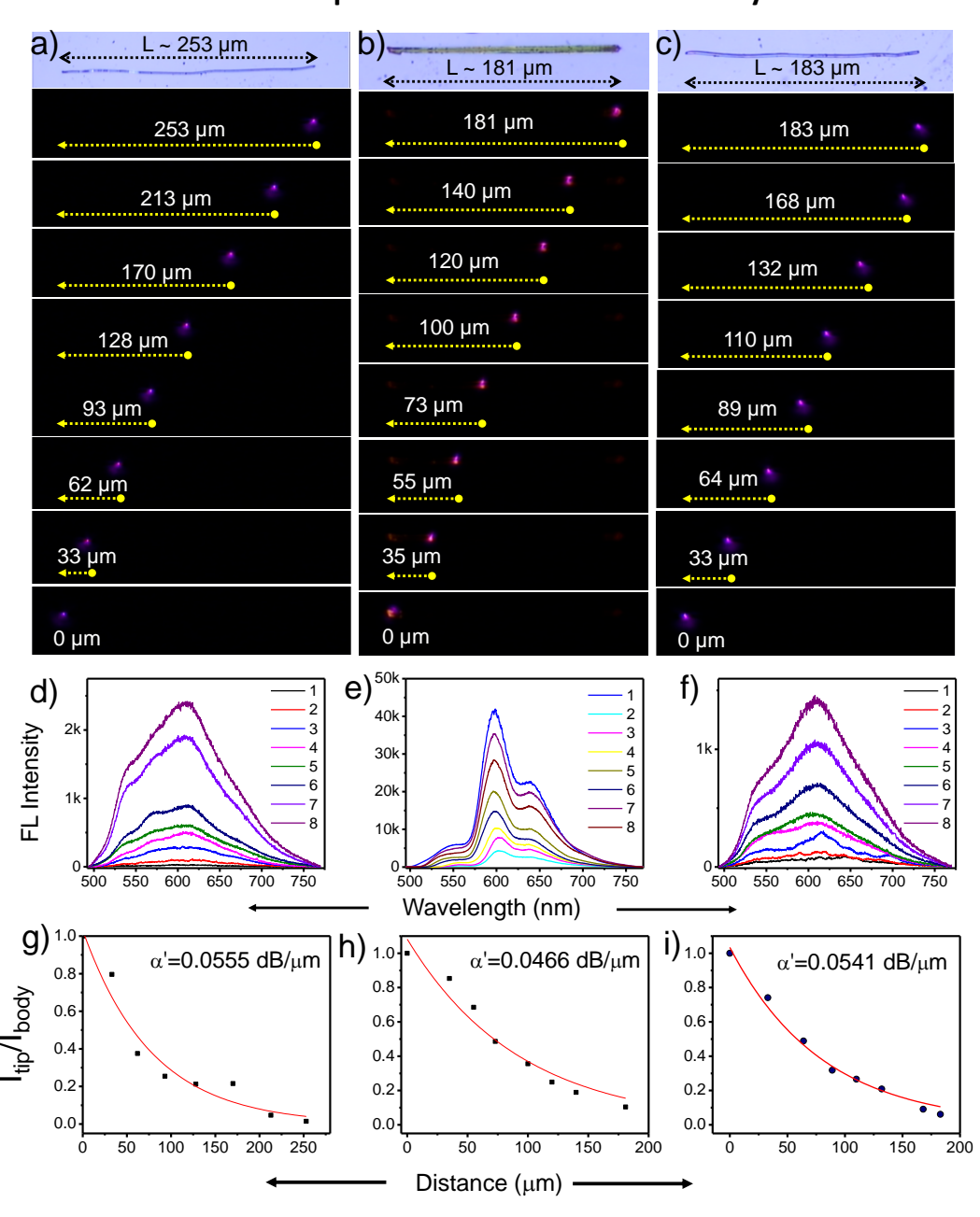


Fig. 4.4. a,c) Confocal microscopy images of NDIPH crystals of L=253 μ m and 183 μ m, respectively, and their corresponding FL images displaying excitation-dependent FL emissions. b) Confocal microscopy image of BPEA crystal and its corresponding FL images displaying excitation position-dependent FL emissions. d-f) Excitation position-dependent FL spectra of crystals shown in (a-c), respectively. g-i) Plots displaying optical loss coefficient calculated using the equation $y = A^*e^{-\alpha D}$ for crystals shown in (a-c).

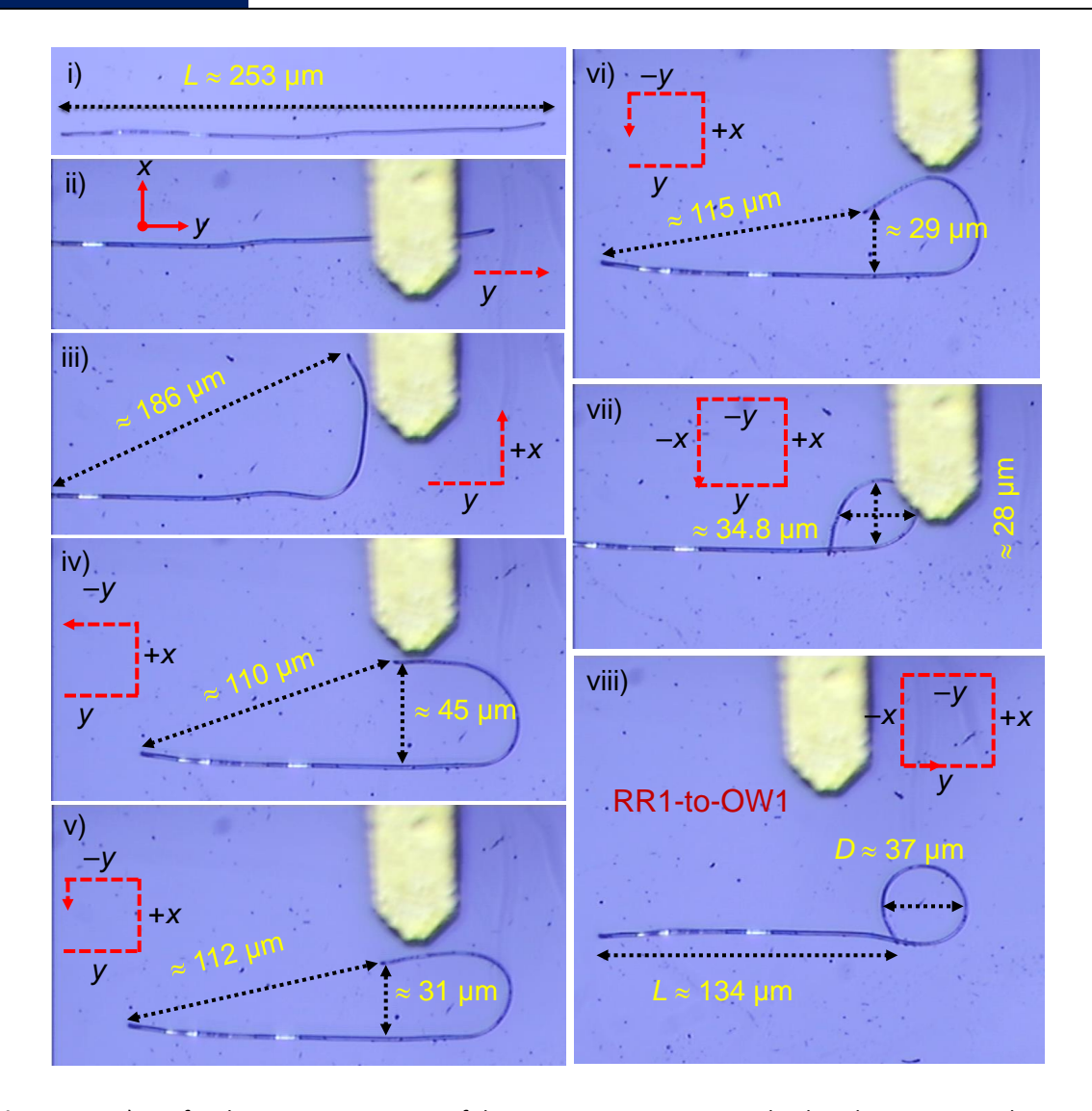


Fig. 4.5. i-viii) Confocal microscopy images of depicting various steps involved in shaping a straight NDIPH crystal of length $\approx 253~\mu m$ into RR1-to-OW1 via mechanical micromanipulation. The direction of motion of the AFM cantilever during micromanipulation is shown in red dotted arrows in Cartesian coordinates.

To test the optical waveguiding nature of NDIPH and BPEA microcrystals, initially, the NDIPH crystal of length ($L\approx253$ and ≈183 µm) were selected (**Fig. 4.4a,c**). The excitation-position-dependent studies were carried out using a 405 nm laser and collected the FL spectra at the left tip of the crystal (**Fig. 4.4d,f**). From the excitation point, the generated FL was transduced to both the tips of the crystal, confirming the waveguiding behavior of the NDIPH micro-rods. The emission spectra intensity increases with a decrease in optical path distance and its corresponding optical loss were measured to be 0.0555 ($L\approx253$ µm) and 0.0541 dB µm⁻¹ ($L\approx183$ µm) (**Fig. 4.4g,i**). Similarly, the BPEA crystal of $L\approx181$ µm (**Fig. 4.4b**) was excited at different positions on the crystal body, and



recorded the spectra (**Fig. 4.4e**), and the optical loss was found to be 0.0466 dB μ m⁻¹ (**Fig. 4.4h**).

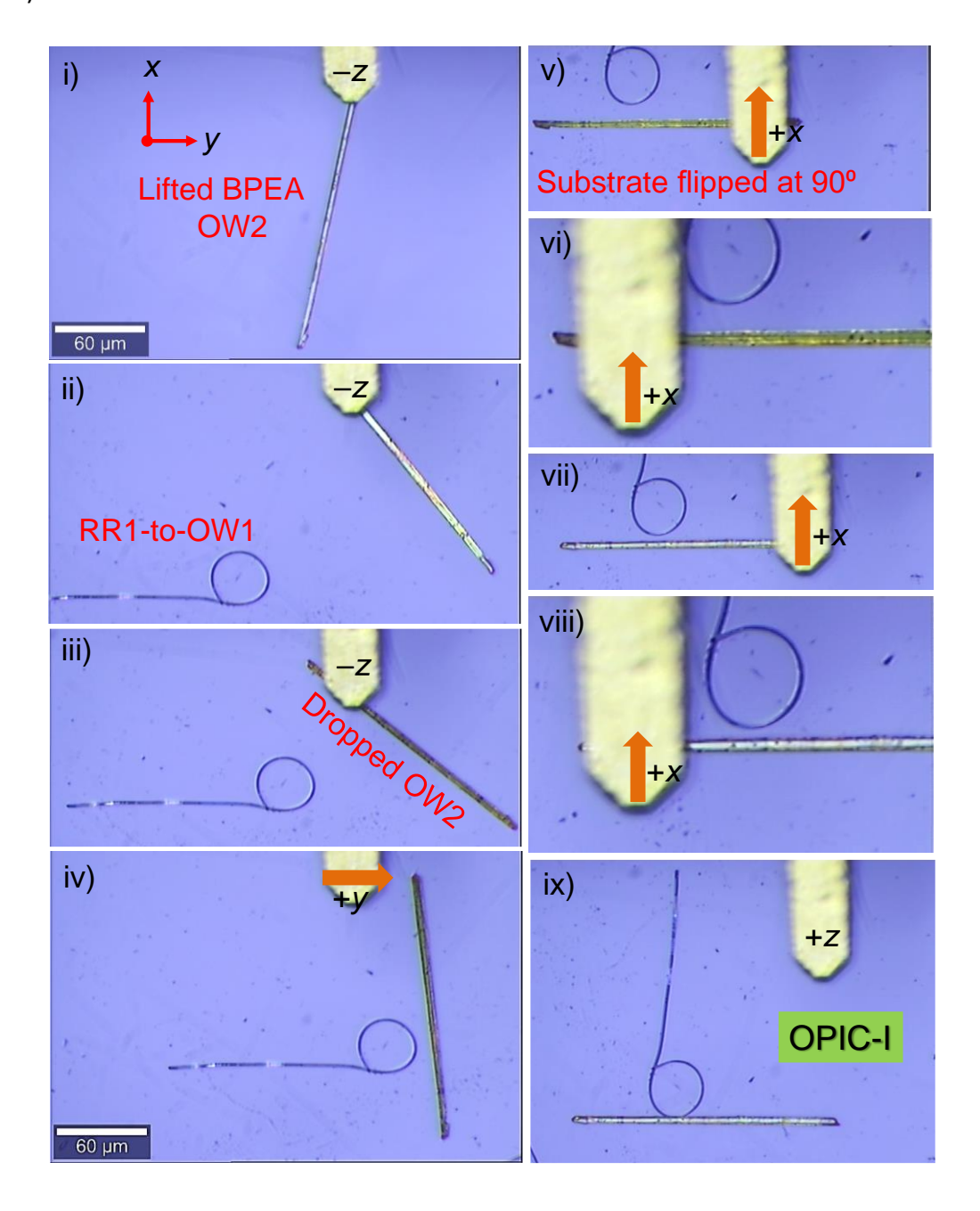


Fig. 4.6. i-ix) Confocal microscopy images depicting lifting of a BPEA crystal from substrate-1 and transferring it to substrate-2 and integrating with RR1-to-OW1 to fabricate OPIC-I via a mechanical micromanipulation approach.

For the construction of RR1-to-OW1, initially, a straight NDIPH crystal of $L \approx 253$ µm was selected (Fig. 4.5i) then AFM cantilever tip was adjusted to the right side of the crystal and gently moved in the +x direction resulting in an L-shaped geometry ($\approx 90^\circ$), the tip-to-tip distance was reduced from ≈ 186 to 110 µm (Fig. 4.5ii-iv). Later the right-side



crystal tip was pushed along the -y and -x directions, and the tip-to-tip and tip-to-body distance were reduced to 115 and 29 μ m, respectively (**Fig. 4.5v,vi**). Finally obtained elliptical loop was pushed in the -y direction forms the nearly circular loop (D \approx 37 μ m) with a long tail length of 134 μ m (**Fig. 4.5vii-viii**).

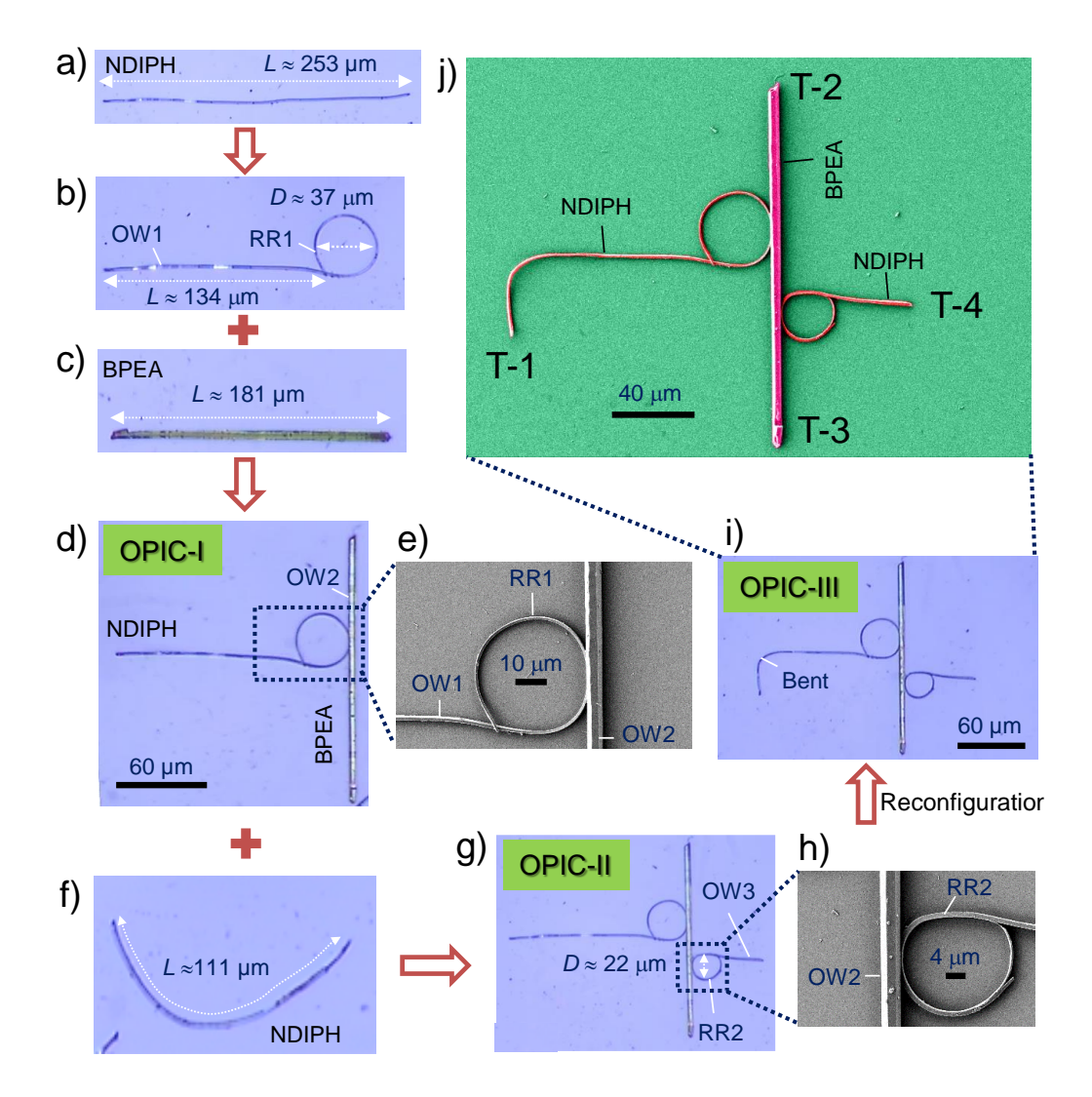


Fig. 4.7. Confocal microscopy images depicting the selected of mechanical micromanipulation operations of NDIPH and BPEA crystals towards the construction of OPICs. a) NDIPH crystal waveguide. b) Shaping the crystal into a combined ring resonator and waveguide (RR1-to-OW1). c) An isolated BPEA crystal OW2. d) Creation of OPIC-I by integrating RR1-to-OW1 with BPEA OW2. The FESEM of a part of the OPIC-I is shown in panel e). f) A bent NDIPH crystal is used for the fabrication of RR2-to-OW3 after cutting. g) Fabrication of OPIC-II by integrating OPIC-I with RR2-to-OW3. h) FESEM image of a part of the OPIC-II. i) Reconfiguration of OPIC-II into OPIC-III. j) False color-coded FESEM image of OPIC-III.

For the integration of a linear BPEA crystal to RR1-to-OW1, primarily the BPEA crystal ($L \approx 181 \, \mu m$) was carefully lifted from the glass substrate-2 by applying force in the -z direction using the AFM cantilever tip (**Fig. 4.6i**). The lifted crystal was slowly transferred

onto substrate-1, near the RR1-to-OW1 (**Fig. 4.6ii-iv**). The cantilever was pushed to the left, right, and left sides of the crystal upon applying force in the +x direction, resulting in an OPIC-I (**Fig. 4.6vi-ix**). Optical loss for bent crystal is higher than the former one due to more light leakages at the curvature of the bent area shown in **Fig. 4.7b**. To fabricate a combination of a ring resonator and optical waveguide (RR1-to-OW1) starting from a single crystal, a straight NDIPH crystal waveguide of length $L \approx 253 \, \mu m$ was selected

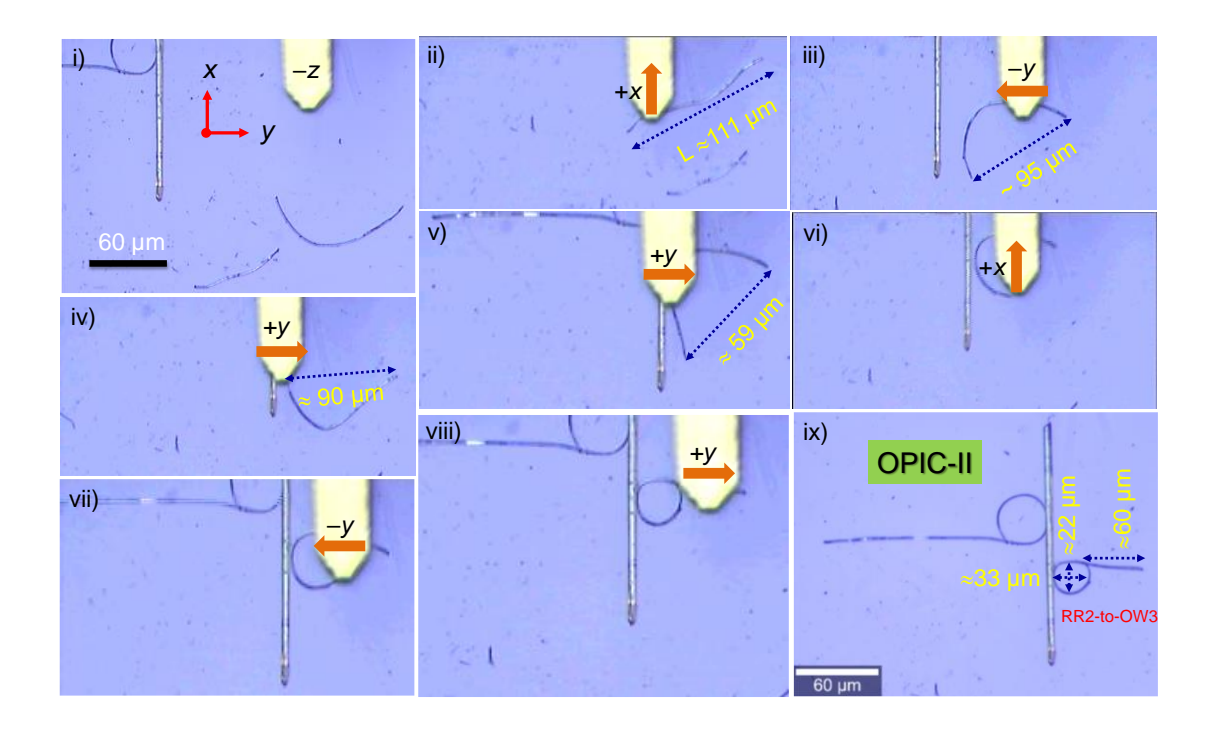


Fig. 4.8. i-ix) Confocal microscopy images of depicitng bending of an NDIPH crystal of length \approx 111 μ m (which was cut from \approx 183 μ m long crystal) into OW3-RR2 and its integration with OPIC-I to create OPIC-II via mechanical micromanipulation technique.

(Fig. 4.7a). The right side of the crystal was bent into a closed circle as a ring resonator (RR1), leaving the left part of the crystal unaltered and available to be used as an optical waveguide (OW1). In the resulting optical element, RR1-to-OW1, the diameter (D) of RR1 and the length of OW1 were \approx 37 μ m and \approx 134 μ m, respectively (Fig. 4.7b).

Construction of an OPIC (OPIC-I) was accomplished by attaching the BPEA waveguide (OW2) shown in **Fig. 4.7c**, orthogonal to RR1-to-OW1 (**Fig. 4.7d**). Notably, in this critical step, OW2 was lifted from substrate-1 using an AFM cantilever, carefully transferred close to RR1-to-OW1 prepared in substrate-2, and precisely manipulated to achieve OPIC-I. The field emission scanning electron microscopic (FESEM) image of a part



of the OPIC-I showed that the horizontal and vertical diameters of RR1 were \approx 37 µm (**Fig. 4.7e**). The shaping of another NDIPH crystal waveguide of $L \approx$ 111 µm (**Fig. 4.7f**), which was cut from the crystal waveguide of $L \approx$ 183 µm, as ring resonator and optical waveguide (RR2-to-OW3; vertical ring $D \approx 22$ µm and $L \approx 60$ µm), and positioning of it orthogonal to the right side of OW2 of OPIC-I resulted in a more complex OPIC, namely, OPIC-II (**Fig. 4.7g,h**). Using various micromechanical manipulation techniques like *cutting*, *moving*, and *bending* of NDIPH crystal ($L \approx$ 111 µm) produces OPIC-II (**Fig. 4.8i-ix**). The reconfigurability of OPIC-II was demonstrated by mechanical bending the OW1's output terminal to an angle of about 90° to prepare another OPIC, OPIC-III (**Fig. 4.7i,j**).

4.3.6. Mechano-photonic Studies of OPICs

The design of the OPIC-I is such that the first terminal (T-1) is oriented in the -ydirection, while the second and the third terminals (T-2 and T-3) are pointing toward the x and -x directions (Fig. 4.9a). OPIC-I is expected to guide fluorescence (with or without energy transfer mechanism or passively) depending on the incident light at the terminal. When T-1 of OW1 orthogonally excited with 405 nm laser light, it generated red fluorescence with two maxima ($\lambda_{\text{max,1}}$ = 608 nm and $\lambda_{\text{max,2}}$ = 550 nm; coded as "signal 1"). This fluorescence propagated along the y-coordinate toward RR1 as signal 1(y), which circulated within the resonator in an anticlockwise direction. The circulating light within RR1 evanescently coupled to BPEA crystal at the junction and electronically excited it via energy transfer. Subsequently, BPEA waveguide produced strong fluorescence ($\lambda_{max,1}$ = 640 nm, $\lambda_{\text{max},2}$ = 598 nm, and $\lambda_{\text{max},3}$ = 550 nm; coded as "signal -1"). Due to the coupling with light from RR1 circulating in an anticlockwise direction, the BPEA waveguide actively transduced its fluorescence along its x-axis to T-2 as output signal -1(x). A weak signal, -1(-x) was observed at T-3 (**Fig. 4.9b,e**). Given the circuit design, the reason for this observation is that after the RR1-OW2 junction, where evanescent coupling followed by the energy transfer of the input light takes place, the light cannot travel to T-3. However, due to the OW's high photoluminescence quantum yield of BPEA (internal quantum efficiency, IQE, is 10.69%; τ_{FL} = 8.74 ns) compared to NDIPH (IQE, is nearly 0%; τ_{FL} = 1.84 ns), the generated fluorescence at the junction in OW2 travels in both directions, giving outputs at T-2 and T-3.

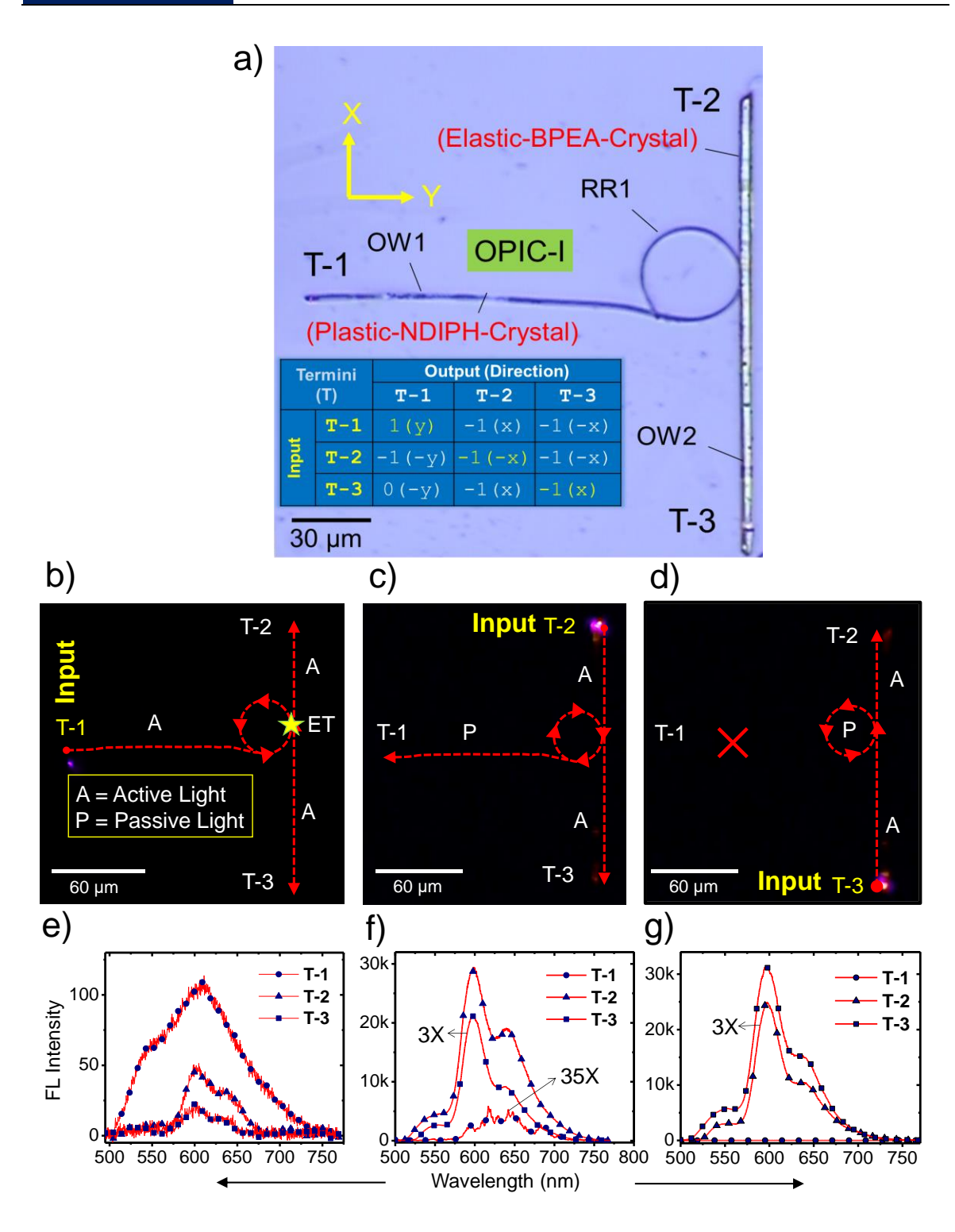


Fig. 4.9. OPIC-I having one input and two possible output terminals. a) Confocal microscopic image of OPIC-I. The inset table displays spectral signal output codes, and the direction of light propagation is given within the brackets for terminals T-1, T-2, and T-3. The inputs are labelled in yellow. b–d) Fluorescence images with light inputs at terminals, T-1, T-2, and T-3, respectively. e–g) Fluorescence spectra at different output terminals for the light inputs given at T-1, T-2, and T-3, respectively. Note: Spectra in plots (e-g) are rescaled by indicated factors.

On the other hand, when the light was introduced at T-2 (**Fig. 4.9c**), the -1(-x) signal travelled actively in a straight path in the -x direction to T-3 and outcoupled as -1(-x) signal (**Fig. 4.9f**). During propagation, the same -1(-x) signal evanescently coupled to RR1, passively at the junction, and circulated in a clockwise direction. As a result, some light was directed to T-3 again, and some emerged at T-1 of OW1 as a -1 (-y) signal. Interestingly, when the light input was introduced at T-3 (**Fig. 4.9d**), the output -1(x) was detected only at T-2, and no output signal, 0(-y) could be observed at T-1 (**Fig. 4.9g**). The absence of any detectable passive light at T-1 is due to the re-entry of light from RR1 back to OW2 caused by the resonator's anticlockwise light path.

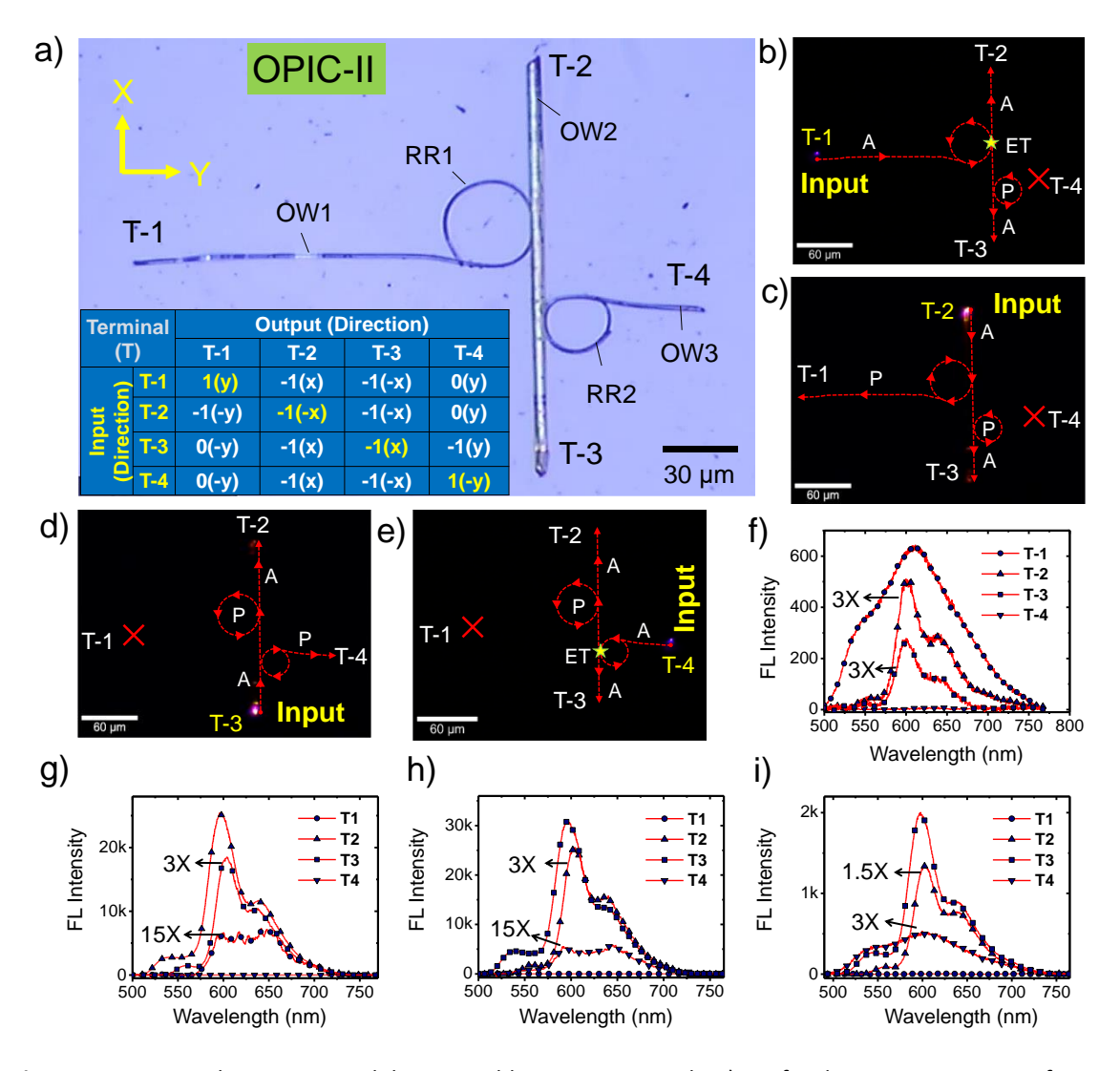


Fig. 4.10. OPIC-II with one input and three possible output terminals. a) Confocal microscopic image of OPIC-II. The table in the inset displays spectral signal output codes, and the direction of light propagation is given within the brackets for terminals T-1, T-2, T-3, and T-4. Fluorescence images at inputs b) T-1, c) T-2, d) T-3, and e) T-4. Fluorescence spectra graphs when input is given at f) T-1, g) T-2, h) T-3, and i) T-4. The spectra in plots (f–i) are rescaled by indicated factors.

This input-terminal-dependent signal output further confirmed the directional specific function of the OPIC-I, delivering signals –1 and 0. These observations are in line with the expected optical path trajectories of RR1 designed in OPIC-1.

The design of OPIC-II allows three possible outputs for any given input light (**Fig. 4.10a**). In this circuit, the RR2-to-OW3 element is connected to OPIC-I. When T-1 of OW1 was excited with 405 nm light (**Fig. 4.10b**), the actively outcoupled light signals -1(x) and -1(-x) were detected from T-2 and T-3 of OW2, respectively (**Fig. 4.10f**), similar to the OPIC-I outputs. However, compared to the difference in light intensities of T-2 and T-3 in OPIC-I, the difference in OPIC-II was higher. Since light travels toward the end of T-3, beyond the junction, part of the light also couples passively with RR-2, decreasing the output intensity of T-3. Consistent with the light circulation path dictated by the circuit

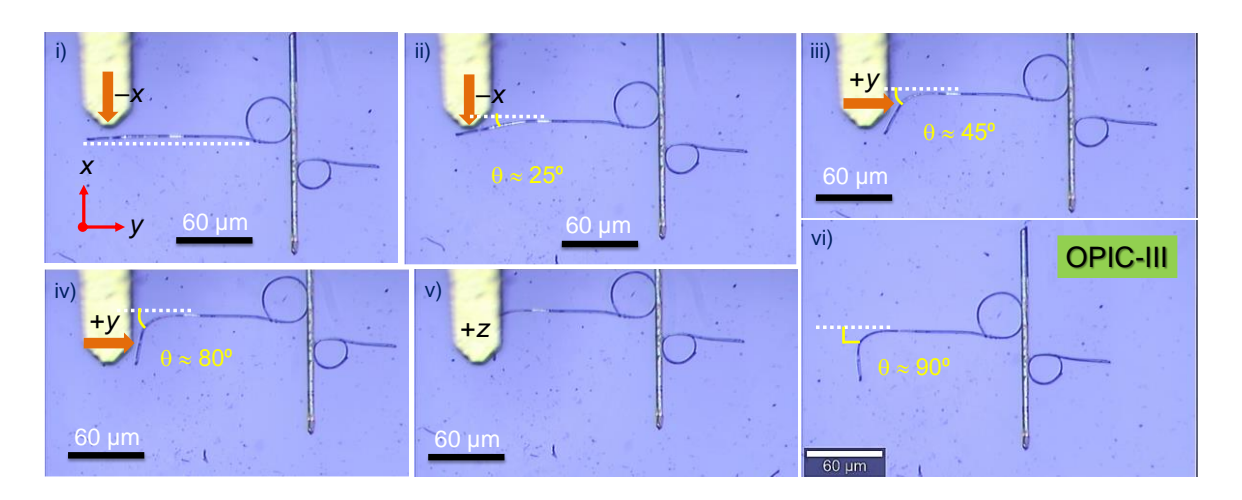


Fig. 4.11. Confocal microscopy images depicting various mechanical micromanipulation steps involved in selective ≈90° bending of terminal OW1 of OPIC-II to create a reconfigured OPIC-III.

design, no light signal was detected at T-4, and the output was O(y). The passage of light beyond the ring region (RR2) is prohibited due to the passively coupled light's anticlockwise path, directing the light toward T-3 and not allowing it toward T-4. Similarly, light input at T-2 (**Fig. 4.10c**) results in passive -1(-y) and active -1(-x) output signals at T-1 and T-3 terminals, respectively, but a O(y) output signal at T-4 (**Fig. 4.10g**). Notably, the delivery of -1(-y) passive signal (with optical modes) at T-1 only occurs for the input given at T-2. When the input signal was given at T-3 (**Fig. 4.10d**), a passive light output from T-4 of the RR2-to-OW3 component is expected due to its clockwise light transmission geometry (**Fig.4.10h**). As expected, a feeble passive -1(y) signal at T-4 was detected with

optical modes in the spectral feature. An obvious -1(x) signal was also recorded at T-2. At T-1, no output signal was detected, 0(-y), which follows our previous discussion. Likewise, excitation at T-4 (**Fig. 4.10e**), gives an output signal of -1(x) at T-2 and -1(-x) signal at T-3 but no signal, 0(-y) at T-1 (**Fig. 4.10i**).

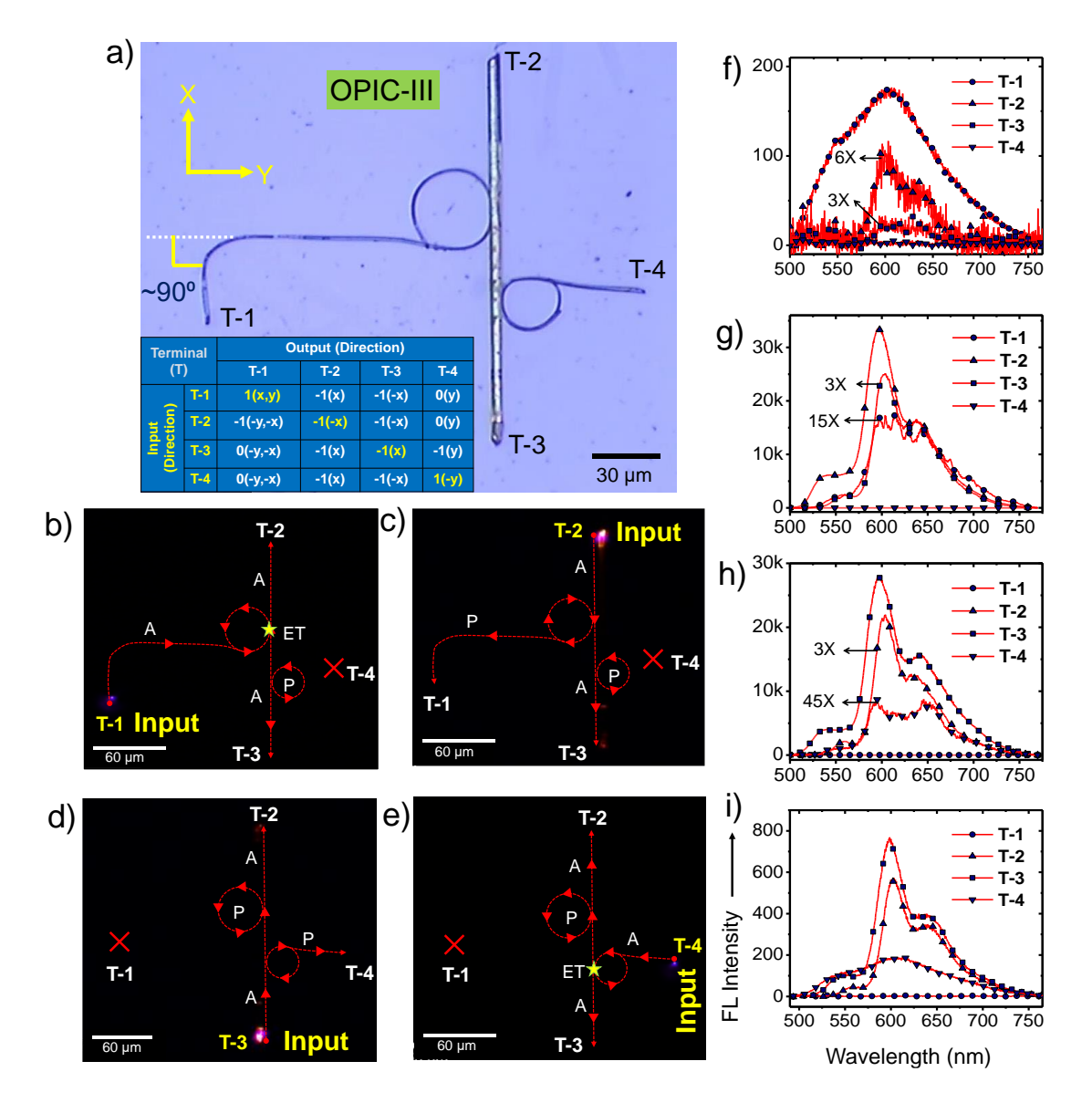


Fig. 4.12. The reconfigured OPIC-III with one input and three possible output terminals. a) Confocal microscopic image of OPIC-III. The table in the inset lists the signal output's nature (active/passive) and direction when input is given at terminals T-1, T-2, T-3, and T-4. Fluorescence images for inputs b) T-1, c) T-2, d) T-3, and e) T-4. Corresponding fluorescence spectra graphs when the light input is introduced at f) T-1, g) T-2, h) T-3, and i) T-4. The spectra in plots (f—i) are rescaled by indicated factors.

Finally, to demonstrate the mechanical compliance and structural reconfigurability of the resulting OPIC-II the orientation of T-1 was changed from -y to -x direction by mechanically bending the terminal to an angle of 90° (**Fig. 4.11i-vi**). This geometrical



reconfiguration of the circuit produced OPIC-III with two light transduction trajectories for T-1, in the (x, y) or (-x, -y) coordinates during input and output, respectively (**Fig.4.12a**). The number of possible light outputs at T-1 for any input at T-2, T-3, and T-4 are -1(-y, -x), 0(-y, -x), and 0(-y, -x), respectively (**Fig. 4.12c-e,g-i**).

The passive signal detection at T-1 shows that light has undergone 90° bends in the (-y, -x) coordinates, demonstrating matching performance with the silicon-based photonic circuits. In the reconfigured OPIC-III, when the input was given at T-1, the difference in out-coupled light intensities at T-2 and T-3 was smaller compared to the difference in OPIC-I and OPIC-II (**Fig. 4.12f**). These results further confirmed the simultaneous transduction of light in both directions due to the excitation of high photoluminescent (BPEA) OW2. The slight decrease in the intensity of outcoupled light at T-2 before ($I_{\text{output}}/I_{\text{input}} = 29\%$) and after ($I_{\text{output}}/I_{\text{input}} = 19\%$) reconfiguration can be ascribed to the expected leakage of light at the curvatures of the bent crystals. The advantage of OPIC-III is the light output direction through T-1, which has been completely switched from -y to -x direction compared to OPIC-II. Although this circuit reconfigurability is necessary, it has not been accomplished with silicon-based PICs.

4.4. Conclusion

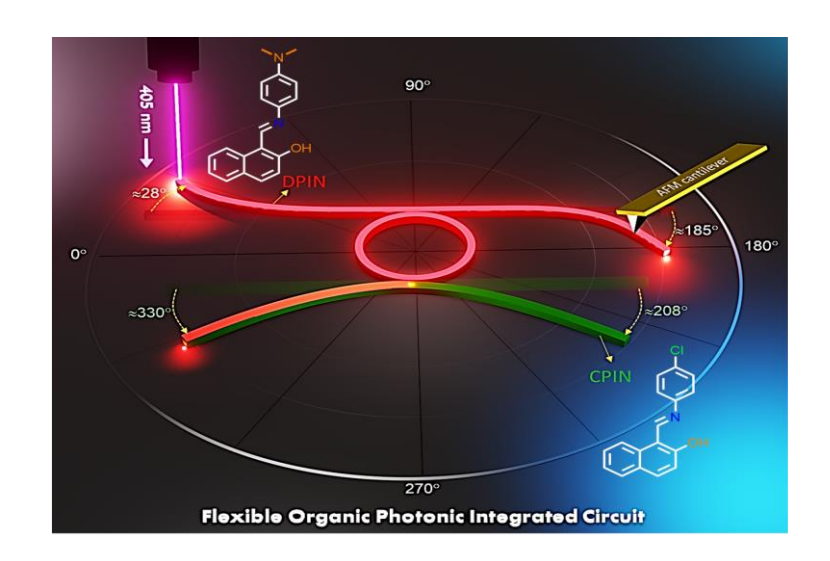
The results described above showcase an example of the construction of non-silicon-based OPIC by micromanipulation of two mechanically and optically distinct organic crystals via the mechanophotonics approach. [55,57,69,96,145,147,148,173,174] This chapter presented a successful integration of two different crystalline materials, one of which is plastically bendable, by transferring one of the crystals between substrates. The superior plasticity of the NDIPH crystals was necessary and even essential to be able to fabricate two unique RR-to-OW geometries of different sizes. These deformed optical waveguides were further integrated with a straight BPEA waveguide by routing the light clockwise or anticlockwise, depending on the input terminal. Finally, the geometrical reconfiguration of the resulting circuit was demonstrated by bending one of its optical waveguides at a right angle. As the optical crystal elements used here are chemically different and optically complementary, we could operate the resulting circuits via energy transfer between the



individual components. The resulting OPICs deliver input-position-selective and direction-specific optical signals by manipulating the light via active, passive, and energy-transfer mechanisms. A unique feature of the resulting circuits is that they can operate in both active and passive modes. The design strategy is such that the same waveguide can transduce passive or active signals depending upon the light input terminal, an important property required for a PIC. The direction-modulation of the optical output demonstrated the application of the OPIC reconfiguration. The ensuing circuit design is robust and readily transferrable to other mechanically compliant crystals. The results presented here provide new insights into the field of PICs and may open up new routes for the realization of ultrafast, energy-efficient OPICs for quantum computation, data transfer, sensing, and other applications. However, challenges such as optical loss due to surface damage and accumulation of defects during bending, optical attenuation, low quantum yield, photodegradation at high laser power, and unavailability of methods for mass production of microcrystals with defined specific aspect ratio will need to be addressed in the future developments of this burgeoning research field.



Realization of Mechanically Maneuverable
Circuit Ports in Organic Hybrid Photonic
Chip for 360° Steering of BandwidthEngineered Signals



This chapter is adapted from:

J. Ravi, A. V. Kumar, M. Annadhasan, and R. Chandrasekar.* Adv. Opt. Mater. 2022, 10, 2102545.



5.1. Abstract

The conventional silicon-based photonic circuits possess several inherent shortcomings. One of them is the mechanical rigidity of circuits. Realizing a flexible OPIC (FOPIC) or organic photonic chip with functional complexity requires innovative materials and a hybrid materials platform. Mechanically flexible organic acicular crystals with fewer imperfections, high n, and high quantum yield are promising materials for FOPIC fabrication. Here, the fabrication of a hybrid FOPIC using (E)-1-(4-(N,Ndimethyl)phenyl)iminomethyl-2-hydroxyl-naphthalene (DPIN) and (E)-1-(4-(chloro)phenyl) iminomethyl-2-hydroxyl-naphthalene (CPIN) crystals for precise steering of output light at different angles is presented. The crystals of DPIN and CPIN are mechanically compliant and optically dissimilar. Mechanical micromanipulation of DPIN and CPIN flexible crystals provides a four-port FOPIC that comprises a waveguide integrated ring resonator. Mechanical maneuverability of the circuit ports enables selective routing of six bandwidthengineered signals at desirable angles (0-360°) in 2D. The circuit applies active/passive light-guiding principles, reabsorbance, and energy-transfer mechanisms for its operation. The presented proof-of-principle reconfigurable photonic circuit concept is advantageous in programmable circuits, navigable detectors, and intelligent sensors.

5.2. Introduction

Silicon-based PICs possess three significant challenges. Firstly, they operate as passive elements and cannot produce active output signals for a given input without optical modulators. [5,181] Secondly, because of their non-reconfigurability, most silicon-based PICs are meant to perform only a specific post-fabrication function. Fabrication of a reconfigurable circuit is the first evolutionary step towards intelligent and programmable PICs. [7] In reconfigurable PICs, the circuit geometry could be modified as and when required based on the requirement, avoiding the reconstruction of the entire circuit. Thirdly, technological difficulty in constructing hybrid PICs with two different optical materials using conventional fabrication techniques. Hence, the fabrication of non-silicon-based reconfigurable PICs requires a new photonic materials platform matching the advantages and filling the potential gaps of silicon-based PICs.

Flexible organic crystals waveguides are a promising material platform to achieve port-reconfigurable FOPICs to route optical signals at different angles in two dimensions. For the construction of FOPICs, *mechanophotonics* is a powerful tool. [57,69,96,97,145,146,148] As a result, the mechanophotonic approach offers unprecedented ease of circuit fabrication and post-fabrication circuit reconfigurability.

This chapter presents the realization of a reconfigurable hybrid FOPIC to generate and route six different optical signals at different angles on the chip plane. Here two chemically and optically different flexible microcrystals, namely, (DPIN)^[97] and CPIN are used, for the circuit fabrication. The crystals of DPIN and CPIN emit red and green fluorescence, respectively. Their solid-state structures closely resemble each other in molecular packing and intermolecular interactions without affecting their mechanical flexibility. Applying mechanophotonics techniques such as *moving*, *bending*, *lifting*, *dropping*, *transferring*, and *integrating* to CPIN and DPIN crystals provides a four-port hybrid FOPIC encompassing waveguides integrated ring resonator. The FOPIC generates six different optical signals and allows reconfiguring signal routing direction at various angles (0° to 360°) on a chip surface, illustrating its use in programmable nanophotonic applications.

5.3. Results and Discussion

5.3.1. Synthesis of CPIN

2-Hydroxy-1-naphthaldehyde (10 mmol, 1eq) and 4-chloroaniline (10 mmol, 1eq) were taken in ethanol in a 250 mL two-necked round-bottom flask. Then the mixture was dissolved and heated by stirring at 85 °C for 4 hours. [169] The formed precipitate was cooled to room temperature and purified by recrystallization in chloroform solvent to obtain yellow needles of CPIN.

Scheme 5.1. Synthesis of CPIN molecule.

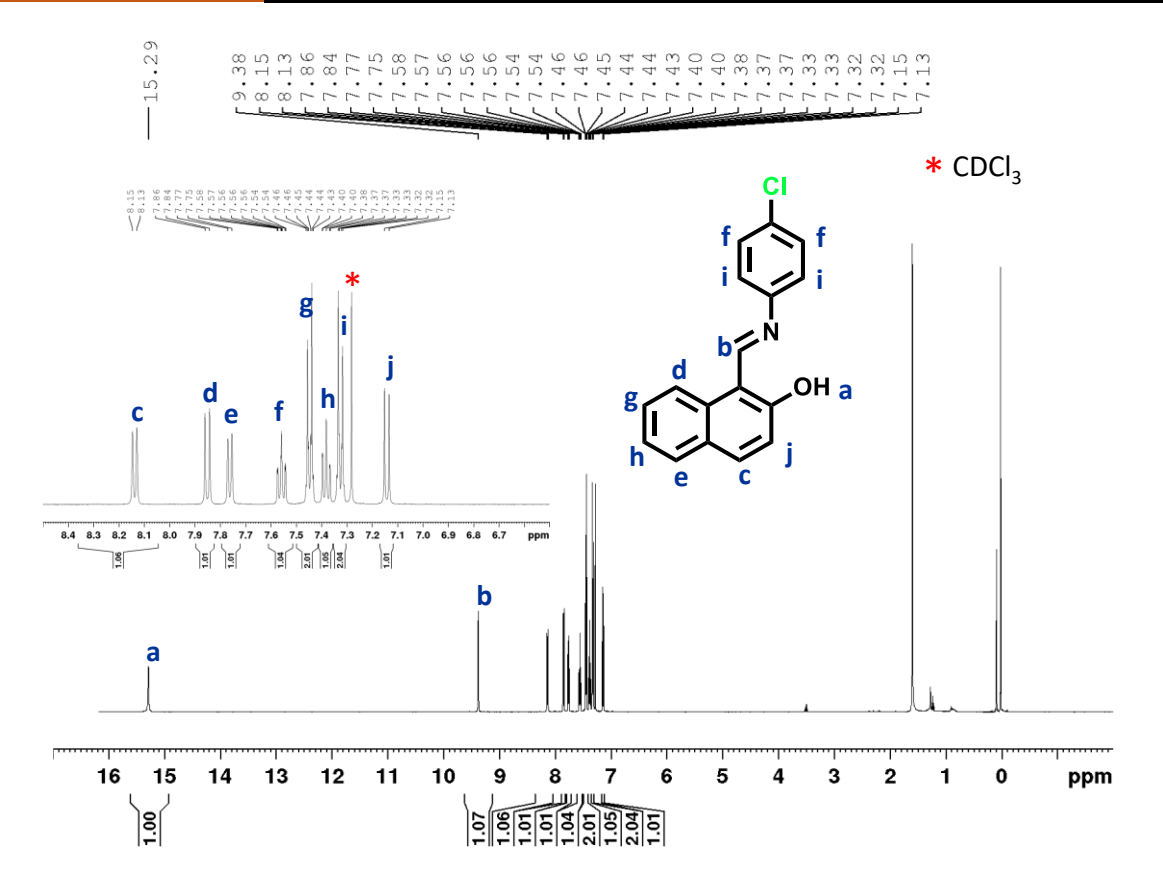


Fig. 5.1. ¹H-NMR spectrum of CPIN in CDCl₃ solvent.

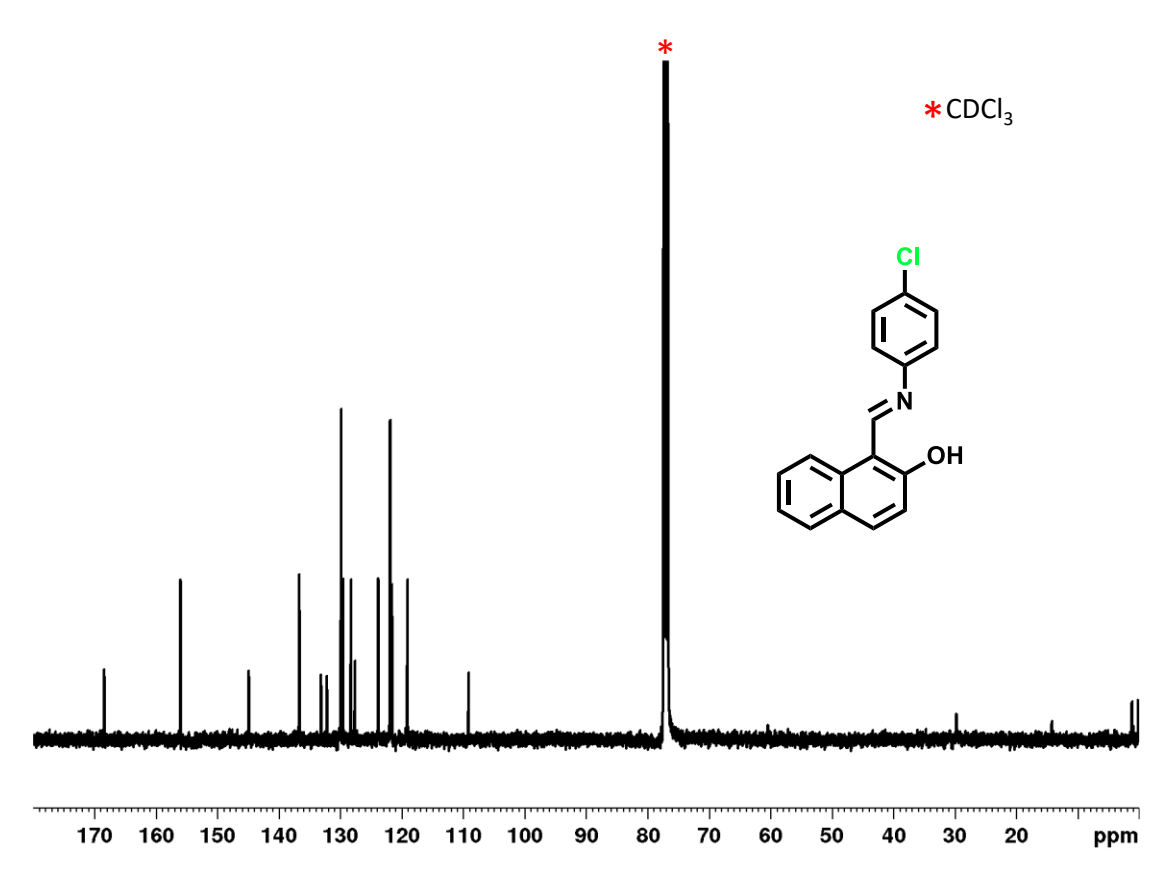


Fig. 5.2. 13 C-NMR spectrum of CPIN in CDCl $_3$ solvent.

CPIN: ¹**H-NMR** (400 MHz, CDCl₃): δ (ppm) 15.28 (s, 1H), 9.37 (s, 1H), 8.13 (d, 1H), 7.85 (d, 1H), 7.76 (d, 1H), 7.55 (t, 1H), 7.44 (d, 2H), 7.38 (t, 1H), 7.32 (d, 2H), 7.14 (d, 1H); ¹³**C-NMR** (100 MHz, CDCl₃): δ (ppm) 168.47, 155.94, 144.83, 136.62, 133.05, 132.13, 129.79, 129.47, 128.20, 127.54, 123.75, 121.83, 121.81, 121.54, 119.00, 109.03. Yield: 86%, m. p.: 188-191 °C, Solid-sate absorption range: 300–560 nm and $\lambda_{max.}$ = 532 nm (green emission).

5.3.2. Preparation of DPIN and CPIN Microcrystals

Preparation of DPIN microcrystals: Synthesis and preparation of DPIN microcrystals is described in Chapter-2.

Preparation of CPIN microcrystals: 2 mg of the CPIN compound was dissolved in 2 mL chloroform under slow evaporation conditions, forming the rod-like microcrystals for microscopic studies.

5.3.3. Structural Basis for Flexibility of CPIN and DPIN Crystals

Weak intermolecular interactions and molecular packing greatly influence the mechanical properties of organic crystals. The detailed structural basis for mechanical flexibility of DPIN was reported earlier. [169] The X-ray structure analysis of CPIN revealed its close resemblance with DPIN in molecular packing and intermolecular interactions. Both CPIN and DPIN crystals exhibit an O-H···N hydrogen bond with a distance of 1.77 Å (Fig. 5.3a). However, the torsional angle (Θ) between naphthyl and phenyl groups of CPIN molecule (Θ≈16.86°) suggested improved molecular planarity of CPIN compared to DPIN molecule (Θ≈23.07°). The CPIN molecular packing in the crystal lattice is stabilized by various other non-covalent interactions such as C-Cl···H (\approx 3.26 Å), π ··· π (\approx 3.5 Å) stacking, intermolecular hydrogen bonding (C-O···H; \approx 2.52 Å) and C-H··· π (\approx 2.93 Å) (Fig. 5.3b,f,g). The molecules form crisscross-packed one-dimensional chains, which are supported by $\pi \cdots \pi$ and C-H··· π interactions. The crisscross chains form layers that propagate along the (001) plane (Fig. 5.3e). The CPIN crystals exhibit flexibility when these layers experience a mechanical force perpendicular to the (001) plane (Fig. 5.3d,e). The weak interactions assist dissipation of applied energy by the expansion and contraction of crisscross chains on the convex and concave sides of the bent crystal, respectively (Fig. 5.3e). Further, the application of mechanical force perpendicular to the (011) plane (Fig. 5.3c) damages the crystal due to non-effective stress distribution.

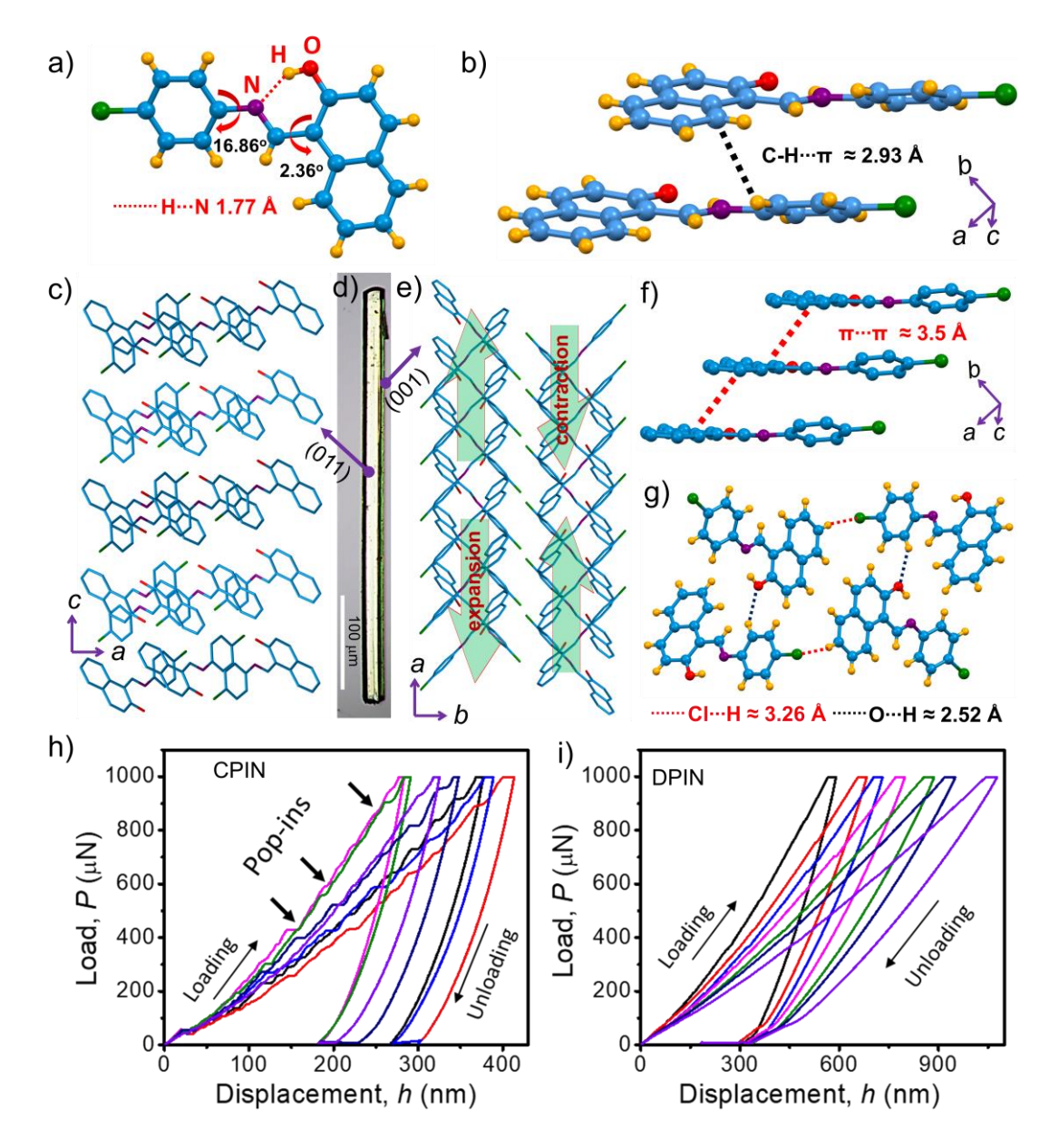


Fig. 5.3. a) Crystal structure of CPIN. b) C-H··· π interactions between CPIN molecules. c) Molecular packing of CPIN on the (011) face. d) Optical image of a CPIN single crystal. e) Molecular packing on the bendable (001) face showing crisscross molecular chains. The inset arrows show the molecule's possible expansion and contraction movement from the equilibrium position. f,g) π ··· π stacking, C-H···O and C-Cl···H intermolecular interactions in the crystal structure. h,i) Load versus displacement plots obtained from nanoindentation on the bending faces of CPIN and DPIN, respectively.

The nanoindentation studies performed on the bending faces of CPIN and DPIN suggested a significant difference in their mechanical properties despite similar molecular packing (**Fig. 5.3e**). The load (p), versus displacement (h), plots obtained from nanoindentation experiments are shown in **Fig. 5.3h**,i. The estimated E and H_c values of DPIN are 1.02±0.4955 GPa and 0.1168±0.0307 GPa, respectively; literature reports such values for super-soft and super-compliant crystals (**Fig. 5.3i**). [177] Similarly, the E and H_c of



CPIN are 8.22 ± 1.62 GPa and 0.3532 ± 0.0959 GPa, respectively, indicating crystals' moderate elasticity (**Fig. 5.3h**). The difference in mechanical properties may be attributed to compact molecular packing in DPIN (cell volume occupied: 1454.09 ų) compared to CPIN (cell volume occupied: 1288.49 ų) (**Table 5.1**). Interestingly, the 'pop-ins' on the p vs h curve illustrate the CPIN crystal's non-homogenous resistive response during the indentation loading process. The molecular layers directly beneath the indenting tip undergo abrupt changes that lead to sporadic local plastic deformations and result in pop-ins. [183]

Table 5.1. Comparative intra/intermolecular interactions and mechanical properties of CPIN and DPIN crystals.

Interactions	CPIN	DPIN
N···H (intra)	≈ 1.77 Å	≈ 1.77 Å
О…Н	≈ 2.52 Å	≈ 2.61 Å
Cl···H	≈ 3.26 Å	-
π…π	≈ 3.50 Å	≈ 3.44 Å
C-H···π	≈ 2.93 Å	≈ 2.88 Å
Ph-Napth (T.A.)	≈ 16.86°	≈ 24.16°
Elastic modulus (<i>E</i>)	8.22±1.62 GPa	1.02±0.4955 GPa
Hardness (H _c)	0.3532±0.095 9 GPa	0.1168±0.0307 GPa

5.3.4. Optical Properties of CPIN and DPIN

The FL images of bulk macro-crystals of CPIN (green) and DPIN (orange) under UV light irradiation were shown in **Fig. 5.4a**. The solid-state optical absorption range of DPIN is broader (300–610 nm) than the CPIN (300–560 nm) (**Fig. 5.4b,c**). The CPIN emits green FL in the 470–700 nm region, while the DPIN's red FL appears in the 540–750 nm region. The overlap of CPIN FL with the absorption of DPIN facilitates energy transfer (ET) from former crystals to the latter (**Fig. 5.4b**). On the contrary, the absorption spectrum of CPIN showed no significant overlap with the emission spectrum of DIPN (**Fig. 5.4c**). The absolute FL quantum yield of DPIN and CPIN crystals were estimated to be 0.567% and 6.31%, respectively.

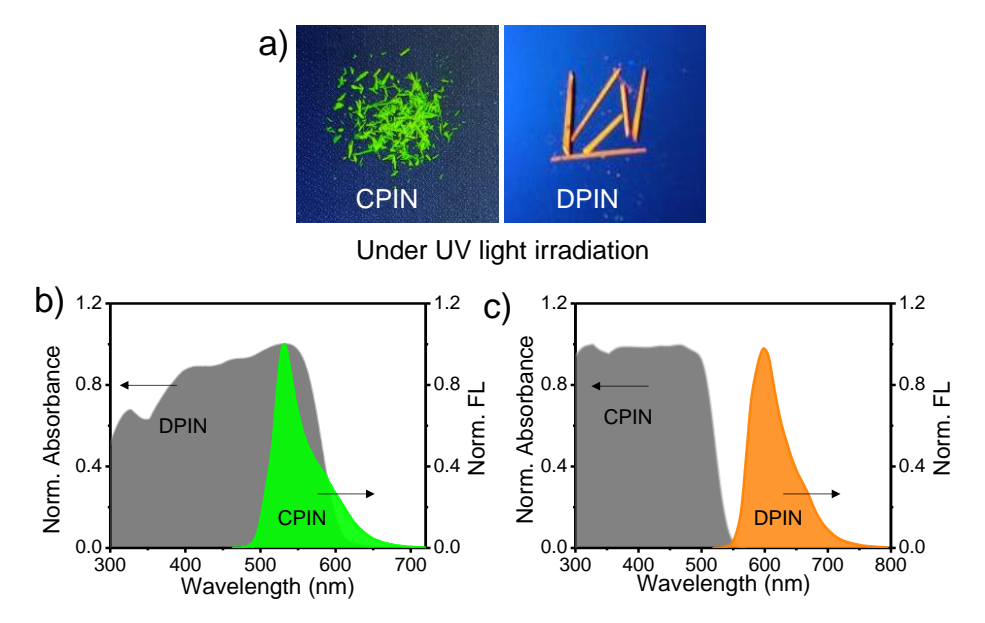


Fig. 5.4. a) CPIN (green) and DPIN (orange) crystals under UV light irradiation. b,c) Solid-state UV-Visible absorption and emission spectra of DPIN and CPIN.

Building a FOPIC requires microcrystals of CPIN and DPIN. Therefore, the CHCl₃ solution of the respective compound was drop casted on a silica substrate to obtain needle-shaped microcrystals under slow solvent evaporation at ambient conditions. The mechanical compliance of microcrystals could be different from macro-crystals. Unlike macro-sized crystals, surface adherence energy contributes significantly to the microcrystal's mechanical response. When the crystal overcomes surface adherence force, i.e., the restoration force of the crystal being larger than the surface adherence force, elastic bending can be observed. Otherwise, the microcrystals display *pseudo-plasticity*. [55,96,147,148,173,182] Therefore, elastic micro-crystals on a silica substrate usually do not revert to their original shape upon removal of applied mechanical force. The *pseudo-plasticity* of microcrystals has been capitalized to fabricate reconfigurable FOPICs on a silica substrate.

5.3.5. Construction of Ring Resonator (RR) and its Photonic Properties

To create a ring resonator (RR) for circuit fabrication from a straight DPIN crystal (OW1), a crystal with a length of \approx 205 μ m was selected (**Fig. 5.5a**). Initially, the waveguiding property of the chosen microcrystal was investigated by optically exciting (continuous wave; 405 nm) the crystal at one of its termini (input port) and collecting output FL($\lambda_{max} \approx$ 606 nm) signal at its opposite terminal (output port). Due to the

reabsorption of FL in the range of 525-580 nm, the output signal bandwidth gradually decreased with the increase of optical path length (**Fig. 5.5a,b**).

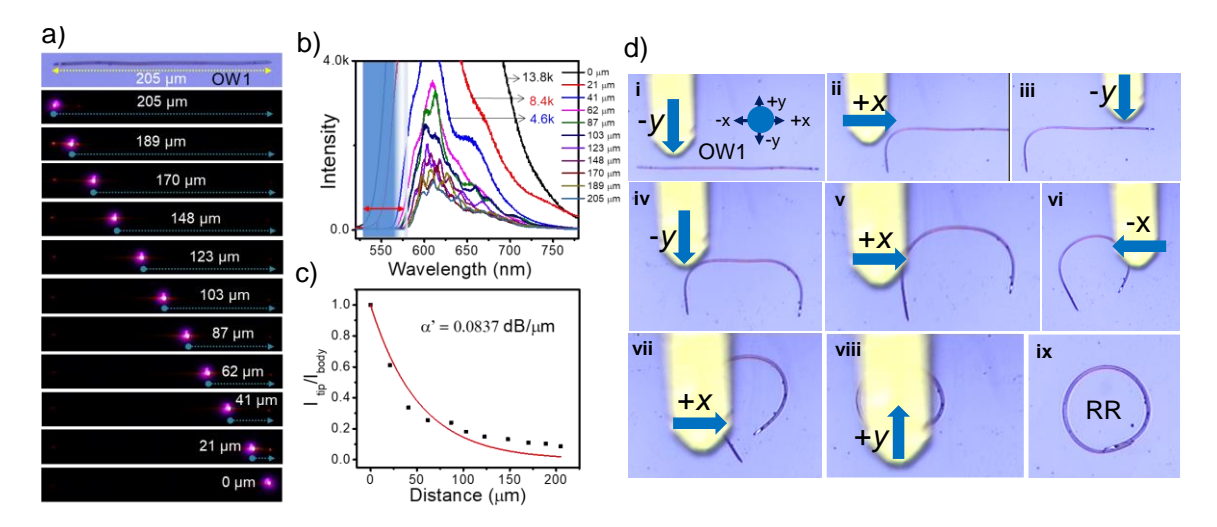


Fig. 5.5. a) Confocal microscope image of a straight DPIN single crystal and its corresponding FL images when the crystal was excited with a 405 nm laser at different positions. b) The corresponding FL spectra. The double-headed arrow (red color) in the inset shows the reabsorption region. c) Estimation of optical loss coefficient by fitting (red line) the data plot of I_{tip}/I_{body} versus propagation distance. d) Confocal microscope images displaying the steps involved in the mechanical micromanipulation of straight DPIN microcrystal into a nearly-circular RR using AFM cantilever tip.

The optical loss coefficient (α '), a parameter describing the light transduction ability of the waveguide, was estimated to be 0.0837 dB μ m⁻¹ (**Fig. 5.5c**).

Later, using micromechanical operations such as *bending* and *moving* of OW1 straight crystal were used to convert 205 μ m long waveguide into RR in a stepwise manner a nearly ring-shaped crystal geometry (RR). Initially, the AFM cantilever was positioned on the left side of the crystal and slowly moved forward direction (–y direction) (**Fig. 5.5di**). As a result, the crystal was bent by an angle of ~ 90° (**Fig. 5.5dii**). Later, additional force was applied along the -y directions at the right and left side of the crystal respectively, producing curved shape geometry with an angle of $\approx 90^\circ$ (**Fig. 5.5diii,iv**). These two sequential operations created inverted U-shaped geometry. Applying force in the +x, and –x directions (**Fig. 5.5dv,vi**), formed a nearly half-circular geometry with two termini very close to each other. Finally, the two terminals are connected by pushing the left tip towards the right body of the crystal in the +x and +y directions, respectively (**Fig. 5.5d vii,viii**), creating a nearly-circular-shaped geometry ring resonator (RR).

The fabricated RR (**Fig. 5.6a,b**) was optically excited along its body and showed light outputs at both termini, confirming its clockwise and anti-clockwise light routing ability (**Fig. 5.6c**). Later, RR was optically excited at various positions along its body (**Fig. 5.6d,ii-viii**), and the FL spectra were recorded at one of the termini. The FL spectra displayed excitation-position optical modes indicating the resonator characteristics of RR (**Fig. 5.6e**). The α' was estimated to be 0.1098 dB μ m⁻¹, and the bending-induced $\alpha' = \alpha'_{bent} - \alpha'_{straight}$ was estimated to be 0.0261 dB μ m⁻¹ (**Fig. 5.6f**).

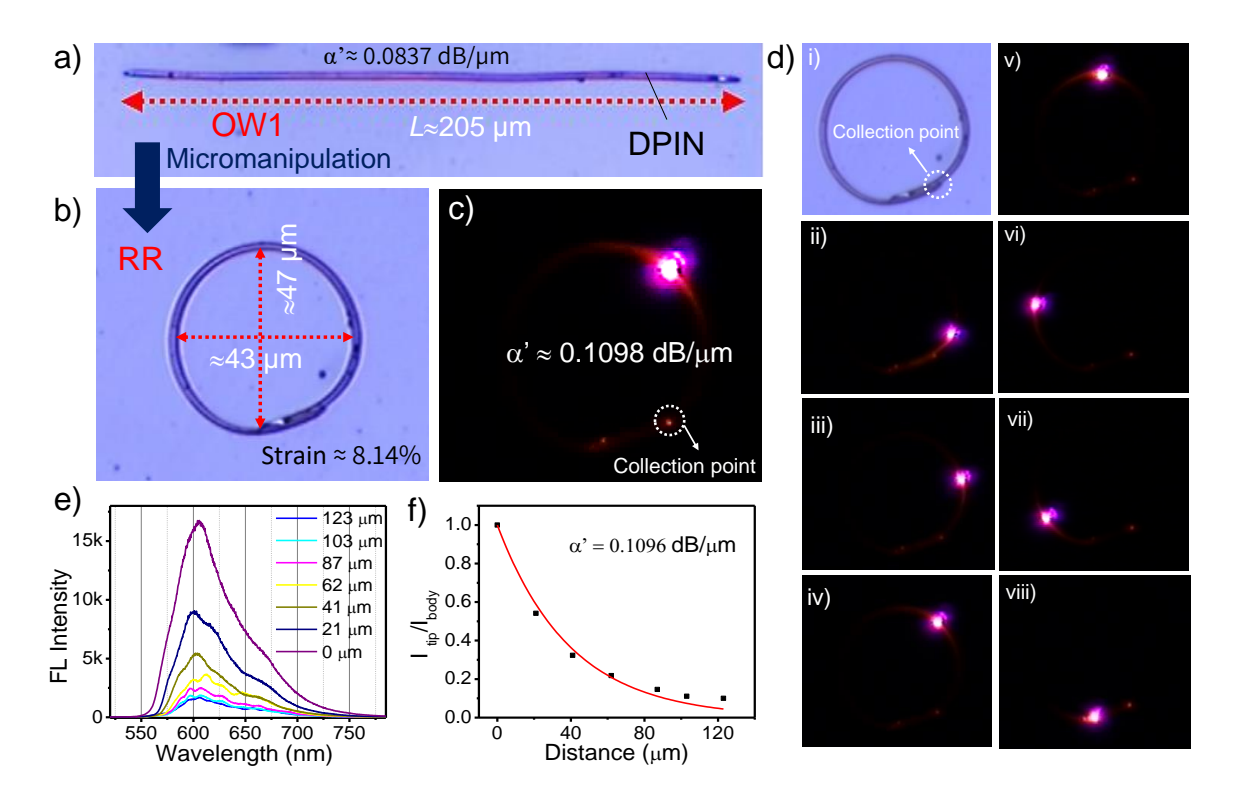


Fig. 5.6. Confocal microscope image of a) a straight DPIN microcrystal, b) after mechanically shaping it into a RR. c,d) FL image of RR excited at various positions on the crystal body with a 405 nm laser. The white dotted circle indicates the spectral collection point. e) Excitation-position-dependent FL spectra of RR. f) Estimated optical loss coefficient (α') plot of RR.

5.3.6. Fabrication of FOPIC-A from RR and OW2 of CPIN

To create an OW2-RR (FOPIC-A) from straight OW2 of CPIN microrod. Initially, the optical properties of CPIN crystal having a length of $L^{\sim}199~\mu m$ was studied (**Fig. 5.7a**). The crystal was excited at different positions along its long axis of the crystal with a 405 nm laser and recorded the spectra at the right terminal of the crystal. The generated green FL from the excitation point travels along the body to both the termini of the crystal, revealing the optical waveguiding nature of the CPIN crystal (**Fig. 5.7a**). The corresponding

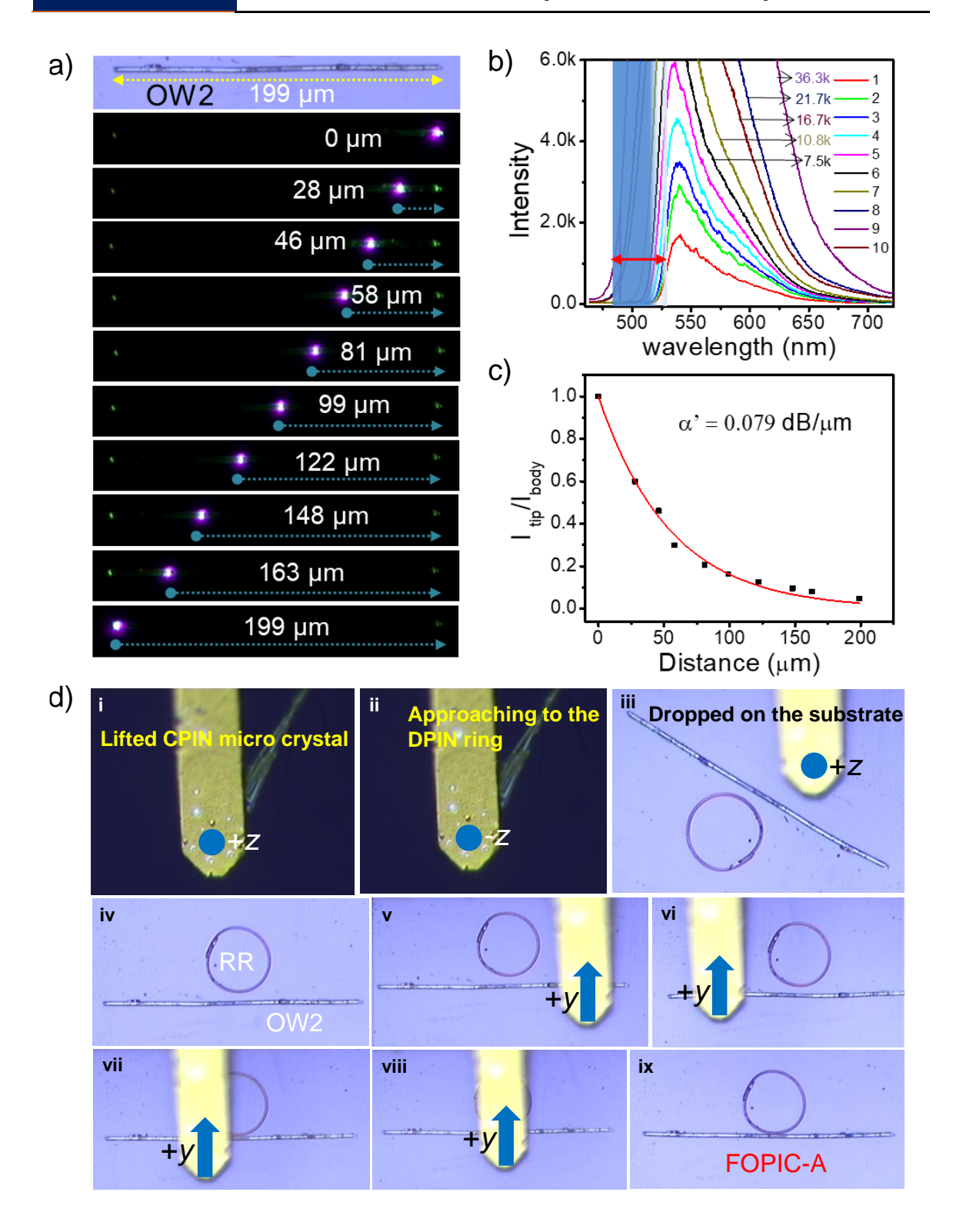


Fig. 5.7. a) Confocal microscope image of a straight CPIN crystal (OW2) and its FL images when the crystal was excited with a 405 nm laser at different positions. b) The corresponding FL spectra. The red double-headed arrow of the inset shows the reabsorption region. c) The optical loss coefficient estimation by fitting (red line) the data plot of $I_{\rm tip}/I_{\rm body}$ versus propagation length. d) Confocal optical microscope photographs show the steps involved in the mechanical micromanipulation of OW2 towards RR to produce FOPIC-A using AFM cantilever force.



FL emission spectra intensity decreases with increasing the optical path length (0 to 199 μ m) of the crystal (**Fig. 5.7b**). The optical loss coefficient was measured to be 0.079 dB μ m⁻¹ (**Fig. 5.7c**).

The integration of straight CPIN crystal (OW1) with RR via micromanipulation using an AFM cantilever tip is a challenging task. For that, initially, the CPIN crystal was lifted from glass substrate-2 and carefully transferred to substrate-1 near the RR (Fig. 5.7di-iv the deposited crystal was pushed towards RR with AFM tip, by applying force in the +y direction, starting from left, right, and finally in the middle of the crystal (Fig 5.7dv-viii). This mechanical process produces the OW2-RR (FOPIC-A) (Fig 5.7dix).

5.3.7. Optical Waveguiding Studies of FOPIC-A

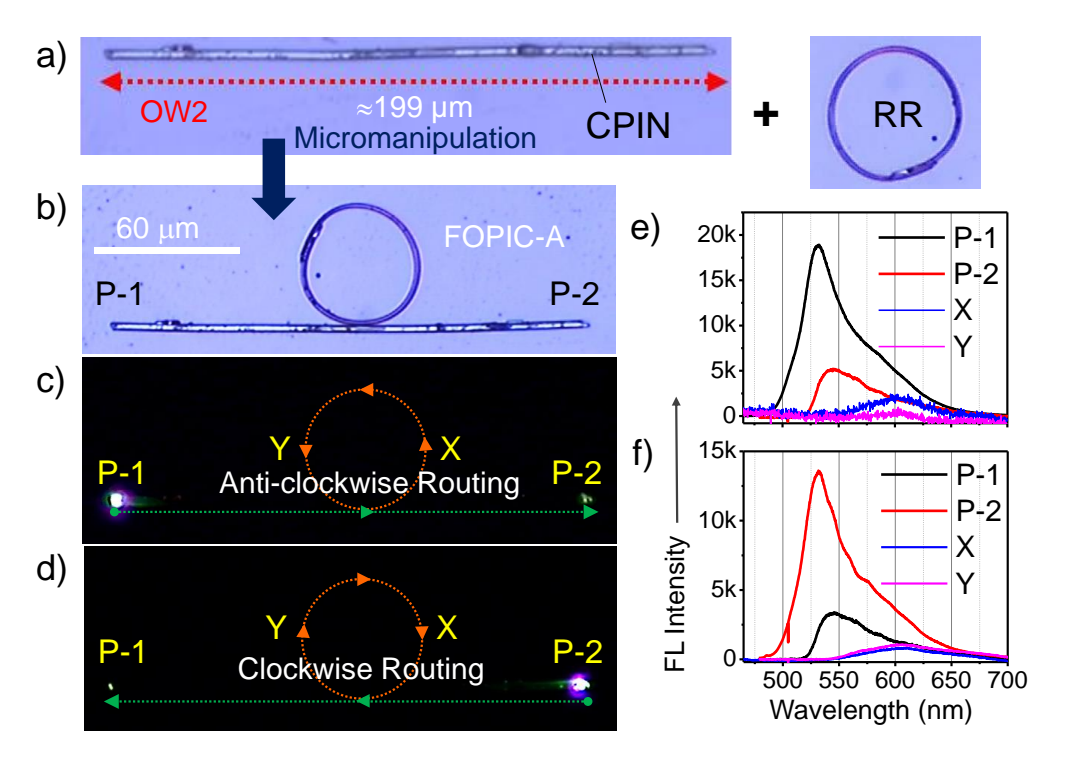


Fig. 5.8. a) Optical image of a straight CPIN crystal waveguide, OW2 (left side), and DPIN crystal RR (right side). b) Fabrication of a hybrid FOPIC-A by integrating OW2 with RR via mechanical micromanipulation. c,d) FL images of FOPIC-A. The excitation termini are P-1 and P-2, respectively. e,f) The corresponding FL spectra at P-2 and P-1 output termini, respectively.

The complex mechanical maneuvers (*lifting, dropping, moving,* and *integrating*) of the CPIN crystal waveguide towards DPIN crystal RR resulted in a hybrid integrated circuit, FOPIC-A, with two ports, namely P-1 and P-2 (**Fig. 5.8a,b**). Optical excitation of OW2 at the port-1 and -2, initially the excitation of OW2 at the P-1 terminal produced a bright-

green FL, which transduced towards the opposite crystal terminal and outcoupled at P-2 (**Fig. 5.8c**). Due to the overlap of CPIN FL with the absorption of DPIN, the green FL of OW2 excited the RR via the ET mechanism. The spectrum recorded at point X of RR exhibited FL with the λ_{max} of \approx 610 nm corresponding to the DPIN FL, confirming the ET (**Fig. 5.8e**). Here, the RR routes the light in a counterclockwise path. Similar optical behavior was observed when P-2 was excited (**Fig. 5.8d**), and the optical signal traveled in a clockwise direction to deliver the output signal at P-1 (**Fig. 5.8f**). These results suggest the directional routing of light achieved using the tailor-made FOPIC-A.

5.3.8. Construction of FOPIC-B from FOPIC-A

For the integration of FOPIC-A with another DPIN crystal ($L^{\sim}217~\mu m$), primarily the OW3 deposited parallel to OW2. The OW3 was pushed towards the FOPIC-A, by applying force along the -y direction, left, right and center of the crystal (**Fig. 5.9i-iii**). Later the additional force was applied in the -y direction, producing FOPIC-B (**Fig. 5.9iv-vi**).

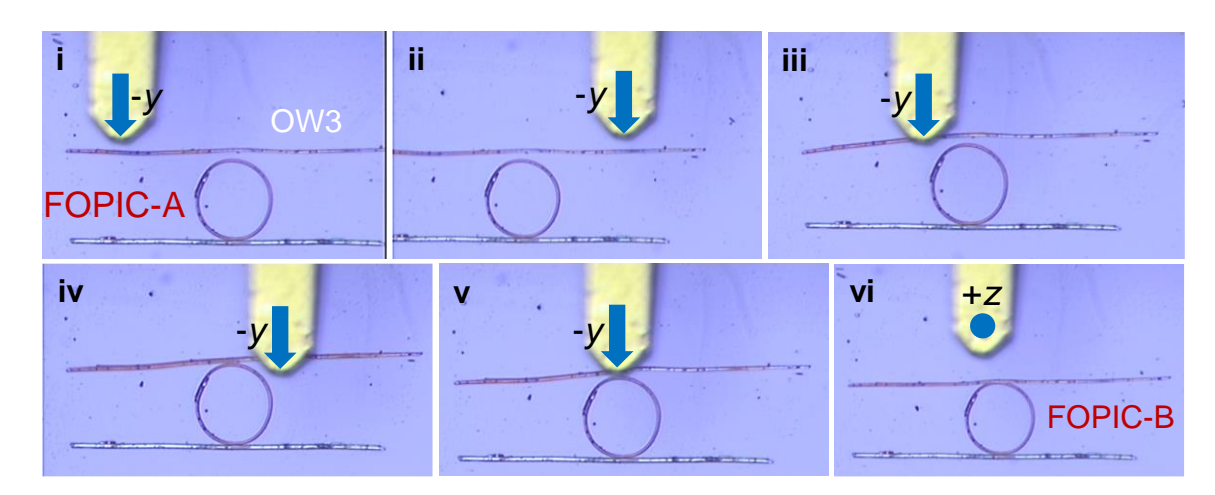


Fig. 5.9. Confocal microscope images displaying the steps involved in the micromechanical manipulation process from FOPIC-A to FOPIC-B.

5.3.9. Fabrication of FOPICs I–IV from FOPIC-B

To fabricate a FOPIC-I, II, III, and IV from FOPIC-B via mechanical micromanipulation technique, initially OW3 crystal of hybrid FOPIC-B was bent at the left side of the crystal by an angle of ~28° upon applying force in the +y direction with AFM cantilever tip, generate a FOPIC-I (**Fig. 5.10ai-iii**). The FOPIC-I was converted into FOPIC-II, by pushing at the right side of the OW3 crystal towards the forward direction (+y

direction), producing FOPIC-II with an angle ~185° (**Fig. 5.10bi-iii**). Later the straight CPIN (OW2) crystal was bent (~330°) at the left side of the crystal by pushing in the -y direction (forward direction), creating a FOPIC-III (**Fig. 5.10ci-iv**). Finally, the FOPIC-IV was obtained from FOPIC-III, when force was applied in the forward direction at the right side of the OW2 crystal with an angle of \approx 208° (**Fig. 5.10di-iii**). All these mechanical processes produce the various angles at both left and right terminals of the OW2 and OW3 crystals to manipulate the optical light propagation direction.

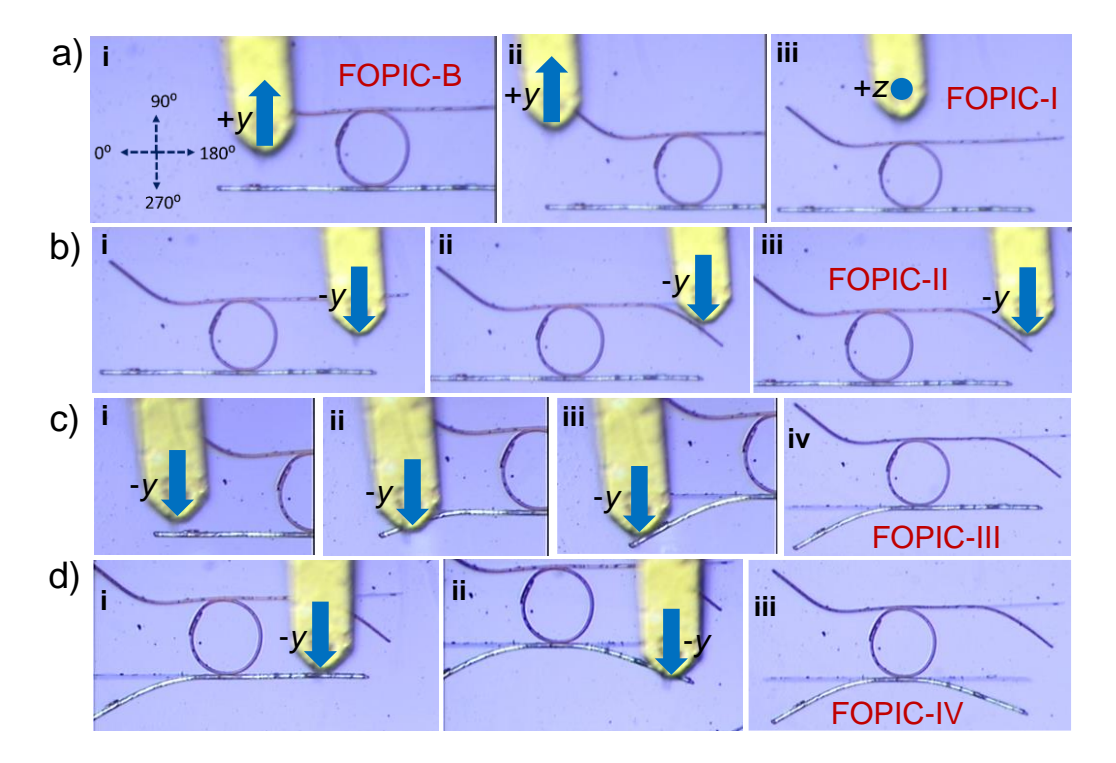


Fig. 5.10. a-d) Confocal microscopy images show the reconfiguration of FOPIC-I to -IV from FOPIC-B via a mechanical micromanipulation process.

5.3.10. Optical Waveguiding Studies of FOPIC-I-IV

Micromechanical integration of a straight DPIN waveguide (OW3) with RR of FOPIC-A (**Fig. 5.11a,b**) provided a FOPIC-B with four ports, P-1 to P-4 (**Fig. 5.11c**). This FOPIC-B widens the scope of varying the light output directions and operational spectral bandwidth. The optical performance of reconfigurable FOPIC-I was examined by exciting any specific port and recording the spectral output of the remaining ports. When P-1 was excited, it produced a red FL signal with a wide bandwidth of \approx 525-750 nm and $\lambda_{max} \approx$ 605 nm (Signal 1A, where A stands for *active* signal). The same light actively propagated through bent OW3 to reach P-2 with a slightly narrow bandwidth of \approx 575-750 nm (Signal

-1A, where the negative sign denotes a narrow bandwidth signal). Further, the broad bandwidth light evanescently coupled to RR and traveled passively as a 1P signal (P stands for *passive* signal) in a clockwise direction (**Fig. 5.11ci, 5.11di**), and again evanescently

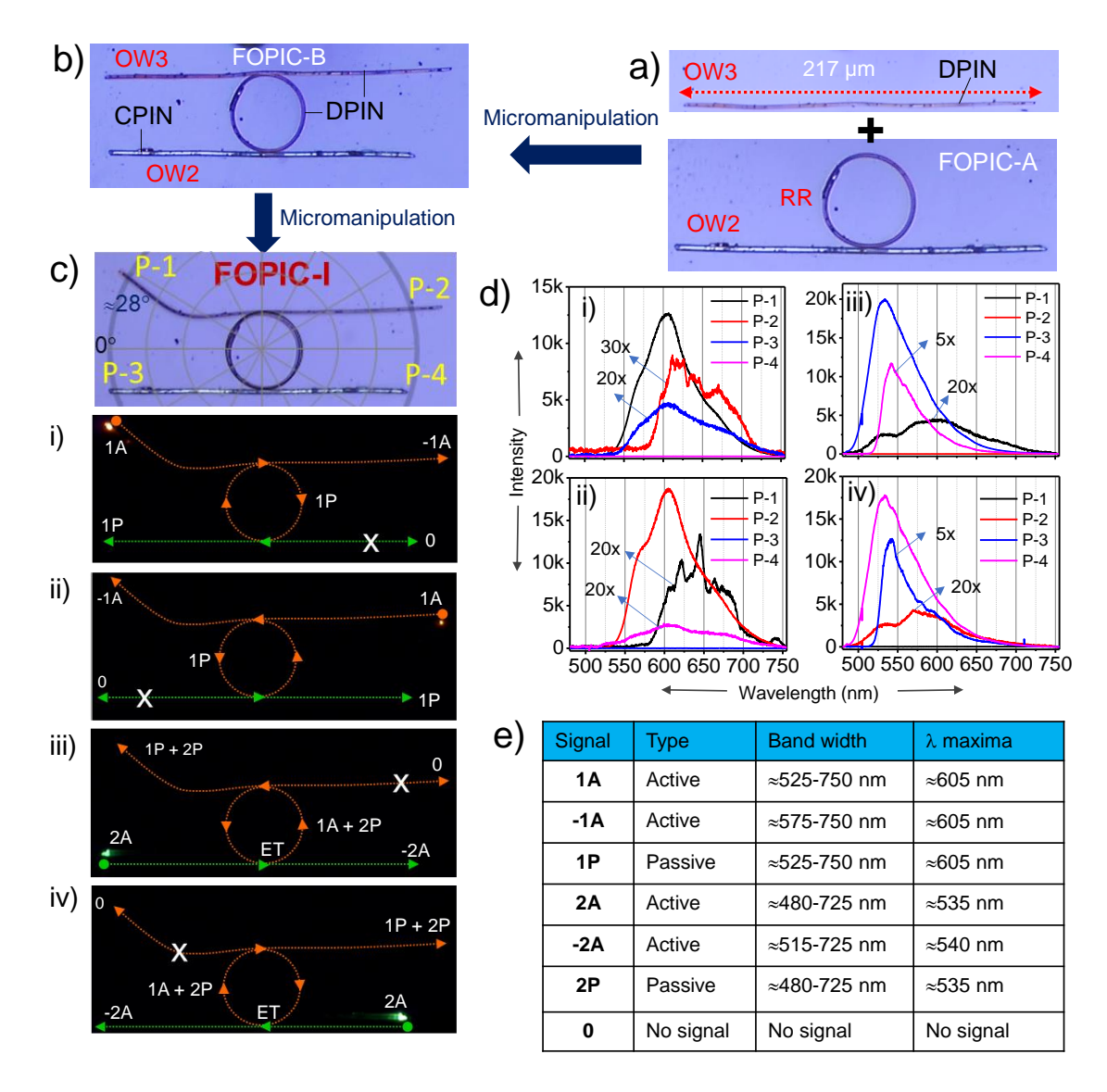


Fig. 5.11. a,b) Fabrication of a hybrid organic circuit, FOPIC using OW3 and FOPIC-A via mechanical manipulation. c) Mechanical reconfiguration of port, P-1 direction to $\approx 28^{\circ}$ of FOPIC-I, and i-iv) FL images of FOPIC-I excited at P-1, P-2, P-3, and P-4 positions. d) Its corresponding FL spectra were recorded at output terminals (i-iv). e) Table explaining the signal codes, type, spectral bandwidth range, and FL λ_{max} .

coupled to OW2, yielding a 1P signal at *drop port* P-3. Due to the clockwise optical trajectory of RR, the output light was not (Signal 0) detected at P-4.

Similarly, P-2 excitation delivered -1A signal at *through port* P-1, 1P signal at *drop port* P-4, and 0 signal at P-3 (**Fig. 5.11cii, 5.11dii**). Interestingly, when P-3 was excited, the green FL with a bandwidth of \approx 480-725 nm and $\lambda_{max} \approx$ 535 nm (Signal 2A) propagated

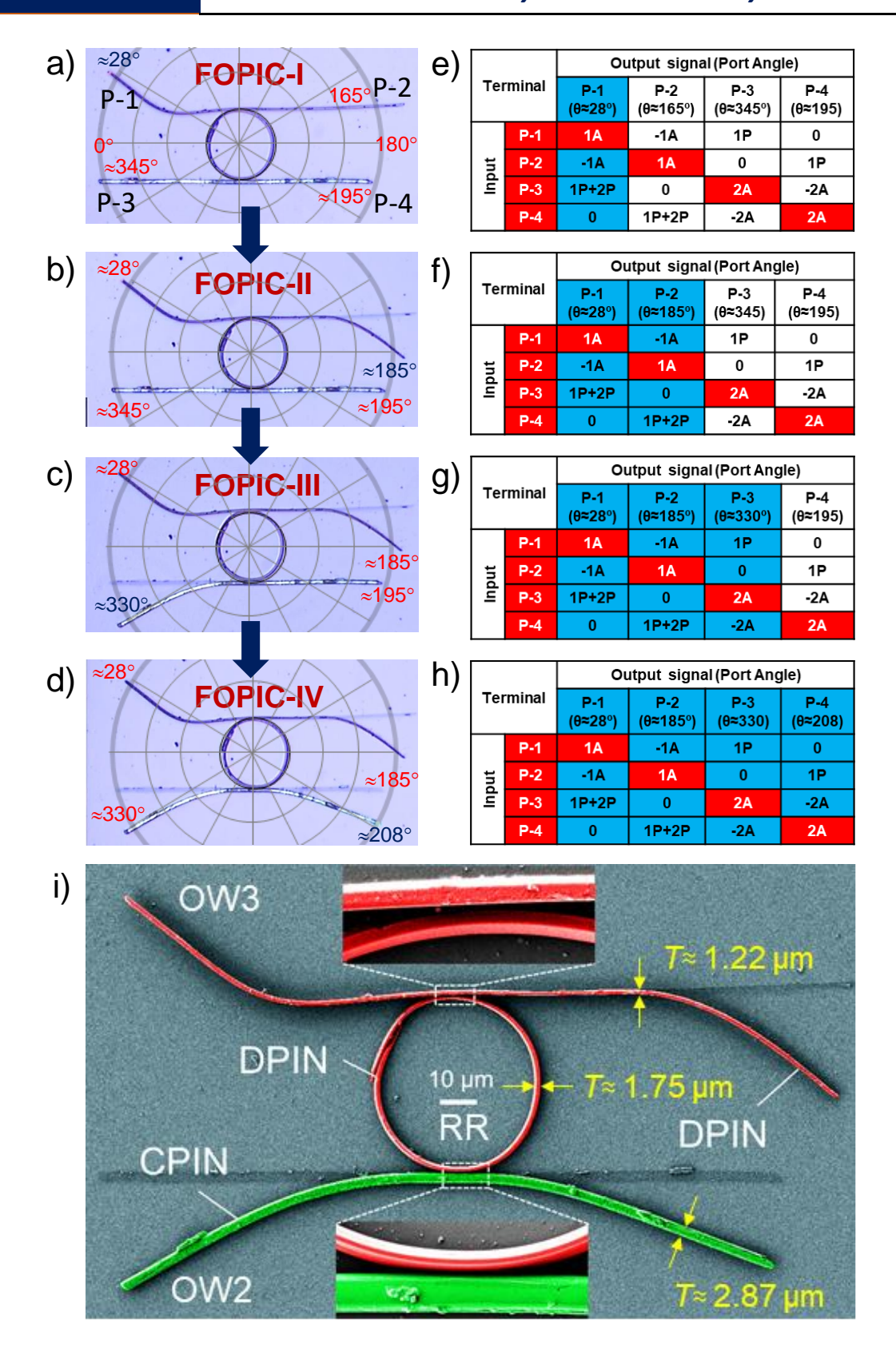


Fig. 5.12. a-d) Confocal optical microscope images of step-wise port-angle reconfigured FOPICs for the need-based altering of light output direction. e-h) Optical performance tables demonstrating the light input-dependent output signals at P-1, P-2, P-3, and P-4 over various angles. i) False-color coded FESEM image of FOPIC-IV. The inset shows a close-up view of the evanescent contact region between CPIN and DPIN crystals with RR.

towards P-4 and outcoupled as a narrowband (≈515-725 nm) -2A signal (Fig. 5.11ciii, 5.11diii). Along the way, it evanescently coupled to RR and excited it to generate signal 1A via ET. Due to an incomplete ET, signal 2A passively propagated (2P signal) counterclockwise along with signal 1A and outcoupled at *drop port* P-1 (1P+2P signal). Because of the RR's counterclockwise light path, 0 signal was recorded at P-2. Similarly, P-4 excitation showcased a *through port* signal -2A at P-3 and a *drop port* signal of 1P+2P at P-2, while no output at P-1(Fig. 5.11civ, 5.11div). The results demonstrate the ability of FOPIC-I in producing six (1A, -1A, 1P, 2A, -2A, and 2P) distinct optical signals and selectively deliver them to three different ports (Fig. 5.11e).

Further, the steering of six different optical signals at different angles in the two-dimensional plane was demonstrated by mechanically reconfiguring the orientation of each port of FOPC-I (**Fig. 5.12a**). The P-2 of FOPIC-I was reconfigured to $\approx 185^{\circ}$ to fabricate FOPIC-II (**Fig. 5.12b**). Here, compared to FOPIC-I, the signal output directions in FOPIC-II differs selectively at one port. Similar reconfiguration of P-3 in FOPIC-II by $\approx 330^{\circ}$ and P-4 in FOPIC-III by $\approx 208^{\circ}$ resulted in FOPIC-III and FOPIC-IV, respectively (**Fig. 5.12c,d**). In FOPIC-IV, the contact between OW-2 and RR at their convex sides is expected to improve the optical coupling compared to FOPIC-I. As a result of step-wise port reconfiguration in FOPICs, the light output direction of any specific port could also be correspondingly altered (**Fig. 5.12e-h**; **Fig. 5.13a,b**; **Fig. 5.14a**). The false-colour FESEM image of FOPIC-IV presented in **Fig. 5.12i** shows the dimension and physical contact between RR and OWs. The thickness (*T*) of OW-3, RR, and OW-2 was found to be ≈ 1.22 , ≈ 1.75 , and ≈ 2.87 µm, respectively.

In FOPIC-II, -III, and -IV, the type of optical signals (1A, -1A, 1P, 2A, -2A, and 2P) steered by ports are nearly the same as FOPIC-I (Fig. 5.13a,b; Fig. 5.14a), except for their radial output directions (Fig. 5.12f-h). The diagonal red boxes of the tables show input signals at various ports. Here, P-1 and P-2 could selectively reroute any signal (-1A or 1P+2P) from 15 to 28° and 165 to 185°, respectively, depending upon input ports (Fig. 5.12e,f).

In contrast, P-3 and P-4 could selectively reroute any signal (1P or -2A) from 345 to 330° and 195 to 208° depending upon input ports (**Fig. 5.12g,h**). The effect of circuit

reconfiguration on the optical performance was assessed by comparing FOPIC-I and FOPIC-IV. FOPIC-I has only one bent in a waveguide, while in FOPIC-IV, it increased to three. The higher number of bends in a circuit implies a high bending-induced optical loss leading to the lower light intensity at the output ports. For example, the intensity

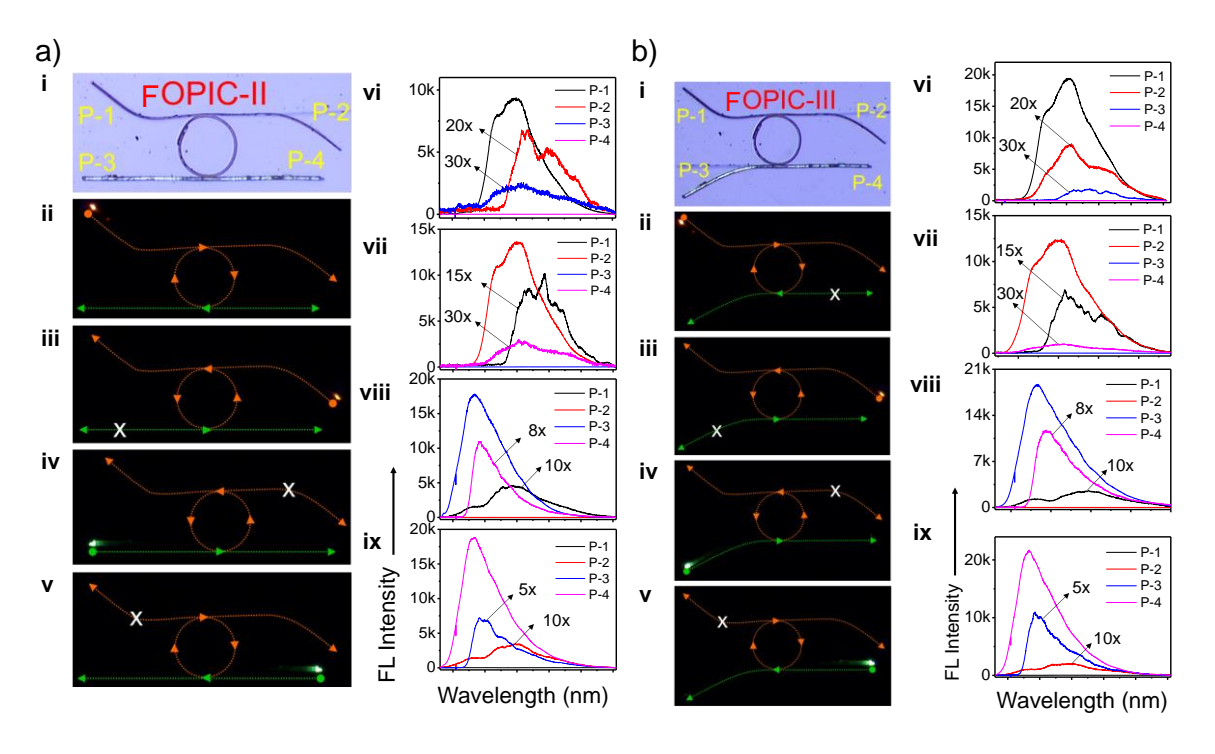


Fig. 5.13. a) Confocal optical images of FOPIC-II (ai), its corresponding FL emission images (aii-v), excited with 405 nm laser at P-1, -2, -3, and -4 positions, and its corresponding FL spectra (avi-ix). b) Confocal images of FOPIC-III (bi), its FL images excited at P-1, -2, -3, and -4 points (bii-v), and the respective FL spectra (bvi-ix).

difference between FOPIC-I and FOPIC-IV for the *through port* signal collected at P-4 for excitation at P-3 is 20% lower, owing to the bending-induced light leakage in OW2 (**Fig. 5.11diii**; **Fig. 5.14aviii**). At the *drop port* (P-1), signal intensity decreased only \approx 6%. One would expect a much lower light intensity around the *drop port* than *through port* due to the increase in the optical path. FOPIC-IV showed nearly a comparable optical performance with FOPIC-I when input ports were changed. The optical performance shown by the presented reconfigurable FOPICs, transducing six different optical signals is essential for programmable organic circuit technologies.

The bending-induced strain was estimated using the formula Strain (%) = $(T/R) \times 100$, Here T = thickness of the crystal, and R = radius of the crystal. In OPIC-IV, the top DPIN crystal (OW3) strain was measured to be $\approx 1.95\%$, its average thickness, $T_{avg} \approx 1.95\%$

1.22 μ m, and its diameter, D \approx 123 μ m (**Fig.5.14b**). Similarly, the RR ($T_{avg}\approx$ 1.75 μ m; D \approx 48 μ m) and OW2 ($T_{avg}\approx$ 2.87 μ m; R \approx 296 μ m) strains were calculated \approx 8.14% and \approx 1.89%, respectively (**Fig.5.14c,d**).

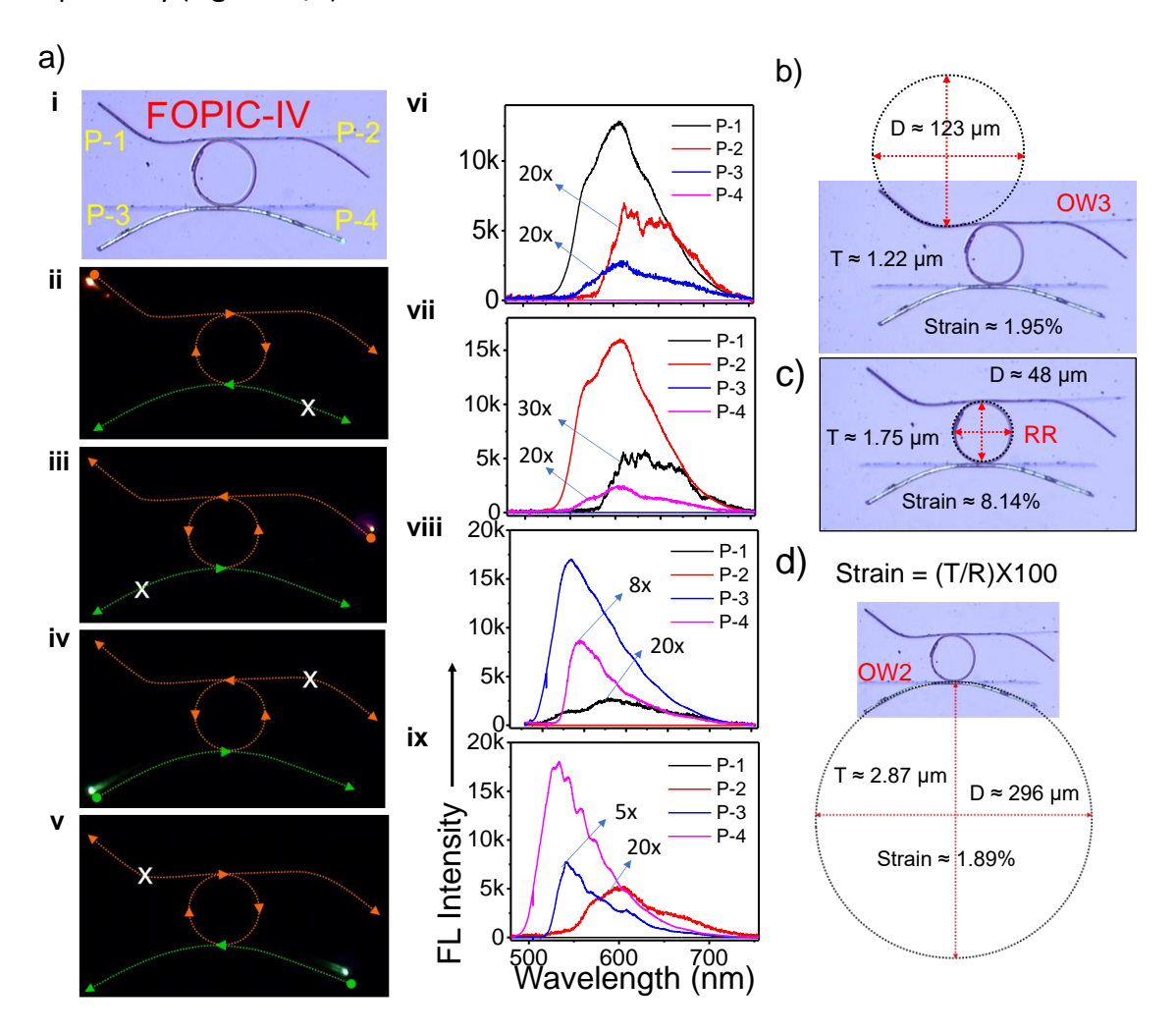


Fig. 5.14. ai-v) Confocal optical and FL images of FOPIC-IV when a selected port is irradiated with a 405 nm laser. avi-ix) The corresponding FL spectra. b-d) The calculated strain of top DPIN microcrystal (OW3), middle DPIN RR, and bottom bow-shaped CPIN crystal (OW2).

5.4. Conclusion

In summary, the mechanical and photonic attributes of reconfigurable OPICs micromechanically fabricated using two optically and mechanically distinct CPIN and DPIN flexible crystals were studied. The substitution of *chloro* group in place of *N,N,-dimethyl amine* shifted the fluorescence of DPIN from red to green. The crystal structure of CPIN closely resembles DPIN. The soft mechanical characteristics of DPIN compared to CPIN possibly result from a compact crystal packing. The CPIN crystals displayed flexibility when crisscross type $\pi \cdots \pi$ stacked molecular chains experienced a mechanical force

perpendicular to the (001) plane. However, both crystals exhibit pseudo-plasticity at the micro-regime due to stronger adhesion between microcrystal and substrate compared to crystal shape regaining force. The micro-crystals pseudo-plasticity on the substrate was successfully exploited to fabricate reconfigurable FOPICs. The mechanophotonics approach allowed port-angle reconfiguration in FOPICs, which is impossible in silicon-based circuits. The need-based steering of six different output signals over 360° via port-reconfiguration demonstrated the superiority of flexible crystal FOPICs. The better optical performance of FOPICs proves the usefulness of flexible organic crystals as an alternative material for many advanced nanophotonic applications.

Chapter-6



Summary

This thesis entitled "Flexible Organic Crystalline Materials for Photonic Integrated Circuits" described the versatility of flexible organic microcrystals achieved from the self-assembly process and utilization of these organic single-crystals for PICs fabrication using a *mechanophotonic* approach.

Chapter-1 described the important characteristics of conventional Si and Si-based PICs, the advantages of flexible organic crystalline materials over inorganic materials (Si and Si-based), and their utility in miniaturized photonic circuit applications. Special attention had been paid to micro-cavities classes and their several useful parameters like free spectral range, photon lifetime, finesse, and Q-factor. A gist of important Si-based optical components such as waveguides, ring resonators (RRs), waveguide coupled RRs, directional couplers, and add-drop filters were described. The optical functions and operational mechanisms possible in Si and organic materials were summarized.

Flexible organic single-crystal waveguides are quite rare and are essential for the fabrication of photonic microcircuits and organic optoelectronics. Integration of flexible crystals in microcircuits necessitates precise spatial control of crystal position and its geometry via a mechanical *micromanipulation* approach. Research in this area will lead to next-generation photonic circuitry components. In *Chapter-2* two electronically and optically different flexible organic micro-crystals were employed (BPIN and DPIN) to

fabricate mechanically reconfigurable and geometrically different three μ -OPICs using atomic force microscopy (AFM) micromanipulation technique. Depending upon the crystal's electronic nature (either BPIN or DPIN) receiving the optical signal input, the μ -OPICs executed mechanism-selective and directional-specific optical outputs. These μ -OPICs performed complex optical functions through active/passive waveguiding, and energy transfer mechanisms. Thus, demonstrating the versatility of achieving multiple functions in hybrid organic PICs.

Chapter-3 revealed the first micromechanical fabrication of a ring resonator (RR) from a linear waveguide using a mechanophotonics approach. The RR was extended to fabricate an OPIC which comprised of a micro-RR (a ring-shaped crystal) integrated into two straight optical waveguides using the AFM micromanipulation technique. The constructed dual waveguide coupled RR performed complex optical operations via energy transfer, and passive, and active waveguiding mechanisms. Based on the port receiving light input, the circuit implemented directional-specific and mechanism-selective optical output signals.

Mechanically responsive organic plastic single-crystals are one of the attractive novel materials for future-generation all-organic photonic circuits. *Chapter-4* demonstrated the fabrication of geometrically dissimilar and mechanically reconfigurable OPICs using two mechanically (plastic and elastic) and optically different crystals of NDIPH and BPEA using an AFM cantilever tip. NDIPH single-crystals show exceptional plasticity to external mechanical stress and its mechanical plasticity was established by crystal structure analysis. Depending upon the electronic character of the crystal (NDIPH or BPEA) and laser input signal, OPIC performed mechanism-selective and directional-specific light outputs. Remarkably, these OPICs comprised complex optical operations *via* passive/active waveguiding, and energy transfer mechanisms. The fabricated OPICs were reconfigurable, thus the light output signal was manipulated in an orthogonal direction on a two-dimensional chip.

Chapter-5 demonstrated the fabrication of flexible organic single-crystal-based PICs (FOPICs) on a 2D chip using micromanipulation. For this, the optomechanical properties of organic micro-crystals of CPIN (green-emitting) and DPIN (red-emitting)

were thoroughly studied using a laser-based microspectroscopy technique. Later, the sequential micromechanical manipulation of DPIN single-crystal was performed to fabricate a RR, which was integrated with a linear waveguide, resulting in a bus waveguide coupled RR (BWCR). This homo photonic circuit (constructed from one type of material) was coupled with CPIN microcrystal to yield a two-component PIC named hybrid dual bus waveguide coupled RR (HDBWCR). The versatility of FOPICs lies in the post-fabrication reconfigurability to modulate optical signal routing in a 2D plane. Thus, rendering their utility in multi-tasking photonic devices. The mechanical bendability of the circuit ports was exploited at varying angles (from 0° to 360°) in a 2D plane to demonstrate the mechanically reprogrammable optical signal routing. Therefore, depending on the need, the same circuit can be reconfigured to extract the desired function. Hence, the superiority of single-crystal organic flexible waveguides for PICs has been demonstrated.

Remarkably, these findings pertaining to the use of organic microcrystal waveguides for reconfigurable OPICs pave the path toward achieving reprogrammable PICs in near future. The active, passive, reabsorption, and energy transfer operational mechanisms proved to be vital optical mechanisms to derive complex photonic functions in hybrid circuits. In conclusion, the combination of *mechanophotonics* and crystal engineering at the interface of nanophotonics opened a new dimension in the rapid advancement of organic photonic technologies.

REFERENCES

- [1] https://creativemarket.com/Raimundas/4398751-Electronic-circuit-board-close-up-featuring-background-board-and-card#fullscreen.
- [2] https://www.shutterstock.com/search/electronic+circuit.
- [3] https://www.synopsys.com/glossary/
- [4] M. Wale, in Advanced Photonics Congress, Optical Society of America, Colorado Springs, USA **2012**, JTu1B, 1.
- [5] D. Thomson, A. Zilkie, J. E. Bowers, T. Komljenovic, G. T. Reed, L. Vivien, D. Marris-Morini, E. Cassan, L. Virot, J. M. F'ed'eli, J. Hartmann, J. Schmid, D. X. Xu, F. Boeuf, P. O'Brien, G. Z. Mashanovich and M. Nedeljkovic, J. Optics. 2016, 18, 073003.
- [6] L. Chrostowski and M. Hochberg, Silicon Photonics Design: From Devices to Systems, Cambridge University Press, Cambridge, **2015**.
- [7] W. Bogaerts, D. Pérez, J. Capmany, D. A. B. Miller, J. Poon, D. Englund, F. Morichetti and A. Melloni, *Nature*, **2020**, *586*, 207.
- [8] S. Yuzhi, L. Zhenyu, L. P. Yang, N. B. T. Thanh, W. Wenshuai, Z. Qianbin, C. L. Ket, W. Minggui, Y. P. Huat, Z. X. Z. Hongwei, Y. Dan, T. D. Ping, and L. A. Qun, *Adv. Photonics Res.* **2021**, *2*, 2000150.
- [9] Q. Cheng, M. Bahadori, M. Glick, S. Rumley and K. Bergman, Optica, 2018, 5, 1354.
- [10] I. R. Ruiz, T. N. Ackermann, X. M. Berbel and A. Llobera, *Anal. Chem.* **2016**, *88*, 1354.
- [11] R. Corneliu, *Proc. of SPIE*, **2019**, *11143*, 111430.
- [12] R. Chandrasekar, Z. J. Lapin, A. S. Nichols, R. M. Braun and A. W. Fountain, *Optical Engineering*, **2019**, *58*, 020901.
- [13] W. Bogaerts and L. Chrostowski, Laser Photonics Rev. 2018, 12, 1700237.
- [14] X. Chen, M. M. Milosevic, S. Stanković, S. Reynolds, T. D. Bucio, K. Li, D. J. Thomson, F. Gardes and G. T. Reed, *Proc. IEEE*, **2018**, *106*, 2101.
- [15] S. Lourdodoss, R. T. Chen and C. Jagadish, Semiconductors and Semimetals Book Series, Academic Press, Cambridge **2018**, *99*, 228.
- [16] P. Dong, Y. K. Chen, G. H. Duan and D. T. Neilson, *Nanophotonics*, **2014**, *3*, 215.
- [17] I. R. Ruiz, T. N. Ackermann, X. M. Berbel and A. Llobera, Anal. Chem. 2016, 88, 6630.
- [18] D. X. Xu, J. H. Schmid, G. T. Reed, G. Z. Mashanovich, D. J. Thomson, M. Nedeljkovic, X. Chen, D. V. Thourhout, S. Keyvaninia and S. K. Selvaraja, *IEEE J. Sel. Top. Quantum Electron.* **2014**, *20*, 189.
- [19] K.Fujii, H. Bettin, P. Becker, E. Massa, O. Rienitz, A. Pramann, A. Nicolaus, N. Kuramoto, I. Busch and M. Borys, *Metrologia*, **2016**, *53*, 19.
- [20] https://www.toppr.com/ask/en-bd/question/which-one-of-the-following-is-true-with-respect-to-sio2/.
- [21] J. Fayomi, A. P. I. Popoola, O. M. Popoola, O. P. Oladijo and O. S. I. Fayomi, *Int. J. Adv. Manuf. Technol*, **2020**, *111*, 53.
- [22] Y. Su, Y. Zhang, C. Qiu, X. Guo and L. Sun, Adv. Mater. Technol. 2020, 8, 1901153.

- [23] T. Hu, B. Dong, X. Luo, T. Y. Liow, J. Song, C. Lee and G. Q. Lo, Photonics Res., 2017, 5, 417.
- [24] E. D. Palik, Handbook of Optical Constants of Solids, Academic, New York 1998.
- [25] P. E. Barclay, K. Srinivasan and O. Painter, Opt. Express, 2005, 13, 801.
- [26] A. Arbabi and L. L. Goddard, Opt. Lett. 2013, 38, 3878.
- [27] T. Miya, IEEE J. Sel. Top. Quantum Electron. **2000**, *6*, 38.
- [28] T. D. Bucio, C. Lacava, M. Clementi, J. Faneca, I. Skandalos, A. Baldycheva, M. Galli, K. Debnath, P. Petropoulos, and F. Gardes, *IEEE J. Sel. Top. Quantum Electron.* **2020**, *26*, 1.
- [29] Y. Zhang, Y. He, Q. Zhu, X. Guo, C. Qiu, Y. Su and R. Soref, Opt. Lett. 2018, 43, 4518.
- [30] Q. Fang, J. F. Song, T. Y. Liow, H. Cai, M. B. Yu, G. Q. Lo and D. L. Kwong, *IEEE Photonics Technol. Lett.* **2011**, *23*, 525.
- [31] D. J. Moss, R. Morandotti, A. L. Gaeta and M. Lipson, Nat. Photonics, 2013, 7, 597.
- [32] S. Miller, K. Luke, Y. Okawachi, J. Cardenas, A. L. Gaeta and M. Lipson, Opt. Express 2014, 22, 26517.
- [33] T. Byrnes, N. Y. Kim and Y. Yamamoto, *Nat. Phy.* **2014**, *10*, 803.
- [34] Y. Zhang, Y.Liu, C. Li, X. Chen and Q. Wang, J. Phys. Chem. C. 2014, 118, 4918.
- [35] J. Kasprzak, M. Richard, S. Kundermann, A. Baas, P. Jeambrun, J. M. J. Keeling, F. M. Marchetti, M. H. Szymaska, R. André, J. L. Staehli, V. Savona, P. B. Littlewood, B. Deveaud and L. S. Dang, *Nature* 2006, 443, 409.
- [36] R. Balili, V. Hartwell, D. Snoke, L. Pfeier and K. West, *Science* **2007**, *316*, 1007.
- [37] H. Deng, G. Weihs, C. Santori, J. Bloch and Y. Yamamoto, Science, 2002, 298, 199.
- [38] J. Keeling and N. G. Berlo, Contemp. Phys. 2011, 52, 131.
- [39] V. Timofeev, and D. Sanvitto Springer, 2012, 172.
- [40] I. Carusotto and C. Ciuti, Rev. Mod. Phys, 2013, 85, 299.
- [41] Y. Yamamoto and A. Imamoglu, *Mesoscopic Quantum Optics*, John Wiley and Sons, New York, **1999**. 26.
- [42] D. Venkatakrishnarao, Ph.D. Thesis, University of Hyderabad, 2018, chapter-1, 5.
- [43] S. Christopoulos, G. B. H. V. Hogersthal, A. J. D. Grundy, P. G. Lagoudakis, A. V. Kavokin and J. J. Baumberg, *Phys. Rev. Lett.* **2007**, *98*, 126405.
- [44] J. J. Baumberg, A. V. Kavokin, S. Christopoulos, A. J. Grundy, R. Butté, G. Christmann, D. D. Solnyshkov, G. Malpuech, G. B. H. V. Hogersthal, E. Feltin, J. F. Carlin and N. Grandjean, *Phys. Rev. Lett.* 2008, 101, 136409.
- [45] S. Kéna-Cohen and S. R. Forrest, Nat. Phot. 2010, 4, 371.
- [46] G. H. Wannier, Phy. Rev. 1937, 52, 191.
- [47] J. Frenkel, Phy. Rev. 1931, 37, 17.
- [48] H. Dong, Y. Wei, W. Zhang, C. Wei, C. Zhang, J. Yao and Y. S. Zhao, J. Am. Chem. Soc. 2016, 138, 1118.
- [49] S. Grimme. Angew. Chem. Int. Ed. 2008, 47, 3430.

- [50] H. Kar and S. Ghosh, Chem. Commun. 2014, 50, 1064.
- [51] E. Busseron, Y. Ruff, E. Moulin and N. Giuseppone, Nanoscale. 2013, 5, 7098.
- [52] C. Weissm, C. Wagner, R. Temirov and F. S. Tautz, J. Am. Chem. Soc. 2010, 132, 11864.
- [53] T. Dong, Y. Zhou, D. Hu, P. Xiao, Q. Wang, J. Wang, J. Pei and Y. Cao, J. coll. Inter. Sci. 2015, 445, 213.
- [54] Y. K. Che, X. M. Yang, K. Balakrishnan, J. M. Zuo and L. Zang, Chem. Mater. 2009, 21, 2930.
- [55] R. Chandrasekar, Small 2021, 17, 2100277.
- [56] C. Tardío, V. V. Pradeep, R.I Martín, A. M. Rodríguez, A. D. L. Hoz, J. Ravi, M. Annadhasan, P. Prieto and R. Chandrasekar, *Chem Asian J.* **2021**, *16*, 3476.
- [57] M. Annadhasan, S. Basak, N. Chandrasekhar and R. Chandrasekar, *Adv. Optical Mater.* **2020**, *8*, 2000959.
- [58] B. E. A. Saleh and M. C. Teich, Fundamentals of Photonics, John Wiley & Sons, Inc., Hoboken, NJ 1991.
- [59] R. S. Quimby, Photonics and Lasers—An Introduction, John Wiley & Sons, Inc, Hoboken, NJ 2006.
- [60] W. Yao, Y. Yan, L. Xue, C. Zhang, G. Li, Q. Zheng, Y. S. Zhao, H. Jiang and J. Yao, *Angew. Chem., Int. Ed.* **2013**, *52*, 8713.
- [61] R. Chandrasekar, Chem. Commun. 2022, 58, 3415.
- [62] https://gl.m.wikipedia.org/wiki/Interfer%C3%B3metro_Fabry-P%C3%A9rot.
- [63] T. J. A. Kippenberg, Ph.D. Thesis, California Institute of Technology 2004.
- [64] G. Righini, Y. Dumeige, P. F. Eron, M. Ferrari, G. N. Conti, D. Ristic and S. Soria, *Riv. Nuovo Cimento* **2011**, *34*, 435.
- [65] X. Wang, Q. Liao, Q. Kong, Y. Zhang, Z. Xu, X. Lu and H. Fu, Angew. Chem., Int. Ed. 2014, 126, 5973.
- [66] K. Tabata, D. Braam, S. Kushida, L. Tong, J. Kuwabara, T. Kanbara, A. Beckel, A. Lorke and Y. Yamamoto, *Sci. Rep.* **2014**, *4*, 5902.
- [67] D. Venkatakrishnarao, C. Sahoo, E. A. Mamonov, I. A. Kolmychek, A. I. Maydykovskiy, N. V. Mitetelo, V. B. Novikov, S. R. G. Naraharisetty, T. V. Murzina and R. Chandrasekar, J. Mater. Chem. C 2017, 5, 12349.
- [68] C. Zhang, C.-L. Zou, Y. Yan, C. Wei, J.-M. Cui, F.-W. Sun, J. Yao and Y. S. Zhao, *Adv. Opt. Mater.* **2013**, *1*, 357.
- [69] U. Venkataramudu, D. Venkatakrishnarao, N. Chandrasekhar, M. A. Mohiddon and R. Chandrasekar, *Phys. Chem. Chem. Phys.* **2016**, *18*, 15528.
- [70] D. Venkatakrishnarao and R. Chandrasekar, Adv. Opt. Mater. 2015, 4, 112.
- [71] R. Vattikunta, D. Venkatakrishnarao, C. Sahoo, S. R. G. Naraharisetty, D. N. Rao, K. Müllen and R. Chandrasekar, *ACS Appl. Mater. Interfaces*, **2018**, *10*, 16723.
- [72] D. Venkatakrishnarao, C. Sahoo, R. Vattikunta, M. Annadhasan, S. R. G. Naraharisetty and R. Chandrasekar, *Adv. Opt. Mater.* **2017**, *5*, 1700695.
- [73] G. Schunk, J. U. Fürst, M. Förtsch, D. V. Strekalov, U. Vogl, F. Sedlmeir, H. G. L. Schwefel, G. Leuchs and C. Marquardt, *Opt. Express*, **2014**, *25*, 30795.

- [74] A. N. Oraevsky, Quantum Electron. 2002, 32, 377.
- [75] https://www.photonics.intec.ugent.be/download/pub_2647.pdf.
- [76] K. K. Lee, D. R. Lim, H.-C. Luan, A. Agarwal, J. Foresi and L. C. Kimerling, Appl. Phys. Lett., 2000, 77, 1617.
- [77] R. G Hunsperger, Losses in Optical Waveguides, Integrated Optics Theory and Technology, New York, Springer, **2009**.
- [78] R. Soref. *Nat. Photonics*, **2010**, *4*, 495.
- [79] R. A. Soref and J.P. Lorenzo, *Electron. Lett.* **1985**, *21*, 953.
- [80] R. A. Soref and J.P. Lorenzo, IEEE J. Quantum Electron. 1986, 22, 873.
- [81] T. Barwicz and H. Haus, J. Light. Technol. 2005, 23, 2719.
- [82] http://www.soitec.com/pdf/Soitec-FD-2D-product brief.pdf.
- [83] G. F. R. Chen, J. R. Ong, T. Y. L. Ang, S. T. Lim, C. E. Png and D. T. H. Tan, Sci. Rep. 2017, 7, 7246.
- [84] Q. Li, J. Light. Technol, 2008, 26, 3744.
- [85] A. M. Prabhu, A. Tsay, Z. Han and V. Van, IEEE Photon. Technol. Lett. 2009, 21, 651.
- [86] D. Venkatakrishnarao, E. A. Mamonov, T. V. Murzina and R. Chandrasekar, *Adv. Opt. Mater.* **2018**, *6*, 1800343.
- [87] N. Mitetelo, D. Venkatakrishnarao, J. Ravi, M. Popov, E. Mamonov, T. V. Murzina and R. Chandrasekar, *Adv. Opt. Mater.* **2019**, *7*, 1801775.
- [88] N. V. Mitetelo, M. E. Popov, E. A. Mamonov, A. I. Maydykovskiy, D. Venkatakrishnarao, J. Ravi, R. Chandrasekar and T. V. Murzina, *Laser Phys. Lett.* **2020**, *17*, 036201.
- [89] Y. S. Zhao, Organic Nanophotonics: Fundamentals and Applications, Springer, Berlin 2014.
- [90] R. Chandrasekar, Phys. Chem. Chem. Phys. **2014**, 16, 7173.
- [91] D. Venkatakrishnarao, E. A. Mamonov, T. V. Murzina and R. Chandrasekar, *Adv. Opt. Mater.* **2018**, *6*, 1800343.
- [92] N. Chandrasekhar, S. Basak, M. A. Mohiddon and R. Chandrasekar, *ACS Appl. Mater. Interfaces* **2014**, *6*, 1488.
- [93] V. V. Pradeep, M. Annadhasan and R. Chandrasekar, Chem. Asian J. 2019, 14, 4577.
- [94] Y. Zhang, Q. Liao, X. G. Wang, J. N. A. Yao and H. B. Fu, Angew. Chem., Int. Ed. 2017, 56, 3616.
- [95] M. P. Zhuo, J. J. Wu, X. D. Wang, Y. C. Tao, Y. Yuan and L. S. Liao, Nat. Commun. 2019, 10, 9.
- [96] M. Annadhasan, D. P. Karothu, R. Chinnasamy, E. Ahmed, L. Catalano, S. Ghosh, P. Naumov and R. Chandrasekar, *Angew. Chem., Int. Ed.* **2020**, *59*, 13821.
- [97] H. Liu, Z. Lu, Z. Zhang, Y. Wang and H. Zhang, Angew. Chem., Int. Ed. 2018, 57, 8448.
- [98] Z. Lu, Y. Zhang, H. Liu, K. Ye, W. Liu and H. Zhang, Angew. Chem., Int. Ed. 2020, 59, 4299
- [99] S. Hayashi and T. Koizumi, Angew. Chem., Int. Ed. 2016, 55, 2701.
- [100] L. Catalano, D. P. Karothu, S. Schramm, E. Ahmed, R. Rezgui, T. J. Barber, A. Famulari and P. Naumov, *Angew. Chem., Int. Ed.* **2018**, *57*, 17254.

- [101] J. M. Halabi, E. Ahmed, L. Catalano, D. P. Karothu, R. Rezgui and P. Naumov, *J. Am. Chem. Soc.* **2019**, *141*, 14966.
- [102] P. Hui and R. Chandrasekar, Adv. Mater. 2013, 25, 2963.
- [103] N. Chandrasekhar, R. Reddy, M. D. Prasad and R. Chandrasekar, Cryst. Eng. Comm. 2014, 16, 4696.
- [104] N. Chandrasekhar, M. A. Mohiddon and R. Chandrasekar, Adv. Opt. Mater. 2013, 1, 305.
- [105] D. Venkatakrishnarao, M. A. Mohiddon, N. Chandrasekhar and R. Chandrasekar, *Adv. Opt. Mater.* **2015**, *3*, 1035.
- [106] K. Takazawa, Y. Kitahama, Y. Kimura and G. Kido, Nano Lett., 2005, 5, 1293.
- [107] K. Takazawa, Chem. Mater. 2007, 19, 5293.
- [108] F. Balzer, V. G. Bordo, A. C. Simonsen and H. G. Rubahn, Appl. Phys. Lett. 2003, 82, 10.
- [109] F. Quochi, F. Cordella, A. Mura, G. Bongiovanni, F. Balzer and H. G. Rubahn, *Appl. Phys. Lett.* **2006**, *88*, 041106.
- [110] Y. S. Zhao, A. Peng, H. Fu, Y. Ma and J. Yao, Adv. Mater. 2008, 20, 1661.
- [111] H. Yanagi and T. Morikawa, Appl. Phys. Lett. 1999, 75, 187.
- [112] C. Zhang, C.-L. Zou, Y. Yan, R. Hao, F.-W. Sun, Z.-F. Han, Y. S. Zhao and J. Yao, *J. Am. Chem. Soc.* **2011**, 133, 7276.
- [113] Q. H. Cui, Q. Peng, Y. Luo, Y. Jiang, Y. Yan, C. Wei, Z. Shuai, C. Sun, J. Yao and Y. S. Zhao, *Sci. Adv.* **2018**, *57*, 11300.
- [114] M.-P. Zhuo, Y.-C. Tao, X.-D. Wang, Y. Wu, S. Chen, L.-S. Liao and L. Jiang, *Angew. Chem., Int. Ed.* **2018**, *57*, 11300.
- [115] J. D. Wright, Molecular Crystals, Cambridge University Press, Cambridge 1996.
- [116] C. Wang and C. C. Sun, Cryst. Eng. Comm. 2020, 22, 1149.
- [117] I. Azuri, E. Meirzadeh, D. Ehre, S. R. Cohen, A. M. Rappe, M. Lahav, I. Lubomirsky and L. Kronik, *Angew. Chem., Int. Ed.* **2015**, *54*, 13566.
- [118] S. Ghosh and C. M. Reddy, Angew. Chem. Int. Ed. 2012, 51, 10319.
- [119] Su. Saha, M. K. Mishra, C. M. Reddy and G. R. Desiraju, Acc. Chem. Res. 2018, 51, 2957.
- [120] C. M. Reddy, K. A. Padmanabhan and G. R. Desiraju, Cryst. Growth Des., 2006, 6, 2720.
- [121] M. Tonogaki, T. Kawata, S. Ohba, Y. Iwata and I. Shibuya, *Acta Crystallogr., Sect. B: Struct. Sci.,* **1993**, 49, 1031.
- [122] S. Varughese, M. S. R. N. Kiran, U. Ramamurty and G. R. Desiraju, *Angew. Chem. Int. Ed.* **2013**, *52*, 2701.
- [123] S. Saha and G. R. Desiraju, Chem. Eur. J. 2017, 23, 4936.
- [124] S. Saha and G. R. Desiraju, J. Am. Chem. Soc. 2017, 139, 1975.
- [125] S. Saha and G. R. Desiraju, *Chem. Commun.* **2017**, *53*, 6371.
- [126] S. Ghosh, M. K. Mishra, S. Ganguly and G. R. Desiraju, J. Am. Chem. Soc. 2015, 137, 9912.
- [127] S. Saha and G. R. Desiraju, Chem. Commun. 2016, 52, 7676.

- [128] G. R. Krishna, R. Devarapalli, G. Lal and C. M. Reddy, J. Am. Chem. Soc. 2016, 138, 13561
- [129] O. S. Bushuyev, T. C. Corkery, C. J. Barrett and T. Friščić, Chem. Sci. 2014, 5, 3158.
- [130] A. Worthy, A. Grosjean, M. C. Pfrunder, Y. Xu, C. Yan, G. Edwards, J. K. Clegg and J. C. Mc. Murtrie, *Nat. Chem.* **2018**, *10*, 65.
- [131] S. Ghosh and C. M. Reddy, Angew. Chem. Int. Ed. 2012, 124, 10465.
- [132] K. Takazawa, Y. Kitahama, Y. Kimura and G. Kido, Nano Lett. 2005, 7, 1293.
- [133] K. Takazawa, J-I. Inoue, K. Mitsuishi and T. Kuroda, Adv. Funct. Mater. 2013, 23, 839.
- [134] R. Huang, C. Wang, Y. Wang and H. Zhang, Adv. Mater., 2018, 30, 1800814.
- [135] K. Takazawa, J.-I. Inoue, K. Mitsuishi and T. Takamasu, Adv. Mater., 2011, 23, 3659.
- [136] C. T. Chen, S. Ghosh, C. M. Reddy and M. J. Buehler, Phys. Chem. Chem. Phys. 2014, 16, 13165.
- [137] M. A. Ferreira, M. A. Luersen and P. C. Borges, Dental Press J. Orthod. 2012, 17, 71.
- [138] N. Nayan, V. Buravalla and U. Ramamurty, Mater. Sci. Eng. A 2009, 525, 60.
- [139] C. M. Reddy, R. C. Gundakaram, S. Basavoju, M. T. Kirchner, K. A. Padmanabhan and G. R. Desiraju, *Chem. Commun.*, **2005**, 3945.
- [140] C. M. Reddy, M. T. Kirchner, R. C. Gundakaram, K. A. Padmanabhan and G. R. Desiraju, *Chem. Eur. J.*, **2006**, *12*, 2222.
- [141] G. M. Brown and O. A. W. Strydom, Acta Cryst. 1974, B30, 801.
- [142] L. Catalano, D. P. Karothu, S. Schramm, E. Ahmed, R. Rezgui, T. J. Barber, A. Famulari and P. Naumov, *Angew. Chem. Int. Ed.* **2018**, *57*, 17254.
- [143] E. Ahmed, D. P. Karothu and P. Naumov, Angew. Chem. Int. Ed. 2018, 57, 8837.
- [144] M. Owczarek at el. Nat. Commun. 2016, 7, 13108.
- [145] S. Basak and R. Chandrasekar. J. Mater. Chem. C 2014, 2, 1404.
- [146] D. Venkatakrishnarao and R. Chandrasekar, Adv. Opt. Mater. 2016, 4, 112.
- [147] J. Ravi, M. Annadhasan, A. V. Kumar and R. Chandrasekar, Adv. Funct. Mater. 2021, 31, 2100642.
- [148] M. Annadhasan, A. R. Agrawal, S. Bhunia, V. V. Pradeep, S. S. Zade, C. M. Reddy and R. Chandrasekar, *Angew. Chem., Int. Ed.* **2020**, *59*, 13852.
- [149] S. Dey, S. Das, S. Bhunia, R. Chowdhury, A. Mondal, B. Bhattacharya, R. Devarapalli, N. Yasuda, T. Moriwaki, K. Mandal, G. D. Mukherjee and C. M. Reddy, *Nat. Commun.* **2019**, *10*, 3711.
- [150] M. Đaković, M. Borovina, M. Pisačić, C. B. Aakeröy, Ž. Soldin, B. M. Kukovec and I. Kodrin, *Angew. Chem., Int. Ed.* **2018**, *57*, 14801.
- [151] N. Chandrasekhar and R. Chandrasekar, Angew. Chem., Int. Ed. 2012, 51, 3556.
- [152] Y. C. Tao, X. D. Wang and L. S. Liao, J. Mater. Chem. C 2019, 7, 3443.
- [153] J. Ravi, D. Venkatakrishnarao, C. Sahoo, S. R. G. Naraharisetty, N. Mitetelo, A. A. Ezhov, E. Mamonov, T. Murzina and R. Chandrasekar, *Chem. Nano. Mat.* **2018**, *4*, 764.
- [154] V. V. Pradeep, N. Mitetelo, M. Annadhasan, E. Mamonov, T. V. Murzina and R. Chandrasekar, *Adv. Opt. Mater.* **2020**, *8*, 1901317.

- [155] W. Zhang, J. Yao and Y. S. Zhao, Acc. Chem. Res. 2016, 49, 1691.
- [156] X. Wang, Q. Liao, H. Li, S. Bai, Y. Wau, X. Lu, H. Hu, Q. Shi, H. Fu, J. Am. Chem. Soc. 2015, 137, 9289.
- [157] D. Venkatakrishnarao, Y. S. L. V. Narayana, M. A. Mohaiddon, E. A. Mamonov, I. A. Kolmychek, A. I. Maydykovskiy, V. B. Novikov, T. V. Murzina and R. Chandrasekar, *Adv. Mater.* **2017**, *29*, 1605260.
- [158] J. Ravi, M. Annadhasan, A. V. Kumar and R. Chandrasekar, Adv. Funct. Mater. 2021, 31, 2100642.
- [159] C. M. Reddy, G. R. Krishna and S. Ghosh, Cryst. Eng. Comm, 2010, 12, 2296.
- [160] P. Naumov, S. Chizhik, M. K. Panda, N. K. Nath and E. Boldyreva, Chem. Rev., 2015, 115, 12440.
- [161] K. Takazawa, Chem. Phys. Lett. 2008, 452, 168.
- [162] K. Takazawa, J. Phys. Chem. C 2007, 111, 8671.
- [163] B. E. Little, S. T. Chu, H. A. Haus, J. Foresi and J. P. Laine, J. Lightwave Technol. 1997, 15, 998.
- [164] K. Takazawa, J. Inoue, K. Mitsuishi and T. Takamasu, Phys. Rev. Lett. 2010, 105, 067401.
- [165] A. Ksendzov and Y. Lin, Opt. Lett. 2005, 30, 3344.
- [166] I. M. White, H. Oveys and X. D. Fan, Opt. Lett. 2006, 31, 1319.
- [167] L. Coldren, S. Corzine and M. Mashanovitch, *Diode Lasers and Photonic Integrated Circuits*, 2nd ed., John Wiley and Sons, New York, **2012**.
- [168] A. Rauf, A. S. Abbas, U. A. Rana, S. U-D. Khan, S. Ali, Z-U. Rehman, R. Qureshi, H-B. Kraatz and F. Belanger-Gariepy, *Spectrochim. Acta A*, **2015**, *138*, 58.
- [169] H. Liu, Z. Lu, Z. Zhang, Y. Wang and H. Zhang, Angew. Chem., Int. Ed. 2018, 130, 8584.
- [170] S. Saha and G. R. Desiraju, Chem. Commun. 2018, 54, 6348.
- [171] G. Q. Wei, Y. Yu, M. P. Zhuo, X. D. Wang and L. S. Liao, J. Mater. Chem. C, 2020, 8, 11916.
- [172] M-P. Zhuo, G-P. He, Y. Yuan, Y-C. Tao, G-Q. Wei, X-D. Wang, S-T. Lee and L-S. Liao, *CCS Chem.* **2020**, *2*, 413.
- [173] J. Ravi and R. Chandrasekar, Adv. Opt. Mater. 2021, 9, 2100550.
- [174] M. Annadhasan, A. Vinod Kumar, D. Venkatakrishnarao, E. A. Mamonov and R. Chandrasekar, *Nanoscale Adv.* **2020**, *2*, 5584.
- [175] M. R. Molla, A. Das and S. Ghosh, Chem. Eur. J. 2010, 16, 10084.
- [176] J. Cao, H. Liu and H. Zhang, CCS Chem. 2020, 2, 2569.
- [177] G. R. Krishna, L. Shi, P. P. Bag, C. C. Sun and C. M. Reddy, Cryst. Growth Des. 2015, 15, 1827.
- [178] G. R. Krishna, R. Devarapalli, R. Prusty, T. Liu, C. L. Fraser, U. Ramamurty and C. M. Reddy, *IUCrJ*, **2015**, *2*, 611.
- [179] G. R. Krishna, M. S. R. N. Kiran, C. L. Fraser, U. Ramamurty and C. M. Reddy, Adv. Funct. Mater. 2013, 23, 1422.
- [180] M. J. Turner, S. P. Thomas, M. W. Shi, D. Jayatilaka and M. A. Spackman, *Chem. Commun.* **2015**, *51*, 3735.
- [181] F. Y. Gardes, D. J. Thomson, N. G. Emerson and G. T. Reed, Optics Express 2011, 19, 11804.

^[182] J. Ravi, A. V. Kumar, D. P. Karothu, M. Annadhasan, P. Naumov and R. Chandrasekar. *Adv. Funct. Mater.* **2021**, *31*, 2105415.

^[183] S. Varughese, M. Kiran, U. Ramamurty and G. R. Desiraju, Angew. Chem. Int. Ed. 2013, 125, 2765.

Appendix-A

Materials

2-Hydroxy-1-naphthaldehyde Sigma-Aldrich, 98%

4-Bromoaniline Sigma-Aldrich, ≥99.0%

N',N'-Dimethylbenzene-1,4-diamine TCI Chemicals Pvt. Ltd. 98%

Ethanol Analytical CDs reagent, 99.9%

4-Chloroaniline Sigma-Aldrich, 98%

1,4,5,8-naphthalenetetracarboxylic Sigma-Aldrich, 97%

dianhydride

p-toluidine Sigma-Aldrich, 99.6%

9,10-bis(phenylethynyl)anthracene (BPEA; Sigma-Aldrich, 97%

form A)

DMF Finar Chemicals Pvt. Ltd. 99.5%

Ethyl acetate Finar Chemicals Pvt. Ltd. 99.5%

Toluene Sigma-Aldrich, 99.5%

Dichloromethane Sigma-Aldrich, 99.5%

Hexane Finar Chemicals Pvt. Ltd. 95%

Methanol Sigma-Aldrich, 99.7%

Chloroform Sigma-Aldrich, 99.4%

Acetone Finar Chemicals Pvt. Ltd. 99.5%

CDCl₃ Sigma-Aldrich, 99.96%

Appendix-B

Instrumentation

Nuclear Magnetic Resonance (NMR) Spectroscopy

 1 H and 13 C NMR spectra were recorded on a Bruker DPX 400 and 500 MHz spectrometer with a solvent proton as internal standard (CDCl₃: 1 H: 7.26 ppm, 13 C: 77.16 ppm). Commercially available deuterated CDCl₃ was used. Chemical shifts (δ) are given in parts per million (ppm). Spectra were processed using topspin 4. 1. 1. software.

Single Crystal X-ray Diffraction (SCXRD)

Single-crystal X-ray diffraction data was recorded on Rigaku Oxford XtaLAB ProPilatus3 R 200K-A detector system equipped with a CuK α (λ = 1.54184 Å) MicroMax-003 microfocus sealed tube operated at 50 kV and 0.6 mA. All data were collected at 293 K, and the data reduction was performed using CrysAlisPro software. The crystal structure was refined and solved by using the OLEX software.

Nanoindentation

Nanoindentation was performed on Hysitron TI-950 Triboindenter with a peak load of 1000 μ N, loading rate 100 μ N/s, and holding time of 5 s with a spacing of 5 μ m between the two consecutive indents. The Berkovich tip (radius \approx 50 nm) was used for indentation.

Energy Framework Analysis

CrystalExplorer17 was used to construct energy frameworks for N,N'-bis(p-tolyl)-1,4,5,8-naphthalene diimide. Intermolecular interaction energies, which were separated into dispersion (E_{disp}), polarization (E_{pol}), electrostatic (E_{elec}), and repulsion (E_{rep}) energy elements, were calculated based on B3LYP/6-31 G(d,p) molecular wave-functions calculated using the CIF. The attained interaction energies were further utilized to map the network of energy frameworks across dissimilar planes. The radii of these cylinders are directly proportional to the strength of the corresponding intermolecular interactions.

Optical Absorption Spectroscopy

The solution-state and solid absorption spectra were collected using Jasco V-750 spectrophotometer in a diffuse reflectance UV-visible (DR-UV-vis) mode. The reflectance spectra were converted to absorbance using the Kubelka-Munk function.

Fluorescence Spectroscopy

The solution-state and solid emission spectra were recorded using an FP-8500 fluorescence spectrometer. The parameters used where Ex and Em bandwidth are 2.5 nm, sensitivity= medium, data interval=0.5 nm, response=1 sec, and scan speed 500 nm/min.

Photoluminescence Quantum Yield (PLQY) Estimation

$$QY_s = QY_r \times \left(\frac{I_s}{I_r}\right) \times \left(\frac{OD_r}{OD_s}\right) \times \left(\frac{n_s}{n_r}\right)^2$$

Where r and s correspond to reference and sample (Rhodamine 6G, PLQY = 0.95), I represent the integrated area under the PL spectrum, n and OD represent the n of the medium and optical density at the excitation wavelength, respectively.

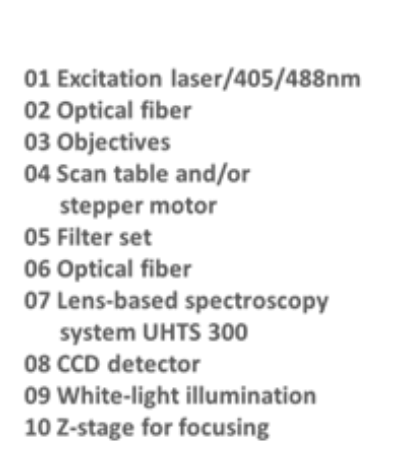
Micromanipulation (Mechanophotonics)

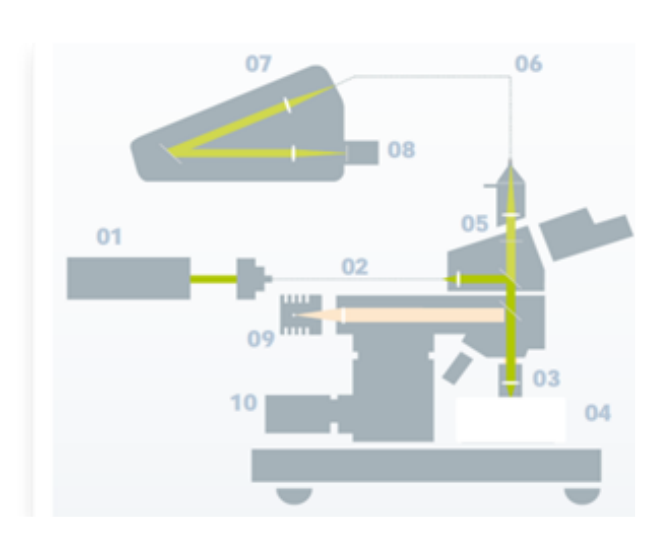
Fabrication of all the OPICs was realized using a mechanical micromanipulation approach manually. For this, a WITec alpha 300 confocal optical microscopy equipped with atomic force microscopy (AFM) was employed. The AFM cantilever (TipsNano: NSG10, Force constant $3.1-37.6 \, \text{N/m}$) was loaded on the holder and attached to the objective ($20\times$). The AFM tip radius of curvature is around 10 nm. The cantilever was moved in x-, y-, and z-directions for carrying out various micromechanical operations viz. bending, moving, cutting, and transferring (lifting + dropping).

Confocal Raman Micro-Spectroscopy

The optical properties were examined using a WITec alpha 300 confocal optical microscopy integrated with a Peltier-cooled CCD detector in the transmission mode setup. The excitation source was chosen to be a 355/405 nm diode laser with a 40×/60× bottom objective. The produced FL signal was recorded using 20× and 150× top objectives. Using

300 grooves/mm grating BLZ = 750 nm, each spectrum required five accumulations while integrating time being 0.5 s. The spectral data were processed using WITec 2.0 software. The optical waveguides/circuits/OPICs kept on the coverslip were excited with a laser in an orthogonal direction. The optical response of the fabricated OPICs was studied with different laser input powers. The signal intensities were sensitive to the excitation and collection position of the micro-crystal terminals, objective focus, and laser spot size. All the photonic experiments were performed in such a way to keep the above parameters nearly constant within the experimental limitation. All the spectral data were baseline corrected and analyzed. Laser power was measured using the THOR Labs power meter.

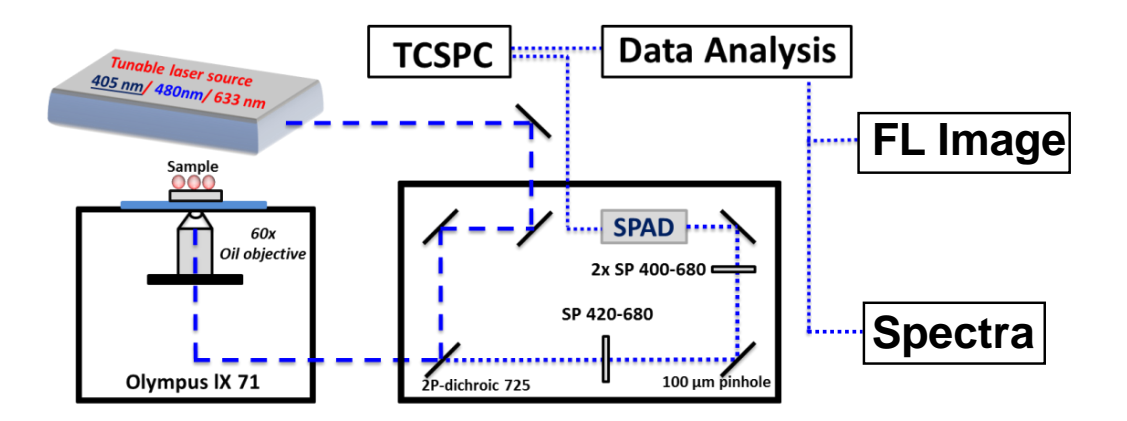




Fluorescence Lifetime Decay Studies (FLIM)

PL decays and PL lifetime images were recorded on a time-resolved Micro-Time 200 confocal fluorescence lifetime imaging microscopy (FLIM) setup (PicoQuant) equipped with an inverted microscope (Olympus IX 71). Measurements were performed under ambient conditions, at room temperature, on a microparticle deposited cover-slip.

Samples were excited by a 405 nm ps diode pulse laser with a stable repetition rate of 20 MHz (FWHM: 176 ps). The data acquisition was performed with a SymPhoTime software controlled PicoHarp 300 time-correlated single-photon counting (TCSPC) module in a time-tagged time-resolved mode. The overall resolution of the setup was 4 ps. The FLIM images of microspheres were recorded using a 60× Nikon objective with a scanned speed of 0.60 ms/pixel. The image pixels for micro-particles are 72×72 and 512×512, respectively.



Field Emission Scanning Electron Microscopy (FESEM)

The morphology of the microcrystals was examined using a Zeiss field-emission scanning electron microscope (FESEM) operating at 3 kV. The samples were fixed on an aluminum stage using carbon tapes. Samples were coated with a thin layer (3-5 nm) of sputtered gold before imaging, samples were coated with a thin layer (3-5 nm) of sputtered gold.

Appendix-C

Table A1: Crystal data and structure refinement parameters of NDIPH (CCDC: 2085175)

X-ray crystal structure information		
Compound	NDIPH	
Formula weight	446.44	
Temperature	296 K	
Crystal System	Monoclinic	
Space group	P2 ₁ /c	
a/Å	7.9835(6)	
b/Å	4.5105(4)	
c/Å	28.895(2)	
α/°	90	
β/°	91.884(3)	
γ/°	90	
Volume / Å ³	1039.94(14)	
Z	2	
ρ _{cal} cg / cm ³	1.426	
μ / mm ⁻¹	0.787	
F(000)	464.0	
Radiation	Cu Kα (λ = 1.54178 Å)	
2θ range for data collection/°	11.088 to 132.41	
Index ranges	-9 ≤ h ≤ 9, -4 ≤ k ≤ 5, -34 ≤ l ≤ 33	
Reflections collected	15589	
Independent reflections	1769 [R _{int} = 0.0815, R _{sigma} = 0.0529]	
Data/restraints/parameters	1769/0/155	
Goodness-of-fit on F ²	1.126	
Final R indexes [I>=2σ (I)]	R ₁ = 0.0739, wR ₂ = 0.1855	
Final R indexes [all data]	R ₁ = 0.0811, wR ₂ = 0.1905	
Largest diff. Peak/hole/e Å-3	0.25/-0.26	

Table A2: Crystal data and structure refinement parameters of *BPEA (form A)* (CCDC: 2085175)

Formula weight 378.44 Temperature 296 K Crystal System Monocl Space group C2/c a / Å 22.8500 b / Å 5.3568(inic 0(10) 2)
Temperature 296 K Crystal System Monocl Space group C2/c a / Å 22.8500 b / Å 5.3568(D(10) 2)
Crystal System Monocl Space group C2/c a / Å 22.8500 b / Å 5.3568(D(10) 2)
Space group C2/c a / Å 22.8500 b / Å 5.3568(D(10) 2)
a / Å 22.8500 b / Å 5.3568(2)
b / Å 5.3568(2)
	<u> </u>
. / Å	3(7)
c / Å 16.9443	
α/° 90	
β/° 99.952(2)
y/° 90	
Volume / Å ³ 2042.82	2(15)
Z 4	
D _{cal} cg / cm ³ 1.230	
μ / mm ⁻¹ 0.070	
F(000) 792.0	
Radiation Mo Kα	(λ = 0.71073 Å)
2θ range for data collection/° 3.62 to	51.988
Index ranges –28 ≤ h	≤ 28, −6 ≤ k ≤ 6, −20 ≤ l ≤ 20
Reflections collected 21230	
Independent reflections 2007 [R	int = 0.0302, R _{sigma} = 0.0130]
Data/restraints/parameters 2007/0,	/136
Goodness-of-fit on F ² 0.922	
Final R indexes [I>= 2σ (I)] $R_1 = 0.0$	423, wR ₂ = 0.1252
Final R indexes [all data] R ₁ = 0.0	494, wR ₂ = 0.1309
Largest diff. Peak/hole/e Å ⁻³ 0.14/–0).15

Research Publications from Thesis

 J. Ravi, M. Annadhasan, A. V. Kumar, and R. Chandrasekar Mechanically Reconfigurable Organic Photonic Integrated Circuits Made from Two Electronically Different Flexible Microcrystals. Adv. Funct. Mater. 2021. 31. 2100642.

2. J. Ravi, and R. Chandrasekar

Micromechanical Fabrication of Resonator Waveguides Integrated Four-Port Photonic Circuit from Flexible Organic Single Crystals.

Adv. Optical Mater. 2021, 9, 2100550.

3. J. Ravi, A. V. Kumar, D. P. Karothu, M. Annadhasan, P. Naumov, and R. Chandrasekar Geometrically Reconfigurable, 2D, All-Organic Photonic Integrated Circuits Made from Two Mechanically and Optically Dissimilar Crystals.

Adv. Funct. Mater. **2021**, 31, 2105415.

4. J. Ravi, A. V. Kumar, M. Annadhasan, and R. Chandrasekar Realization of Mechanically Maneuverable Circuit Ports in Organic Hybrid Photonic Chip for 360° Steering of Bandwidth-Engineered Signals.

Adv. Optical Mater. **2022**, 10, 2102545.

Other Research Publications

- 5. J. Ravi, R. Chinnasamy, V. V. Pradeep, D. Manoharan, F. Emmerling, B. Bhattacharya, S. Ghosh, and R. Chandrasekar Adaptable Optical Microwaveguides from Mechanically Flexible Crystalline Materials. Chem. Eur. J. 2022; doi.org/10.1002/chem.202200905.
- 6. M. Rohullah, V. V. Pradeep, J. Ravi, A. V. Kumar, and R. Chandrasekar Micromechanically-Powered Rolling Locomotion of a Twisted Crystal Optical-Waveguide Cavity as a Mobile Light Polarization Rotor. Angew. Chem. Int. Ed. 2022, 61, e202202114.
- 7. M. Annadhasan, V. V. Pradeep, A. V. Kumar, J. Ravi, and R. Chandrasekar Integrating Triply- and Singly-Bent Highly Flexible Crystal Optical Waveguides for Organic Photonic Circuit with a Long-Pass-Filter Effect.

 Small Struct. 2022, 3, 2100163.
- 8. C. Tardío, V. V. Pradeep, R. Martín, A. M. Rodríguez, A. D. L. Hoz, J. Ravi, M. Annadhasan, P. Prieto, and R. Chandrasekar *Polarised Optical Emission from Organic Anisotropic Microoptical Waveguides Grown by Ambient Pressure Vapour-deposition.*Chem. Asian J. 2021, 16, 1–6.
- **9.** M. Annadhasan, A. V. Kumar, **J. Ravi**, E. Mamonov, T. Murzina, and R. Chandrasekar *Magnetic Field–Assisted Manipulation of Polymer Optical Microcavities*.

Adv. Photonics Res. 2021, 2, 2000146.

10. A. V. Kumar, M. Rohullah, **J. Ravi**, M. Godumala, M. Annadhasan, and R. Chandrasekar *Mechanophotonic aspects of a room temperature phosphorescent flexible organic microcrystal.*

Cryst. Eng. Comm. 2021, 23, 5774-5779.

11. M. Popov, E. Mamonov, N. Mitetelo, K. Zhdanova, **J. Ravi**, R. Chandrasekar, and T. Murizina

Laser intensity-dependent nonlinear-optical effects in organic whispering gallery mode cavity microstructures.

Opt. Lett. 2020, 16, 4622-4625.

12. V. Radhika, M. Annadhasan, **J. Ravi**, M. D. Prasad, N. Mitetelo, K. Zhdanova, E. Mamonov, K. Müllen, T. Murzina, and R. Chandrasekar

Multifunctional Chiral π -Conjugated Polymer Microspheres: Production and Confinement of NLO signal, Detection of Circularly Polarized Light, and Display of Laser-Triggered NLO Emission Shifts.

Adv. Optical Mater. 2020, 8, 2000431.

13. N. V Mitetelo, M. E. Popov, E. A. Mamonov, A. I. Maydykovskiy, D. Venkatakrishnarao, **J. Ravi**, R. Chandrasekar, and T. V Murzina

Chirality Driven Effects in Multiphoton Excited Whispering Gallery Mode Microresonators Prepared by A Self-Assembly Technique.

Laser Phys. Lett. 2020, 17, 036201.

14. J. Ravi, D. Venkatakrishnarao, C. Sahoo, N. Mitetelo, A. A. Ezhov, E. Mamonov, T. Murzina, R. Chandrasekar

A Two-Photon Pumped Supramolecular Upconversion Microresonator.

Chem. Nano. Mat. 2018, 8, 764-768.

15. Mitetelo, D. Venkatakrishnarao, **J. Ravi**, M. Popov, E. Mamonov, T. V. Murzina, and R. Chandrasekar

Chirality-Controlled Multiphoton Luminescence and Second-Harmonic Generation from Enantiomeric Organic Micro-Optical Waveguides.

Adv. Optical Mater. 2019, 11, 1801775.

Presentations in Conferences and Symposiums

1. **J. Ravi**, and R. Chandrasekar

Mechanically Reconfigurable Organic Photonic Integrated Circuits Made from Two Electronically Different Flexible Microcrystals.

Poster presentation in DCBCS-2021, GITAM University, Visakhapatnam, and Hyderabad, India.

2. J. Ravi, and R. Chandrasekar

A Two-Photon Pumped Supramolecular Upconversion Microresonator. Poster presented at the Chem-Fest-2021, School of Chemistry, UOH, India.

3. J. Ravi, and R. Chandrasekar

Mechanically Reconfigurable Organic Photonic Integrated Circuits Made from Two Electronically Different Flexible Microcrystals.

Oral presentation at the Chem-Fest-2021, School of Chemistry, UOH, India.

Curriculum Vitae

Personal Details:

Name Jada Ravi Father's name Jada Lachaiah

Nationality Indian

D. O. B. 08. 06. 1990 Ph. No. +91-9494861928

E-mail jadaravi02@gmail.com

Permanent Address H.No: 21-76, Ramakistapur, Kodimial,

Jagtial, Telangana, India

Ph.D. in Materials Chemistry under the supervision of Prof. R.



2016-2022

Chandrasekar, School of Chemistry, University of Hyderabad,
India. Thesis Title: "Flexible Organic Crystalline Materials for
Photonic Integrated Circuits".

2012-2014 M.Sc in Chemistry (First Class) at the University of Hyderabad,
Hyderabad, Telangana, India.

2007-2010 B.Sc in Chemistry, Biotechnology and Zoology (First Class with
Distinction) at Sree Chaitanya Degree and PG College.
Karimnagar, Andhra Pradesh, India.

Kariffilagar, Affulla Frauesii, Iliula.

2005-2007 Intermediate in Chemistry, Physics and Biology (First Class) at

Govt. Junior College, Kodimial, Andhra Pradesh, India.

2000-2005 S.S.C. (First Class) at Z. P. P. High School, Kodimial, Andhra

Pradesh, India.

Awards and Recognitions:

- 2018-2021 Awarded as a Senior Research Fellow by CSIR-UGC, India.
- 2016-2018 Awarded as a Junior Research Fellow by CSIR-UGC, India.
- 2015 Qualified Junior Research Fellow by CSIR-UGC, India.
- March-2015 Qualified GATE in All India Level by New Delhi, India.
- Number of Publications: 15
- H-Index: 6

Flexible Organic Crystalline Materials for Photonic Integrated Circuits

by Jada Ravi

Submission date: 30-Jun-2022 10:03AM (UTC+0530)

Submission ID: 1864873137

File name: Jada_Ravi.pdf (11.34M)

Word count: 31258

Character count: 162766

Flexible Organic Crystalline Materials for Photonic Integrated Circuits

ORIGINALITY REPORT

37% SIMILARITY INDEX

4%

INTERNET SOURCES

J

35% PUBLICATIONS

2%

STUDENT PAPERS

PRIMARY SOURCES

Jada Ravi, Avulu Vinod Kumar, Durga Prasad Karothu, Mari Annadhasan, Panče Naumov, Rajadurai Chandrasekar. "Geometrically Reconfigurable, 2D, All - Organic Photonic Integrated Circuits Made from Two Mechanically and Optically Dissimilar Crystals", Advanced Functional Material 2021

Publication

Jada Ravi, Avulu Vinod Kumar, Mari Annadhasan, Rajadurai Chandrasekar. "Realization of Mechanically Maneuverable Circuit Ports in Organic Hybrid Photonic Chip for 360° Steering of Bandwidth - Engine Signals", Advanced Optical Materials, 20

Publication

//

Dr. R. CHANDRASEKAR Professor School of Chemistry University of Hyderabad Hyderabad-500046, India

choc! of Chemistry Iniversity of Hyderabad

lyderabad-500046, India

Jada Ravi, Mari Annadhasan, Avulu Vinod Kumar, Rajadurai Chandrasekar. "Mechanically Reconfigurable Organic

"Mechanically Reconfigurable Organic Photonic Integrated Circuits Made from Two 8%

A CHANDRA SELVARA

Electronically Different Flexible Microcrystals", Advanced Functional Materials, 2021

Jada Ravi, Rajadurai Chandrasekar. 6% "Micromechanical Fabrication of Resonator Waveguides Integrated Four - Port Photonic Circuit from Flexible Organic Single Crystals", Advanced Optical Materials, 2021 f Chemistry Publication derabad-500046, India Submitted to Higher Education Commission Pakistan Student Paper Rajadurai Chandrasekar. "Mechanophotonics < 1% -Mechanical Micromanipulation of Single -Crystals toward Organic Photonic Integrated Circuits", Small, 2021 Publication Rajadurai Chandrasekar. "Mechanophotonics < 1% - A guide to integrating microcrystals toward monolithic and hybrid all-organic photonic circuits", Chemical Communications, 2022 Publication Mari Annadhasan, Supratim Basak, Naisa < 1% Chandrasekhar, Rajadurai Chandrasekar. "Next - Generation Organic Photonics: The **Emergence of Flexible Crystal Optical** Waveguides", Advanced Optical Materials, 2020

9	Submitted to University of Hyderabad, Hyderabad Student Paper	<1%
10	www.freepatentsonline.com Internet Source	<1%
11	Ragaverthini Chinnasamy, Ravi Jada, Vuppu Vinay Pradeep, Deepak Manoharan et al. "Adaptable optical microwaveguides from mechanically flexible crystalline materials", Chemistry – A European Journal, 2022 Publication	<1%
12	Pance Naumov, Mari Annadhasan, Durga Prasad Karothu, Ragaverthini Chinnasamy et al. "Micromanipulation of Mechanically Compliant Organic Single-Crystal Optical Microwaveguides", Angewandte Chemie International Edition, 2020 Publication	<1%
13	arxiv.org Internet Source	<1%
14	export.arxiv.org Internet Source	<1%
15	www.mdpi.com Internet Source	<1%

lib.unisayogya.ac.id

		<1%
17	repository.hkbu.edu.hk Internet Source	<1%
18	Mari Annadhasan, Vuppu Vinay Pradeep, Avulu Vinod Kumar, Jada Ravi, Rajadurai Chandrasekar. "Integrating Triply - and Singly - Bent Highly Flexible Crystal Optical Waveguides for Organic Photonic Circuit with a Long - Pass - Filter Effect", Small Structures, 2021 Publication	<1%
19	drops.dagstuhl.de Internet Source	<1%
20	Submitted to VIT University Student Paper	<1%
21	gyan.iitg.ac.in Internet Source	<1%
22	Submitted to Leeds Metropolitan University Student Paper	<1%
23	"Photonic Microresonator Research and Applications", Springer Science and Business Media LLC, 2010 Publication	<1%
24	Mallesham Godumala, Avulu Vinod Kumar, Rajadurai Chandrasekar. "Room-temperature	<1%

phosphorescent organic materials for optical waveguides", Journal of Materials Chemistry C, 2021

Publication

25	130.15.90.245 Internet Source	<1%
26	Di Tian, Yulan Chen. "Optical Waveguides in Organic Crystals of Polycyclic Arenes", Advanced Optical Materials, 2021	<1%
27	candorgc.com Internet Source	<1%
28	epdf.pub Internet Source	<1%
29	Submitted to Somerset College Student Paper	<1%
30	artsandsciences.sc.edu Internet Source	<1%
31	cyberleninka.org Internet Source	<1%
32	Mari Annadhasan, Abhijeet R. Agrawal, Surojit Bhunia, Vuppu Vinay Pradeep et al. "Mechanophotonics: Flexible Single - Crystal Organic Waveguides and Circuits", Angewandte Chemie International Edition, 2020	<1%

34

<1%

Dasari Venkatakrishnarao, Evgeniy A. Mamonov, Tatiana V. Murzina, Rajadurai Chandrasekar. "Advanced Organic and Polymer Whispering-Gallery-Mode Microresonators for Enhanced Nonlinear Optical Light", Advanced Optical Materials, 2018

\ | %

Publication

Mehdi Rohullah, Vuppu Vinay Pradeep, Jada Ravi, Avulu Vinod Kumar, Rajadurai Chandrasekar. "Micromechanically - Powered Rolling Locomotion of Twisted - Crystal Optical - Waveguide - Cavity as a Mobile Light Polarization Rotor", Angewandte Chemie, 2022

<1%

Publication

Ragaverthini Chinnasamy, Jada Ravi, Vuppu Vinay Pradeep, Deepak Manoharan et al. "Adaptable Optical Microwaveguides From Mechanically Flexible Crystalline Materials", Chemistry – A European Journal, 2022 Publication

<1%

Rajadurai Chandrasekar. "Mechanophotonics – a guide to integrating microcrystals toward

<1%

monolithic and hybrid all-organic photonic circuits", Chemical Communications, 2022

Publication

38	wjgnet.com Internet Source	<1%
39	Submitted to Jawaharlal Nehru Technological University Student Paper	<1%
40	Soumyajit Ghosh, Manish Kumar Mishra. "Elastic Molecular Crystals: From Serendipity to Design to Applications", Crystal Growth & Design, 2021 Publication	<1%
41	Habib Ullah, Asif A. Tahir, Tapas K. Mallick. "Structural and electronic properties of oxygen defective and Se-doped p -type BiVO 4 (001) thin film for the applications of photocatalysis", Applied Catalysis B: Environmental, 2018 Publication	<1%
42	Submitted to University College London Student Paper	<1%
43	Submitted to University of Liverpool Student Paper	<1%
44	dottorati.unica.it Internet Source	<1%



<1%

46

Bin Liu, Hao Liu, Houyu Zhang, Qi Di, Hongyu Zhang. "Crystal Engineering of a Hydrazone Molecule toward High Elasticity and Bright Luminescence", The Journal of Physical Chemistry Letters, 2020

<1%

Publication



www.ico.uni-jena.de

Internet Source

<1%

Exclude quotes

On

Exclude matches

< 14 words

Exclude bibliography On